



materials

Volume 2

Environment- Friendly Construction Materials

Edited by
Shaopeng Wu, Inge Hoff, Serji N. Amirkhanian and Yue Xiao
Printed Edition of the Special Issue Published in *Materials*

Environment-Friendly Construction Materials

Environment-Friendly Construction Materials

Volume 2

Special Issue Editors

Shaopeng Wu

Inge Hoff

Serji N. Amirkhanian

Yue Xiao

MDPI • Basel • Beijing • Wuhan • Barcelona • Belgrade



Special Issue Editors

Shaopeng Wu

Wuhan University of Technology

(WUT)

China

Serji N. Amirkhanian

University of Alabama

USA

Inge Hoff

Norwegian University of Science and Technology

(NTNU)

Norway

Yue Xiao

Wuhan University of Technology (WUT)

China

Editorial Office

MDPI

St. Alban-Anlage 66

4052 Basel, Switzerland

This is a reprint of articles from the Special Issue published online in the open access journal *Materials* (ISSN 1996-1944) from 2018 to 2019 (available at: https://www.mdpi.com/journal/materials/special_issues/EFCM).

For citation purposes, cite each article independently as indicated on the article page online and as indicated below:

LastName, A.A.; LastName, B.B.; LastName, C.C. Article Title. *Journal Name* **Year**, Article Number, Page Range.

Volume 2

ISBN 978-3-03921-014-5 (Pbk)

ISBN 978-3-03921-015-2 (PDF)

Volume 1-3

ISBN 978-3-03897-418-5 (Pbk)

ISBN 978-3-03897-419-2 (PDF)

© 2019 by the authors. Articles in this book are Open Access and distributed under the Creative Commons Attribution (CC BY) license, which allows users to download, copy and build upon published articles, as long as the author and publisher are properly credited, which ensures maximum dissemination and a wider impact of our publications.

The book as a whole is distributed by MDPI under the terms and conditions of the Creative Commons license CC BY-NC-ND.

Contents

About the Special Issue Editors	vii
Yue Xiao, Feng Wang, Peide Cui, Lei Lei, Juntao Lin and Mingwei Yi Evaluation of Fine Aggregate Morphology by Image Method and Its Effect on Skid-Resistance of Micro-Surfacing Reprinted from: <i>Materials</i> 2018 , <i>11</i> , 920, doi:10.3390/ma11060920	1
Yongchun Cheng, Wensheng Wang, Jinglin Tao, Meng Xu, Xiaoli Xu, Guirong Ma and Shurong Wang Influence Analysis and Optimization for Aggregate Morphological Characteristics on High- and Low-Temperature Viscoelasticity of Asphalt Mixtures Reprinted from: <i>Materials</i> 2018 , <i>11</i> , 2034, doi:10.3390/ma11102034	15
Wensheng Wang, Yongchun Cheng, Guojin Tan and Jinglin Tao Analysis of Aggregate Morphological Characteristics for Viscoelastic Properties of Asphalt Mixes Using Simplex Lattice Design Reprinted from: <i>Materials</i> 2018 , <i>11</i> , 1908, doi:10.3390/ma11101908	41
Fanlong Tang, Guangji Xu, Tao Ma and Lingyun Kong Study on the Effect of Demulsification Speed of Emulsified Asphalt Based on Surface Characteristics of Aggregates Reprinted from: <i>Materials</i> 2018 , <i>11</i> , 1488, doi:10.3390/ma11091488	61
Zhuangzhuang Liu, Xiaonan Huang, Aimin Sha, Hao Wang, Jiaqi Chen and Cheng Li Improvement of Asphalt-Aggregate Adhesion Using Plant Ash Byproduct Reprinted from: <i>Materials</i> 2019 , <i>12</i> , 605, doi:10.3390/ma12040605	77
Dongliang Kuang, Yuan Jiao, Zhou Ye, Zaihong Lu, Huaxin Chen, Jianying Yu and Ning Liu Diffusibility Enhancement of Rejuvenator by Epoxidized Soybean Oil and Its Influence on the Performance of Recycled Hot Mix Asphalt Mixtures Reprinted from: <i>Materials</i> 2018 , <i>11</i> , 833, doi:10.3390/ma11050833	93
Dongliang Kuang, Zhou Ye, Lifeng Yang, Ning Liu, Zaihong Lu and Huaxin Chen Effect of Rejuvenator Containing Dodecyl Benzene Sulfonic Acid (DBSA) on Physical Properties, Chemical Components, Colloidal Structure and Micro-Morphology of Aged Bitumen Reprinted from: <i>Materials</i> 2018 , <i>11</i> , 1476, doi:10.3390/ma11081476	104
Tianyuan Yang, Meizhu Chen, Xinxing Zhou and Jun Xie Evaluation of Thermal-Mechanical Properties of Bio-Oil Regenerated Aged Asphalt Reprinted from: <i>Materials</i> 2018 , <i>11</i> , 2224, doi:10.3390/ma11112224	117
Pan Pan, Yi Kuang, Xiaodi Hu and Xiao Zhang A Comprehensive Evaluation of Rejuvenator on Mechanical Properties, Durability, and Dynamic Characteristics of Artificially Aged Asphalt Mixture Reprinted from: <i>Materials</i> 2018 , <i>11</i> , 1554, doi:10.3390/ma11091554	129
Zhelun Li, Xiong Xu, Jianying Yu and Shaopeng Wu Assessment on Physical and Rheological Properties of Aged SBS Modified Bitumen Containing Rejuvenating Systems of Isocyanate and Epoxy Substances Reprinted from: <i>Materials</i> 2019 , <i>12</i> , 618, doi:10.3390/ma12040618	147

Shi Xu, Xueyan Liu, Amir Tabaković and Erik Schlangen Investigation of the Potential Use of Calcium Alginate Capsules for Self-Healing in Porous Asphalt Concrete Reprinted from: <i>Materials</i> 2019 , <i>12</i> , 168, doi:10.3390/ma12010168	158
Benan Shu, Shaopeng Wu, Lijie Dong, Qing Wang and Quantao Liu Microfluidic Synthesis of Ca-Alginate Microcapsules for Self-Healing of Bituminous Binder Reprinted from: <i>Materials</i> 2018 , <i>11</i> , 630, doi:10.3390/ma11040630	171
Jiuming Wan, Yue Xiao, Wei Song, Cheng Chen, Pan Pan and Dong Zhang Self-Healing Property of Ultra-Thin Wearing Courses by Induction Heating Reprinted from: <i>Materials</i> 2018 , <i>11</i> , 1392, doi:10.3390/ma11081392	186
Changluan Pan, Ping Tang, Martin Riará, Liantong Mo, Mingliang Li and Meng Guo Effect of Healing Agents on Crack Healing of Asphalt and Asphalt Mortar Reprinted from: <i>Materials</i> 2018 , <i>11</i> , 1373, doi:10.3390/ma11081373	199
Quantao Liu, Cheng Chen, Bin Li, Yihan Sun and Hechuan Li Heating Characteristics and Induced Healing Efficiencies of Asphalt Mixture via Induction and Microwave Heating Reprinted from: <i>Materials</i> 2018 , <i>11</i> , 913, doi:10.3390/ma11060913	217
Chao Li, Shaopeng Wu, Guanyu Tao and Yue Xiao Initial Self-Healing Temperatures of Asphalt Mastics Based on Flow Behavior Index Reprinted from: <i>Materials</i> 2018 , <i>11</i> , 917, doi:10.3390/ma11060917	230

About the Special Issue Editors

Shaopeng Wu is a chief professor of materials science and engineering at Wuhan University of Technology. Dr. Wu is a prominent researcher in the field of bituminous materials and asphalt pavement. He has completed research projects on subjects including electrically conductive asphalt pavement, rubberized asphalt binder, recycling asphalt materials, self-healing asphalt, and asphalt preventive maintenance technologies. Dr. Wu is an editor of “Journal of Testing and Evaluation” and “International Journal of Pavement Research and Technology”, and a member of the International Society of Asphalt Pavement. He has received 14 provincial awards, including 3 first-prize Science and Technology Progress Awards. He has already supervised more than 30 research projects and published more than 300 SCI peer-reviewed journal papers.

Inge Hoff started his research career in the independent research organization SINTEF (Norway) doing contracted research projects for 10 years. Most of the projects were laboratory-based projects financed by the Norwegian Public Roads Administration or producers of different types of materials. Dr. Hoff was appointed to professor in 2009 and has been working at NTNU since then. He was a supervisor of nine completed Ph.D. projects and is currently supervising six Ph.D. students. Dr. Hoff has authored more than 80 scientific and popular scientific papers and is an active reviewer for several international scientific journals. In addition, he has authored several SINTEF reports. Dr. Hoff is the leader of the only research laboratory for materials for transport infrastructure in Norway. The laboratory is used for education of master’s and Ph.D. students, project-based testing for industry, and research purposes.

Serji N. Amirkhanian was the Mays Professor of Transportation and the director of the Asphalt Rubber Technology Services (ARTS) in the Department of Civil Engineering at Clemson University until June of 2010, before becoming a professor of civil engineering at the University of Alabama, Tuscaloosa, USA. He is also a professor of civil engineering at Wuhan University of Technology (Wuhan, China), in addition to being an adjunct professor of materials at Norwegian University of Science and Technology (NTNU), Norway.

His research has resulted in over 300 refereed journal papers, conference papers, and research reports. He has also published several book chapters. In addition, he has given over 300 presentations, presenting his research findings in the US and internationally. He has supported over 100 graduate students and over 15 post-doctoral scholars, conducting research for many agencies (e.g., the Federal Highway Administration (FHWA)). He has consulted for many companies or agencies, such as the World Bank, United Nations (UNIDO), BMW, Owens Corning, Michelin, Honeywell International, Ontario Ministry of Transportation, and Honduras Ministry of Transportation, among many others.

Yue Xiao has been an associate research professor at State Key Lab of Silicate Materials for Architectures in the Wuhan University of Technology since 2014. He was named the Fok Ying Tung Outstanding Young Teacher by the Ministry of Education of China in 2018. He received the title of CHUTIAN Scholar in material science and engineering from the Hubei provincial department of education in 2014. Dr. Xiao obtained his PhD degree in road and railway engineering from Delft University of Technology, the Netherlands. Subsequently, he joined Wuhan University of Technology. His research interests include eco-efficient pavement materials and construction material recycling.

Dr. Xiao is now conducting three innovative projects founded by the National Natural Science Foundation of China (NSFC), as well as projects supported by provincial departments. Since 2011, Dr. Xiao has published 49 SCI peer-reviewed journal papers.

Article

Evaluation of Fine Aggregate Morphology by Image Method and Its Effect on Skid-Resistance of Micro-Surfacing

Yue Xiao ^{1,†} , Feng Wang ¹, Peide Cui ^{1,*}, Lei Lei ^{2,†} , Juntao Lin ³ and Mingwei Yi ^{4,5}

¹ State Key Laboratory of Silicate Materials for Architectures, Wuhan University of Technology, Wuhan 430070, China; xiaoy@whut.edu.cn (Y.X.); wangfengfeng@whut.edu.cn (F.W.)

² Shenzhen MacRitchie Technology Co., Ltd., Shen Zhen 518101, China; nm3rnd@gmail.com

³ Faculty of Engineering, China University of Geosciences (Wuhan), Wuhan 430074, China; linjt@cug.edu.cn

⁴ National Engineering Research Center of Road Maintenance Technologies, Beijing 100095, China; cw hymw@gmail.com

⁵ Research Institute of Highway Ministry of Transport, Beijing 100088, China

* Correspondence: cuipeide@whut.edu.cn (P.C.); Tel.: +86-131-2519-2356

† These authors contributed equally to this work.

Received: 5 May 2018; Accepted: 29 May 2018; Published: 29 May 2018

Abstract: Micro-surfacing is a widely used pavement preventive maintenance technology used all over the world, due to its advantages of fast construction, low maintenance cost, good waterproofness, and skid-resistance performance. This study evaluated the fine aggregate morphology and surface texture of micro-surfacing by AIMS (aggregate image measurement system), and explored the effect of aggregate morphology on skid-resistance of single-grade micro-surfacing. Sand patch test and British pendulum test were also used to detect skid-resistance for comparison with the image-based method. Wet abrasion test was used to measure skid-resistance durability for feasibility verification of single-grade micro-surfacing. The results show that the effect of Form2D on the skid-resistance of micro-surfacing is much stronger than that of angularity. Combining the feasibility analysis of durability and skid-resistance, 1.18–2.36 grade micro-surfacing meets the requirements of durability and skid-resistance at the same time. This study also determined that, compared with British pendulum test, the texture result obtained by sand patch test fits better with results of image method.

Keywords: aggregate morphology; aggregate image measurement system; micro-surfacing; skid-resistance; surface texture

1. Introduction

With the development of transportation industry, the construction of the world's highway networks has gradually improved. The maintenance and disease prevention of asphalt pavements have already attracted widespread attention. Micro-surfacing is a widely used pavement preventive maintenance technology used all over the world, due to its advantages of fast construction, low maintenance cost, good waterproofness, and skid-resistance performance [1–4]. It consists of modified emulsified asphalt, aggregates, fillers, water, and additives. The number of traffic accident can be reduced if there is enough friction between tire and pavement surface [5,6]. Safe and comfortable conditions of micro-surfacing are directly related to abundant surface texture characteristics, which makes great contributes to skid-resistance [7–9].

Evaluation of asphalt pavement texture mainly includes microtexture and macrotexture. Macrotexture is closely related to the distribution and gradation of aggregates, while microtexture is dependent on aggregate morphological characteristics [10–13]. The traditional test methods

for texture property of asphalt pavements mainly include sand patch test and British pendulum test. These traditional testing methods are not only time-consuming, but also depend largely on the operator's subjective judgment, making the experimental results imprecise and incomplete. Accurate quantification of texture characteristics has great significance to fully understanding the skid-resistance of pavement.

Digital image processing technology has been used for accurately quantifying the texture characteristics of pavement, and a variety of equipment and image testing methods based on digital image processing technology has been rapidly developed [14–17]. AIMS (aggregate image measurement system) is an objective and credible instrument for evaluating morphological characteristics of aggregates and surface texture of pavements, which allows accurate and comprehensive analysis, and calculation of texture based on digital images collected by a high resolution digital camera and a variable magnification microscope [18–21].

Asi et al. performed a comparative study to find the British pendulum skid-resistance number for a number of mixes. It was found that the mix with 30% slag has the highest skid number, followed by Superpave, SMA, and Marshall mixes, respectively. Also, increasing the asphalt content above the optimal asphalt content value decreases the skid-resistance of these mixes [7]. Puzzo et al. presented an image-based technique for the assessment of a 3D model of pavement texture to calculate the digital mean texture depth (MTD), starting from the digital surface model (DSM) generated by the photos [22]. Araujo et al. detected characterization of three hot mix asphalt (HMA) texture properties using digital image processing techniques, and the results indicated that the HMA particle size distribution directly affects its texture characteristics [15]. Chen et al. used fractal dimension of the fracture surface to evaluate impact of contact stress distribution on skid-resistance of asphalt pavements. The result showed that the stress distribution increased with an increase of pavement texture depth or tire load, or a decrease of the tire inflation pressure. The influence of pavement roughness and tire load was more significant than tire inflation pressure on the stress concentration [23]. El-Desouky used a special fluid to conduct skid-resistance tests at below freezing temperatures, and test results were used to develop correction models for skid-resistance under temperature variations [24]. Although many studies focus on skid-resistance of asphalt pavements, no research has been done to correlate skid-resistance of micro-surfacing with fine aggregate morphologies.

The objective of this study is to evaluate fine aggregate morphology and surface texture of micro-surfacing by AIMS, and explore the effect of aggregate morphology on skid-resistance of single-grade micro-surfacing. A comparison between single-grade micro-surfacing and MS-2 (which will be explained in Section 2.1.3) standard micro-surfacing was conducted for exploring the feasibility of single-grade micro-surfacing. This study also aimed to correlate conventional texture characteristics with texture results detected by image method.

2. Materials and Research Methodologies

The specific contents of this paper are as follows:

1. Three types of fine aggregate are chosen which are steel slag, basalt, and limestone. Three grades 0.6–1.18, 1.18–2.36, and 2.36–4.75 are selected for each type of aggregate.
2. AIMS was used to evaluate morphological characteristics of nine (3×3) kinds of fine aggregates.
3. Modified emulsified asphalt used in micro-surfacing was prepared.
4. Nine kinds of micro-surfacing slurry mixture with single-grade aggregate was prepared, corresponding to nine kinds of aggregate. Another normal-grade micro-surfacing mixture was also prepared for comparison with single-grade micro-surfacing. There are, in total, 10 kinds of micro-surfacing in this study.
5. Sand patch test, British pendulum test, and image method were used to evaluate the skid-resistance of micro-surfacing. Wet abrasion test was used to test durability for verifying feasibility of single-grade micro-surfacing.

2.1. Materials

2.1.1. Aggregates

Basalt, limestone, and steel slag were selected as fine aggregates of micro-surfacing. Basalt is a basic volcanic rock, with a large compressive strength, low water absorption, and good wear resistance. Limestone has satisfactory physical properties, such as good workability, excellent sturdiness, and good cementation. However, it is generally not used on the surface of asphalt pavement, due to its lower strength than volcanic rocks, such as basalt [25,26]. Steel slag, as an industrial waste, has been more and more widely used in road engineering in recent years [27]. The fine aggregates used in this study were nine types in total: 0.6–1.18, 1.18–2.36, and 2.36–4.75; three grades for each type of aggregate. The basic performance indicators of fine aggregates are shown in Table 1.

Table 1. Fine aggregate basic characteristics.

Properties	Unit	Technical Requirements	Tested Value			Specification Used
			Basalt	Limestone	Steel Slag	
Sand equivalent	%	≥60	68	71	75	ASTM D 2419 [28]
Soundness	%	≥12	15.7	15.1	13.6	ASTM C 88 [29]
Apparent relative density	—	≥2.5	2.978	2.708	2.872	ASTM C 128 [30]
Angularity	s	≥30	42	45	43	ASTM C 1252 [31]

2.1.2. Modified Emulsified Asphalt

Modified emulsified asphalt uses asphalt as base material, macromolecule polymer as modifier, and emulsifier added to make asphalt droplets, dissolved in water. It is the binding material of micro-surfacing, and its quality has direct impact on the micro-surfacing's performance. In order to meet the requirements of rapid open traffic, the emulsifier used in the micro-surface must be slow-breaking and quick-curing cationic emulsifier. The commonly used modifiers are styrene–butadiene–styrene (SBS), styrene–butadiene rubber (SBR), and chloroprene rubber (CR) [32].

The asphalt used in this study was AH-70, where AH stands for heavy traffic paving asphalt, and 70 (unit is 0.1 mm) stands for its penetration. This kind of asphalt has moderate viscoelastic properties and good adhesion properties with aggregates. The modifier was styrene–butadiene rubber (SBR), and the emulsifier is the type of quick-set cationic emulsifier produced by Zhengtong Technology Company. Calcium chloride and polyvinyl alcohol (PVA) are chosen as additives to improve the stability of modified emulsified asphalt, preventing it from quick demulsification during mixing with aggregate.

Colloid mill was used to produce modified emulsified asphalt in this study. The basic principle of colloid mill is that the raw materials, such as asphalt, emulsifier, and water, pass through the gap between the fixed gear and the moving gear, which proceeds at high-speed relative motion, so that the material is subjected to powerful shearing force, friction force, and high-frequency vibration, making it effectively crushed, emulsified, and mixed.

The production process is that stabilizer, emulsifier, and SBR were sequentially added to the water, and mixed uniformly at 65 °C. After adjusting the pH to 2.5, it is put into colloid mill together with hot asphalt to make a modified emulsified asphalt. The proportion of raw materials and basic characteristics of modified emulsified asphalt are shown in Tables 2 and 3.

Table 2. Composition of modified emulsified asphalt.

Materials	Modified Emulsified Asphalt	Asphalt	Water	SBR	Emulsifier	Calcium Chloride	PVA
Weight (g)	500	300	177	12	10	0.5	0.5
Ratio (%)	100	60	35.4	2.4	2	0.1	0.1

Table 3. Basic characteristics of modified emulsified asphalt.

Properties	Unit	Technical Requirements	Tested Value	Specification Used	
Sieve residue (1.18)	%	≤0.1	0.04	ASTM D 244 [33]	
Charge	—	+	+	ASTM D 244 [33]	
Rotary viscosity	Pa · s	—	98	ASTM D 4402 [34]	
Evaporated residue content	%	≥60	62.5	ASTM D 244 [33]	
Evaporated residue properties	Penetration	0.1 mm	40–100	57.3	ASTM D 5 [35]
	Softening point	°C	≥53	54.8	ASTM D 36 [36]
	Ductility	cm	≥20	56	ASTM D 113 [37]
	Solubility	%	≥97.5	99.3	ASTM D 2042 [38]
Storage stability	1 day	%	≤1	ASTM D 244 [33]	
	5 day	%	≤5		

2.1.3. Micro-Surfacing Mixture

In order to obtain larger texture depth and skid-resistance than ordinary micro-surfacing, this study attempts to prepare single-grade micro-surfacing, which means aggregates in the micro-surfacing mixture have only one size. Corresponding to nine kinds of fine aggregate, nine kinds of single-grade micro-surfacing mixture were prepared. At the same time, in order to verify the feasibility of single-grade micro-surfacing, standard MS-2 micro-surfacing made with basalt was also designed for performance comparison with single-grade micro-surfacing. The grading curve of MS-2 mixture is shown in Figure 1. The proportion of materials in the 10 types of micro-surfacing mix are shown in Table 4. The percentage of cement and water in the table is with regard to the mass of aggregates as denominator.

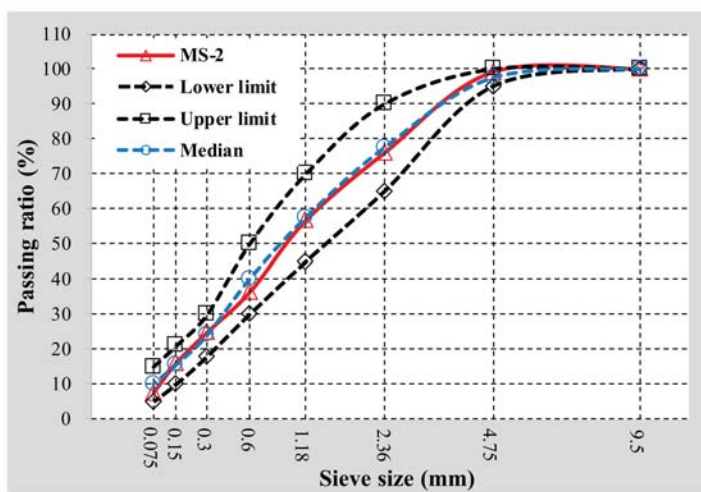


Figure 1. Gradation curves of MS-2 used in this work.

Table 4. Composition of 10 types of micro-surfacing.

Mixture Types	Limestone			Basalt			Steel Slag			MS-2
	0.6–1.18	1.18–2.36	2.36–4.75	0.6–1.18	1.18–2.36	2.36–4.75	0.6–1.18	1.18–2.36	2.36–4.75	
Thickness (mm)	6	6	6	6	6	6	6	6	6	6
Cement (%)	1	1	1	1	1	1	1	1	1	1
Water (%)	9.5	8.5	7.5	9.5	8.5	7.5	9.5	8.5	7.5	10
Asphalt-aggregate ratio (%)	7.5	7	6.5	7.5	7	6.5	7.5	7	6.5	10

The preparation procedures of micro-surfacing specimens used in this study are as follows: (1) Mix a certain amount of aggregate and cement, and then add water and modified emulsified asphalt in proportion according to Table 4 and mixed for one minute; (2) Flatten asphaltic felt and place a circular mold on it. Pour the flowing micro-surface mixture into the 6 mm height circular hole of the mold; (3) Scrape the excess mixture on template surface with a squeegee; (4) Take away the template and put specimens in oven at 60 °C until it reaches constant weight. The instruments for preparation and micro-surfacing specimens are shown in Figure 2.

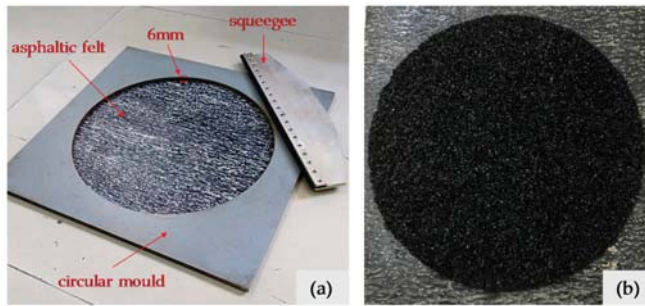


Figure 2. Instruments (a) for preparing micro-surfacing specimens (b).

2.2. Research Methodologies

2.2.1. Aggregates Morphology Test

The behaviors of asphalt pavement are directly affected by morphological characteristics of aggregate, which have been demonstrated by many researchers [39–43]. Most traditional test methods of aggregate morphology are indirect and subjective, while AIMS can obtain accurate aggregate morphology information, such as sphericity, angularity, flat and elongated ratio, and texture for coarse aggregate, angularity, and Form2D for fine aggregates through digital image processing.

AIMS consists of image capture hardware and software downloaded on a computer to operate the system and analyze information, which is shown in Figure 3. The image acquisition hardware consists of camera, microscope, aggregate tray, top-lighting, and backlighting systems. The image capture hardware obtains images and detects aggregate by a digital camera and a variable magnification microscope. A profile image of the aggregate is generated by backlighting, from which angularity gradients of the edges are evaluated. Then, top-lighting and variable magnification are utilized to capture surface texture, and test the height of each aggregate particle.

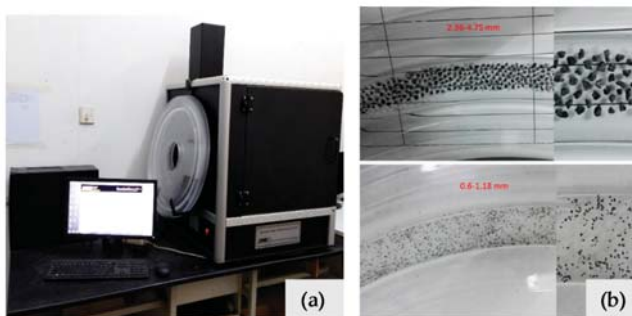


Figure 3. Aggregate image measurement system (a) and the tested fine aggregates placed on a tray (b).

2.2.2. Micro-Surfacing Skid-Resistance Test

Sand patch test [44], British pendulum test [45], and AIMS surface scanning were used to evaluate the texture characteristics in this study. British pendulum test evaluates surface texture of pavement using British pendulum number (BPN). The pendulum, which contains a standard rubber slide, is raised to a locked position, and then it is released, allowing the contact with the specimens' surface. The BPN is represented by the index where the pointer indicated. Although it is used over the world, it presents some critical issues, since it only describes the friction properties at very low speed.

Sand patch test was conducted in order to make up for the lack of BPN. It consists of spreading 25 cm³ of standard sand on clean and dry pavement surface, forming a circle. The diameter of the sand circle is measured, and then the texture depth can be calculated using following equation:

$$TD = 4V/\pi D^2, \quad (1)$$

where TD is texture depth, V is volume of standard sand, and D is diameter of sand circle.

In addition to testing the morphological characteristics of aggregates, AIMS can also provide texture characteristics of the surface of a mixture. It uses a camera to test the height of a 150 mm line on the specimen surface. Each specimen was rotated 45° for new line acquisition, resulting in four scan lines of each specimen. The variances of the heights were used to represent the surface texture of micro-surfacing.

2.2.3. Wet Abrasion Test

Due to the use of a single-grade micro-surfacing, verification of its durability is necessary. Wet abrasion test was used to measure skid-resistance durability. Its main steps include recording the specimen's mass as m_1 , then fixing the specimen in the tray, adding 25 °C water to completely immerse the sample, and insulation for one hour. The tray was raised so that the sample can jack the abrasion head and make the instrument operate for 300 s. The mass of specimens being abraded were recorded as m_2 . The wet abrasion loss can be calculated using the following equation:

$$WTAT = (m_1 - m_2)/A, \quad (2)$$

where WTAT is wet abrasion loss, m_1 and m_2 are the mass of specimens before and after abrasion, respectively, and A is the abrasion area of the instrument.

3. Results and Discussions

3.1. Fine Aggregates Morphology Characteristics

AIMS can evaluate angularity and Form2D for fine aggregate based on digital images. Angularity indicates the edge sharpness of aggregate particles. As the aggregate boundary features change, the angularity of aggregate also changes. AIMS uses the numbers 0–10,000 to express the angularity of each particle. The larger the angularity of aggregate, the sharper the edge of the aggregate is. The value of angularity is calculated based on the gradient on the particle boundary. The gradient technique is operated by calculating the inclination of gradient vectors on particle boundary points from the x-axis (horizontal axis in an image). The average change in the inclination of the gradient vectors is taken as an indication of angularity shown in equation (3).

$$\text{Angularity} = 1/\left(\frac{n}{3} - 1\right) \sum_{i=1}^{n-3} |\theta_i - \theta_{i+3}|, \quad (3)$$

where θ is angle of orientation of the edge points, n is the total number of points, and i is the ith point on the edge of the particle, as shown in Figure 4.

Form2D quantifies the relative form from 2-dimensional images of aggregate particles. Form2D has a relative scale of 0 to 20. A perfect circle has a 2D value of zero. The form index of Form2D is expressed by Equation (4).

$$\text{Form2D} = \sum_{\theta=0}^{\theta=360-\Delta\theta} \left[\frac{R_{\theta+\Delta\theta} - R_{\theta}}{R_{\theta}} \right], \tag{4}$$

where R_{θ} is the radius of particle at an angle of θ , and $\Delta\theta$ is the incremental difference in the angle. Illustration of Form2D and angularity is shown in Figure 4.

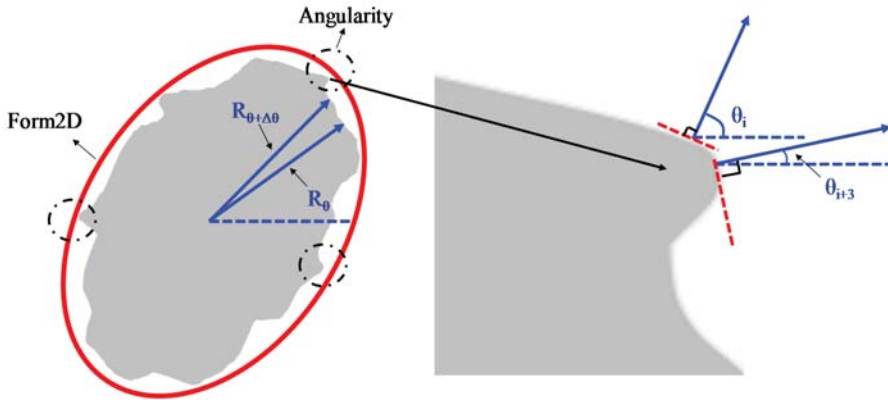


Figure 4. Illustration of Form2D and angularity.

Table 5 summarizes the morphological properties results of fine aggregates. AIMS provides the individual results for each particle analyzed, so the result shown in Table 5 is average values of 200 particles.

Table 5. Morphological properties of fine aggregates.

Properties	Limestone			Basalt			Steel Slag		
	0.6–1.18	1.18–2.36	2.36–4.75	0.6–1.18	1.18–2.36	2.36–4.75	0.6–1.18	1.18–2.36	2.36–4.75
Angularity	3285	3050	2923	3706	3502	3327	3789	4124	4546
Form2D	7.35	7.89	7.20	7.71	7.85	7.64	7.69	7.92	8.33

According to Table 5, the angularity and Form2D of steel slag are the largest among the three kinds of aggregate, which indicates that the used steel slag in this research has the most abundant morphology characteristics, followed by basalt. Limestone has the closest shape to circle, and the edges of the particles are the smoothest. For different sizes of the same kind of aggregate, angularity and Form2D of 2.36–4.75 grade are the largest of the three sizes of steel slag. For basalt and limestone, aggregate size with the largest angularity is 0.6–1.18, and with the largest, Form2D, is 1.18–2.36. The morphology of aggregates mainly depends on the method of mining and crushing, and there is no specific relationship with the aggregate type and size.

3.2. Skid-Resistance and Feasibility of Micro-Surfacing

Texture depths of 10 kinds of micro-surfacing evaluated by sand patch test are shown in Figure 5. Firstly, the texture depths of micro-surfacing mixture become larger as the aggregate particle sizes increases when the aggregate source is same. The reason is that the larger the average size of the aggregate particles, the more voids on the surface of the mixture, so that the standard sand can more easily enter the tiny gaps on the surface forming a smaller sand circle. Secondly, the texture depths of 1.18–2.36 and 2.36–4.75 grade micro-surfacing are both greater than those of standard MS-2. It is

demonstrated that single-grade micro-surfacing can indeed increase the surface texture characteristic, consequently increasing the skid-resistance.

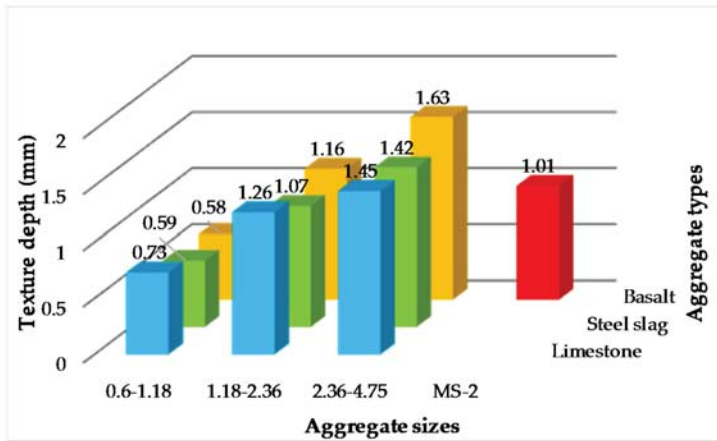


Figure 5. Texture depths of micro-surfacing.

BPN of 10 kinds of micro-surfacing evaluated by British pendulum test are shown in Figure 6. Firstly, the BPN of micro-surfacing mixture become larger as the aggregate particle sizes increases when the aggregate source is the same, except 0.6–1.18 of steel slag. Secondly, the BPN of micro-surfacing are all larger than those of standard MS-2 except 0.6–1.18 of limestone and basalt. The results also indicated that single-grade micro-surfacing can enlarge the skid-resistance of micro-surfacing.

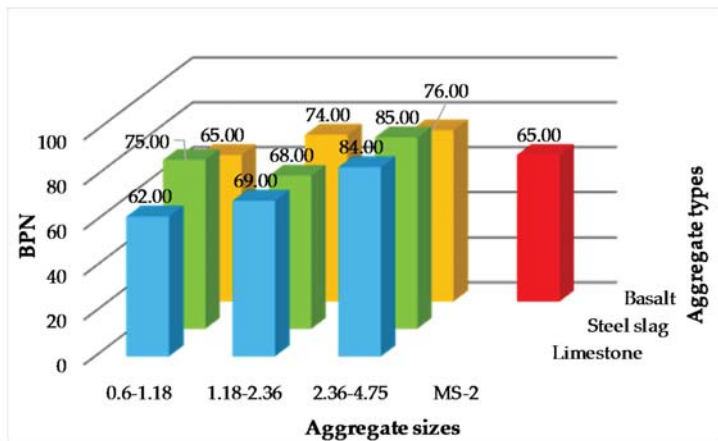


Figure 6. BPN of micro-surfacing.

The variances of heights detected by AIMS were also used to represent the surface texture of micro-surfacing, as shown in Figure 7. Same as the results obtained by the two previous conventional methods, only the 0.6–1.18 of steel slag and basalt micro-surfacing are smoother than standard MS-2. From the results of three kinds of surface texture tests, it can be seen that the surface textures of 1.18–2.36 and 2.36–4.75 single-grade micro-surfacing are larger than MS-2, regardless of the aggregate

sources. Therefore, from the perspective of skid-resistance performance, it is feasible to use the 1.18–2.36 and 2.36–4.75 grade aggregates to prepare single-grade micro-surfacing.

Since there is only one size of aggregate in single-grade micro-surfacing, it will lead to the loss of skeleton-embedded structure in mixture, which will then have a certain impact on the strength of micro-surfacing. Therefore, the verification of single-grade micro-surfacing’s durability is necessary. The WTAT of micro-surfacing are shown in Figure 8. The requirement of WTAT is less than 540 in specification. It can be seen that the 0.6–1.18 and 1.18–2.36 grade micro-surfacing meet the requirements. Therefore, 0.6–1.18 and 1.18–2.36 grade micro-surfacing is feasible from the perspective of durability. Combining the feasibility analysis of durability and skid-resistance, it can be seen that the 1.18–2.36 type micro-surfacing meets the requirements of durability and skid-resistance at the same time.

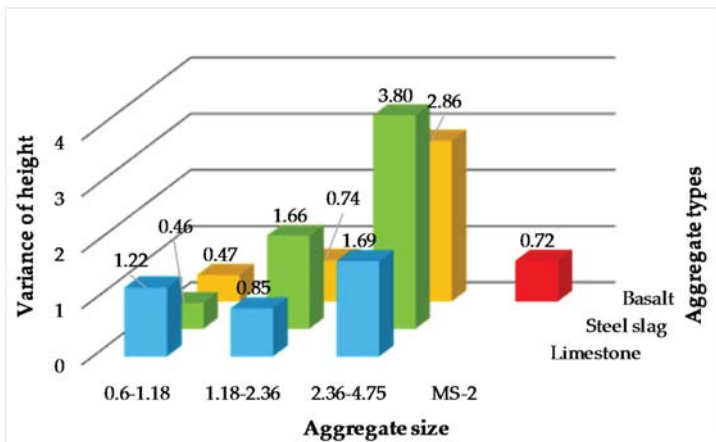


Figure 7. Height’s variance of micro-surfacing.

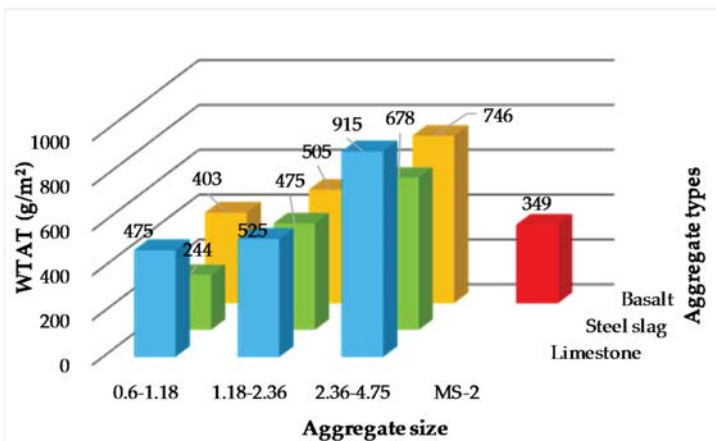


Figure 8. WTAT of micro-surfacing.

3.3. Correlation between Aggregate Morphology and Skid-Resistance

From the contents of previous chapter, it can be seen that 1.18–2.36 type micro-surfacing meets the feasibility requirements. Therefore, in this section, the influence of the fine aggregates’ morphological

characteristics on the surface texture of 1.18–2.36 micro-surfacing was discussed. The effect of aggregate morphology on texture depth, BPN and variance of height are shown in Figures 9–11, respectively.

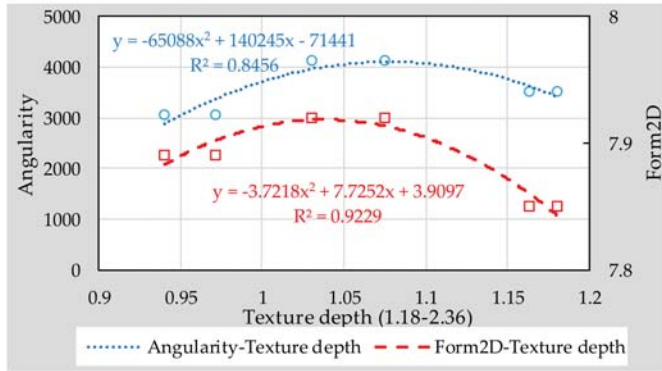


Figure 9. Correlation between aggregate morphology and texture depth.

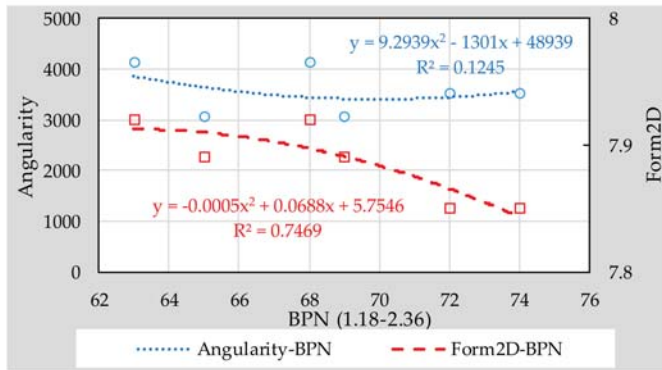


Figure 10. Correlation between aggregate morphology and British pendulum number (BPN).

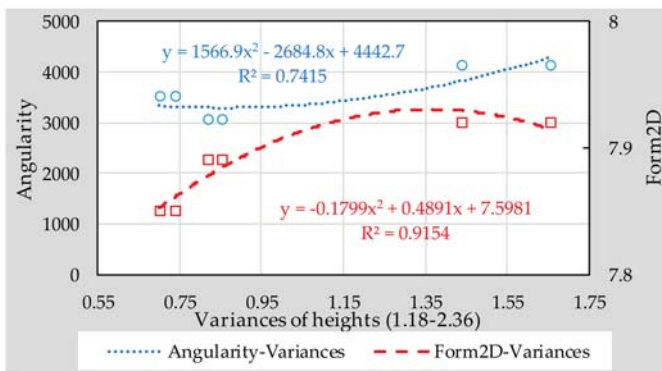


Figure 11. Correlation between aggregate morphology and variances of heights.

It can be seen from Figures 9–11 that the R^2 values of the relationship between Form2D and skid-resistance are all larger than those of angularity. This shows that the effect of angularity on the skid-resistance of micro-surfacing is weaker than that of Form2D. The reason might be that the angularity indicates the edge sharpness of aggregate, and the edge sharpness of fine aggregates is too small compared to the surface texture of micro-surfacing, so that there is no obvious relationship between them.

Compared to the BPN, Form2D correlated better with height of variance and texture depth, and the R^2 values reached 0.9154 and 0.9229, respectively. The reason might be that pendulum head's sliding length of the instrument is difficult to control precisely, resulting in a different friction distance between each specimen, thereby affecting the BPN results. So accurate quantification of texture characteristics should be considered for inclusion in the specification for fully understanding the skid-resistance of pavement.

3.4. Correlation between Traditional Test and Digital Image Method

Correlations between the traditional test and digital image method for skid resistance were analyzed, as shown in Figure 12. It can be seen that the texture results obtained by sand patch test fit better with the results of image method, compared with British pendulum test. However, the results of R^2 are only 0.6224 and 0.3945 for sand patch test and British pendulum test, respectively, indicating that the proposed quadratic functions between traditional skid-resistance results and image method results are not strong. More data is therefore needed to finalize a more accuracy correlation between traditional test and digital image method, regarding characterization of the texture depth of micro-surfacing.

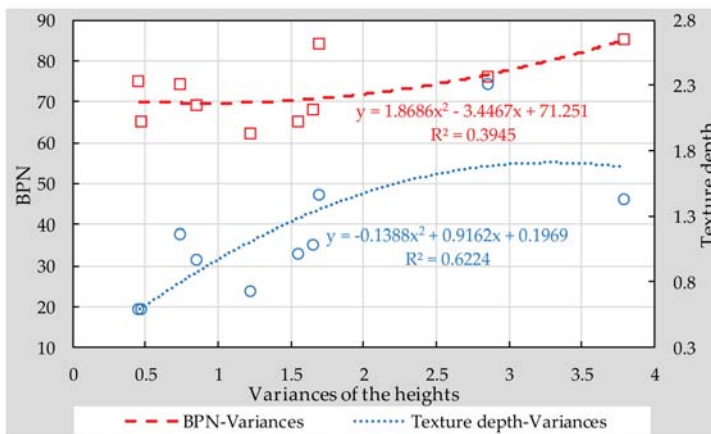


Figure 12. Correlation between traditional test and digital image method for skid-resistance.

4. Conclusions

The main objective of this study is to explore the effect of aggregate morphology on skid-resistance of single-grade micro-surfacing made with basalt, limestone, and steel slag. A comparison between single-grade micro-surfacing made with three kinds of aggregate and MS-2 standard micro-surfacing consists of basalt was firstly conducted for exploring the feasibility of single-grade micro-surfacing. Then, the correlation between conventional texture characteristics and texture results detected by image method was also discussed. Based on the above results, the following conclusions can be drawn:

1. Single-grade micro-surfacing can indeed increase the surface texture characteristics compared with standard micro-surfacing, thus increasing the skid-resistance.

2. Combining the feasibility analysis of durability and skid-resistance, it can be summarized that the 1.18–2.36 type micro-surfacing meets the requirements of durability and skid-resistance at the same time.
3. Form2D and angularity were characterized as morphologic indices of fine aggregates. Research results indicated that the effect of Form2D on skid-resistance of micro-surfacing is much stronger than that of angularity. Compared with BPN results, height of variance and texture depth correlated better with Form2D.
4. The texture result obtained by sand patch test fits better with results of image method compared with British pendulum test. However, both of them are not strong.

Author Contributions: F.W., Y.X., L.L. and P.C. conceived and designed the experiments; P.C. and F.W. performed the experiments; Y.X., L.L. and P.C. analyzed the data; J.L. and M.Y. contributed reagents/materials/analysis tools; Y.X., L.L. and F.W. wrote the paper.

Acknowledgments: This work is supported by the Natural Science Foundation of China (No. U1733121) and the Fundamental Research Funds for the Central Universities, China University of Geosciences (Wuhan) (CUG170621). The authors gratefully acknowledge their financial supports.

Conflicts of Interest: The authors declare no conflict of interest.

References

1. Wang, Z.J.; Gao, J.; Ai, T.; Zhao, P. Laboratory investigation on microwave deicing function of micro surfacing asphalt mixtures reinforced by carbon fiber. *J. Test. Eval.* **2014**, *42*, 498–507. [[CrossRef](#)]
2. Yu, J.M.; Zhang, X.N.; Xiong, C.L. A methodology for evaluating micro-surfacing treatment on asphalt pavement based on grey system models and grey rational degree theory. *Constr. Build. Mater.* **2017**, *150*, 214–226. [[CrossRef](#)]
3. Xiu, S.C.; Liu, M.H.; Chao, C.X.; Li, S.J. Study on micro-surface texture and tribology characters of ground surface in point grinding process. *Int. J. Surf. Sci. Eng.* **2014**, *8*, 225–238.
4. Kamaraj, C.; Lakshmi, S.; Rose, C.; Mani, U.; Paul, E.; Mandal, A.B.; Gangopadhyay, S. Experimental study on micro surfacing using chrome shaving impregnated with modified bitumen emulsion. *J. Sci. Ind. Res.* **2016**, *75*, 378–382.
5. Huang, C.Y.; Huang, X. Effects of pavement texture on pavement friction: A review. *Int. J. Veh. Des.* **2014**, *65*, 256–269. [[CrossRef](#)]
6. Xiao, Y.; Wang, Y.; Wu, S.; Yi, M. Assessment of bonding behaviours between ultrathin surface layer and asphalt mixture layer using modified pull test. *J. Adhes. Sci. Technol.* **2015**, *29*, 1508–1521. [[CrossRef](#)]
7. Asi, I.M. Evaluating skid resistance of different asphalt concrete mixes. *Build. Environ.* **2007**, *42*, 325–329. [[CrossRef](#)]
8. Kogbara, R.B.; Masad, E.A.; Kassem, E.; Scarpas, A.; Anupam, K. A state-of-the-art review of parameters influencing measurement and modeling of skid resistance of asphalt pavements. *Constr. Build. Mater.* **2016**, *114*, 602–617. [[CrossRef](#)]
9. Fwa, T.F. Skid resistance determination for pavement management and wet-weather road safety. *Int. J. Transp. Sci. Technol.* **2017**, *6*, 217–227. [[CrossRef](#)]
10. Kanafi, M.M.; Kuosmanen, A.; Pellinen, T.K.; Tuononen, A.J. Macro- and micro-texture evolution of road pavements and correlation with friction. *Int. J. Pavement Eng.* **2015**, *16*, 168–179. [[CrossRef](#)]
11. Pratico, F.G.; Astolfi, A. A new and simplified approach to assess the pavement surface micro- and macrotexture. *Constr. Build. Mater.* **2017**, *148*, 476–483. [[CrossRef](#)]
12. Kong, D.; Xiao, Y.; Wu, S.; Tang, N.; Ling, J.; Wang, F. Comparative evaluation of designing asphalt treated base mixture with composite aggregate types. *Constr. Build. Mater.* **2017**, *156*, 819–827. [[CrossRef](#)]
13. Cui, P.; Wu, S.; Xiao, Y.; Wan, M.; Cui, P. Inhibiting effect of layered double hydroxides on the emissions of volatile organic compounds from bituminous materials. *J. Clean. Prod.* **2015**, *108*, 987–991. [[CrossRef](#)]
14. Amarasiri, S.; Gunaratne, M.; Sarkar, S. Use of digital image modeling for evaluation of concrete pavement macrotexture and wear. *J. Transp. Eng.* **2012**, *138*, 589–602. [[CrossRef](#)]
15. Araujo, V.M.C.; Bessa, I.S.; Castelo Branco, V.T.F. Measuring skid resistance of hot mix asphalt using the aggregate image measurement system (aims). *Constr. Build. Mater.* **2015**, *98*, 476–481. [[CrossRef](#)]

16. Loprencipe, G.; Cantisani, G. Unified analysis of road pavement profiles for evaluation of surface characteristics. *Mod. Appl. Sci.* **2013**, *7*, 1–14. [[CrossRef](#)]
17. Chen, J.; Wang, H.; Li, L. Virtual testing of asphalt mixture with two-dimensional and three-dimensional random aggregate structures. *Int. J. Pavement Eng.* **2015**, *18*, 824–836. [[CrossRef](#)]
18. Mahmoud, E.; Gates, L.; Masad, E.; Erdogan, S.; Garboczi, E. Comprehensive evaluation of aims texture, angularity, and dimension measurements. *J. Mater. Civ. Eng.* **2010**, *22*, 369–379. [[CrossRef](#)]
19. Wang, L.B.; Sun, W.J.; Tutumluer, E.; Druta, C. Evaluation of aggregate imaging techniques for quantification of morphological characteristics. *Transp. Res. Rec.* **2013**, *2335*, 39–49. [[CrossRef](#)]
20. Bessa, I.S.; Franco Castelo Branco, V.T.; Soares, J.B. Evaluation of polishing and degradation resistance of natural aggregates and steel slag using the aggregate image measurement system. *Road Mater. Pavement Des.* **2014**, *15*, 385–405. [[CrossRef](#)]
21. Ding, X.; Ma, T.; Gao, W. Morphological characterization and mechanical analysis for coarse aggregate skeleton of asphalt mixture based on discrete-element modeling. *Constr. Build. Mater.* **2017**, *154*, 1048–1061. [[CrossRef](#)]
22. Puzzo, L.; Loprencipe, G.; Tozzo, C.; D'Andrea, A. Three-dimensional survey method of pavement texture using photographic equipment. *Measurement* **2017**, *111*, 146–157. [[CrossRef](#)]
23. Chen, B.; Zhang, X.; Yu, J.; Wang, Y. Impact of contact stress distribution on skid resistance of asphalt pavements. *Constr. Build. Mater.* **2017**, *133*, 330–339. [[CrossRef](#)]
24. El-Desouky, A. Investigating the effect of temperature variations on the measured airfield pavement skid resistance. *Constr. Build. Mater.* **2018**, *161*, 649–653. [[CrossRef](#)]
25. Wang, D.; Leng, Z.; Yu, H.; Hueben, M.; Kollmann, J.; Oeser, M. Durability of epoxy-bonded tio2-modified aggregate as a photocatalytic coating layer for asphalt pavement under vehicle tire polishing. *Wear* **2017**, *382*, 1–7. [[CrossRef](#)]
26. Xiao, F.; Punith, V.S.; Amirkhanian, S.N.; Thodesen, C. Improved resistance of long-term aged warm-mix asphalt to moisture damage containing moist aggregates. *J. Mater. Civ. Eng.* **2013**, *25*, 913–922. [[CrossRef](#)]
27. Chen, Z.; Wu, S.; Xiao, Y.; Zeng, W.; Yi, M.; Wan, J. Effect of hydration and silicone resin on basic oxygen furnace slag and its asphalt mixture. *J. Clean. Prod.* **2016**, *112*, 392–400. [[CrossRef](#)]
28. ASTM. *Test Method for Sand Equivalent Value of Soils and Fine Aggregate*; D2419-02; ASTM: West Conshohocken, PA, USA, 2005.
29. ASTM. *Test Method for Soundness of Aggregates by Use of Sodium Sulfate or Magnesium Sulfate*; C0088-99A; ASTM: West Conshohocken, PA, USA, 2013.
30. ASTM. *Test Method for Density, Relative Density (Specific Gravity), and Absorption of Fine Aggregate*; C0128-04A; ASTM: West Conshohocken, PA, USA, 2015.
31. ASTM. *Test Methods for Uncompacted Void Content of Fine Aggregate (as Influenced by Particle Shape, Surface Texture, and Grading)*; C1252-03; ASTM: West Conshohocken, PA, USA, 2017.
32. Guo, Y.; Ma, B.; Zhi, Z.; Tan, H.; Liu, M.; Jian, S.; Guo, Y. Effect of polyacrylic acid emulsion on fluidity of cement paste. *Coll. Surf. A Physicochem. Eng. Asp.* **2017**, *535*, 139–148. [[CrossRef](#)]
33. ASTM. *Test Methods and Practices for Emulsified Asphalts*; D0244-04; ASTM: West Conshohocken, PA, USA, 2015.
34. ASTM. *Test Method for Viscosity Determination of Asphalt at Elevated Temperatures Using a Rotational Viscometer*; D4402-02; ASTM: West Conshohocken, PA, USA, 2015.
35. ASTM. *Test Method for Penetration of Bituminous Materials*; D0005-05; ASTM: West Conshohocken, PA, USA, 2013.
36. ASTM. *Test Method for Softening Point of Bitumen (Ring-and-Ball Apparatus)*; D0036-95R00E01; ASTM: West Conshohocken, PA, USA, 2005.
37. ASTM. *Test Method for Ductility of Bituminous Materials*; D0113-99; ASTM: West Conshohocken, PA, USA, 2005.
38. ASTM. *Test Method for Solubility of Asphalt Materials in Trichloroethylene*; D2042-01; ASTM: West Conshohocken, PA, USA, 2015.
39. Chen, J.S.; Hsieh, W.; Liao, M.C. Effect of coarse aggregate shape on engineering properties of stone mastic asphalt applied to airport pavements. *Int. J. Pavement Res. Technol.* **2013**, *6*, 595–601.
40. Fletcher, T.; Chandan, C.; Masad, E.; Sivakumar, K. Measurement of aggregate texture and its influence on hot mix asphalt (hma) permanent deformation. *J. Test. Eval.* **2002**, *30*, 524–531.

41. Souza, L.T.; Kim, Y.R.; Souza, F.V.; Castro, L.S. Experimental testing and finite-element modeling to evaluate the effects of aggregate angularity on bituminous mixture performance. *J. Mater. Civ. Eng.* **2012**, *24*, 249–258. [[CrossRef](#)]
42. Maerz, N.H. Technical and computational aspects of the measurement of aggregate shape by digital image analysis. *J. Comput. Civ. Eng.* **2004**, *18*, 10–18. [[CrossRef](#)]
43. Bessa, I.S.; Castelo Branco, V.T.F.; Soares, J.B.; Nogueira Neto, J.A. Aggregate shape properties and their influence on the behavior of hot-mix asphalt. *J. Mater. Civ. Eng.* **2015**, *27*, 04014212. [[CrossRef](#)]
44. ASTM. *Standard Test Method for Measuring Pavement Macrotexture Depth Using a Volumetric Technique*; E965–96; ASTM: West Conshohocken, PA, USA, 2015.
45. ASTM. *Standard Test Method for Measuring Surface Frictional Properties Using the British Pendulum Tester*; E303–93; ASTM: West Conshohocken, PA, USA, 2005.



© 2018 by the authors. Licensee MDPI, Basel, Switzerland. This article is an open access article distributed under the terms and conditions of the Creative Commons Attribution (CC BY) license (<http://creativecommons.org/licenses/by/4.0/>).

Article

Influence Analysis and Optimization for Aggregate Morphological Characteristics on High- and Low-Temperature Viscoelasticity of Asphalt Mixtures

Yongchun Cheng ¹, Wensheng Wang ^{1,*} , Jinglin Tao ^{2,*}, Meng Xu ³, Xiaoli Xu ³, Guirong Ma ¹ and Shurong Wang ¹

¹ College of Transportation, Jilin University, Changchun 130025, China; chengyc@jlu.edu.cn (Y.C.); magrjlu@163.com (G.M.); wangsrjlu@163.com (S.W.)

² Jiangxi Transportation Institute, Nanchang 330200, China

³ Jilin Zhongteng Road & Bridge Construction Co., Ltd., Changchun 130022, China; xumeng2018jlu@163.com (M.X.); xuxiaoli2018jlu@163.com (X.X.)

* Correspondence: wangws17@mails.jlu.edu.cn (W.W.); taojl18@163.com (J.T.); Tel.: +86-8509-5446 (W.W.)

Received: 27 September 2018; Accepted: 16 October 2018; Published: 19 October 2018

Abstract: Aggregate is an indispensable raw material for asphalt pavement construction. This study evaluates the influences of aggregate morphological characteristics on the high- and low-temperature viscoelasticity of asphalt mixtures. Based on simplex lattice mixture design (SLD), asphalt mix samples were designed and prepared with the same gradation but three different types of aggregates. Subsequently, three morphological characteristics of aggregate (roundness, perimeter index, and erosion-dilation area ratio) are presented to characterize fine and coarse aggregates. Then based on Burgers viscoelastic model, uniaxial compression static creep test was carried out to analyze the high-temperature viscoelastic properties for asphalt mortar and mixture. Meanwhile fitting Prony series models have been utilized to represent relaxation modulus conversed from creep compliance and the low-temperature relaxation characteristics can be also discussed. The experimental results indicated that morphological characteristics of aggregate, especially fine aggregates, are strongly correlated with the viscoelastic parameters of asphalt mixtures. However, the complex morphological characteristics of aggregates have opposite influences on the high- and low-temperature viscoelastic parameters. Therefore, when considering both high- and low-temperature viscoelastic properties, the aggregate proportion was optimized for the appropriate morphological characteristics, which will provide a reference for asphalt mixture design.

Keywords: asphalt mixture; viscoelastic properties; creep; relaxation; aggregates; morphology

1. Introduction

Aggregate is an important raw material and it directly affects the performances of asphalt pavement engineering, which is highly related to the efficiency of asphalt pavement maintenance [1]. Aggregate in asphalt mixtures generally accounts for approximately over 90% by weight, which plays a major role for its stability, durability, and mechanical properties.

Researchers have constantly developed research methods to study the aggregates morphological characteristics. Wilson and Klotz [2] presented a method of measuring angularity using Hough transform for quantitative analysis of aggregate angularity. Kuo et al. [3] used a digital image-analysis method to investigate the coarse aggregates morphologies and quantified the morphological characteristics in an effective way. Masad and Button [4] investigated the angularity and texture of fine aggregates by using erosion-dilation method and form factor, in which angularity is analyzed by high-resolution images and texture is described by low-resolution images. Kuo and Freeman [5]

defined three image indices called aspect ratio, angularity, and roughness to characterize overall shape, roundness of corners and particle surface texture of fine aggregates. Wang et al. [6] developed a unified Fourier morphological analysis method for quantifying the aggregate morphological characteristics, including shape, angularity, and surface texture. Hu et al. [7] studied the effects of aggregate particles on internal structure in asphalt concrete and results showed that high-temperature damage is mainly caused by coarse aggregate particles. Xie et al. [8] found that digital image processing technique is useful for evaluating morphological characteristics of fine aggregate among three methods. Xiao et al. [9] studied the fine aggregate morphology through using aggregate image measurement system. Ding et al. [10] proposed a modeling algorithm to capture the realistic shape of aggregates and characterize the granular aggregates mechanical properties accurately. Wang et al. [11] proposed an algorithm for modeling two-dimensional virtual aggregates that is based on the Aggregate Imaging Measurement System and the Particle Flow Code in Two Dimensions.

According to existing research on aggregates morphology evaluation, lots of researchers studied the influences of aggregate morphological characteristics on the performances of asphalt mixtures. Chen et al. [12] demonstrated the effects of morphological characteristics of coarse aggregates on the engineering properties of hot-mix asphalt (HMA) mixtures. Masad et al. [13] addressed the relationship between morphological characteristics of fine aggregate and performances of asphalt mixtures and they found that aggregate texture characteristic had the strongest correlation with rutting resistance of asphalt mixtures. Arasan et al. [14] showed that there is a good correlation between some shape indices of aggregate and volumetric performances of asphalt mixtures. Singh et al. [15] utilized aggregate shape parameters to estimate dynamic modulus of asphalt mixes by establishing a model. Pan et al. [16] investigated the effects of coarse aggregate morphology on the permanent deformation of asphalt mixtures. The permanent deformation showed a best correlation with the surface texture and the angularity and surface texture have significant influences on the permanent deformation. Valdes-Vidal et al. [17] investigated the influence of aggregate physical properties on the mechanical properties of asphalt concretes and the results demonstrated that the morphological characteristics of coarse and fine aggregates have influences on strength and anti-cracking of asphalt concretes. Aragao et al. [18] evaluated the influence of morphological properties of aggregates on the mechanical behavior of bituminous mixtures. Thus, the aggregate morphological characteristics have significantly direct influences on the performances of asphalt mixture.

In addition, asphalt mixture is a typical viscoelastic material with the characteristics of both Hookean elasticity and Newtonian viscosity. Its viscoelastic characteristics are the basis for investigation on pavement cracking and permanent deformation of asphalt mixture [19,20]. In general, the physical quantities, such as creep compliance, relaxation modulus, and so on, are used represent the basic viscoelastic characteristics of asphalt mixtures [21]. Despite extensive researches have been conducted to investigate the influence of aggregate morphological characteristics on performances of asphalt mixture, no much study has been conducted for the viscoelastic characteristics of asphalt mixture.

The objective of this study is to relate the aggregate morphological characteristics to the high- and low-temperature viscoelastic properties of asphalt mixture. For that, an experimental proportion design was designed for asphalt mortars and mixtures were prepared with the same gradation but three different types of aggregates based on simplex lattice design (SLD) method. Three aggregate morphological characteristics (roundness, perimeter index and erosion-dilation area ratio) are chosen to characterize fine and coarse aggregates. Then based on Burgers viscoelastic model, uniaxial compression static creep test was carried out to analyze the high-temperature viscoelastic properties for asphalt mix. Meanwhile, by fitting Prony series models, relaxation modulus can be converted from creep compliance and the low-temperature relaxation characteristics can be also discussed.

2. Materials and Experimental Methods

2.1. Raw Materials

In this study, the base asphalt AH-90 obtained from Panjin of Liaoning Province in China was used and its physical properties are listed in Table 1. The mineral filler used is limestone powder, for which the diameter with percent passing 50% is 2.326 μm , and its properties are shown in Table 2. In order to demonstrate the effects of morphological characteristics of aggregates, three different types of coarse and fine aggregates from Jilin Province in China were selected, in which the coarse aggregates include basalt stone, andesite stone, and pebble, and the fine aggregates are basalt manufactured sand, andesite manufactured sand, and river sand. Their physical properties are shown in Tables 3 and 4.

Table 1. Physical properties of base asphalt AH-90.

Property	Unit	Measurement	Technical Criterion
Penetration @ 25 °C, 100 g, 5 s	0.1 mm	90	80~100
Softening point	°C	42.6	≥ 42
Ductility @ 15 °C, 5 cm/min	cm	195.2	≥ 100
Density @ 15 °C	g/cm^3	1.014	-
<i>After TFOT</i>			
Mass loss	%	0.37	± 0.8
Penetration ratio @ 25 °C	%	59	≥ 54

Table 2. Properties of limestone powder.

Property	Specific Gravity	Specific Surface Area	Hydrophilic Coefficient	Main Composition
Value	2.652	0.886	0.80	CaCO_3
Unit	g/cm^3	m^2/g	-	-

Table 3. Apparent densities of coarse and fine aggregates (Unit: g/cm^3).

Size (mm)	13.2	9.5	4.75	2.36	1.18	0.6	0.3	0.15	0.075
Basalt	2.782	2.774	2.770	2.758	2.713	2.720	2.699	2.647	2.700
Andesite	2.785	2.853	2.729	2.717	2.658	2.701	2.639	2.645	2.648
Pebble/River Sand	2.656	2.644	2.645	2.636	2.624	2.606	2.635	2.698	2.597

Table 4. Properties of coarse aggregate.

Property	Natural Bulk Density (%)	Tapped Bulk Density (%)	Wearing Value (%)
Basalt Stone	1.511	1.636	10.18
Andesite Stone	1.502	1.635	11.26
Pebble	1.536	1.640	23.64

2.2. Sample Preparation and Aggregates Morphological Characteristics

2.2.1. Sample Preparation

(1) Aggregate Proportion Design

Based on the mathematical theory, statistical analysis, and experimental design [22], SLD as a common mixture design method, has been utilized to investigate the influences of the proportions of three mixture components on the viscoelastic characteristics of asphalt mixes using Design-Expert 8.0 software (Stat-Ease Inc., Minneapolis, MN, USA). Three types of aggregates, namely basalt, andesite, and pebble/river sand, are considered as three different components, and the samples of asphalt mixes can be prepared through mixing the three ingredients at different proportions. Then, a larger range of morphological parameters for these aggregates could be designed by using SLD. The designed

proportions of three components in asphalt mixes are listed in Table 5, for example, in sample group 1, basalt:andesite:pebble/river sand = 0.167:0.667:0.167.

Table 5. Experimental proportion design based on simplex lattice design (SLD).

Mix Component	Sample Group									
	1	2	3	4	5	6	7	8	9	10
Basalt	0.167	0.167	0.000	0.500	1.000	0.500	0.667	0.000	0.000	0.333
Andesite	0.667	0.167	1.000	0.000	0.000	0.500	0.167	0.000	0.500	0.333
Pebble/River Sand	0.167	0.667	0.000	0.500	0.000	0.000	0.167	1.000	0.500	0.333

(2) Asphalt Mortar and Mixture Preparation

In this study, asphalt mixes including mortar and mixture samples were prepared to analyze and demonstrate the influences of morphological characteristics of coarse and fine aggregates on the high- and low-temperature viscoelastic characteristics, respectively. The gradation of asphalt mixture was selected the typical dense gradation with a nominal maximum size of 13.2 mm, i.e., AC-13. Asphalt mortar consists of asphalt, mineral filler and fine aggregate passing through 2.36 mm sieve size, and its gradation was similar to AC-13. The detailed sample preparation process was given in a previous study [23]. After determining asphalt contents, each component content in asphalt mortar and mixture could be calculated according to the densities of aggregate and asphalt, which are listed in Table 6. Then, the cylindrical samples of asphalt mortar with 50 mm in height and 50 mm in diameter were prepared through the static pressure method [24], and the Marshall specimens of asphalt mixture with 63.5 mm in height and 101 mm in diameter were made by Marshall compactor (Lambert Testing Machine Co., Ltd., Tianjin, China) according to the Chinese specification JTG E20-2011 [25]. However, beam samples are generally used for low-temperature property test. Therefore, beam samples with a length of 250 mm, width of 30 mm, and height of 35 mm, were prepared for asphalt mortar by a self-designed mould under static pressure; the square slab with length and width of 300 mm and thickness of 50 mm were prepared and then made into beam samples with 250 mm × 30 mm × 35 mm for asphalt mixture. These samples are shown in Figure 1.

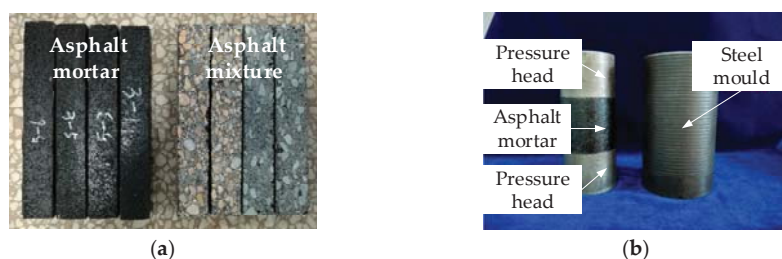


Figure 1. Samples of asphalt mixture and mortar: (a) Beam samples; and, (b) Cylindrical samples.

Table 6. Each component content of asphalt mixes.

Component	Proportion	Aggregate	Filler	Asphalt	Air Void
Asphalt Mixture	Mass (%)	89.5	5.7	4.8	-
	Volume (%)	79.3	5.2	11.5	4
Asphalt Mortar	Mass (%)	74.1	14.3	11.6	-
	Volume (%)	59.8	11.6	24.6	4

2.2.2. Morphological Characteristics of Aggregates: Shape, Angularity and Texture

The image processing technique is employed to process (image denoising and enhancement) these color images, in which the images of coarse and fine aggregate were obtained by scanner and

stereo microscope (Opt Vision Technology Co., Ltd., Dongguan, China). Then, the morphological characteristics of aggregates, including shape, angularity, and texture characteristics, can be obtained according to previous study [23]. Roundness, perimeter index, and erosion-dilation area ratio were used to represent the shape, angularity, and texture characteristics of aggregates, which were defined and could be measured in previous study [23]. The mean values of logarithmic normal distribution were selected to represent aggregate morphological characteristics. *Composite index* for fine and coarse aggregates is adopted to unify and account for these three morphological characteristics, i.e., roundness, perimeter index, and erosion-dilation area ratio. Composite morphological characteristics for fine and coarse aggregates are abbreviated as *FR* and *CR* for roundness, *FPI* and *CPI* for angularity, and *FEDR* and *CEDR* for texture, respectively. The results of *Composite index* for fine aggregate in asphalt mortar (abbreviated as F1~F10) and coarse aggregate in asphalt mixture (abbreviated as C1~C10) are listed in Table 7.

Table 7. Composite morphological index of fine and coarse aggregates.

Group	1	2	3	4	5	6	7	8	9	10
Asphalt Mortar	F1	F2	F3	F4	F5	F6	F7	F8	F9	F10
<i>FR</i>	1.5658	1.4175	1.6143	1.4641	1.6103	1.6123	1.5638	1.3178	1.4661	1.5127
<i>FPI</i>	1.2385	1.1526	1.2723	1.1673	1.2340	1.2532	1.2194	1.1005	1.1864	1.2011
<i>FEDR</i>	0.7821	0.5729	0.8645	0.6151	0.7842	0.8244	0.7419	0.4461	0.6553	0.6976
Asphalt Mixture	C1	C2	C3	C4	C5	C6	C7	C8	C9	C10
<i>CR</i>	1.6889	1.4974	1.7586	1.5447	1.7140	1.7363	1.6666	1.3755	1.5671	1.6144
<i>CPI</i>	1.2367	1.1682	1.2612	1.1840	1.2438	1.2525	1.2280	1.1242	1.1927	1.2085
<i>CEDR</i>	0.9329	0.7794	0.9928	0.8106	0.9355	0.9642	0.9043	0.6857	0.8392	0.8705

2.3. Experimental Methods

2.3.1. High-Temperature Viscoelastic Property Tests

Uniaxial compression failure test (Jinli testing technology Co., Ltd., Changchun, China) and uniaxial compression static creep test (Cooper Research Technology Ltd., Ripley, UK) were adopted to study the high-temperature viscoelastic characteristics of asphalt mixes and they were conducted in accordance with previous study [23,26–28]. Due to different asphalt contents in asphalt mortar and mixture, three test temperatures were selected to reduce the error caused by temperature, in which the test temperatures were set as 10 °C, 20 °C, and 30 °C for asphalt mortar and 30 °C, 40 °C and 50 °C for asphalt mixture. Uniaxial compression failure test is shown in Figure 2a and a servo-pneumatic universal testing machine, as shown in Figure 2b, was employed to conduct the uniaxial compression static creep test at a fixed stress level and creep time for asphalt mixes.

The stress level is $\sigma = \sigma_0$, the creep compliance of asphalt mortar and mixture is defined as follows:

$$J(t) = \varepsilon(t)/\sigma_0, \quad (1)$$

where $J(t)$ is creep compliance; $\varepsilon(t)$ is creep strain; and, σ_0 is constant stress.

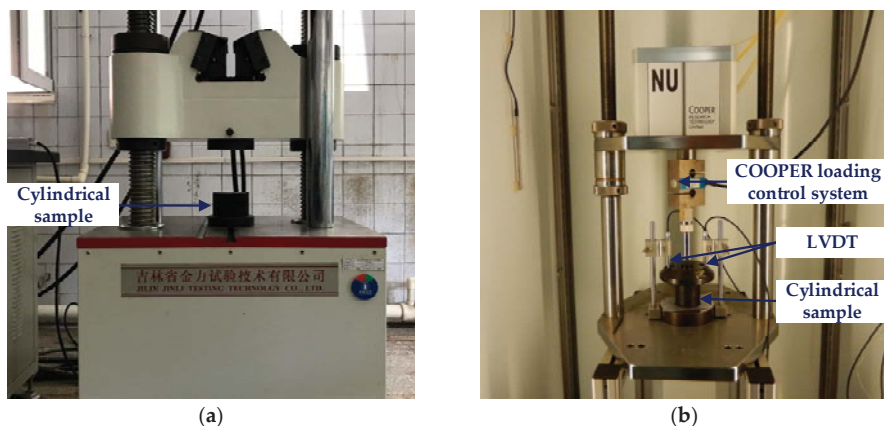


Figure 2. High-temperature viscoelastic property tests: (a) Uniaxial compression failure test; and, (b) Uniaxial compression static creep test.

2.3.2. Low-Temperature Viscoelastic Property Tests

(1) Beam Bending Failure Test

Beam bending failure test (Jinli testing technology Co., Ltd., Changchun, China) was used to determine the stress level of the beam bending creep test. The beam samples of asphalt mortar and mixture were placed in an environmental chamber for at least 4 h and the test temperature is $-5\text{ }^{\circ}\text{C}$. Then a concentrated load was applied at the middle span of the beam sample until the beam was broken, which is shown in Figure 3a. The applied load and corresponding vertical deformation at the middle span were recorded, therefore, the failure stress, failure strain, and stiffness modulus could be calculated by using the following equations.

$$R_B = (3 \times L \times P_B) / (2 \times b \times h^2), \quad (2)$$

$$\varepsilon_B = (6 \times h \times d) / L^2, \quad (3)$$

$$S_B = R_B / \varepsilon_B, \quad (4)$$

where R_B , ε_B , S_B are the failure stress, failure strain and stiffness modulus, respectively; b , h , L are the width, height, and length of the test beam sample, respectively; P_B is the failure load; and, d is the failure deformation at the middle span.

(2) Beam Bending Creep Test

In the beam bending creep test (Cooper Research Technology Ltd., Ripley, UK), a constant load was applied at the middle span of beam sample and the deformation versus time was recorded to evaluate the creep property of asphalt mortar and mixture. The test procedure is similar to uniaxial compression static creep test and the beam bending creep test is shown in Figure 3b. Then, the strain versus time in the beam bending creep could be obtained and the creep compliance of asphalt mortar and mixture was also calculated by Equation (1).



Figure 3. Low-temperature viscoelastic property tests: (a) Beam bending failure test; and, (b) Beam bending creep test.

3. Results and Analysis for High-Temperature Creep Properties of Asphalt Mixes

A Burgers model is developed as a combination of Maxwell and Kelvin models in series, which is a four-element model indicating elastic deformation, viscous flow, and viscoelastic deformation [29,30]. And the Burgers model used in this study has been described in details [23]. For the Burgers model, E_1 , E_2 , η_1 , η_2 are viscoelastic constants, which could be determined through the fitting creep test. E_1 is the modulus of immediate elasticity Burgers model, E_2 is the modulus of delayed elasticity Burgers model, η_1 is the coefficient of viscosity Burgers model, η_2 is the coefficient of elastic delay viscosity Burgers model and $\tau = \eta_2/E_2$ is defined as the retardation time.

3.1. Analysis for Fine Aggregate Morphological Characteristics on Creep Properties of Asphalt Mortar

3.1.1. Uniaxial Compression Failure Test Results of Asphalt Mortar

For uniaxial compression failure tests of asphalt mortar, the test temperatures were selected as 10 °C, 20 °C, and 30 °C, respectively, and the applied loading speed was set as 50 mm/min. According to the recorded relation curve between force and displacement, the maximum stress, corresponding strain, and the ratio of two were obtained as the compression failure stress, failure strain and secant modulus. The uniaxial compression failure test results are plotted in Figure 4.

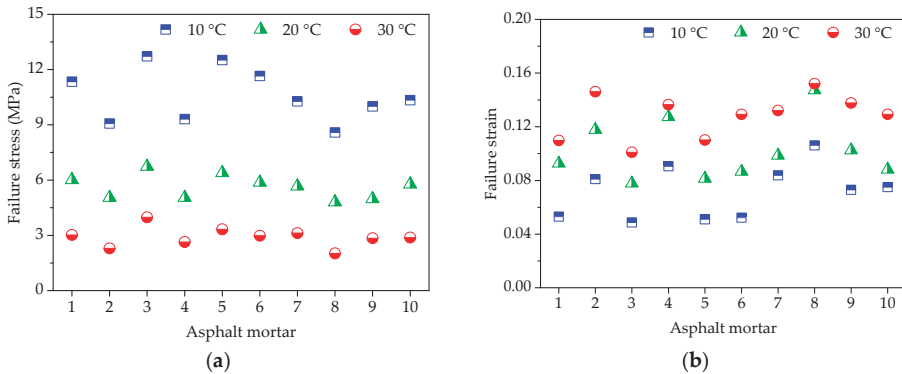


Figure 4. Cont.

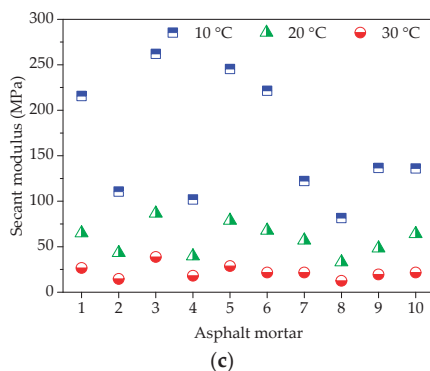


Figure 4. Failure results of asphalt mortars: (a) Failure stress; (b) Failure strain; and, (c) Secant modulus.

As shown in Figure 4a, asphalt mortars with different morphological characteristics of fine aggregate have obvious different mechanical properties when subjected to the constant strain rate loading. At the same temperature, F3 has the highest failure stress, and followed by F5, the failure stress of F8 is the lowest. A higher failure stress is preferable due to the better bearing capacity. Simultaneously, it could be observed that temperature has a significant influence on failure stress of asphalt mortar. The failure stress of asphalt mortar decreases dramatically with temperature.

As for the failure strain in Figure 4b, it illustrates the deformation characteristics of asphalt mortars while loading, which has an opposite trend with the failure stress in Figure 4a. For any test temperature, F8 has the largest failure strain, whereas the failure strain of F3 is the smallest among all of the asphalt mortars. The failure strain indicates the deformation before asphalt mortar being broken, which could help to reduce the occur of crack at low temperature but would be easy to produce greater permanent deformation at high temperature. In addition, it is clear that the higher the test temperature is, the larger the failure strain of asphalt mortar becomes, which is attributed to the high fluidity of asphalt at higher temperature.

Secant modulus is the ratio of failure stress to failure strain, comprehensively reflecting the compatibility of deformation. Normally, a higher secant modulus stands for the better compatibility of deformation and anti-compression failure performance. The variation trend of secant modulus results that was observed in Figure 4c is consistent with the trend of failure stress in Figure 4a, in which F3 has the highest secant modulus, and followed by F5, the secant modulus of F8 is the lowest among all the asphalt mortars for any test temperature. As the designed experimental proportion listed in Table 5, the asphalt mortar F3 was prepared by andesite manufactured sand, basalt manufactured sand was used for F5 and F8 was made by river sand. Thus, it is evident that manufactured sands can improve the anti-compression failure performance of asphalt mortar and the asphalt mortar made by natural sands has the largest failure strain. Due to asphalt as a typical viscoelastic material, temperature has an obvious effect on its mechanical properties. Asphalt binder has a higher cohesive force and the inlay effect of aggregate is more significant, resulting in a bigger difference among different asphalt mortars at a lower temperature. However, the high fluidity of asphalt at higher temperature causes the cohesive force of asphalt binder to decrease and the aggregate has a weak influence.

3.1.2. Uniaxial Compression Creep Test Results of Asphalt Mortar

(1) Strain Results of High-Temperature Creep Test

Before each uniaxial compression static creep test, uniaxial compression failure test was conducted to determine an appropriate stress level for asphalt mortar. Figure 4a shows the range of failure stress, i.e., 8.62 MPa~12.74 MPa at 10 °C, 4.83 MPa~6.76 MPa at 20 °C, 2.07 MPa~4.03 MPa at 30 °C. Therefore, the applied stress level of 0.2 MPa was kept constant for the uniaxial compression creep

test. Then, a preconditioning stress of 5% loading was applied to asphalt mortar samples for 90 s. Subsequently, a servo-pneumatic universal testing machine was adopted to apply a stress-controlled uniaxial compressive loading for 1800 s at 10 °C, 20 °C, and 30 °C, respectively. Figure 5 compares the creep strain for 10 groups of asphalt mortars at different temperatures.

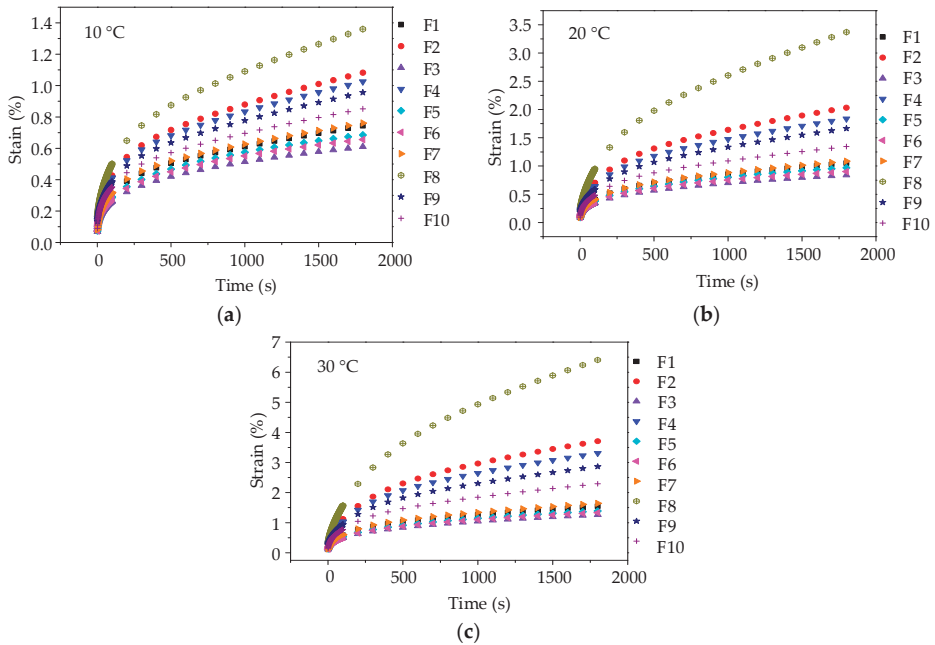


Figure 5. Creep strain-time curves of asphalt mortars: (a) 10 °C; (b) 20 °C; and, (c) 30 °C.

As illustrated in Figure 5, the creep deformations of asphalt mortars increase gradually with the test temperature and loading time increasing. When the test temperature changes from 10 °C to 30 °C, the creep strain at 1800 s increases 2–4 times, which could be explained by the viscoelastic property of asphalt mortar. Besides, it could be observed that at the same loading time, the creep strains of 10 groups of asphalt mortars at any test temperature are ranked as $F8 > F2 > F4 > F9 > F10 > F7 > F1 > F5 > F6 > F3$. A larger creep strain means a worse anti-deformation performance, that is, F3 has the best anti-deformation performance and the anti-deformation performance of F8 is the worst. Thus, andesite manufactured sand could improve the anti-deformation performance of asphalt mortar with respect to river sand.

(2) Influence of Fine Aggregate on High-Temperature Viscoelastic Parameters

As different fine aggregates lead to different viscoelastic performances of asphalt mortars, it is necessary to quantitatively analyze the influence of morphological characteristics of fine aggregates on viscoelastic performances of asphalt mortar. The relationship between morphological characteristics of fine aggregate and viscoelastic performances of asphalt mortar could be obtained by using linear regression, in which morphological characteristics (i.e., FR , FPI , and $FEDR$) are regarded as independent variables and viscoelastic parameters (i.e., E_1 , η_1 , and τ) are response variables. These relationship and correlation analysis are presented in Figures 6–8.

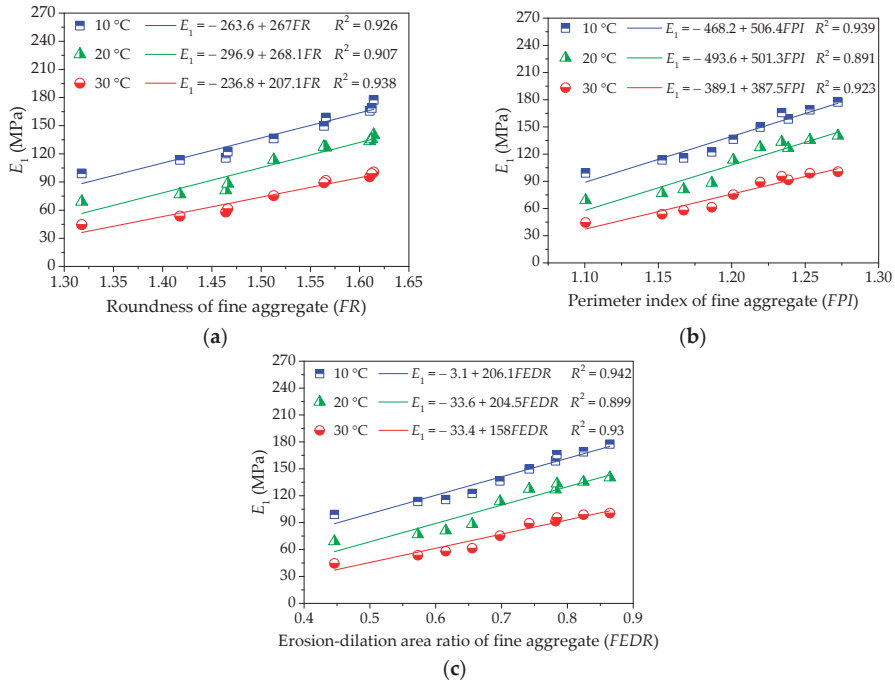


Figure 6. Influences of fine aggregate morphological characteristics of on E_1 of asphalt mortar: (a) Shape (FR); (b) Angularity (FPI); and, (c) Texture (FEDR).

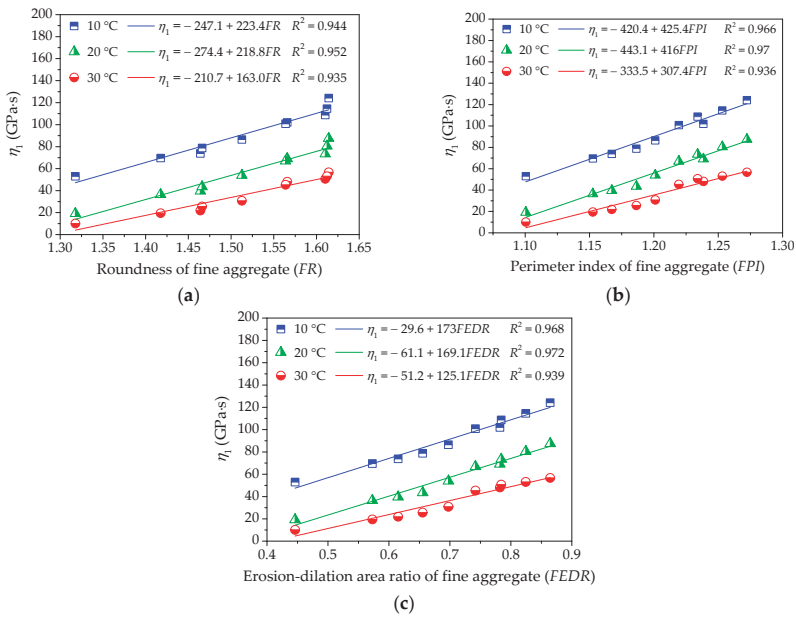


Figure 7. Influences of fine aggregate morphological characteristics of on η_1 of asphalt mortar: (a) Shape (FR); (b) Angularity (FPI); and, (c) Texture (FEDR).

As shown in Figures 6 and 7, the values of E_1 and η_1 increase with morphological characteristics of fine aggregate increasing. There could be a positive correlation among these parameters and the correlation coefficient values R^2 are above 0.89. The linear regression models show a strong correlation with test results, indicating that the linear regression models are efficient in characterizing their relationship. A higher value of E_1 stands for a larger resistance to deformation while loading as well as a better recovery capacity after unloading, and the larger the viscosity coefficient η_1 , the smaller the permanent deformation. Thus, fine aggregate with complex morphological characteristics could improve the anti-deformation performance of asphalt mortar. In addition, the slopes of linear regression models decrease slightly with temperature increasing, which may be more related to the rheological property of asphalt binder.

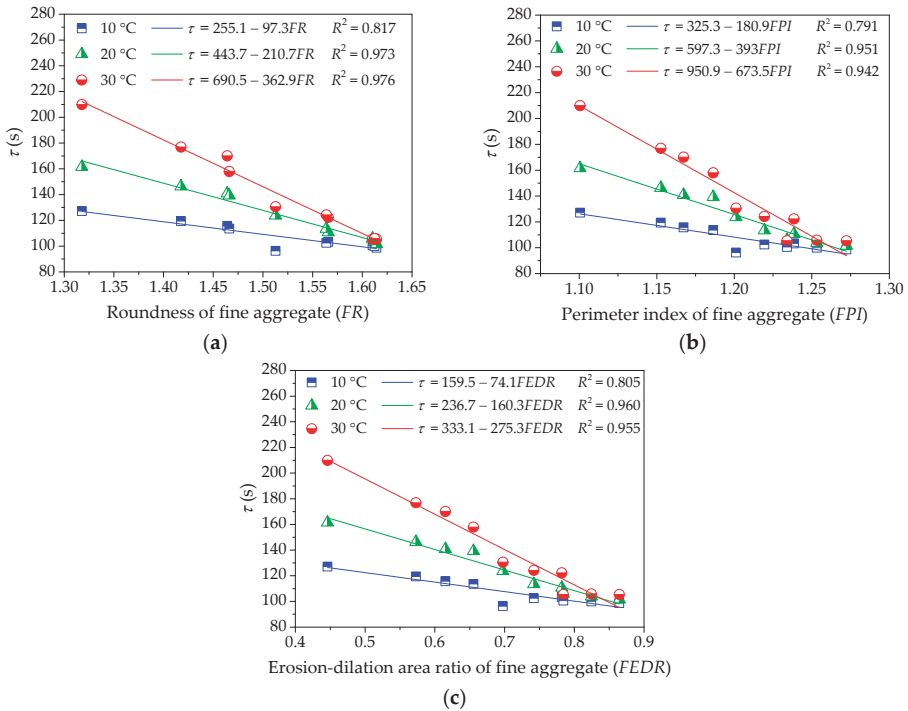


Figure 8. Influences of fine aggregate morphological characteristics of on τ of asphalt mortar: (a) Shape (FR); (b) Angularity (FPI); and, (c) Texture (FEDR).

Figure 8 shows the influence of morphological characteristics of fine aggregate on the retardation time τ of asphalt mortar. It clearly shows that the retardation time of asphalt mortar decreases with increase in morphological characteristics of fine aggregates and the slopes of the descending segments increase with temperature. Morphological characteristics of fine aggregate are shown to be strongly correlated with the retardation time of asphalt mortar at lower temperature (all the R^2 values are above 0.9), whereas a relatively small correlation is observed at higher temperature. Due to the retardation time that is related to the recovery time of viscoelastic deformation, fine aggregate with complex morphological characteristics helps to improve the deformation recovery capacity of asphalt mortar.

3.2. Analysis for Coarse Aggregate Morphological Characteristics on Creep Properties of Asphalt Mixture

3.2.1. Uniaxial Compression Failure Test Results of Asphalt Mixture

Figure 9 presents the uniaxial compression failure test results of asphalt mixtures at the three test temperatures of 10 °C, 20 °C, and 30 °C. The speed of applied loading was also 50 mm/min. As shown in Figure 9, for constant strain rate loading, different types of coarse aggregate lead to a large difference in mechanical property distribution of asphalt mixtures. At the same temperature, asphalt mixtures without pebbles have larger failure stress and secant modulus and those with pebbles have smaller failure strain, i.e., the failure stress and secant modulus of C3, C5, and C6 are larger than the others, while these failure strains are smaller than the other groups. What's more, the change of mechanical properties for asphalt mixtures should be more related to the pebble content. This is because manufactured stones (basalt stone and andesite stone) have the more complex morphological characteristics than pebble and pebble is more spherical. With loading time and increasing deformation, the inlay effect of coarse aggregate becomes more and more significant. However, asphalt mixture with pebble would occur cracks prematurely when compared to asphalt mixture made with manufactured stones, resulting in stress reduction as well as broken specimens.

Regarding the influence of temperature on the mechanical properties of asphalt mixtures, it is also consistent with the finding of asphalt mortars. The failure stress and secant modulus of asphalt mixture decrease significantly and the failure strain increases with temperature increasing. These simple observations indicate that asphalt mixture has significant temperature susceptibility, which is due to the viscoelastic property of asphalt.

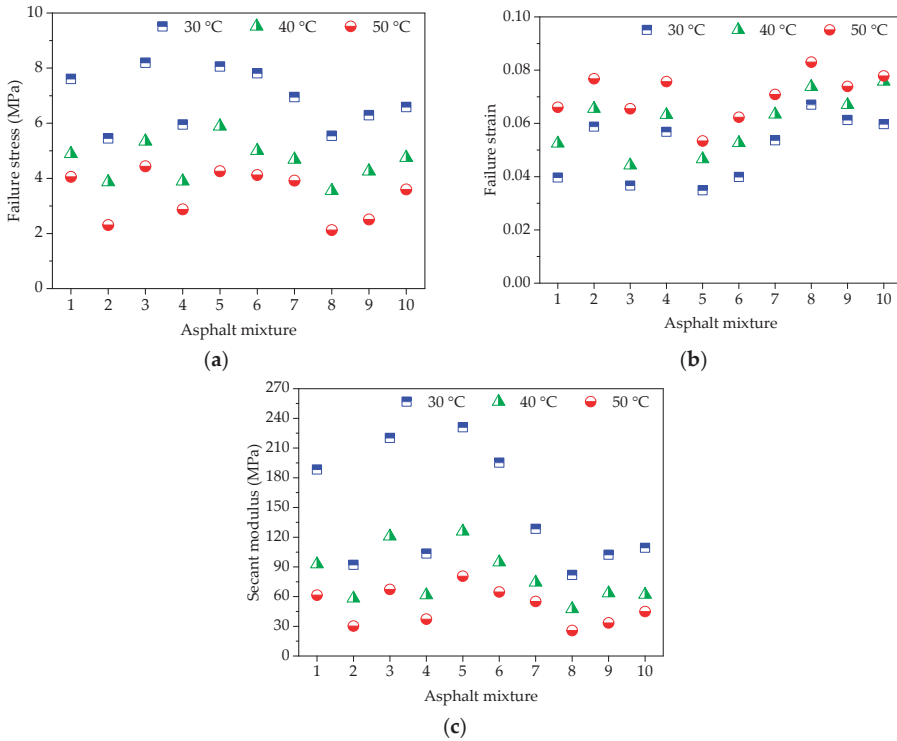


Figure 9. Failure results of asphalt mixtures: (a) Failure stress; (b) Failure strain; and, (c) Secant modulus.

3.2.2. Uniaxial Compression Creep Test Results of Asphalt Mixture

(1) Strain Results of High-Temperature Creep Test

The range of failure stress for asphalt mixtures are 5.48 MPa~8.21 MPa at 30 °C, 3.55 MPa~5.91 MPa at 40 °C, and 2.13 MPa~4.46 MPa at 50 °C. Thus, the applied stress level of 0.4 MPa was kept constant for the creep test. A preconditioning stress of 5% loading was also applied to asphalt mixture specimens for 90 s. Subsequently, a servo-pneumatic universal testing machine was adopted to apply a stress-controlled uniaxial compressive loading for 2400 s at three test temperatures. The creep strain results for 10 groups of asphalt mixtures are depicted in Figure 10.

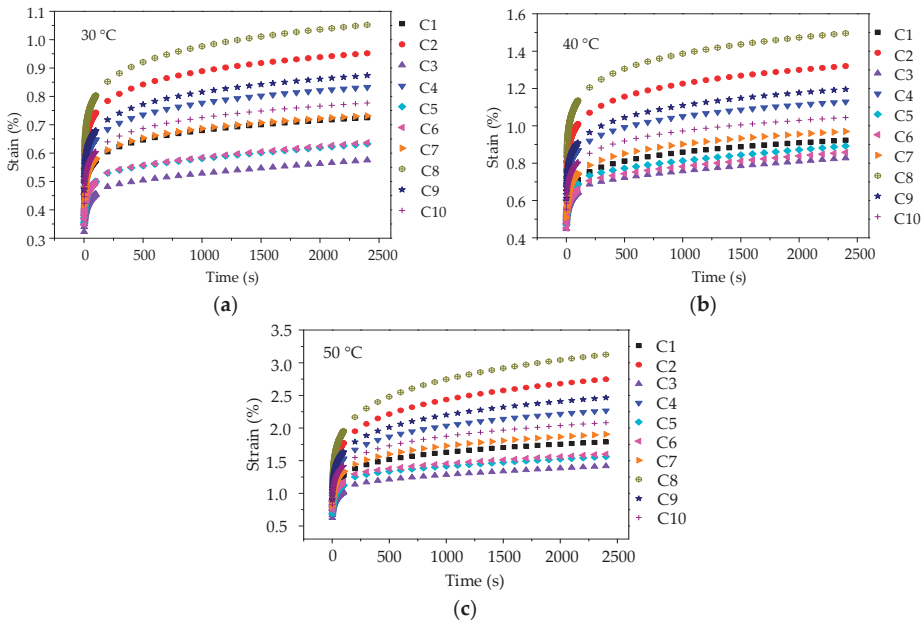


Figure 10. Creep strain-time curves of asphalt mixtures: (a) 30 °C; (b) 40 °C; and, (c) 50 °C.

As illustrated in Figure 10, it is also observed that the creep deformations of asphalt mixtures increase gradually with test temperature increasing due to the viscoelastic property of asphalt. However, it is worth noting that when compared with the creep curves of asphalt mortars, the creep strains of asphalt mixtures are still lower under the condition that stress level is twice, test temperature is 20 °C higher and creep time is 600 s longer. This observation fully demonstrated that the skeleton effect of coarse aggregate could enhance the anti-deformation performance of asphalt mixture effectively. Besides, it could be also observed that, at the same loading time and test temperature, the anti-deformation performance of asphalt mixture that was prepared by manufactured stones (basalt stone and andesite stone) is better than that of asphalt mixture with pebble, and the creep strains of 10 groups of asphalt mixtures at any test temperature are ranked as C8 > C2 > C9 > C4 > C10 > C7 > C1 > C6 > C5 > C3. Thus, coarse aggregate with complex morphological characteristics could improve the anti-deformation performance of asphalt mixture.

(2) Influence of Coarse Aggregate on High-Temperature Viscoelastic Parameters

To further investigate the influence of morphological characteristics of coarse aggregate on the viscoelastic performances of asphalt mixture at a high temperature, the viscoelastic constants in Burgers model can be given by fitting the uniaxial compression creep curve results. Then, this study

respectively takes morphological characteristics and viscoelastic parameters as independent variables and response variables and their relationships are depicted in Figures 11–13, which is convenient for the quantitative regression analysis.

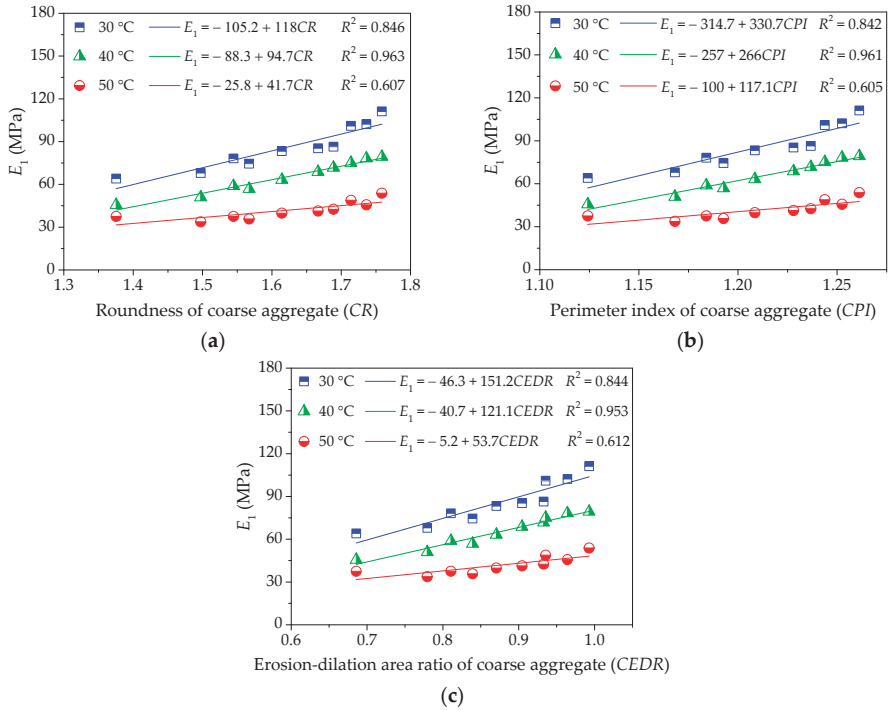


Figure 11. Influences of coarse aggregate morphological characteristics of on E_1 of asphalt mixture: (a) Shape (CR); (b) Angularity (CPI); and, (c) Texture (CEDR).

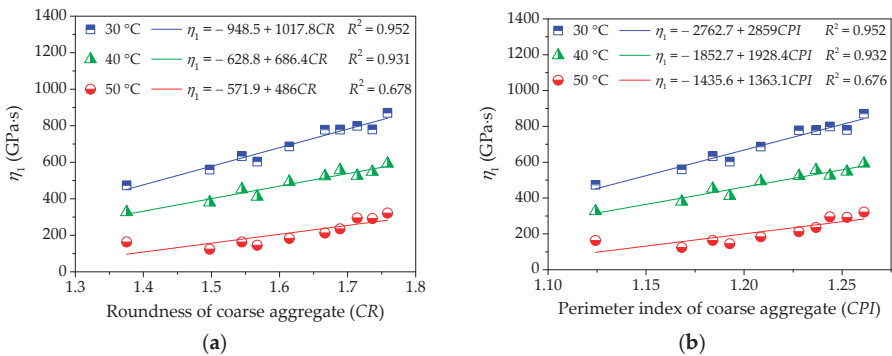
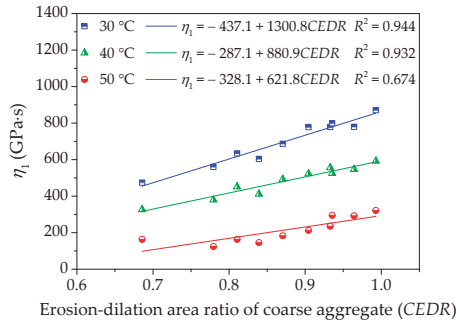
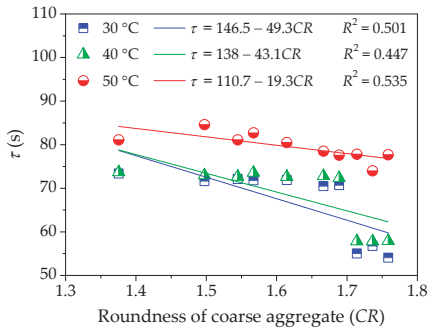


Figure 12. Cont.

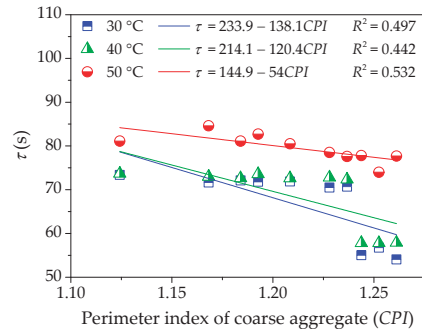


(c)

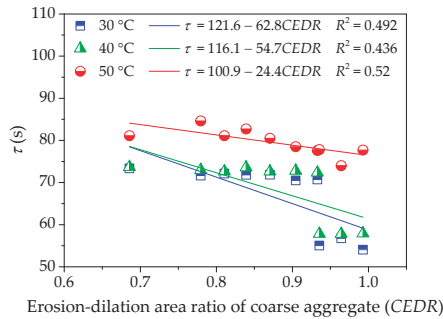
Figure 12. Influences of coarse aggregate morphological characteristics of on η_1 of asphalt mixture: (a) Shape (CR); (b) Angularity (CPI); and, (c) Texture (CEDR).



(a)



(b)



(c)

Figure 13. Influences of coarse aggregate morphological characteristics of on τ of asphalt mixture: (a) Shape (CR); (b) Angularity (CPI); and, (c) Texture (CEDR).

Figures 11 and 12 clearly show that the modulus E_1 of immediate elasticity Burgers model and coefficient η_1 of viscosity Burgers model increase gradually with morphological characteristics of coarse aggregate. The higher correlation efficient values R^2 indicate that the linear regression models show a strong correlation with test results at a lower temperature. However, the slopes of linear regression models decrease slightly with temperature increasing and the correlation efficient values R^2 also become relatively smaller, which means a relatively insignificant influence of coarse aggregate on E_1 and η_1 and a higher dispersion at higher temperature. Morphological characteristics of coarse aggregate are typically more related to the resistance to deformation while loading as well as

the permanent deformation at lower temperature, but they present a relatively less and discretized influence on viscoelastic characteristics of asphalt mixture.

As for the effects of morphological characteristics of coarse aggregate on the retardation time of asphalt mixture, the correlation efficient values R^2 are much lower than 0.54, showing that there is no clear linear correlation between the retardation time of asphalt mixture and morphological characteristics of coarse aggregates. In fact, the retardation time of asphalt mixtures generally decreases with increase in morphological characteristics. This is expected because the viscoelastic deformation in the creep process mainly occurs in asphalt mortar, which plays the roles of bonding with coarse aggregates and filling internal voids. Hence, coarse aggregates are not as strongly correlated with the retardation time as fine aggregates.

4. Results and Analysis for Low-Temperature Relaxation Properties of Asphalt Mixes

4.1. Conversion between Relaxation Modulus and Creep Compliance

In low-temperature relaxation analysis, it is necessary to convert the creep compliance into the relaxation modulus [21,31]. The creep compliance in time domain for the asphalt mixture can be formulated in the form of Prony series:

Taking the inverse Laplace transform, the creep strain versus time is given by:

$$J(t) = J_0 + \frac{t}{\eta} + \sum_{i=1}^n J_i \left(1 - e^{-t/\tau_i}\right), \tag{5}$$

where $J(t)$, J_0 and η are Prony series parameters, τ_i is the retardation time.

Applying the Laplace transform gives

$$\hat{J}(s) = \frac{J_0}{s} + \frac{1}{\eta \cdot s^2} + \sum_{i=1}^n \frac{J_i}{s(\tau_i \cdot s + 1)}, \tag{6}$$

A relationship between $\hat{E}(s)$ and $\hat{J}(s)$ is presented as:

$$\hat{E}(s)\hat{J}(s) = \frac{1}{s^2}, \tag{7}$$

Thus, it yields

$$\hat{E}(s) = \frac{1}{s\left(J_0 + \frac{1}{\eta \cdot s} + \sum_{i=1}^n \frac{J_i}{\tau_i \cdot s + 1}\right)}, \tag{8}$$

Equation (8) could be rewritten as the polynomial form:

$$\hat{E}(s) = \frac{(a_n \cdot s^n + a_{n-1} \cdot s^{n-1} + \dots + a_1)}{(b_{n+1} \cdot s^{n+1} + b_n \cdot s^n + \dots + b_1)}, \tag{9}$$

where a and b are the coefficients of polynomial function. Then, Equation (9) is expanded using the factorization as:

$$\bar{E}(s) = \frac{C_1}{s + \frac{1}{\lambda_1}} + \frac{C_2}{s + \frac{1}{\lambda_2}} + \dots + \frac{C_n}{s + \frac{1}{\lambda_n}}, \tag{10}$$

where $1/\lambda_1, 1/\lambda_2$ and $1/\lambda_n$ are the roots of denominator polynomial; $C_1, C_2,$ and C_n are the values for decomposing polynomial.

Applying the inverse Laplace transform to Equation (10) leads to the relaxation modulus of the generalized Maxwell model with an individual spring element:

$$E(t) = E_{\infty} + \sum_{i=1}^n E_i e^{-t/\rho_i}, \tag{11}$$

where E_{∞} is the equilibrium modulus; E_i is the elastic modulus of the i th Maxwell element and ρ_i is the relaxation time of the i th Maxwell element; and, n is the number of Maxwell element.

4.2. Analysis for Fine Aggregate Morphological Characteristics on Relaxation Properties of Asphalt Mortar

4.2.1. Beam Bending Failure Test Results of Asphalt Mortar

The test temperature was -5°C and the speed of applied loading was 50 mm/min in the beam bending failure test of asphalt mortar to determine an appropriate stress level for further beam bending creep test. The beam specimens of asphalt mortars were placed in an environmental chamber for at least 4 h and the beam bending failure test results could be expressed as the average of three replicates for each group of asphalt mortars. Figure 14 shows the bending failure stress, bending failure strain, and stiffness modulus results of all the asphalt mortars.

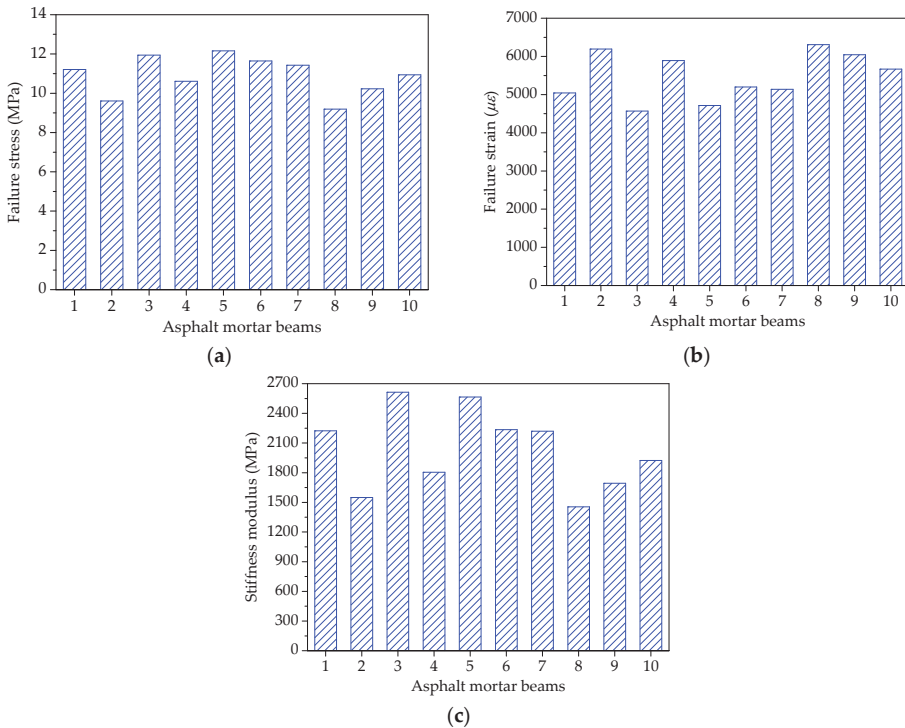


Figure 14. Failure results of asphalt mortar beams: (a) Failure stress; (b) Failure strain; and, (c) Stiffness modulus.

As shown in Figure 14a, asphalt mortars with different morphological characteristics of fine aggregate have obvious different ultimate loads in the beam bending failure test. The bending failure stress could be ranked from big to small, as follows: F5 > F3 > F6 > F7 > F1 > F10 > F4 > F9 > F2 > F8. The bigger the bending failure stress, the more the ultimate load and the better the bending

failure performance. Therefore, due to the better cohesive effect between fine aggregate with complex morphological characteristics and asphalt binder, it is evident that manufactured sands can improve the bending failure strength of asphalt mortar.

Figure 14b compares the maximum deformation of asphalt mortars in the beam bending failure test. The bending failure strains for 10 groups of asphalt mortars are ranked as $F8 > F2 > F9 > F4 > F10 > F6 > F7 > F1 > F5 > F3$. A higher bending failure strain is preferable for the low-temperature cracking resistance, which indicates that the asphalt mortar made by manufactured sands is easier to produce the low-temperature embrittlement. This is because fine aggregate with complex morphological characteristics would occur the stress concentration phenomenon while loading, leading to cracks at stress concentration points.

As for the stiffness modulus in Figure 14c, stiffness modulus characterizes the compatibility of deformation, comprehensively reflecting the relationship between load and deformation. Figure 14c clearly shows that the stiffness modulus can be ranked as: $F3 > F5 > F6 > F1 > F7 > F10 > F4 > F9 > F2 > F8$. Asphalt mortar prepared by river sand has the smallest stiffness modulus, suggesting that river sand could improve the low-temperature cracking resistance of the asphalt mortar.

4.2.2. Beam Bending Creep Test Results of Asphalt Mortar

(1) Strain Results of Low-Temperature Creep Test

A servo-pneumatic universal testing machine was used to conduct the low-temperature creep test at $-5\text{ }^{\circ}\text{C}$ for 1800 s. The bending stress level was set as 1.38 MPa for the stress-controlled uniaxial compressive loading. Based on the measured test results, Figure 15 depicts the bending strains against the loading time in the beam bending creep test. It clearly shows that the bending strains of beam samples increase gradually with the loading time and the creep strains for 10 testing groups are ranked as $F8 > F2 > F9 > F4 > F10 > F7 > F1 > F5 > F6 > F3$. Asphalt mortar that is prepared by river sand (i.e., F8) has the largest strain, whereas asphalt mortar prepared by andesite manufactured sand (i.e., F3) has the smallest strain. What is more, the bending creep strain exhibits a rising trend with the content of river sand. This observation is consistent with the morphological analysis that, due to river sands close to spherical, the more river sands asphalt mortar has, the weaker the inlay effect of aggregates.

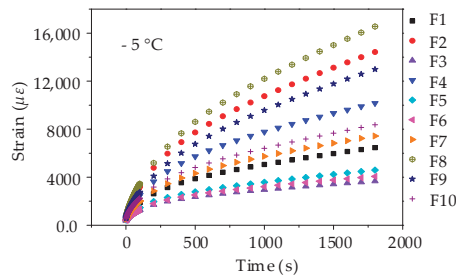


Figure 15. Creep strain-time curves of asphalt mortar beams.

The bending creep strain curves in Figure 15 were used to determine the creep compliance by using the fitting method. Then, based on the conversion between the relaxation modulus and creep compliance, the Prony series model of relaxation modulus could be conducted for 10 groups of asphalt mortars. In general, the relaxation time is on an axis using the logarithmic scale and the relaxation time are selected as 0.5 s, 5 s, 50 s, 500 s, and 5000 s. Table 8 summarizes the parameters of Prony series model of relaxation modulus and the R^2 values for asphalt mortars. It is found that the Prony series model can provide excellent fittings with R^2 values larger than 0.998, indicating that this Prony series model is able to accurately describe the relaxation characteristics of asphalt mortars. Subsequently,

the constructed Prony series models were utilized to fit the relaxation modulus and the curves are plotted in Figure 16.

As shown in Figure 16, the relaxation modulus decreases versus time, in which the change rate of relaxation modulus is larger in the initial loading stage and the rate tends to be stable in the late loading stage. This observation is consistent with the stress relaxation characteristics of asphalt mortar. Besides, the relaxation modulus could be ranked from big to small as: F3 > F6 > F5 > F1 > F7 > F10 > F4 > F9 > F2 > F8, which is in good agreement with the stiffness modulus of the beam bending failure test. The higher the relaxation modulus, the larger the failure possibility, which suggests an adverse low-temperature cracking resistance of asphalt mortar prepared by manufactured sands. From the partial enlarged drawing during a period of 800 s to 1800 s, it can be seen that the relaxation modulus of asphalt mortars made by manufactured sands (i.e., F3, F5 and F6) are still in a clear declining stage, while the relaxation modulus of other groups with river sands trend to be stable.

Table 8. Fitting results of Prony series for asphalt mortars.

Group	F1	F2	F3	F4	F5	F6	F7	F8	F9	F10
E_{∞} (GPa)	7.67	10.79	8.74	7.61	8.62	8.61	7.45	9.58	6.50	9.25
E_1 (GPa)	4.28	2.72	5.72	3.79	5.00	5.57	4.24	2.84	4.03	3.47
E_2 (GPa)	19.84	24.74	24.00	18.32	24.05	23.99	19.43	23.47	19.15	22.71
E_3 (GPa)	1.77	1.10	2.51	1.46	2.11	2.38	1.70	1.10	1.44	1.45
E_4 (GPa)	0.52	0.25	0.90	0.32	0.86	0.89	0.45	0.23	0.29	0.42
E_5 (GPa)	0.17	0.06	0.37	0.10	0.23	0.29	0.14	0.05	0.06	0.12
R^2	0.9991	0.9985	0.9989	0.9994	0.9995	0.9987	0.9992	0.9996	0.9998	0.9997

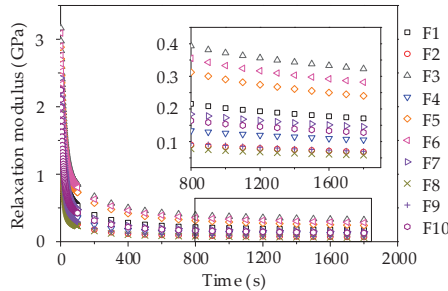


Figure 16. Relaxation modulus curve of asphalt mortars.

(2) Influence of Fine Aggregate on Low-Temperature Viscoelastic Parameters

The change rate of relaxation modulus as an evaluating index is used to reflect the relaxation characteristics of asphalt mortar. A larger change rate of relaxation modulus is preferable, which means a shorter relaxation time and more rapid dissipation of stress. Observe that the relaxation modulus is nearly exponential decline, and then a linear fitting model could be obtained by using the logarithmic transformation. The slopes of linear fitting models were selected to characterize the change rate of relaxation modulus and regarded as the response variable depicted in Figure 17. The regression analysis of change rates versus morphological characteristics of fine aggregates is presented in Figure 17.

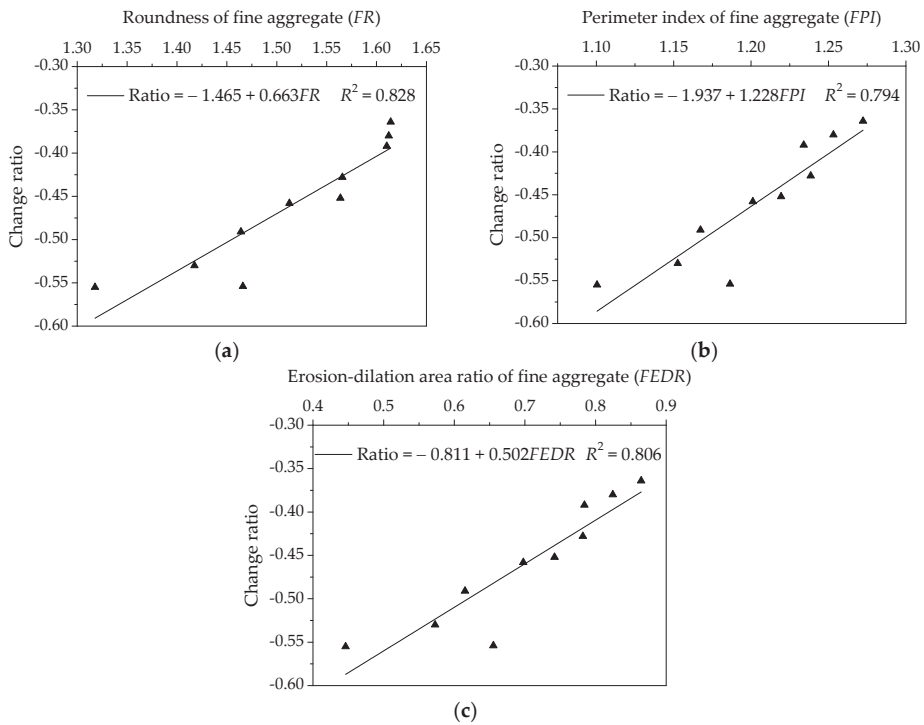


Figure 17. Influences of fine aggregate morphological characteristics of on change rate of relaxation modulus for asphalt mortars: (a) Shape (*FR*); (b) Angularity (*FPI*); and, (c) Texture (*FEDR*).

As shown in Figure 17, the correlation coefficient values R^2 for three morphological characteristics are larger than 0.79, which demonstrates morphological characteristics have a certain correlation with change rate of relaxation modulus. There is a positive correlation among these parameters, that is, the change rate of relaxation modulus increases with morphological characteristics. It is clear that the more complex morphological characteristics the fine aggregate has, the smaller the change rate of relaxation modulus is. Thus, asphalt mortar prepared by manufactured sands has an adverse low-temperature cracking resistance.

4.3. Analysis for Coarse Aggregate Morphological Characteristics on Relaxation Properties of Asphalt Mixture

4.3.1. Beam Bending Failure Test Results of Asphalt Mixture

Figure 18 shows the bending failure stress, strain and stiffness modulus results of all the asphalt mixtures. The beam bending failure test of asphalt mixture was conducted using the same procedure and test condition with asphalt mortar. As shown in Figure 18a, the bending failure stress could be ranked from big to small, as follows: C3 > C6 > C5 > C1 > C7 > C10 > C9 > C4 > C2 > C8. The bending failure stress characterizes the ultimate load under the bending-tension state, and therefore manufactured stones can improve the bending failure strength of asphalt mixture. The bending failure strains for 10 groups of asphalt mixtures are ranked as C8 > C2 > C4 > C9 > C10 > C7 > C3 > C1 > C5 > C6, as shown in Figure 18b. Additionally, corresponding stiffness modulus are ranked as: C6 > C3 > C5 > C1 > C7 > C10 > C9 > C4 > C2 > C8. It is evident that asphalt mixtures with pebble have a larger bending failure strain and lower stiffness modulus when compared with asphalt mixture made by manufactured stones, which implies that pebble could improve the low-temperature ductility and cracking resistance of asphalt mixture. This is expected because pebble is more spherical with lower

angularity values; the inlay effect in asphalt mixture becomes weaker while loaded, leading to smaller failure strength.

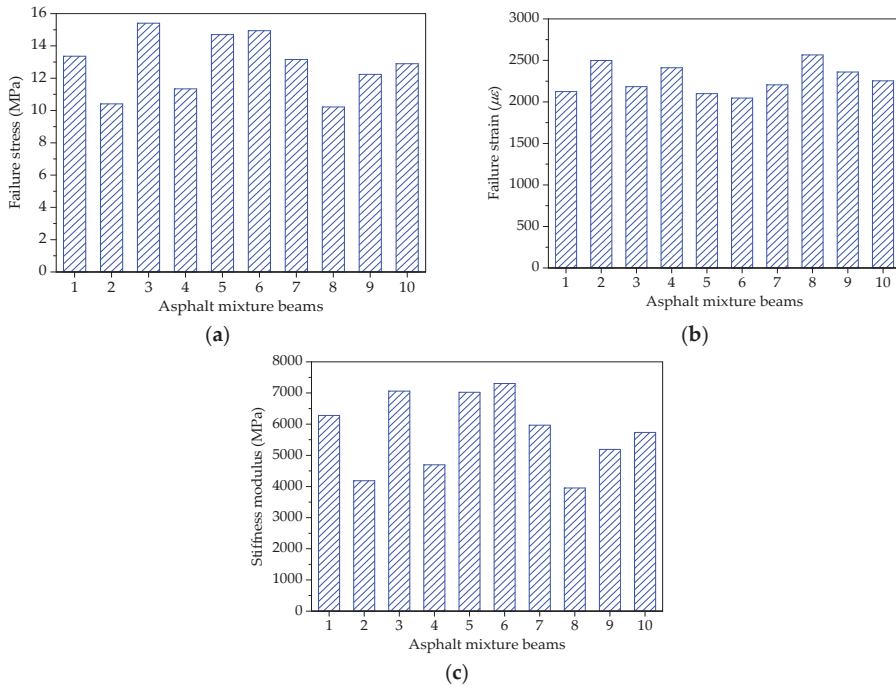


Figure 18. Failure results of asphalt mixture beams: (a) Failure stress; (b) Failure strain; and, (c) Stiffness modulus.

4.3.2. Beam Bending Creep Test Results of Asphalt Mixture

(1) Strain Results of Low-Temperature Creep Test

The procedure of beam bending creep test for asphalt mixture was in accordance with asphalt mortar except for the loading time. The creep strains for 10 testing groups of asphalt mixtures are ranked as C8 > C2 > C4 > C9 > C10 > C7 > C1 > C5 > C6 > C3, as shown in Figure 19. This observation is mainly consistent with the creep results of asphalt mortar, in which asphalt mixture prepared by pebble (i.e., C8) has the largest strain, whereas asphalt mixture prepared by andesite stone (i.e., C3) has the smallest strain. Besides, the bending creep strain also shows a rising trend with pebble proportion.

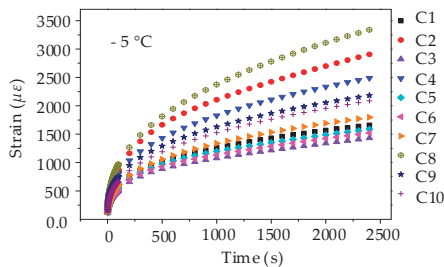


Figure 19. Creep strain-time curves of asphalt mixture beams.

Similarly, by fitting the creep strain results, the parameters of the Prony series model of relaxation modulus could be obtained and have the higher R^2 values above 0.998, as listed in Table 9. The relaxation modulus curves were therefore constructed and plotted in Figure 20. The relaxation modulus could be ranked as: $C3 > C6 > C5 > C1 > C7 > C10 > C9 > C4 > C2 > C8$ and the relaxation modulus are still in a clear declining stage in the partial enlarged drawing. Regarding the comparison of relaxation modulus, it is worth noting that the relaxation modulus exhibits a declining trend with the content of pebble. Hence, it can be concluded that pebble could improve the low-temperature cracking resistance of asphalt mixture.

Table 9. Fitting results of Prony series for asphalt mixtures.

Group	C1	C2	C3	C4	C5	C6	C7	C8	C9	C10
E_∞ (GPa)	19.66	11.31	30.16	18.80	27.41	32.27	22.70	20.15	18.09	23.68
E_1 (GPa)	28.14	8.52	26.22	25.60	30.06	23.55	31.49	25.85	25.21	32.00
E_2 (GPa)	10.06	34.84	12.52	7.96	11.62	12.21	10.31	7.15	8.36	9.76
E_3 (GPa)	5.17	4.05	6.14	3.73	5.80	5.74	5.00	3.05	4.09	4.51
E_4 (GPa)	2.67	1.31	2.87	1.79	2.43	2.84	2.47	1.37	2.03	2.14
E_5 (GPa)	0.85	0.46	1.05	0.50	0.96	0.93	0.73	0.34	0.60	0.59
R^2	0.9999	0.9996	0.9985	0.9994	0.9996	0.9989	0.9992	0.9994	0.9999	0.9993

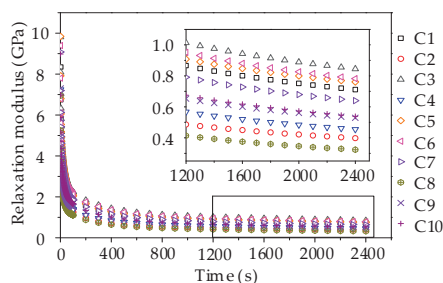


Figure 20. Relaxation modulus curve of asphalt mixtures.

(2) Influence of Coarse Aggregate on Low-Temperature Viscoelastic Parameters

The influence of morphological characteristics of coarse aggregate on low-temperature relaxation characteristics are investigated by using linear regression, in which morphological characteristics (i.e., CR , CPI and $CEDR$) are regarded as independent variables and change rate of relaxation modulus through logarithmic transformation are response variables. The regression analysis results are presented in Figure 21. As shown in Figure 21, the correlation coefficient values R^2 for three morphological characteristics are larger than 0.8, which demonstrates that aggregate morphological characteristics have a certain correlation with the change rate of relaxation modulus. There is a positive correlation among these parameters, thus, asphalt mixture prepared by manufactured stones has an adverse low-temperature cracking resistance.

In addition, it must be noted that the change rate range of relaxation modulus for asphalt mixture is lower when compared to asphalt mortar, in which the change rate range of relaxation modulus is 0.31 to 0.39 (in absolute value) for asphalt mixture, as shown in Figure 21, and the range for asphalt mortar is 0.36 to 0.56 (in absolute value), as shown in Figure 17. This is expected because the stress relaxation mainly relates to asphalt mortar rather than asphalt mixture. However, the proportions of aggregates in asphalt mixtures are basically the same except the coarse aggregates. Therefore, there is a relatively small difference for relaxation characteristics among asphalt mixtures, which also demonstrates a lower correlation with relaxation characteristics for coarse aggregates as compared to fine aggregates.

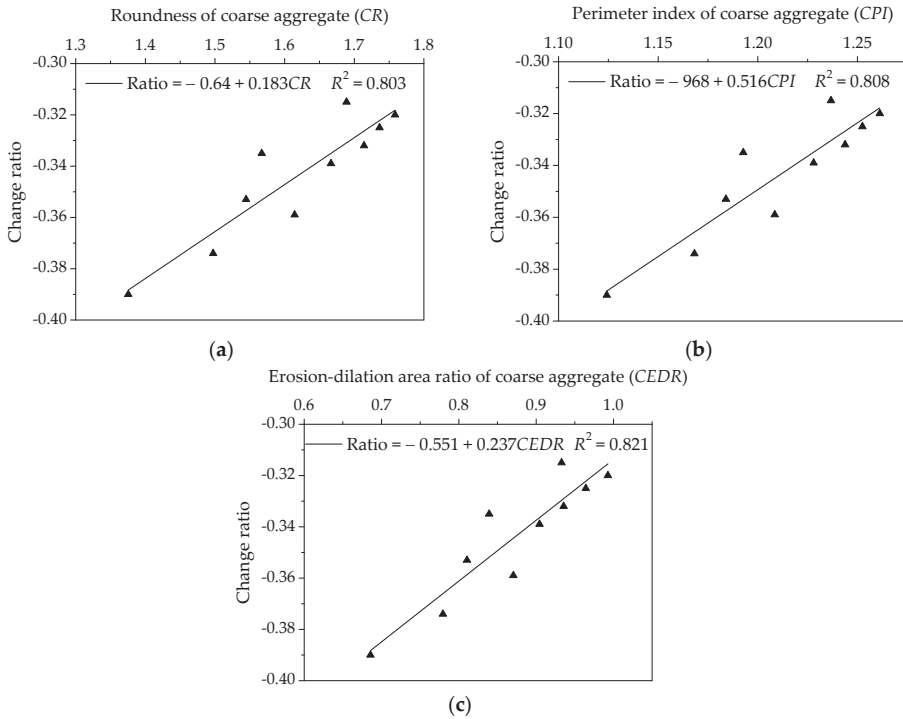


Figure 21. Influences of coarse aggregate morphological characteristics of on change rate of relaxation modulus for asphalt mixtures: (a) Shape (CR); (b) Angularity (CPI); and, (c) Texture (CEDR).

5. Optimization of Aggregate Morphological Characteristics for High- and Low-Temperature Viscoelasticity

The influences of morphological characteristics of fine and coarse aggregates on high and low temperature viscoelastic characteristics of asphalt mortar and mixture have been discussed above. It is evident that aggregates with complex morphological characteristics could improve the resistance to deformation at high temperature and have an adverse low-temperature cracking resistance. Consequently, it is necessary to optimize the aggregate morphological characteristics in asphalt mortar and mixture while considering high and low temperature viscoelastic characteristics.

5.1. Optimization for Morphological Characteristics of Fine Aggregate

In order to better optimize morphological characteristics of fine aggregate, the compression failure stress at 30 °C, retardation time and bending strain at -5 °C, and change rate of relaxation modulus are employed to characterize the high and low temperature viscoelastic characteristics, respectively. Based on the aggregate proportioning design by SLD method and corresponding test results, the regression analysis was conducted for the relationship between morphological characteristics and viscoelastic characteristics. The optimal values of single response for asphalt mortar were obtained firstly at different aggregate proportioning designs. Then, comprehensively considering high and low temperature viscoelastic characteristics, the aggregate proportioning design could be determined, i.e., basalt:andesite:river sand = 0:0.582:0.418, and the predictive values of multi-response as well as test results were also compared and listed in Table 10. As can be seen from the results, the relative errors are less than 4%, indicating a higher predictive accuracy. It could be concluded that asphalt mortar designed by the optimal aggregate proportion has the best high-

and low-temperature viscoelastic characteristics, in which the morphological characteristics of fine aggregate are $FR = 1.4909$, $FPI = 1.2005$, and $FEDR = 0.6896$.

Table 10. Optimal value of multi-response for asphalt mortar.

Property	High-Temperature Property		Low-Temperature Property	
	Failure Stress (MPa)	Retardation Time (s)	Bending Strain	Change Rate
Prediction	2.98	150	5393	−0.523
Experiment	3.06	145	5587	−0.531
Relative Error (%)	2.7	−3.3	3.6	1.5

5.2. Optimization for Morphological Characteristics of Coarse Aggregate

As for the optimization of coarse aggregate, the compression failure stress at 50 °C, retardation time are selected as high-temperature viscoelastic indices and the bending strain at −5 °C, change rate of relaxation modulus are regarded as low-temperature viscoelastic indices. Based on the optimal values of single response, the aggregate proportion for asphalt mixture while considering high and low temperature viscoelastic characteristics was designed as: basalt:andesite:pebble = 0.508:0.050:0.442. Table 11 compares the predictive values of multi-response and test results for asphalt mixture with relative errors less than 6%. When the morphological characteristics of coarse aggregate are $CR = 1.5666$, $CPI = 1.1918$, $CEDR = 0.828$, asphalt mixture has the best high and low temperature viscoelastic characteristics.

Table 11. Optimal value of multi-response for asphalt mixture.

Property	High-Temperature Property		Low-Temperature Property	
	Failure Stress (MPa)	Retardation Time (s)	Bending Strain	Change Rate
Prediction	3.15	81.6	2330	−0.356
Experiment	3.21	86.5	2438	−0.349
Relative Error (%)	1.9	6	4.6	−2

6. Conclusions

This study evaluated the influences of aggregate morphological characteristics on the high- and low-temperature viscoelastic characteristics of asphalt mixtures. Based on SLD, three different types of aggregates were used to prepare asphalt mixtures and aggregates were characterized by three morphological indices. Accordingly, the viscoelastic characteristics of asphalt mortar and mixture were evaluated based on a uniaxial compression static creep test and beam bending creep test. Based on the analysis results, the following conclusions could be drawn:

(1) Aggregate morphological characteristics were proved to strongly correlate with the viscoelastic properties of asphalt mortar and mixture. Asphalt mortar consisted of fine aggregate demonstrated a stronger correlation with the creep characteristics of the mix.

(2) Results showed that the resistance to deformation of asphalt mortar and mixture increases with increasing aggregate morphological characteristics, especially coarse aggregates, could effectively enhance the resistance to deformation of asphalt mixture due to the skeleton effect.

(3) Test analysis results indicated that aggregate morphological characteristics presented high correlations with the high-temperature creep and low-temperature relaxation characteristics. The observations also showed that with morphological characteristics increasing, the capacity of deformation recovery and anti-deformation could be improved, whereas the low-temperature cracking resistance would have an adverse influence.

(4) Based on the comprehensive consideration of high- and low-temperature viscoelastic properties, the aggregate proportion was optimized to obtain the more appropriate aggregate morphological characteristics for asphalt mixtures and the results also showed good agreement between predictive and experimental values. The optimization for aggregate morphological

characteristics should be considered in asphalt mixture design in order to improve the performances of asphalt pavement.

Author Contributions: Conceptualization, Y.C. and W.W.; Methodology, W.W. and J.T.; Validation, Y.C., J.T. and G.M.; Formal Analysis, M.X., X.X. and S.W.; Investigation, W.W., J.T. and S.W.; Writing-Original Draft Preparation, W.W.; Writing-Review & Editing, Y.C., M.X. and X.X.; Project Administration, Y.C.; Funding Acquisition, Y.C.

Funding: This research was funded by [National Natural Science Foundation of China] grant number [51678271] and [Science Technology Development Program of Jilin Province] grant number [20160204008SF] and supported by Graduate Innovation Fund of Jilin University.

Acknowledgments: The authors would like to appreciate anonymous reviewers for their constructive suggestions and comments to improve the quality of the paper.

Conflicts of Interest: The authors declare no conflict of interest.

References

1. Tang, F.L.; Xu, G.J.; Ma, T.; Kong, L.Y. Study on the Effect of Demulsification Speed of Emulsified Asphalt based on Surface Characteristics of Aggregates. *Materials* **2018**, *11*, 1488. [[CrossRef](#)] [[PubMed](#)]
2. Wilson, J.; Klotz, L. Quantitative analysis of aggregate based on hough transform. *Transp. Res. Rec.* **1996**, *1530*, 111–115. [[CrossRef](#)]
3. Kuo, C.Y.; Rollings, R.S.; Lynch, L.N. Morphological study of coarse aggregates using image analysis. *J. Mater. Civ. Eng.* **1998**, *10*, 135–142. [[CrossRef](#)]
4. Masad, E.; Button, J.W. Unified imaging approach for measuring aggregate angularity and texture. *Comput.-Aided Civ. Inf.* **2000**, *15*, 273–280. [[CrossRef](#)]
5. Kuo, C.Y.; Freeman, R. Imaging indices for quantification of shape, angularity, and surface texture of aggregates. *Transp. Res. Rec.* **2000**, *1721*, 57–65. [[CrossRef](#)]
6. Wang, L.B.; Wang, X.R.; Mohammad, L.; Abadie, C. Unified method to quantify aggregate shape angularity and texture using fourier analysis. *J. Mater. Civ. Eng.* **2005**, *17*, 498–504. [[CrossRef](#)]
7. Hu, J.; Qian, Z.D.; Wang, D.; Oeser, M. Influence of aggregate particles on mastic and air-voids in asphalt concrete. *Constr. Build. Mater.* **2015**, *93*, 1–9. [[CrossRef](#)]
8. Xie, X.G.; Lu, G.Y.; Liu, P.F.; Wang, D.W.; Fan, Q.; Oeser, M. Evaluation of morphological characteristics of fine aggregate in asphalt pavement. *Constr. Build. Mater.* **2017**, *139*, 1–8. [[CrossRef](#)]
9. Ding, X.H.; Ma, T.; Gao, W. Morphological characterization and mechanical analysis for coarse aggregate skeleton of asphalt mixture based on discrete-element modeling. *Constr. Build. Mater.* **2017**, *154*, 1048–1061. [[CrossRef](#)]
10. Xiao, Y.; Wang, F.; Cui, P.D.; Lei, L.; Lin, J.T.; Yi, M.W. Evaluation of Fine Aggregate Morphology by Image Method and Its Effect on Skid-Resistance of Micro-Surfacing. *Materials* **2018**, *11*, 920. [[CrossRef](#)] [[PubMed](#)]
11. Wang, D.H.; Ding, X.H.; Ma, T.; Zhang, W.G.; Zhang, D.Y. Algorithm for Virtual Aggregates' Reconstitution Based on Image Processing and Discrete-Element Modeling. *Appl. Sci.* **2018**, *8*, 738. [[CrossRef](#)]
12. Chen, J.S.; Shiah, M.S.; Chen, H.J. Quantification of coarse aggregate shape and its effect on engineering properties of hot-mix asphalt mixtures. *J. Test. Eval.* **2001**, *29*, 513–519.
13. Masad, E.; Olcott, D.; White, T.; Tashman, L. Correlation of fine aggregate imaging shape indices with asphalt mixture performance. *Transp. Res. Rec.* **2001**, *1757*, 148–156. [[CrossRef](#)]
14. Arasan, S.; Yenera, E.; Hattatoglu, F.; Hinislioglu, S.; Akbuluta, S. Correlation between shape of aggregate and mechanical properties of asphalt concrete. *Road Mater. Pavement Des.* **2011**, *12*, 239–262.
15. Singh, D.; Zaman, M.; Commuri, S. Inclusion of aggregate angularity, texture, and form in estimating dynamic modulus of asphalt mixes. *Road Mater. Pavement Des.* **2012**, *13*, 327–344. [[CrossRef](#)]
16. Pan, T.Y.; Tutumluer, E.; Carpenter, S.H. Effect of coarse aggregate morphology on permanent deformation behavior of hot mix asphalt. *J. Transp. Eng.* **2015**, *132*, 580–589. [[CrossRef](#)]
17. Valdes-Vidal, G.; Calabi-Floody, A.; Miro-Recasens, R.; Norambuena-Contreras, J. Mechanical behavior of asphalt mixtures with different aggregate type. *Constr. Build. Mater.* **2015**, *101*, 474–481. [[CrossRef](#)]
18. Aragao, F.T.S.; Pazos, A.R.G.; da Motta, L.M.G.; Kim, Y.R.; do Nascimento, L.A.H. Effects of morphological characteristics of aggregate particles on the mechanical behavior of bituminous paving mixtures. *Constr. Build. Mater.* **2016**, *123*, 444–453. [[CrossRef](#)]

19. Liu, H.Q.; Luo, R.; Lv, H.J. Establishing continuous relaxation spectrum based on complex modulus tests to construct relaxation modulus master curves in compliance with linear viscoelastic theory. *Constr. Build. Mater.* **2018**, *165*, 372–384. [[CrossRef](#)]
20. Luo, R.; Liu, H.Q. Improving the Accuracy of Dynamic Modulus Master Curves of Asphalt Mixtures Constructed Using Uniaxial Compressive Creep Tests. *J. Mater. Civ. Eng.* **2017**, *29*, 04017032. [[CrossRef](#)]
21. Luo, R.; Lv, H.J.; Liu, H.Q. Development of Prony series models based on continuous relaxation spectrums for relaxation moduli determined using creep tests. *Constr. Build. Mater.* **2018**, *168*, 758–770. [[CrossRef](#)]
22. Gorman, J.W.; Hinman, J.E. Simplex lattice designs for multicomponent systems. *Technometrics* **1962**, *4*, 463–487. [[CrossRef](#)]
23. Wang, W.S.; Cheng, Y.C.; Tan, G.J.; Tao, J.L. Analysis of aggregate morphological characteristics for viscoelastic properties of asphalt mixes using simplex lattice design. *Materials* **2018**, *11*, 1908. [[CrossRef](#)] [[PubMed](#)]
24. Wang, C.; Guo, N.S.; Zhao, Y.H.; Tan, Y.Q. Air voids distribution of asphalt mixtures in different compaction methods and aggregate gradations. *J. Jilin Univ. (Eng. Technol. Ed.)* **2014**, *2014*, 74–80. (In Chinese)
25. JTG E20-2011. *Standard Test Methods of Bitumen and Bituminous Mixtures for Highway Engineering*; Ministry of Transport of the People’s Republic of China: Beijing, China, 2011. (In Chinese)
26. Guo, Q.L.; Li, L.L.; Cheng, Y.C.; Jiao, Y.B.; Xu, C. Laboratory evaluation on performance of diatomite and glass fiber compound modified asphalt mixture. *Mater. Des.* **2015**, *66*, 51–59. [[CrossRef](#)]
27. Guo, Q.L. Research on Internal Stress Distribution of Asphalt Mixture and Its Impact on Viscoelastic Performance. Ph.D. Thesis, Jilin University, Changchun, China, 2013.
28. Tao, J.L. Research on Characteristics of Mineral Aggregate and Its Effect on High and Low Temperature Viscoelastic Performance of Asphalt Mixture. Ph.D. Thesis, Jilin University, Changchun, China, 2017.
29. Bai, F.; Yang, X.H.; Zeng, G.W. A stochastic viscoelastic–viscoplastic constitutive model and its application to crumb rubber modified asphalt mixtures. *Mater. Des.* **2016**, *89*, 802–809. [[CrossRef](#)]
30. Arabani, M.; Kamboozia, N. New achievements in visco-elastoplastic constitutive model and temperature sensitivity of glasphalt. *Int. J. Pavement Eng.* **2014**, *2014*, 810–830. [[CrossRef](#)]
31. Zhu, H.R.; Sun, L. A viscoelastic-viscoplastic damage constitutive model for asphalt mixtures based on thermodynamics. *Int. J. Plast.* **2013**, *40*, 81–100. [[CrossRef](#)]



© 2018 by the authors. Licensee MDPI, Basel, Switzerland. This article is an open access article distributed under the terms and conditions of the Creative Commons Attribution (CC BY) license (<http://creativecommons.org/licenses/by/4.0/>).

Article

Analysis of Aggregate Morphological Characteristics for Viscoelastic Properties of Asphalt Mixes Using Simplex Lattice Design

Wensheng Wang ¹, Yongchun Cheng ¹, Guojin Tan ^{1,*} and Jinglin Tao ^{2,*}

¹ College of Transportation, Jilin University, Changchun 130025, China; wangws17@mails.jlu.edu.cn (W.W.); chengyc@jlu.edu.cn (Y.C.)

² Jiangxi Transportation Institute, Nanchang 330200, China

* Correspondence: tgj@jlu.edu.cn (G.T.); taojl18@163.com (J.T.); Tel.: +86-0431-8509-5446 (G.T.)

Received: 24 August 2018; Accepted: 5 October 2018; Published: 8 October 2018

Abstract: Morphological characteristics of aggregates have direct impacts on performances of asphalt mixes. This paper aims to investigate the effects of the morphological characteristics of fine and coarse aggregates on the high-temperature viscoelastic properties of asphalt mortars and mixtures. For this purpose, an experimental proportion scheme was designed for asphalt mixes prepared with three different types of aggregates (basalt, andesite and pebble/river sand) based on the simplex lattice design (SLD) method. Three morphological parameters were chosen to characterize shape, angularity and texture of aggregates. Afterwards, the uniaxial compression creep test was conducted for asphalt mixes and the high-temperature viscoelastic properties were obtained based on Burgers model. The effects of fine and coarse aggregates on the viscoelastic properties are analyzed through asphalt mortars and mixtures, respectively. The results showed that aggregate morphological characteristics correlate with the high-temperature viscoelastic properties of asphalt mixes, especially for fine aggregates. Aggregates with complex morphological characteristics are conducive to improving the deformation recovery and anti-deformation of asphalt mixes. Furthermore, coarse aggregates can enhance the anti-deformation of asphalt mixture effectively due to its skeleton effect.

Keywords: asphalt mixes; aggregate characteristics; simplex lattice design; viscoelastic properties

1. Introduction

Asphalt as a kind of composite material has been widely used in pavement and building constructions. In general, aggregates in asphalt mixtures account for approximately over 90% of mixtures by weight, which play a major role in its stability, durability and mechanical properties. Researchers in many countries have been trying to focus on the influence of aggregate morphological characteristics on performances of asphalt mixture [1–3].

A great number of laboratory tests have been developed in previous research to evaluate the morphological characteristics of aggregates. Wilson and Klotz [4] presented a method of measuring angularity using Hough transform for quantitative analysis of aggregate angularity. Kuo et al. [5] used a digital image-analysis method to investigate the morphologies of coarse aggregates and effectively quantified the morphological characteristics. The morphological characteristics were found to be correlated well with indirect characterization test results by regression analysis. Wang et al. [6] developed a unified Fourier morphological analysis method to quantify aggregate morphological characteristics, which include shape, angularity and surface texture. The above analysis has been conducted on coarse aggregates; however, investigations on fine aggregate morphology have attracted more researchers. Masad and Button [7] investigated the angularity and texture of fine aggregates by using the erosion-dilation method and form factor, in which angularity is analyzed by high-resolution

images and texture is described by low-resolution images. Kuo and Freeman [8] defined three image indices—aspect ratio, angularity and roughness—to characterize overall shape, roundness of corners, and particle surface texture of fine aggregates, which could be calculated by shortest and longest dimensions, perimeters, convex perimeters and perimeters of ellipses. Xie et al. [9] evaluated the morphological characteristics of fine aggregates by using three methods and they found that different methods have respective applicability and precision, in which digital image processing technique is useful for designing bituminous materials. Xiao et al. [10] studied fine aggregate morphology by using the aggregate image measurement system and discussed the influences of aggregate morphological characteristics on skid-resistance of single-grade micro-surfacing.

Based on previous research on aggregates' morphological characteristics, the relationships between aggregate morphological characteristics and performances of asphalt mixtures were also investigated. Petersen et al. [11] aimed at evaluating the rutting resistance of asphalt mixture and found that the morphological characteristics of coarse aggregate correlated well with it. Arasan et al. [12] used the digital image processing method to analyze the shape indices of coarse aggregate and showed a good correlation between some shape indices of aggregate and volumetric performances of asphalt mixtures. Singh et al. [13] utilized aggregate shape parameters to estimate dynamic modulus of asphalt mixes by establishing a model. Pan et al. [14] investigated the effects of coarse aggregate morphology on the permanent deformation of asphalt mixtures. The permanent deformation showed a strong correlation with surface texture and angularity; the former has significant influences on the permanent deformation. Aragao et al. [15] evaluated the influence of morphological properties of aggregates on the mechanical behavior of bituminous mixtures. The results indicated that the morphological characteristics of coarse aggregate are strongly correlated with the resistance to rutting of asphalt mixtures. Besides, the aggregate surface texture was proven to be highly correlated to the performance of mixtures and should be carefully considered in aggregate and asphalt mixture specifications. Valdes-Vidal et al. [16] investigated the influence of aggregate physical properties on the mechanical properties of asphalt concretes. Morphological characteristics as well as surface texture have been conducted for three aggregates. The results demonstrated that the morphological characteristics of coarse and fine aggregates influence strength and anti-cracking properties of asphalt concretes, which depend on the shredding process and the origin of aggregates. Masad et al. [17] addressed the relationship between the morphological characteristics of fine aggregate and performances of asphalt mixtures and they found that texture characteristics had the strongest correlation with rutting resistance of asphalt mixtures. Therefore, the morphological characteristics of coarse and fine aggregates have significantly different influences on the performances of asphalt mixture.

Morphological characteristics of aggregates have direct impacts on performances of asphalt mixtures. Previous research has investigated the influences of aggregate morphological characteristics on the adhesion between the aggregate and asphalt, high- and low-temperature stability performances, and fatigue property. However, not much study has been conducted on the relationship between an aggregate's morphological characteristics and viscoelastic properties of the asphalt mixture. Therefore, in order to investigate the influence of an aggregate's morphological characteristics on asphalt mixture, this paper studied the effects of the morphological characteristics of fine and coarse aggregates on the high-temperature viscoelastic properties of asphalt mortars and mixtures.

In this paper, an experimental proportion design was created for asphalt mortars and mixtures prepared with three different types of aggregates, based on the simplex lattice design (SLD) method. Three indices are chosen to characterize aggregates—shape, angularity and texture. The objective is to relate the aggregate's morphological characteristics to the viscoelastic properties of asphalt mixture. Based on Burgers viscoelastic model, the uniaxial compression static creep test was carried out to analyze the high-temperature viscoelastic properties of asphalt mortar and mixture.

2. Materials and Methods

2.1. Raw Materials

In this study, asphalt AH-90 from Panjin Petrochemical Industry of Liaoning Province, China, was chosen for the asphalt mixes. Table 1 shows the physical properties of AH-90. The mineral fillers and aggregates were obtained from a local stone factory in Jilin Province, China. The selected filler is ordinary limestone powder, and three types of aggregates with various morphological characteristics were chosen for coarse and fine aggregates, respectively. The three types of coarse aggregates were basalt stone, andesite stone and pebble; fine aggregates included basalt manufactured sand, andesite manufactured sand and river sand. Their physical properties are summarized in Table 2.

Table 1. Basic physical properties of asphalt AH-90.

Property	Measurement	Technical Criterion
Penetration @ 25 °C, 100 g, 5 s (0.1 mm)	90	80–100
Softening point (°C)	42.6	≥42
Ductility @ 15 °C, 5 cm/min (cm)	195.2	≥100
Density @ 15 °C (g/cm ³)	1.014	–
<i>After TFOT</i>		
Mass loss (%)	0.37	±0.8
Penetration ratio @ 25 °C (%)	59	≥54

Table 2. Physical properties of aggregates and filler.

Property	Coarse and Fine Aggregates										Filler
	13.2	9.5	4.75	2.36	1.18	0.6	0.3	0.15	0.075	<0.075	
Hydrophilic coefficient	–	–	–	–	–	–	–	–	–	–	0.80
Specific surface area (m ² /g)	–	–	–	–	–	–	–	–	–	–	0.886
Apparent density (g/cm ³)	Basalt	2.782	2.774	2.770	2.758	2.713	2.720	2.699	2.647	2.700	2.652
	Andesite	2.785	2.853	2.729	2.717	2.658	2.701	2.639	2.645	2.648	
	Pebble/River sand	2.656	2.644	2.645	2.636	2.624	2.606	2.635	2.698	2.597	

2.2. Sample Preparation

Asphalt mixes (asphalt mortar and asphalt mixture) were prepared to analyze and demonstrate the influence of coarse and fine aggregates characteristics on high-temperature viscoelastic properties. Figure 1 presents the used gradations of asphalt mixes with a nominal maximum size of 13.2 mm, i.e., AC-13, in which asphalt mortar consists of asphalt, filler and fine aggregate passing through 2.36 mm [18]. Besides, asphalt content is generally regarded as one of the main influencing factors for asphalt mixes. Its consistency is of great importance. According to previous literature [18], asphalt film thickness was kept as a constant of 8 µm and the specific surface area of asphalt mixes was calculated as 14.34 m²/kg for asphalt mortar and 5.935 m²/kg for asphalt mixture. Thus, the optimal asphalt content can be also obtained as 11.6% for asphalt mortar and 4.8% for asphalt mixture. The target air void of asphalt mixes was set as 4% and then the mass and volume proportion of asphalt mixes can be determined through the densities of asphalt and aggregates. The cylindrical specimens of asphalt mortar with height of 50 mm and diameter of 50 mm were prepared through the static pressure method [19]. The Marshall specimens of asphalt mixture with height of 63.5 mm and diameter of 101 mm were prepared through Marshall procedures, according to Chinese specification JTG E20-2011 [20].

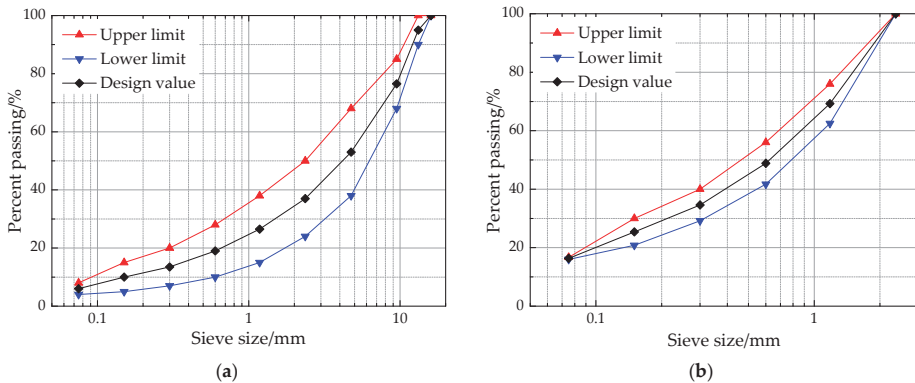


Figure 1. Gradations of asphalt mixes used in this study: (a) asphalt mixture; (b) asphalt mortar.

2.3. Experimental Methods

2.3.1. Morphological Characteristics of Aggregates

A scanner (Opt Vision Technology Co., Ltd., Dongguan, China) is selected to obtain the image information of coarse aggregates, and a stereo microscope (Opt Vision Technology Co., Ltd.) is used to collect the image information of fine aggregate. Before image collection, fine and coarse aggregates need to be cleaned to remove impurities (such as surface dust) and then dried in an oven. The image processing technique is then employed to process (image denoising and enhancement) the color images. Subsequently, the morphological characteristics of aggregates are obtained through the following equations.

(1) Shape

Shape characteristics of aggregates reflect flat and elongated particles, which are undesirable in the preparation of asphalt mixture because they break easily under loading effects. Roundness is used to represent the shape of aggregates, which could be calculated as follows [17]:

$$R = L^2 / 4\pi S \tag{1}$$

where R is shape index, L is the projected perimeter of the particle, S is the corresponding projected area. In general, $R \geq 1$, a larger R value means a slender shape and the aggregate is more spherical if the R value is closer to one.

(2) Angularity

Angularity of the aggregates illustrates the angle change on particle outline, and perimeter index expressed in Equation (2) is used to characterize the angularity characteristics of aggregates [21].

$$PI = P / P_E \tag{2}$$

where PI is perimeter index, P is the perimeter of particle outline, P_E is the perimeter of equivalent ellipse. The larger PI means more angular boundaries or sharp angles of the aggregate.

(3) Texture

Texture is usually considered as the tiny bumps on the particle outline [21]. In this study, the erosion-dilation area ratio is regarded as an evaluation index for texture characteristics of aggregates, which could be expressed as [7]:

$$EDR = (A_1 - A_2)/A_1 \times 100 \tag{3}$$

where *EDR* is texture index, A_1 is area of the original particle, A_2 is area of the particle after successive erosion and dilation operations.

2.3.2. Burgers Viscoelastic Model

Asphalt is a typical viscoelastic material with characteristics of both Hookean elasticity and Newtonian viscosity. The viscoelastic model also has elastic and viscous components, which is general modelled by combining spring and dashpot. Different models study the viscoelastic properties of asphalt materials, such as Maxwell, Kelvin, Burgers models, etc. The Maxwell model is a simple linear model that combines both Hookean springs and Newtonian dashpots in series, while the Kelvin model is a combination of Hookean springs and Newtonian dashpots in parallel. Neither the Maxwell nor the Kelvin model could fully describe the characteristics of viscoelastic materials. Thus, a Burgers model (as shown in Figure 2) is developed as a combination of Maxwell and Kelvin models in series, which is a four-element model, indicating elastic deformation, viscous flow and viscoelastic deformation [22,23].

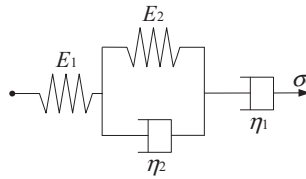


Figure 2. Schematic representation of Burgers model.

The constitutive equation of the Burgers model is given in differential form as:

$$\sigma + p_1\dot{\sigma} + p_2\ddot{\sigma} = q_1\dot{\epsilon} + q_2\ddot{\epsilon} \tag{4}$$

where $p_1 = (\eta_1 E_1 + \eta_1 E_2 + \eta_2 E_1)/(E_1 E_2)$, $p_2 = \eta_1 \eta_2 / E_1 E_2$, $q_1 = \eta_1$, $q_2 = \eta_1 \eta_2 / E_2$.

An applied constant stress $\sigma = \Delta(t)\sigma_0$, is introduced into Equation (4). Applying the Laplace transform can lead to Equation (5), in which *s* is Laplace operator.

$$\sigma_0/s + p_1\sigma_0 + p_2s\sigma_0 = q_1s\bar{\epsilon}(s) + q_2s^2\bar{\epsilon}(s) \tag{5}$$

Then Equation (5) could be solved as:

$$\bar{\epsilon}(s) = \sigma_0 \left[\frac{1}{s^2(q_1 + q_2s)} + \frac{p_1}{s(q_1 + q_2s)} + \frac{p_2}{q_1 + q_2s} \right] \tag{6}$$

Taking the inverse Laplace transform, the creep strain versus time is given by:

$$\epsilon(t) = \sigma_0 \left[\frac{1}{E_1} + \frac{t}{\eta_1} + \frac{1}{E_2} \left(1 - e^{-E_2 t / \eta_2} \right) \right] \tag{7}$$

where E_1, E_2, η_1, η_2 are viscoelastic constants, which could be determined through the fitting creep test.

For the Burgers model, E_1 is the modulus of immediate elasticity Burgers model, and a higher value of E_1 will lead to a larger resistance to deformation while loading, as well as a better recovery capacity after unloading. E_2 is the modulus of delayed elasticity Burgers model, preventing the growing deformation of dashpot in the Kelvin model. η_1 is the coefficient of viscosity Burgers model and related with permanent deformation after unloading. η_2 is the coefficient of elastic delay viscosity Burgers model and corresponding viscoelastic deformation would be fully recovered with recovery time. In addition, retardation time is defined as $\tau = \eta_2/E_2$, and a higher value of τ indicates that the

asphalt material is close to viscous deformation and the recovery time of viscoelastic deformation after unloading is longer.

2.3.3. Uniaxial Compression Failure and Static Creep Tests

(1) Uniaxial Compression Failure Test

Uniaxial compression failure test (Jinli testing technology Co., Ltd, Changchun, China) is adopted to study the stress-strain relationship, which could be calculated through the compression strength of specimens under a constant loading rate [24]. In this study, the uniaxial compression failure tests of asphalt mortar and mixture were conducted in accordance with previous research [25,26]. Asphalt mixes specimens were immersed in a water bath for 4 h at the test temperature. Then a loading with a constant speed of 50 mm/min was applied on specimens and a stress-strain curve was plotted following the test. The compression failure stress, failure strain and secant modulus (i.e., the ratio of failure stress to failure strain) were taken as further comparative analysis parameters [24].

(2) Uniaxial Compression Static Creep Test

The viscoelastic properties of asphalt materials can be determined through the creep test and more details can be referred to previous research [25,26]. Before uniaxial compression static creep test (Cooper Research Technology Ltd., Ripley, UK), the stress level for asphalt mortar and mixture were firstly chosen by using uniaxial compression failure test. Then a servo-pneumatic universal testing machine was employed to conduct the uniaxial compression static creep test at a fixed stress level and creep time for asphalt mortar and mixture, respectively. Due to different asphalt contents in asphalt mortar and mixture, different test temperatures were selected to reduce the error caused by temperature, in which the test temperatures were set as 30 °C for asphalt mortar and 50 °C for asphalt mixture [25,26]. Subsequently, the deformations of asphalt mortar and mixture could be measured using two LVDTs (Linear Variable Differential Transformers) and corresponding creep curves would be also obtained at different test temperatures.

At the stress level is $\sigma = \sigma_0$, the creep compliance of asphalt materials is defined as follows:

$$J(t) = \varepsilon(t) / \sigma_0 \quad (8)$$

where $J(t)$ is creep compliance; $\varepsilon(t)$ is creep strain; σ_0 is constant stress.

2.3.4. Simplex Lattice Design (SLD)

SLD is a common mixture design method for optimizing the proportions of the ingredients in the mixture by combining the mathematical theory, statistical analysis and experimental design [27]. A $[q, m]$ simplex lattice represents q components consisting of points defined by the following coordinate settings in Equations (9) and (10): a “standardized” or “normalized” simplex coordinate is established and generally written as x_i , the proportions assumed each component takes the $(m + 1)$ equally spaced values (x_i) from 0 to 1 and component proportions should be expressed as fractions with a sum (x_i) of one. Figure 3 shows the three-ingredient equilateral triangular simplex-lattice coordinate systems with quadratic and cubic orders.

$$x_i = 0, 1/m, 2/m, \dots, 1, (i = 1, 2, \dots, q) \quad (9)$$

$$\sum_{i=1}^q x_i = 1 \quad (10)$$

where q is the number of ingredients in a mixture, m is usually called the degree of the simplex lattice, x_i is the fractional proportion of the i th ingredient in the $[q, m]$ simplex lattice.

Based on the relationship between mixture components and property responses of asphalt mixes, a regression equation can be fitted to the experimental data at the points of a $[q, m]$ simplex lattice, which is expressed in the terms of the following polynomial equation:

$$y_{[q,m]} = \beta_0 + \sum_{i=1}^q \beta_i x_i + \sum_{i \leq j}^q \beta_{ij} x_i x_j + \sum_{i \leq j \leq k}^q \beta_{ijk} x_i x_j x_k + \dots \tag{11}$$

where $y_{[q,m]}$ is the response, $\beta_0, \beta_i, \beta_{ij}, \beta_{ijk}$ are the regression coefficients, x_i, x_j, x_k are the fractional proportion of the ingredients in the mixture.

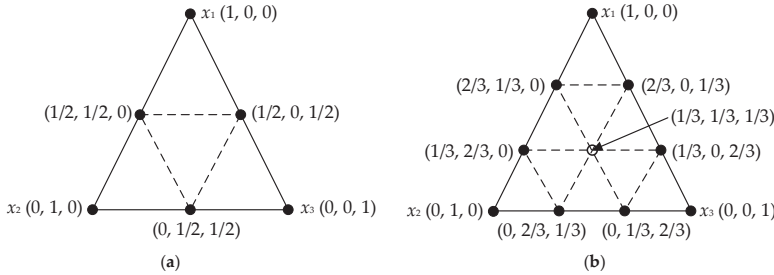


Figure 3. Three-ingredient simplex-lattice coordinate systems: (a) [3, 2] SLD; (b) [3, 3] SLD.

In this study, the simplex lattice of [3, 2] shown in Figure 3a was used to investigate the effects of the proportions of three mixture components on the viscoelastic properties of asphalt mixes using Design-Expert 8.0 software (Stat-Ease Inc., Minneapolis, MN, USA). The samples of asphalt mixes can be prepared through mixing the three ingredients at different proportions. The independent variable factors are the percentages of basalt (X_1), andesite (X_2) and pebble/river sand (X_3), respectively. The high-temperature viscoelastic properties are the modulus of immediate elasticity Burgers model (E_1), coefficient of viscosity Burgers model (η_1) and retardation time (τ), as dependent variables. The designed experimental proportion need ten groups, which include three pure component treatments, three two-component mixtures and four “augment design”. Table 3 lists the proportions of three components in asphalt mixes. And the quadratic order canonical polynomial equation derived from Equation (11) can be given as:

$$y = \beta_1 x_1 + \beta_2 x_2 + \beta_3 x_3 + \beta_{12} x_1 x_2 + \beta_{23} x_2 x_3 + \beta_{13} x_1 x_3 \tag{12}$$

where y is the response, $\beta_1, \beta_2, \beta_3, \beta_{12}, \beta_{23}, \beta_{13}$ are the regression coefficients for linear and non-linear terms.

Table 3. Experimental proportion design for the [3, 2] simplex lattice design (SLD).

Mix Component	Sample Code									
	1	2	3	4	5	6	7	8	9	10
Basalt (X_1)	0.167	0.167	0.000	0.500	1.000	0.500	0.667	0.000	0.000	0.333
Andesite (X_2)	0.667	0.167	1.000	0.000	0.000	0.500	0.167	0.000	0.500	0.333
Pebble/River Sand (X_3)	0.167	0.667	0.000	0.500	0.000	0.000	0.167	1.000	0.500	0.333

3. Results and Discussion

3.1. Results of Morphological Characteristics of Fine and Coarse Aggregates

Due to different morphological characteristics of aggregates with different particle sizes or various combinations, it is necessary to unify them in order to analyze their influence. *Composite index* for fine

and coarse aggregates is adopted to account for three morphological characteristics, i.e., roundness, perimeter index and erosion-dilation area ratio, which is given in Equation (13) [14].

$$\text{Composite index} = \frac{\sum_{i=1}^n [(a_i)(\text{index}_i)]}{\sum_{i=1}^n (a_i)} \quad (13)$$

where *Composite index* includes composite roundness, composite perimeter index, and erosion-dilation area ratio for fine and coarse aggregates abbreviated as *FR*, *CR*, *FPI*, *CPI*, *FEDR*, *CEDR*, respectively. a_i is the gradation percentage of the i th aggregate. index_i is morphological characteristics index (*R*, *PI* and *EDR*) of the i th aggregate. The results of *Composite index* for fine aggregate in asphalt mortar (abbreviated as F1~F10) and coarse aggregate in asphalt mixture (abbreviated as C1~C10) are listed in Table 4.

Table 4. Composite morphological index of fine and coarse aggregates.

Index	Sample Code									
	1	2	3	4	5	6	7	8	9	10
Asphalt Mortar (F1~F10)										
<i>FR</i>	1.5658	1.4175	1.6143	1.4641	1.6103	1.6123	1.5638	1.3178	1.4661	1.5127
<i>FPI</i>	1.2385	1.1526	1.2723	1.1673	1.2340	1.2532	1.2194	1.1005	1.1864	1.2011
<i>FEDR</i>	0.7821	0.5729	0.8645	0.6151	0.7842	0.8244	0.7419	0.4461	0.6553	0.6976
Asphalt Mixture (C1~C10)										
<i>CR</i>	1.6889	1.4974	1.7586	1.5447	1.7140	1.7363	1.6666	1.3755	1.5671	1.6144
<i>CPI</i>	1.2367	1.1682	1.2612	1.1840	1.2438	1.2525	1.2280	1.1242	1.1927	1.2085
<i>CEDR</i>	0.9329	0.7794	0.9928	0.8106	0.9355	0.9642	0.9043	0.6857	0.8392	0.8705

3.2. Analysis of Fine Aggregate Characteristics for Viscoelastic Properties of Asphalt Mortar Using SLD

3.2.1. Uniaxial Compression Failure Test Results

The uniaxial compression failure tests of asphalt mortar were performed at 30 °C, and the speed of applied loading was 50 mm/min. According to the recorded relation curve between force and displacement, the maximum stress, corresponding strain and the ratio of the two were obtained as the compression failure stress, failure strain and secant modulus. The uniaxial compression failure test results are plotted in Figure 4.

As shown in Figure 4a, asphalt mortars with various fine aggregate morphologies have obvious different mechanical properties when subjected to a constant strain-rate loading. Sample F3 has the highest failure stress, followed by F5; the failure stress of F8 is the lowest. In general, a higher failure stress is preferable due to better bearing capacity. Based on the stress results, it can be considered that F3 has a better bearing capacity, and followed by F5, the bearing capacity of F8 is the lowest. As for the failure strain in Figure 4b, it illustrates the deformation characteristics of asphalt mortars while loading, which has the opposite trend with the failure stress in Figure 4a. Sample F8 has the largest failure strain, whereas the failure strain of F3 is the smallest among all the asphalt mortars. The failure strain indicates the deformation before the asphalt material being broken, which could help reduce the occurrence of crack at low temperature, but would be easy to produce a greater permanent deformation at high temperatures. Secant modulus is the ratio of failure stress to failure strain, comprehensively reflecting the compatibility of deformation. Normally, a higher secant modulus stands for the better compatibility of deformation and anti-compression failure performance. Previous research has found that the shape and texture characteristics of aggregates have a strong correlation with the resistance of asphalt mixes to permanent deformation measured using different wheel tracking devices [14,28]. The failure results are consistent with the morphological characteristics results of aggregates. Thus, it could be considered that asphalt mixes with complex morphological characteristics have higher failure stress, smaller strain, and higher secant modulus. The variation trend of secant modulus results observed in

Figure 4c is consistent with the trend of failure stress in Figure 4a, in which sample F3 has the highest secant modulus, followed by F5; the secant modulus of F8 is the lowest among all the asphalt mortars. As the designed experimental proportion listed in Table 3, asphalt mortar F3 was prepared by andesite manufactured sand; basalt manufactured sand was used for F5 and F8 was made by river sand. Thus, it is evident that manufactured sands can improve the anti-compression failure performance of asphalt mortar and the asphalt mortar made by natural sands has the largest failure strain.

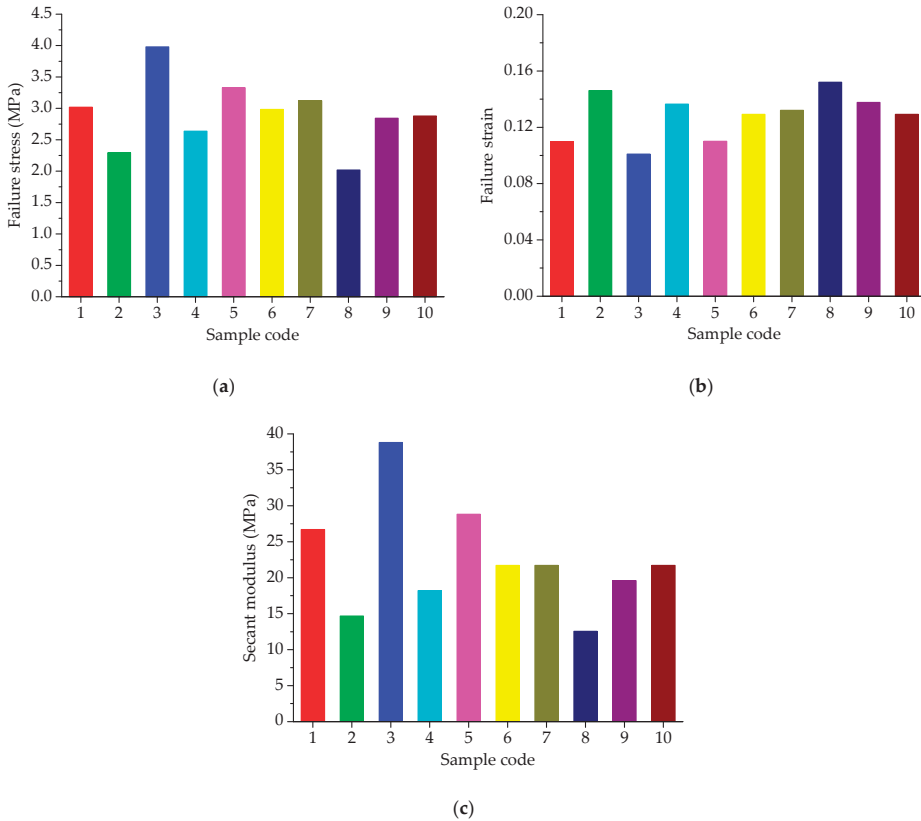


Figure 4. Failure results of asphalt mortars: (a) Failure stress; (b) Failure strain; (c) Secant modulus.

3.2.2. Uniaxial Compression Creep Test Results Based on SLD

Before the uniaxial compression static creep test, the uniaxial compression failure test was conducted to determine an appropriate stress level for asphalt mortar. Figure 4a shows the range of failure stress, i.e., 2.07 MPa–4.03 MPa for asphalt mortars at 30 °C. Thus, the applied stress level of 0.2 MPa was kept constant for the uniaxial compression creep test. Then a preconditioning stress of 5% loading was applied to asphalt mortar samples for 90 s. Subsequently, a servo-pneumatic universal testing machine was adopted to apply a stress-controlled uniaxial compressive loading for 1800 s at 30 °C. Figure 5 compares the creep strain-time curves for 10 groups of asphalt mortars at 30 °C.

As illustrated in Figure 5, the creep deformations of asphalt mortars increase gradually with the loading time increasing. Besides, it could be observed that at the same loading time, the creep strains of 10 groups of asphalt mortars are ranked as F8 > F2 > F4 > F9 > F10 > F7 > F1 > F5 > F6 > F3. A larger creep strain means a worse anti-deformation performance, that is, F3 has the best anti-deformation

performance and the anti-deformation performance of F8 is the worst. Thus, andesite manufactured sand could improve the anti-deformation performance of asphalt mortar compared with river sand.

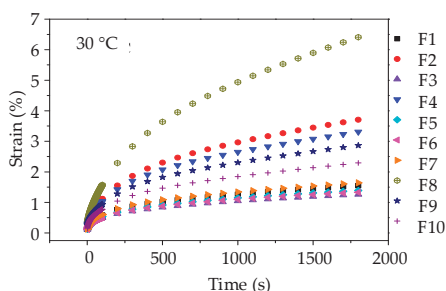


Figure 5. Creep strain-time curves of asphalt mortars at 30 °C.

As different fine aggregates lead to different viscoelastic performances of asphalt mortars, it is necessary to quantitatively analyze the influence of morphological characteristics of fine aggregates on viscoelastic performances of asphalt mortar. The Burgers model (as shown in Figure 2) was then adopted to fit with the creep strain-time curves of asphalt mortars in order to obtain viscoelastic parameters (i.e., E_1 , η_1 and τ). Table 5 details the viscoelastic responses of asphalt mortars, in which all the coefficients of determination (R^2) are more than 0.98, indicating that the fitted Burgers models can well describe the creep characteristics of asphalt mortars.

Table 5. Viscoelastic responses of SLD for asphalt mortars (F1–F10).

Response	Sample Code									
	1	2	3	4	5	6	7	8	9	10
E_1 (MPa)	91.6	53.7	100.6	58.1	95.6	98.9	89.2	44.6	61.5	75.4
η_1 (GPa·s)	48.1	19.5	56.7	21.9	50.7	53.1	45.3	10.1	25.6	30.8
τ (s)	122.3	176.9	105.4	170.1	105.4	105.9	124.2	209.9	157.9	130.6

3.2.3. Statistical Analysis and Discussion

Analysis of Modulus of Immediate Elasticity Burgers Model (E_1)

According to the experimental proportion design and viscoelastic responses using SLD, the analysis of variance (ANOVA) was adopted to determine the regression model and evaluate the statistical significance of independent factors, i.e., basalt (X_1), andesite (X_2) and pebble/river sand (X_3). The statistical significance level was chosen as 0.05, that is, models and independent factors can be considered significant when the p -value falls below 0.05. The ANOVA results for modulus of immediate elasticity Burgers model (E_1) are listed in Table 6, which shows the sum of squares, degree of freedom (DF), mean square, Fisher’s test value (F -value), and probability “Prob > F -value” (p -value).

Table 6. ANOVA results for modulus of immediate elasticity Burgers model (E_1).

Source	Sum of Squares	DF	Mean Square	F -Value	p -Value	Significant
Model	3733.67	2	1866.84	64.23	<0.0001	Yes
Linear mixture	3733.67	2	1866.84	64.23	<0.0001	Yes
Residual	203.46	7	29.07			
Total	3937.14	9				

Based on the ANOVA results in Table 6, the polynomial model of modulus of immediate elasticity Burgers model (E_1) is demonstrated in detail. The linear terms are identified as the significant terms of E_1 . Thus, the quadratic order polynomial equation for E_1 can be finally established as:

$$Y_1 = 94.60X_1 + 99.86X_2 + 36.30X_3 \tag{14}$$

Subsequently, Figure 6a illustrates the three-dimensional (3D) response surface plots for modulus of immediate elasticity Burgers model (E_1), which is plotted by fitting the quadratic polynomial to reveal the effects of the component proportion on E_1 . It is clear from Figure 6a that E_1 of asphalt mortars presents a decreasing trend when the proportion of river sand (X_3) increases, whereas the proportions of basalt (X_1) and andesite (X_2) have opposite effects on E_1 . In order to quantitatively analyze the effects of fine aggregate morphologies on viscoelastic performances of asphalt mortar, morphological characteristics (i.e., FR , FPI and $FEDR$) are regarded as independent variables and the relationships of linear regression for E_1 are illustrated in Figure 6b,c. The values of E_1 increase with the increase of morphological characteristics of fine aggregates, for which there are positive correlations among these variables and the correlation coefficient values R^2 are above 0.92. The linear regression models show a strong correlation with test results, indicating that the linear regression models are efficient in characterizing their relationship. A higher value of E_1 stands for a larger resistance to deformation on loading, as well as a better recovery capacity after unloading. Thus, fine aggregates with complex morphological characteristics could improve the anti-deformation performance of asphalt mortar.

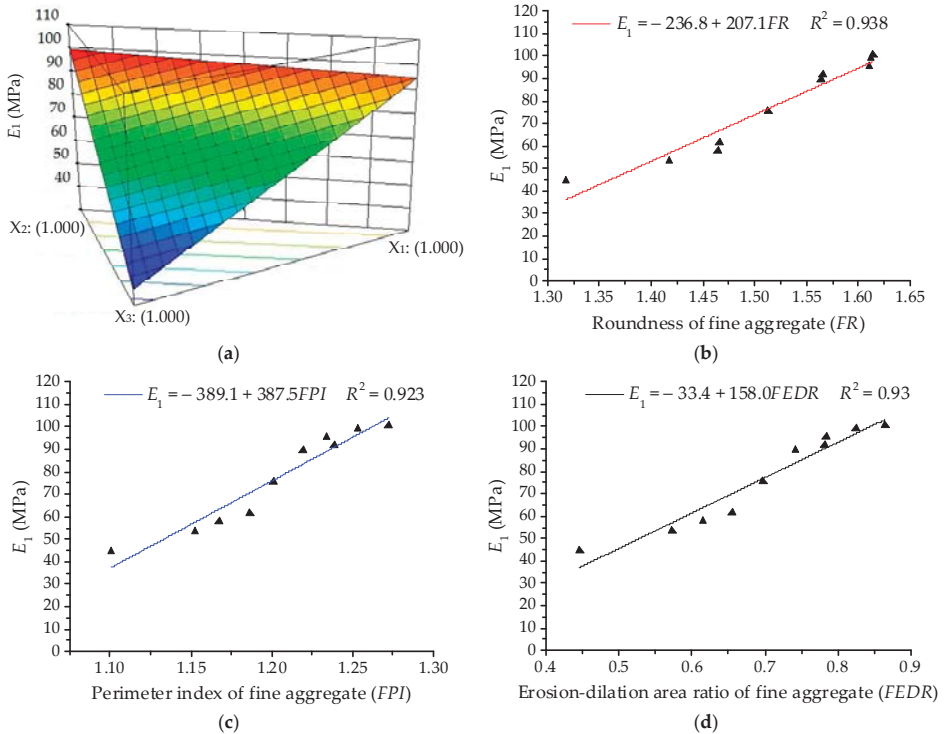


Figure 6. Relationships between E_1 and fine aggregates: (a) Response surface plot for component proportion and E_1 ; (b) FR and E_1 ; (c) FPI and E_1 ; (d) $FEDR$ and E_1 .

Analysis of Coefficient of Viscosity Burgers Model (η_1)

The ANOVA results for coefficient of viscosity Burgers model (η_1) are listed in Table 7 based on SLD. The linear terms are identified as the significant terms of η_1 . Thus, the quadratic order polynomial equation for η_1 can be finally established as:

$$Y_2 = 49.07X_1 + 55.24X_2 + 4.24X_3 \tag{15}$$

Table 7. ANOVA results for coefficient of viscosity Burgers model (η_1).

Source	Sum of Squares	DF	Mean Square	F-Value	p-Value	Significant
Model	2324.53	2	1162.26	66.63	<0.0001	Yes
Linear mixture	2324.53	2	1162.26	66.63	<0.0001	Yes
Residual	122.11	7	17.44			
Total	2446.64	9				

As illustrated in Figure 7a, the 3D response surface plots for coefficient of viscosity Burgers model (η_1) can be obtained by fitting the quadratic polynomial to reveal the effects of component proportion on η_1 . Figure 7b,c illustrate the positive correlation relationships of linear regression between η_1 and morphological characteristics with R^2 more than 0.93. Coefficient η_1 shown in Figure 7 presents a similar trend with modulus of immediate elasticity Burgers model (E_1) in Figure 6. η_1 of asphalt mortars presents a decreasing trend when the proportion of river sand (X_3) increases, whereas the proportions of basalt (X_1) and andesite (X_2) have similar effects on η_1 . The larger the viscosity coefficient η_1 , the smaller the permanent deformation. It also verifies that fine aggregates with complex morphologies would improve the anti-deformation performance of asphalt mortar.

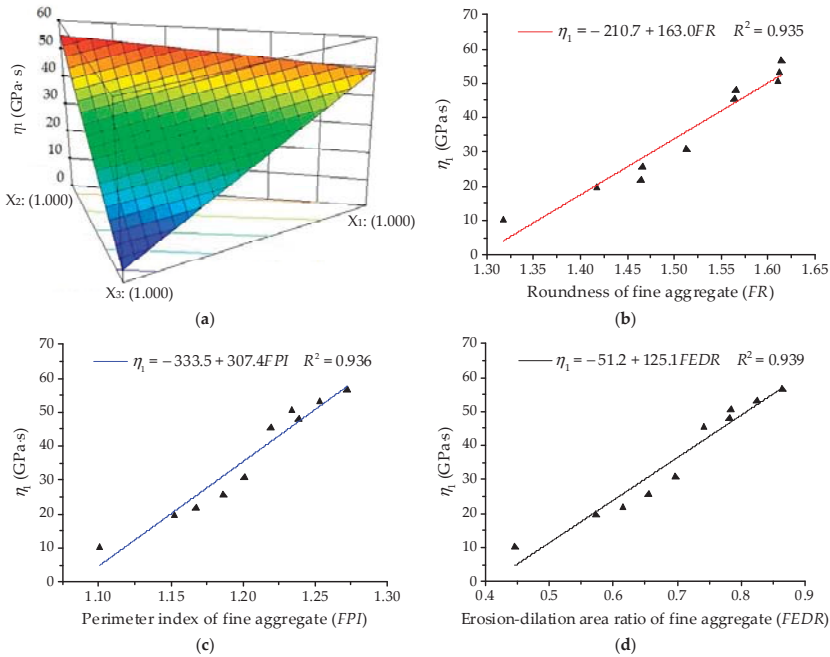


Figure 7. Relationships between η_1 and fine aggregates: (a) Response surface plot for component proportion and η_1 ; (b) FR and η_1 ; (c) FPI and η_1 ; (d) FEDR and η_1 .

Analysis of Retardation Time (τ)

The ANOVA results for retardation time (τ) are listed in Table 8 based on SLD. The linear terms and non-linear terms (X_1X_3 and $X_1X_2X_3$) are identified as the significant terms of τ . Thus, the quadratic order polynomial equation for η_1 can be finally established as:

$$Y_3 = 105.52X_1 + 106.11X_2 + 210.16X_3 + 50.52X_1X_3 - 349.97X_1X_2X_3 \quad (16)$$

Table 8. ANOVA results for retardation time (τ).

Source	Sum of Squares	DF	Mean Square	F-Value	p-Value	Significant
Model	11640.20	6	1940.03	189.13	0.0006	Yes
Linear mixture	11444.80	2	5722.40	557.86	0.0001	Yes
X_1X_2	0.59	1	0.59	0.058	0.8255	No
X_1X_3	107.80	1	107.80	10.51	0.0478	Yes
X_2X_3	0.39	1	0.39	0.038	0.8584	No
$X_1X_2X_3$	119.01	1	119.01	11.60	0.0423	Yes
Residual	30.77	3	10.26			
Total	11670.97	9				

As illustrated in Figure 8a, the 3D response surface plots for retardation time (τ) were also obtained by fitting the quadratic polynomial to reveal the effects of component proportion on τ . τ of asphalt mortars presents a decreasing trend with increase in the proportion of basalt (X_1) and andesite (X_2), whereas the proportions of river sand (X_3) have the opposite effect on τ . Figure 8b,c illustrate a negative correlation of linear regression between τ and morphological characteristics with R^2 more than 0.94. It clearly shows that the retardation time of asphalt mortar decreases with increase in morphological characteristics of fine aggregates. As the retardation time is related to the recovery time of viscoelastic deformation, fine aggregates with complex morphological characteristics help improve the deformation recovery capacity of asphalt mortar.

3.3. Analysis of Coarse Aggregate Characteristics for Viscoelastic Properties of Asphalt Mixture Using SLD

3.3.1. Uniaxial Compression Failure Test Results

Figure 9 presents the uniaxial compression failure test results of asphalt mixtures at the test temperature of 50 °C. The speed of applied loading was set at 50 mm/min. As shown in Figure 9, for constant strain rate loading, different types of coarse aggregates lead to a large difference in mechanical property distribution of asphalt mixtures. Asphalt mixtures without pebbles have larger failure stress and secant modulus and those with pebbles have smaller failure strain, i.e., the failure stress and secant modulus of C3, C5 and C6 are larger than the others, while these failure strains are smaller than the other groups. The change of mechanical properties of asphalt mixtures is more related to pebble content. This is because manufactured stones (basalt stone and andesite stone) have more complex morphological characteristics than pebble and pebble is more spherical. With loading time and increasing deformation, the inlay effect of coarse aggregates becomes more and more significant. However, asphalt mixture with pebbles would cracks prematurely compared to asphalt mixture made with manufactured stones, resulting in stress reduction as well as broken specimens.

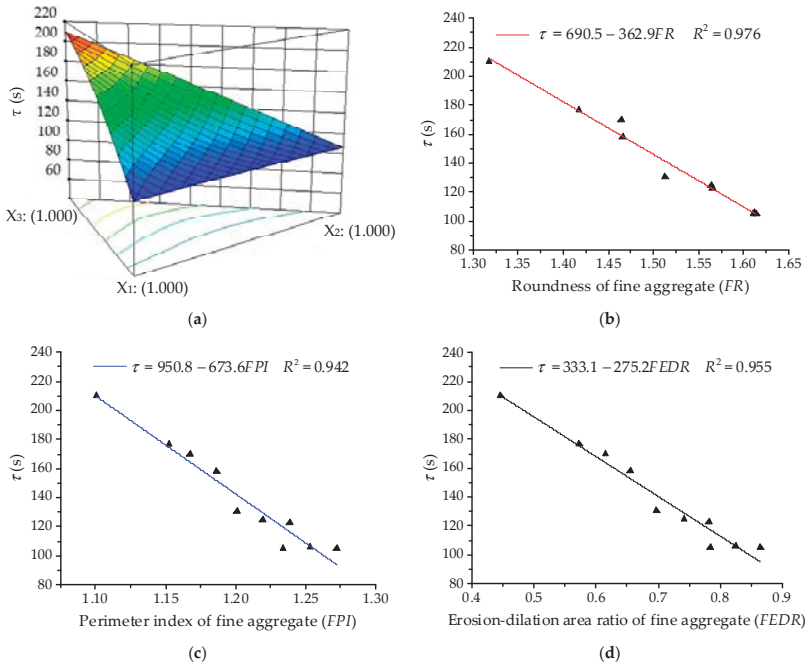


Figure 8. Relationships between τ and fine aggregates: (a) Response surface plot for component proportion and τ ; (b) FR and τ ; (c) FPI and τ ; (d) $FEDR$ and τ .

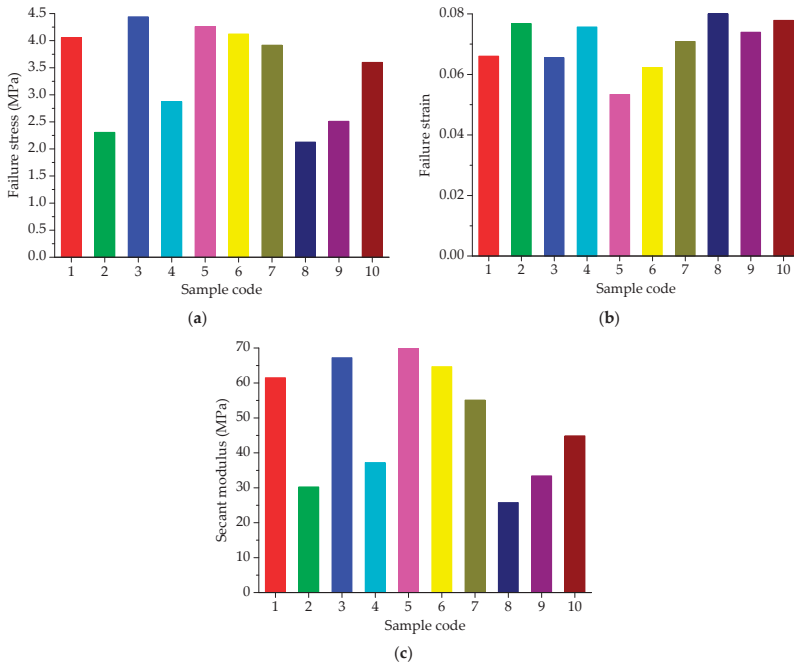


Figure 9. Failure results of asphalt mixtures: (a) failure stress; (b) failure strain; (c) secant modulus.

3.3.2. Uniaxial Compression Creep Test Results Based on SLD

The range of failure stress for asphalt mixtures is 2.13 MPa~4.46 MPa at 50 °C. Thus, the applied stress level of 0.4 MPa was kept constant for the creep test. A preconditioning stress of 5% loading was also applied to asphalt mixture specimens for 90 s. Subsequently, a servo-pneumatic universal testing machine was adopted to apply a stress-controlled uniaxial compressive loading for 2400 s at 50 °C. Figure 10 compares the creep strain for 10 groups of asphalt mixtures.

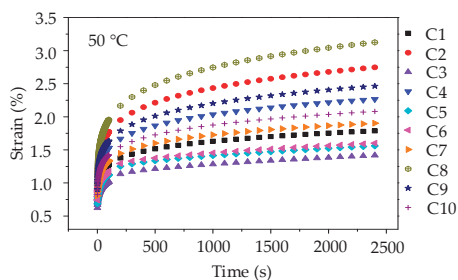


Figure 10. Strain-time curves of asphalt mixtures at 50 °C.

As illustrated in Figure 10, it can be observed that at the same loading time, the anti-deformation performance of asphalt mixture prepared by manufactured stones (basalt stone and andesite stone) is better than asphalt mixture with pebble, and the creep strains of 10 groups of asphalt mixtures at any test temperature are ranked as C8 > C2 > C9 > C4 > C10 > C7 > C1 > C6 > C5 > C3. Besides, it is worth noting that when compared with the creep curves of asphalt mortars shown in Figure 5, the creep strains of asphalt mixtures are still lower under the condition that stress level is twice, test temperature is 20 °C higher, and creep time is 600 s longer. This observation fully demonstrated that the skeleton effect of coarse aggregates could effectively enhance the anti-deformation performance of asphalt mixture. Thus, coarse aggregates with complex morphological characteristics could improve the anti-deformation performance of asphalt mixture.

Similarly, the viscoelastic parameters of Burgers model were adopted to further quantitatively investigate the influence of morphological characteristics of coarse aggregates. Table 9 details the viscoelastic responses of asphalt mixtures, in which all the coefficients of determination (R^2) are more than 0.97, indicating that the fitted Burgers models can well describe the creep characteristics of asphalt mixtures.

Table 9. Viscoelastic responses of SLD for asphalt mixtures (C1~C10).

Response	Sample Code									
	1	2	3	4	5	6	7	8	9	10
E_1 (MPa)	42.5	33.7	53.8	37.5	48.8	45.7	41.3	37.5	35.7	39.8
η_1 (GPa·s)	235.5	124.2	321.9	163.6	294.9	292.3	212.6	163.6	145.5	183.3
τ (s)	77.6	84.6	77.7	81.1	77.8	74.0	78.5	81.1	82.7	80.5

3.3.3. Statistical Analysis and Discussion

Analysis of Modulus of Immediate Elasticity Burgers Model (E_1)

The ANOVA results for modulus of immediate elasticity Burgers model (E_1) are listed in Table 10. The significant terms of E_1 are identified as linear terms and non-linear terms (X_1X_2 , X_1X_3 and X_2X_3). Thus, the quadratic order polynomial equation for η_1 can be finally established as:

$$Y_1 = 48.60X_1 + 53.63X_2 + 37.16X_3 - 20.29X_1X_2 - 20.84X_1X_3 - 37.97X_2X_3 \quad (17)$$

Table 10. ANOVA results for modulus of immediate elasticity Burgers model (E_1).

Source	Sum of Squares	DF	Mean Square	F-Value	p-Value	Significant
Model	345.93	5	69.19	42.38	0.0015	Yes
Linear mixture	231.36	2	115.68	70.86	0.0008	Yes
X_1X_2	20.84	1	20.84	12.77	0.0233	Yes
X_1X_3	21.98	1	21.98	13.46	0.0214	Yes
X_2X_3	72.96	1	72.96	44.69	0.0026	Yes
Residual	6.53	4	1.63			
Total	352.46	9				

Figure 11 illustrates the relationships among modulus of immediate elasticity Burgers model (E_1), component proportion, and morphological characteristics (i.e., CR , CPI and $CEDR$). Coarse aggregates of various components present a similar trend with fine aggregates, E_1 of asphalt mixtures presents a decreasing trend with increase in the proportion of river sand (X_3). The values of E_1 increase with increase in morphological characteristics of coarse aggregates, for which there are positive correlations among these variables; the correlation coefficient values R^2 are around 0.6. This means a relatively insignificant influence of coarse aggregates on E_1 . Morphologies of coarse aggregates are generally more related to the resistance to deformation while loading, but they present a relatively less and discretized influence on viscoelastic properties of asphalt mixture.

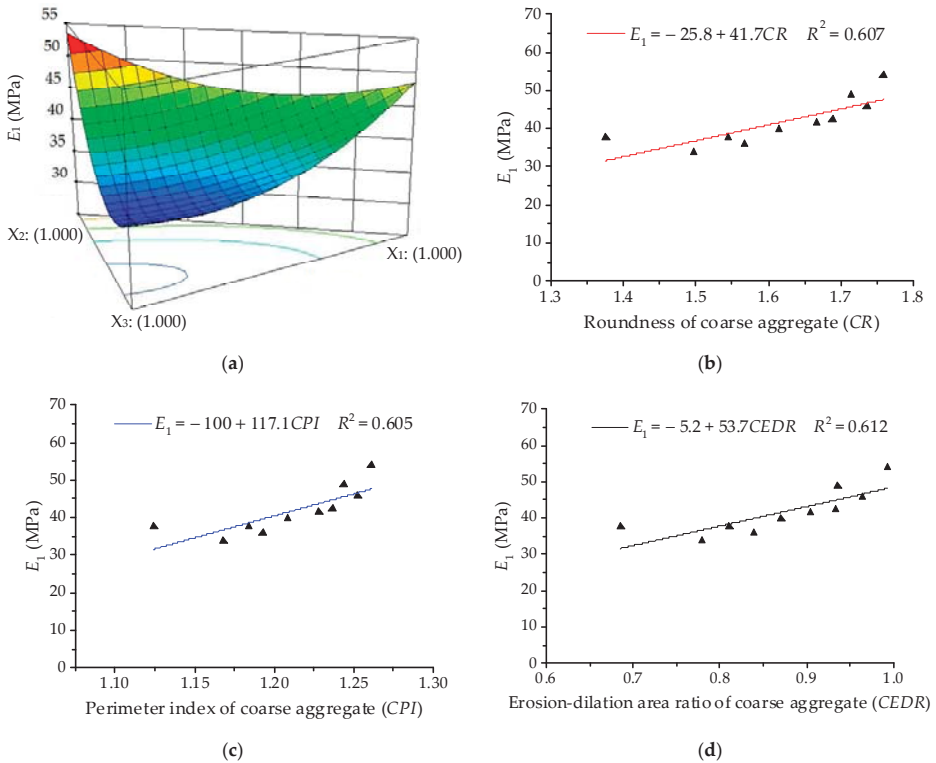


Figure 11. Relationships between E_1 and coarse aggregates: (a) Response surface plot for component proportion and E_1 ; (b) CR and E_1 ; (c) CPI and E_1 ; (d) $CEDR$ and E_1 .

Analysis of Coefficient of Viscosity Burgers Model (η_1)

The ANOVA results for coefficient of viscosity Burgers model (η_1) are listed in Table 11. The significant terms of η_1 are identified as linear terms and non-linear terms (X_1X_3 and X_2X_3). Thus, the quadratic order polynomial equation for η_1 can be finally established as:

$$Y_2 = 291.93X_1 + 324.37X_2 + 161.80X_3 - 279.28X_1X_3 - 394.81X_2X_3 \tag{18}$$

Table 11. ANOVA results for coefficient of viscosity Burgers model (η_1).

Source	Sum of Squares	DF	Mean Square	F-Value	p-Value	Significant
Model	43176.22	5	8635.24	89.83	0.0003	Yes
Linear mixture	31170.32	2	15585.16	162.12	0.0001	Yes
X_1X_2	266.41	1	266.41	2.77	0.1713	No
X_1X_3	3947.65	1	3947.65	41.07	0.0030	Yes
X_2X_3	7889.18	1	7889.18	82.01	0.0008	Yes
Residual	384.52	4	96.13			
Total	43560.74	9				

As illustrated in Figure 12, the 3D response surface and linear regression relationships are plotted for coefficient of viscosity Burgers model (η_1). For coarse aggregates, asphalt mixtures with various components present a similar variation trend of η_1 with asphalt mortars. However, the correlation coefficient values R^2 of linear regression become relatively smaller. Morphological characteristics of coarse aggregates could improve permanent deformation to some extent. Due to the viscoelastic property of asphalt, it presents a relatively less and discretized influence on the viscoelastic properties of asphalt mixture.

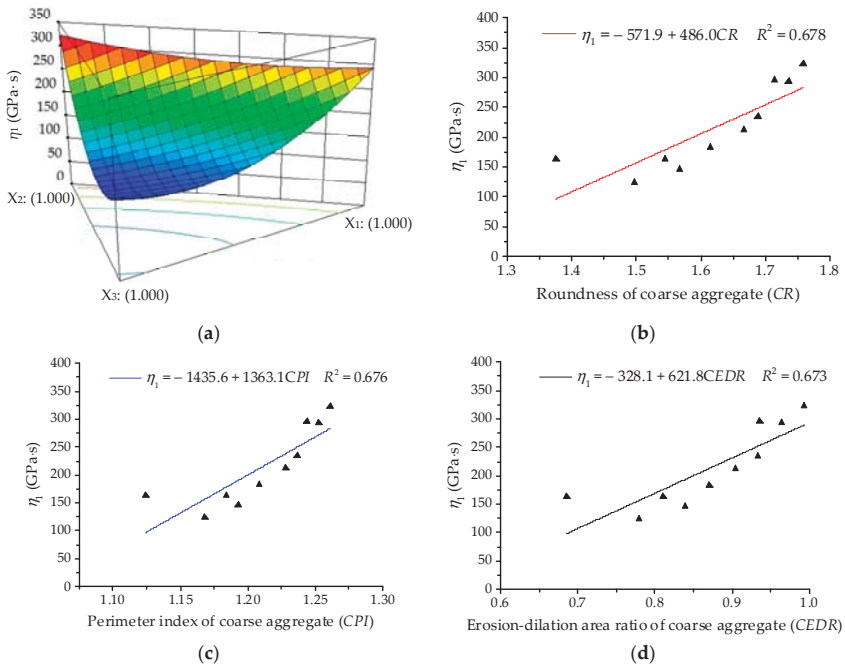


Figure 12. Relationships between η_1 and coarse aggregates: (a) Response surface plot for component proportion and η_1 ; (b) CR and η_1 ; (c) CPI and η_1 ; (d) CEDR and η_1 .

Analysis of Retardation Time (τ)

The ANOVA results for retardation time (τ) are listed in Table 12. The linear terms are identified as the significant terms of τ . Thus, the quadratic order polynomial equation for η_1 can be finally established as:

$$Y_3 = 77.66X_1 + 77.20X_2 + 81.55X_3 \tag{19}$$

Table 12. ANOVA results for retardation time (τ).

Source	Sum of Squares	DF	Mean Square	F-Value	p-Value	Significant
Model	77.00	5	15.40	9.16	0.0260	Yes
Linear mixture	49.91	2	24.95	14.85	0.0141	Yes
X_1X_2	9.28	1	9.28	5.52	0.0785	No
X_1X_3	5.00	1	5.00	2.98	0.1596	No
X_2X_3	12.69	1	12.69	7.55	0.0515	No
Residual	6.72	4	1.68			
Total	83.72	9				

As illustrated in Figure 13, the 3D response surface and linear regression relationships are plotted for retardation time (τ). It can be seen that correlation coefficient values R^2 are much lower than 0.54, showing that there is no clear linear correlation between the retardation time of asphalt mixture and morphological characteristics of coarse aggregates. In fact, the retardation time of asphalt mixtures generally decreases with increase in morphological characteristics. This is expected because the viscoelastic deformation in the creep process mainly occurs in asphalt mortar, which bonds with coarse aggregates and fills internal voids. Hence, coarse aggregates are not as strongly correlated with the retardation time as fine aggregates.

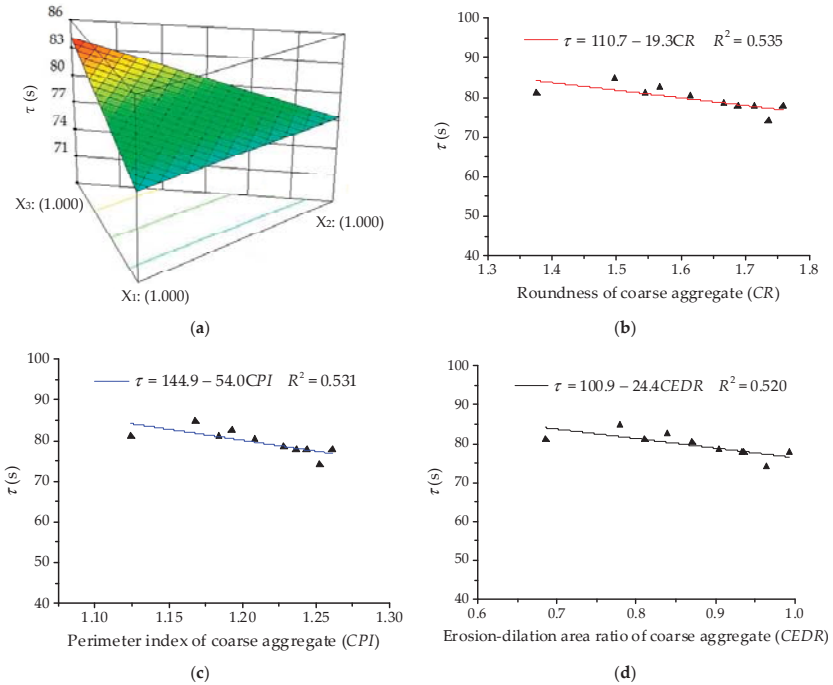


Figure 13. Relationships between τ and coarse aggregates: (a) Response surface plot for component proportion and τ ; (b) CR and τ ; (c) CPI and τ ; (d) CEDR and τ .

4. Conclusions

This paper studied the influences of aggregate morphological characteristics on the high-temperature viscoelastic properties of asphalt mixes by using the SLD method. The experimental proportion scheme was designed for asphalt mixes with three different types of aggregates, i.e., basalt, andesite and pebble/river sand. Meanwhile, three morphological parameters were summarized to characterize shape, angularity and texture of fine and coarse aggregates. The uniaxial compression creep test was then conducted for asphalt mixes. The following conclusions can be drawn:

- According to correlation coefficients R^2 , morphological characteristics of fine aggregates were more correlated with the high-temperature viscoelastic properties of asphalt mixes compared to coarse aggregates. This may be because the viscoelastic deformation in the creep process mainly occurs in asphalt mortar;
- Aggregate morphological characteristics present a positive correlation relationships modulus of immediate elasticity Burgers model (E_1) and coefficient of viscosity Burgers model (η_1), but a negative correlation with retardation time (τ). Therefore, aggregates with more complex morphological characteristics are conducive to improving deformation recovery and anti-deformation of asphalt mixes;
- Basalt, andesite stones/manufactured sands have more complex morphological characteristics than pebble/river sand and can effectively improve the deformation recovery and anti-deformation of asphalt mixes;
- Asphalt mixes with manufactured aggregates have larger failure stress and secant modulus but lower failure strain. Meanwhile, uniaxial compression failure test results showed that coarse aggregates can effectively enhance the anti-deformation of asphalt mixture due to its skeleton effect.

Author Contributions: Conceptualization, W.W. and Y.C.; Methodology, W.W. and G.T.; Validation, Y.C. and J.T.; Formal Analysis, G.T. and J.T.; Investigation, W.W. and J.T.; Writing-Original Draft Preparation, W.W.; Writing-Review & Editing, Y.C. and G.T.; Project Administration, Y.C.; Funding Acquisition, Y.C.

Funding: This research was funded by [National Natural Science Foundation of China] grant number [51678271] and [Science Technology Development Program of Jilin Province] grant number [20160204008SF] and supported by Graduate Innovation Fund of Jilin University.

Acknowledgments: The authors would like to appreciate anonymous reviewers for their constructive suggestions and comments to improve the quality of the paper.

Conflicts of Interest: The authors declare no conflict of interest.

References

1. Topal, A.; Sengoz, B. Effect of basalt fiber distribution on the flexural-tensile rheological performance of asphalt mortar. *Constr. Build. Mater.* **2005**, *19*, 155–163. [[CrossRef](#)]
2. Liu, Y.F.; Sun, W.J.; Nair, H.; Lane, D.S.; Wang, L.B. Quantification of Aggregate Morphologic Characteristics as Related to Mechanical Properties of Asphalt Concrete with Improved FTI System. *J. Mater. Civ. Eng.* **2016**, *28*, 04016046. [[CrossRef](#)]
3. Hu, J.; Qian, Z.D.; Wang, D.; Oeser, M. Influence of aggregate particles on mastic and air-voids in asphalt concrete. *Constr. Build. Mater.* **2015**, *93*, 1–9. [[CrossRef](#)]
4. Wilson, J.; Klotz, L. Quantitative analysis of aggregate based on hough transform. *Transport. Res. Rec.* **1996**, *1530*, 111–115. [[CrossRef](#)]
5. Kuo, C.Y.; Rollings, R.S.; Lynch, L.N. Morphological study of coarse aggregates using image analysis. *J. Mater. Civ. Eng.* **1998**, *10*, 135–142. [[CrossRef](#)]
6. Wang, L.B.; Wang, X.R.; Mohammad, L.; Abadie, C. Unified method to quantify aggregate shape angularity and texture using fourier analysis. *J. Mater. Civ. Eng.* **2005**, *17*, 498–504. [[CrossRef](#)]
7. Masad, E.; Button, J.W. Unified imaging approach for measuring aggregate angularity and texture. *Comput. Aided. Civ. Inf.* **2000**, *15*, 273–280. [[CrossRef](#)]



8. Kuo, C.Y.; Freeman, R. Imaging indices for quantification of shape, angularity, and surface texture of aggregates. *Transport. Res. Rec.* **2000**, *1721*, 57–65. [[CrossRef](#)]
9. Xie, X.G.; Lu, G.Y.; Liu, P.F.; Wang, D.W.; Fan, Q.; Oeser, M. Evaluation of morphological characteristics of fine aggregate in asphalt pavement. *Constr. Build. Mater.* **2017**, *139*, 1–8. [[CrossRef](#)]
10. Xiao, Y.; Wang, F.; Cui, P.D.; Lei, L.; Lin, J.T.; Yi, M.W. Evaluation of Fine Aggregate Morphology by Image Method and Its Effect on Skid-Resistance of Micro-Surfacing. *Materials* **2018**, *11*, 920. [[CrossRef](#)] [[PubMed](#)]
11. Chen, J.S.; Shiah, M.S.; Chen, H.J. Quantification of coarse aggregate shape and its effect on engineering properties of hot-mix asphalt mixtures. *J. Test. Eval.* **2001**, *29*, 513–519.
12. Arasan, S.; Yenera, E.; Hattatoglu, F.; Hınıslioglu, S.; Akbuluta, S. Correlation between shape of aggregate and mechanical properties of asphalt concrete. *Road. Mater. Pavement.* **2011**, *12*, 239–262. [[CrossRef](#)]
13. Singh, D.; Zaman, M.; Commuri, S. Inclusion of aggregate angularity, texture, and form in estimating dynamic modulus of asphalt mixes. *Road. Mater. Pavement.* **2012**, *13*, 327–344. [[CrossRef](#)]
14. Pan, T.Y.; Tutumluer, E.; Carpenter, S.H. Effect of coarse aggregate morphology on permanent deformation behavior of hot mix asphalt. *J. Transp. Eng.* **2015**, *132*, 580–589. [[CrossRef](#)]
15. Aragao, F.T.S.; Pazos, A.R.G.; da Motta, L.M.G.; Kim, Y.R.; do Nascimento, L.A.H. Effects of morphological characteristics of aggregate particles on the mechanical behavior of bituminous paving mixtures. *Constr. Build. Mater.* **2016**, *123*, 444–453. [[CrossRef](#)]
16. Valdes-Vidal, G.; Calabi-Floody, A.; Miro-Recasens, R.; Norambuena-Contreras, J. Mechanical behavior of asphalt mixtures with different aggregate type. *Constr. Build. Mater.* **2015**, *101*, 474–481. [[CrossRef](#)]
17. Masad, E.; Olcott, D.; White, T.; Tashman, L. Correlation of fine aggregate imaging shape indices with asphalt mixture performance. *Transport. Res. Rec.* **2001**, *1757*, 148–156. [[CrossRef](#)]
18. Cheng, Y.C.; Zhu, C.F.; Tao, J.L.; Jiao, Y.B.; Yu, D.; Xiao, B. Effects of Diatomite–Limestone Powder Ratio on Mechanical and Anti-Deformation Properties of Sustainable Sand Asphalt Composite. *Sustainability* **2018**, *10*, 808. [[CrossRef](#)]
19. Wang, C.; Guo, N.S.; Zhao, Y.H.; Tan, Y.Q. Air voids distribution of asphalt mixtures in different compaction methods and aggregate gradations. *J. Jilin Univ.* **2014**, *44*, 74–80. (In Chinese)
20. JTG E20-2011. *Standard Test Methods of Bitumen and Bituminous Mixtures for Highway Engineering*; Ministry of Transport of the People’s Republic of China: Beijing, China, 2011. (In Chinese)
21. Li, J.; Lin, H. Quantification research of coarse aggregate angularity based on digital image processing. *J. Highw. Transport. Res. Dev.* **2008**, *25*, 27–31. (In Chinese)
22. Bai, F.; Yang, X.H.; Zeng, G.W. A stochastic viscoelastic–viscoplastic constitutive model and its application to crumb rubber modified asphalt mixtures. *Mater. Des.* **2016**, *89*, 802–809. [[CrossRef](#)]
23. Arabani, M.; Kamboozia, N. New achievements in visco-elastoplastic constitutive model and temperature sensitivity of asphalt. *Int. J. Pavement. Eng.* **2014**, *15*, 810–830. [[CrossRef](#)]
24. Guo, Q.L.; Li, L.L.; Cheng, Y.C.; Jiao, Y.B.; Xu, C. Laboratory evaluation on performance of diatomite and glass fiber compound modified asphalt mixture. *Mater. Des.* **2015**, *66*, 51–59. [[CrossRef](#)]
25. Guo, Q.L. Research on internal stress distribution of asphalt mixture and its impact on viscoelastic performance. Ph.D. Thesis, Jilin University, Changchun, China, June 2013.
26. Tao, J.L. Research on characteristics of mineral aggregate and its effect on high and low temperature viscoelastic performance of asphalt mixture. Ph.D. Thesis, Jilin University, Changchun, China, June 2017.
27. Gorman, J.W.; Hinman, J.E. Simplex lattice designs for multicomponent systems. *Technometrics* **1962**, *4*, 463–487. [[CrossRef](#)]
28. Fletcher, T.; Chandan, C.; Masad, E.; Sivakumar, K. Measurement of aggregate texture and its influence on hot mix asphalt (HMA) permanent deformation. *J. Test. Eval.* **2002**, *30*, 524–531.



© 2018 by the authors. Licensee MDPI, Basel, Switzerland. This article is an open access article distributed under the terms and conditions of the Creative Commons Attribution (CC BY) license (<http://creativecommons.org/licenses/by/4.0/>).

Article

Study on the Effect of Demulsification Speed of Emulsified Asphalt Based on Surface Characteristics of Aggregates

Fanlong Tang ¹ , Guangji Xu ¹, Tao Ma ^{1,*}  and Lingyun Kong ²

¹ School of Transportation, Southeast University, Nanjing, Jiangsu 210096, China; 230179227@seu.edu.cn (F.T.); guangji_xu@seu.edu.cn (G.X.)

² School of Civil Engineering & Architecture, Chongqing Jiaotong University, Chongqing 400074, China; klyyqr2002@163.com

* Correspondence: matao@seu.edu.cn

Received: 19 July 2018; Accepted: 14 August 2018; Published: 21 August 2018

Abstract: Aggregate is an indispensable raw material for emulsified asphalt construction. For the purpose of explaining the influence of aggregate characteristics on the demulsification speed of emulsified asphalt, the surface energy and specific surface area (SSA) characteristics of aggregates were calculated based on the capillary rise method and the BET (Brunauer-Emmett-Teller) adsorption test. Afterwards, the effect of the surface energy and specific surface area of the aggregate on the emulsified asphalt demulsification speed was systematically studied by using ultraviolet spectroscopy as well as the orthogonal test. Experimental results indicate that the specific surface energy parameter of the aggregate is certainly related to the particle size of the aggregate. That is, the surface free energy of the unit system is proportional to the surface area A and the density of the interface unit. The specific surface area parameter of aggregates increases with the decrease of particle size, when the particle size is reduced to 600 mesh, the specific surface area parameters of the three aggregates selected in this paper tend to be consistent. Orthogonal experimental analysis demonstrates that the surface energy and specific surface area have an impact on the emulsion breaking speed and they are proven to be positively correlated. Meanwhile, in the case of small particle sizes, there is no statistically significant correlation between the physical properties of aggregates and the demulsification speed of emulsified asphalt, and the physical property of aggregates is not the main factor that affects the demulsification speed of the emulsified asphalt. On the contrary, the material properties of the aggregate, such as acid-base property and chargeability, are the dominant factors.

Keywords: limestone aggregates; emulsified asphalt; demulsification speed; surface energy; specific surface area

1. Introduction

With the advent of the world's energy crisis and the enhancement of human consciousness of nature, emulsified asphalt, famous for its clean and eco-friendly properties, presents a prospect for large-scale use, and shows an increasing tendency of usage year-by-year [1–3].

By using this kind of asphalt emulsion to build a road, no heating is needed at room temperature to spray, to pour into or mix, or to pave the surface or base layer of various structural pavements. Emulsified asphalt can be used in normal temperature construction and has the advantages of saving energy, facilitating construction, saving asphalt, and protecting the environment [4–6]. In particular, the performance of emulsified asphalt modified with polymer is better than that without. It is generally expected that the asphalt modification can be used to help asphalt material to resist deformation at high temperature, and to resist cracking at low temperature. Thus, high-temperature rutting and

low temperature cracking can be alleviated. Besides, it can not only greatly improve the interlayer combination of asphalt pavement, but also reduce the occurrence of various diseases in its service period. This provides great economic and social benefits in the maintenance of the road, especially for high grade pavement [7,8].

Emulsified asphalt property directly affects the production, storage, construction, and long-term serviceability of emulsified asphalt. During the production process, asphalt should be easily emulsified, and the emulsified asphalt has certain storage stability. However, in the construction process, it is hoped that the emulsified asphalt has an appropriate demulsification time, and it should fully meet the requirements of construction and to open traffic [9]. At the same time, emulsified asphalt should have good adhesion with aggregate, so that asphalt mixture has a strong ability to resist water damage [10,11]. Obviously, a controllable emulsified asphalt demulsification is extremely important for the performance of emulsified asphalt. Nevertheless, in practical projects, due to poor knowledge of action mechanisms between emulsifier and aggregate which lead to the un-controlled breaking conditions of asphalt emulsion, and the instable long-term performance seriously restricts the large-scale use of energy-saving and environmental-friendly emulsified asphalt mixture. Based on this, a lot of previous studies on the controllable of demulsification have been carried out, mainly on the emulsifier, the type and amount of additives, the emulsified asphalt preparation conditions and so on. MARCHAL et al. found that the amount of emulsifier that is not combined with asphalt or adsorbed on the surface of the aggregate, greatly affects the demulsification speed of the asphalt emulsion [12,13]. According to the analysis of Xie et al., the particle size, density, and continuous phase viscosity have an essential influence on the demulsification speed of the emulsified asphalt [14]. GORMAN et al. explained that the most important factors affecting the demulsification process of emulsified asphalt are the performance of emulsified asphalt and the surface properties of the aggregate [15]. HAGEN et al. concluded that the surface properties of the aggregate have great influence on the demulsification speed and adhesion of emulsified asphalt [16]. ADDERSORI [17] and CASTILLO [18] think the desorption of emulsifier on the asphalt surface and the adsorption on the aggregate surface affect the demulsification of emulsified asphalt. SHELL et al. showed that the increase of temperature can accelerate the breaking speed of the emulsified asphalt [19].

Aggregate is an important raw material and it directly affects the controllability of emulsified asphalt demulsification, which is highly related to the efficiency of the emulsified asphalt construction. However, the research on the controllability of emulsified asphalt demulsification speed based on an aggregate factor, especially the surface characteristics of the aggregate, are rarely reported. In this paper, based on the surface properties of aggregates, the surface energy and specific surface area parameters of the aggregates are qualitatively characterized first. Additionally, the influence of the physical surface characteristics of aggregates on the demulsification speed of emulsified asphalt was systematically evaluated by means of UV spectroscopy and an orthogonal test. The objective of this study intends to give an explanation for the impact of emulsion asphalt breaking speed from the view of the surface characteristics of the aggregate, and it provides a theoretical reference for the aggregate factor, to determine the controllable demulsification of emulsified asphalt.

2. Materials and Methods

2.1. Materials

2.1.1. Emulsified Asphalt Selection

In this paper, the KunLun AH-70 asphalt was chosen as the matrix asphalt, and the corresponding cationic emulsified asphalt was used [20]. A slow-cracking and fast-setting type emulsifier named MQK-1D from MeadWestvaco Corporation in the United States was selected. It mainly consists of amino amide compounds generated from fatty acid and polyamine condensation [21] (under the ultraviolet spectrum, the absorption peak position is $\lambda_{\max} = 304$ nm). Emulsified asphalt properties are presented in in Table 1. MQK-1D Infrared Spectrogram and UV spectrum are shown in Figure 1.

Table 1. Emulsified asphalt performance properties [22,23].

Item	Unit	Required Value	Experimental Value
Emulsifier dosage	wt %	-	2
Appearance	-	Ecru liquid, uniformity, without mechanical impurities	qualified
Particle charge	-	-	positive
Engler viscosity (25 °C)	-	5–30	3.2
Plus sieve surplus (1.18 mm)	%	≤0.1	0
Evaporated residue	Leftover content	%	≥60
	Penetration (25 °C)	0.1 mm	40–120
	Ductility (15 °C)	cm	≥50
	Softening point	°C	-
Cement hybridism	%	<1.0	0.45
Storage stability	1 day	%	≤1.0
	5 day	%	≤5.0

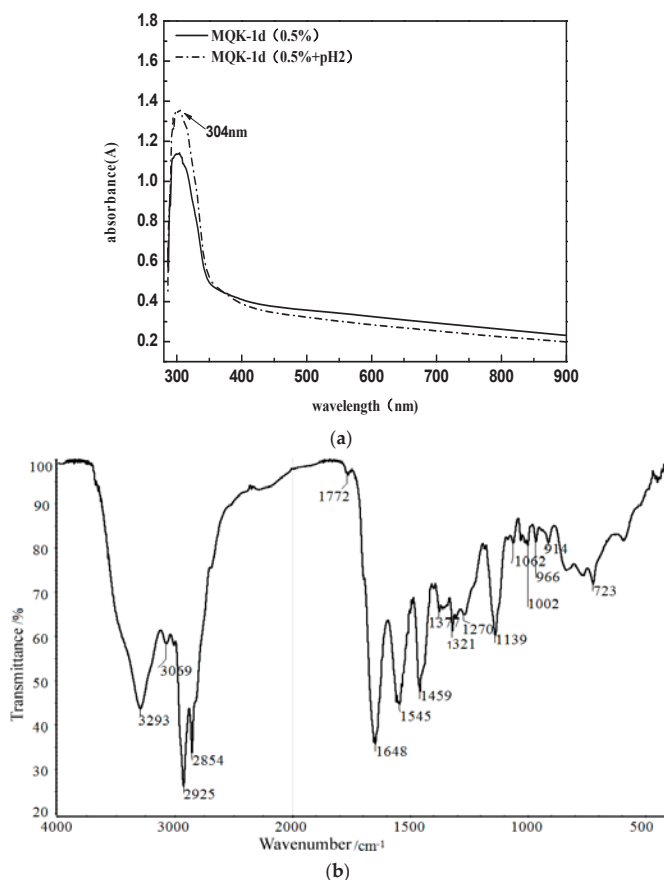


Figure 1. MQK-1D ultraviolet spectrum (a) and Infrared Spectrogram (b).

Since the emulsified asphalt in this research is cationic emulsified asphalt, blue or red shifts of the peaks of the emulsifier may occur in the ultraviolet spectrum under the environment of pH = 2. Thus, the comparison data MQK-1D (0.5% + pH2) were added. Test results suggest that the pH

value has no significant effect on the position of the emulsifier peak, and thus it can be considered $\lambda_{\max} = 304 \text{ nm}$.

2.1.2. Aggregate Selection

Representative domestic road aggregates were selected, followed by limestone, granite, basalt, and quartzite. Particle size distribution is 200 mesh, 300 mesh, 400 mesh, 500 mesh (mesh which is used to indicate the particle size of particles that can pass through the mesh. The higher the mesh number, the smaller the particle size [24]). Then, the four aggregates were sampled by a quartering method [25], and the crush value test, abrasion value test, adhesion test, and apparent density test were performed. The basic performance indexes are shown in Table 2.

Table 2. The basic performance of the aggregate.

Technical Indicators	Crushing Value/%	Los Angeles Wear Value/%	Adhesion Grade With Asphalt	Apparent Density/g/cm ³
Limestone	18.2	15.8	5	2.700
Basalt	9.7	10.3	3	2.707
Granite	15.3	14.1	3	2.677
Quartzite	16.3	12.6	3	2.625
Requirements	≤28	≤30		

According to Table 2, it can be seen that the basic properties of the above four aggregates were entirely able to meet the requirements of JTG E42-2005 of the Highway Engineering Aggregate Test Procedures and they could be used as tests.

2.2. Characterization of Emulsion Asphalt Demulsification Speed

Emulsified asphalt is a black, viscous emulsion at room temperature. When the external conditions change (mechanical agitation, aggregate mixing, demulsifiers), demulsification occurs. However, in the process of demulsification, it is difficult to find the essential difference in the appearance, and it is impossible to directly evaluate the emulsion demulsification speed. Nevertheless, the nature of the demulsification process of emulsified asphalt lies in the separation of oil and water phases. In the centrifugal field outside, oil in water equilibrium system is broken up. The asphalt droplets, which are in a dispersed phase, rapidly aggregate and sink. With the continuous development of emulsified asphalt demulsification, the concentration of emulsifier in the supernatant is continuously increased until the equilibrium of emulsion breaking is reached. Based on this, this study used the UV spectroscopy analysis to characterize the breaking speed of emulsified asphalt by examining the change of emulsifier concentration in the supernatant.

Ultraviolet spectroscopy is based on UV-visible spectrophotometry, which is generally considered to be 200–800 nm, and is a spectral analysis method based on the molecules of different substances [26,27]. According to the Lambert-Beer law, as a beam of parallel monochromatic light passes through an ideal solution of a single homogeneous, the absorbance and concentration of the solution always exhibits a direct positive proportional relationship.

The procedure can be briefly described as follows: First, 40 g of an equal amount of emulsified asphalt was centrifugated (centrifugation temperature 20 °C) for different times. After this, 1 mL supernatant with pipette was diluted with 50 mL distilled water for UV measurement. In order to obtain the proper simulation conditions for the demulsification process, the process was repeated three times first [28]. From the figure below, simulation process 1 used a centrifugal speed of 3000 rpm; the experimental conditions performed in process 2 were invariable, while a second supernatant centrifugation was required. The detailed method of the second centrifugation is that the obtained solution was placed in a centrifuge tube and subjected to high-speed centrifugation again. Because of the difference in density, the asphalt particles were adsorbed onto the tube wall by the action of

a high-speed centrifugal field, so that the elimination of pitch particles suspended in solution in the case of a constant concentration of emulsifier was ensured; simulation process 3 was exactly the same as simulation process 2 except that the centrifugal speed was adjusted to 1500 rpm.

As can be seen from the above Figures 2 and 3, the directly sampled supernatant was turbid, and the solution contained a large amount of suspended asphalt particles. This phenomenon had a great deviation from the experimental results. Simultaneously, it led to the disruption of the UV spectrum measurement and the inability to characterize the emulsion demulsification process. Instead, the treated supernatant contained very few suspended asphalt particles with a clear and transparent solution; meanwhile, the obtained UV spectrum data were consistent with the emulsified asphalt emulsion breaking rules.

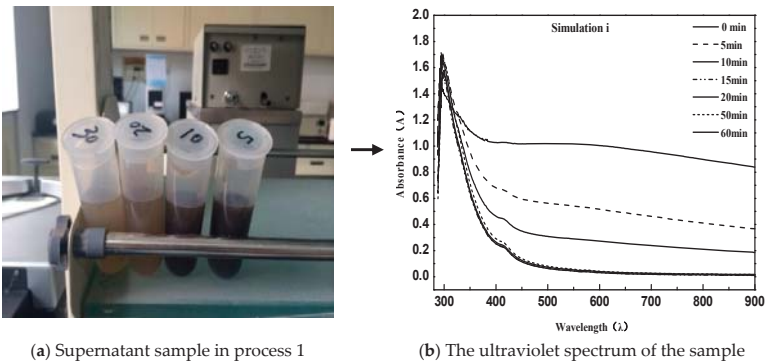


Figure 2. Direct sampling simulation for process 1.

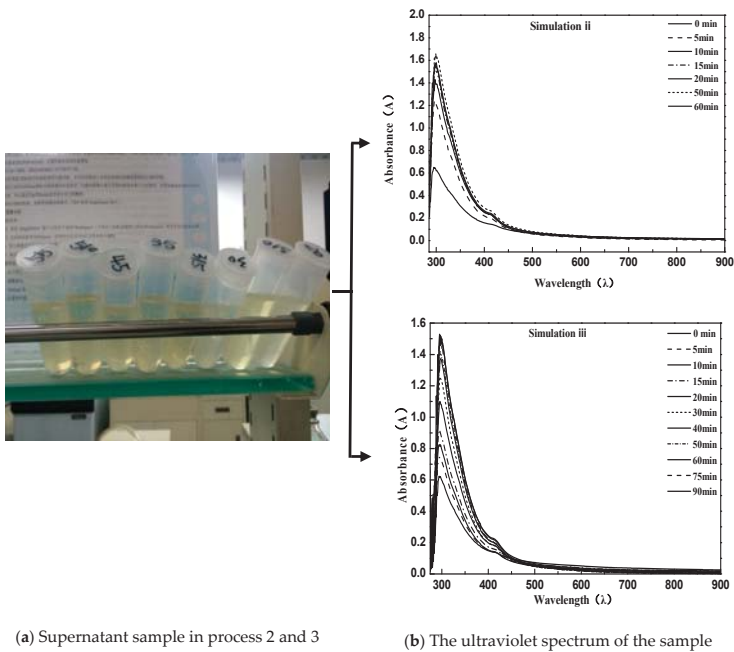


Figure 3. Using secondary centrifugal sampling for simulation process 2 and simulation process 3.

Comparing simulation Process 2 and Simulation Process 3, the emulsified asphalt broke so fast that the demulsification procedure was complete at 15 min at a speed of 3000 rpm. However, a uniform intercept UV spectrum curve appeared in the emulsified asphalt demulsification process when the speed is reduced to 1500 rpm. This indicates that the simulated demulsification process of emulsified asphalt was met under the conditions of a moderate demulsification speed of 1500 rpm.

3. Aggregate Characteristics

3.1. Aggregate Surface Energy Measurement

The approach applied for surface energy trial in our research is known as the capillary rise method [29,30]. The basic principle of this method is that tiny capillary channels will form in the powder gap between solid powders. Through capillary action, liquids can spontaneously penetrate into the powder column in the glass tube by measuring a liquid with known surface tension. While the liquid rises to a certain height and takes time, the contact angle information of the liquid to the powder can be obtained. The principle of experimental is shown in Figure 4.

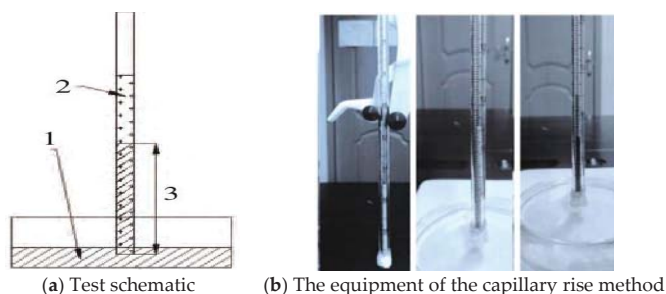


Figure 4. Schematic diagram of the capillary rise method.

Experiment conditions are described as follows: The environment temperature was 25 °C, the reagent was weighed uniformly to 0.50 g using an analytical balance, the capillary was shaken for 5min after injecting the ore powder, and 0.20 mm thick filter paper was stuck onto the bottom of the capillary. The capillary was a pipette with a length of 20 cm and an internal diameter of 2.7 mm. The surface energy parameters of pentane and the immersion liquid used in the experiment are shown in Table 3.

Table 3. Surface energy parameters of an immersed liquid.

Reagent	Surface Free Energy/mJ·m ⁻²	Dispersion Component	Polar Component	Viscosity/mPa·s
Distilled water	72.80	21.80	51.00	0.890
Formamide	58.00	39.00	19.00	3.343
Toluene	27.70	27.70	0	0.560
N,N Dimethylformamide	37.30	32.42	4.88	0.796
Diiodomethane	50.80	50.80	0	1.220
Pentane	15.49	15.49	0	0.224

The following experiments are the surface energy measurements of limestone. Three types of limestone aggregates with different appearances and different sampling points are from Gan he di (Figure 5), Shi wu biao (Figure 6), and Xiao he bian quarries (Figure 7).



(a) Gan he di quarry



(b) The appearance of Gan he di aggregate

Figure 5. Gan he di quarry (a) and stone appearance (b).



(a) Shi wu biao quarry



(b) The appearance of Shi wu biao aggregate

Figure 6. Shi wu biao quarry (a) and stone appearance (b).



(a) Xiao he bian quarry



(b) The appearance of Xiao he bian aggregate

Figure 7. Xiao he bian quarry (a) and stone appearance (b).

In order to reduce the number of experiments and possible chemical interference in the study of physical properties, this test was only performed for limestone aggregates (the effective radius of this experiment was calibrated to use a low surface energy liquid pentane with a contact angle θ close to zero).

The following case uses Gan he di (200 mesh) as an example, and the result as shown in Figure 8.

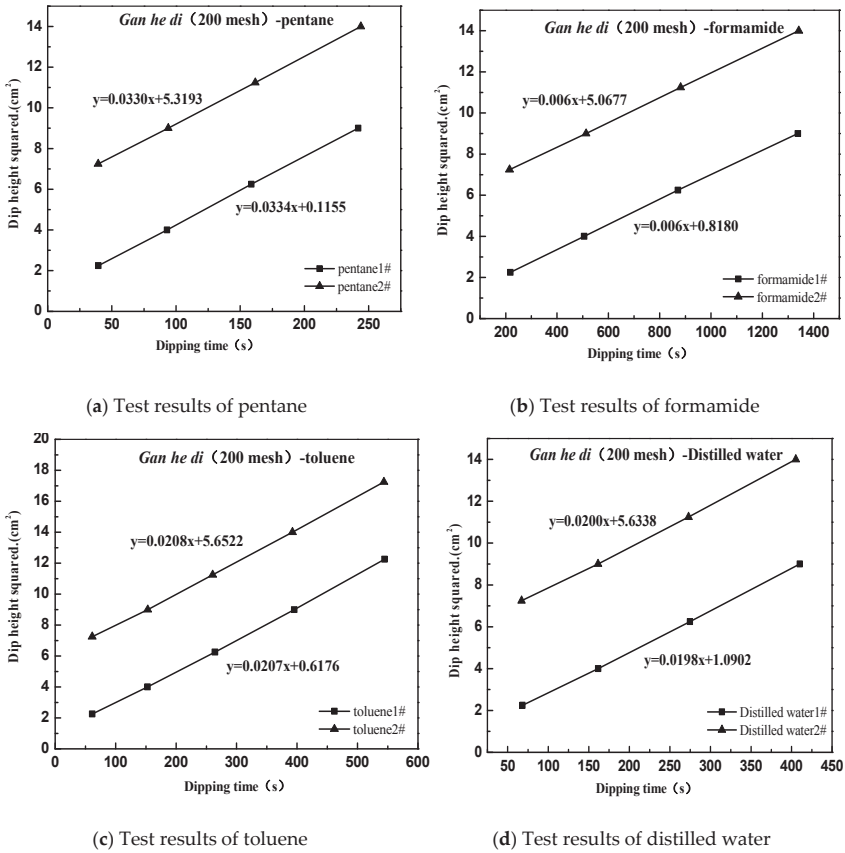


Figure 8. Surface energy test of aggregate. (a) pentane; (b) formamide; (c) toluene; (d) distilled water.

According to the Washburn immersion equation [31], the contact angles for different types of ore powder under different test liquid conditions are calculated as follows:

$$h^2/t = (\gamma_1 R_{eff} \cos \theta) / 2\eta \tag{1}$$

In the formula, h is the liquid rising height, cm; η is the viscosity of the liquid, $mN \cdot m^{-2} \cdot s^{-1}$; R_{eff} is the effective radius of the capillary, μm ; θ is the contact angle between liquid and solid; t is the dipping time, s; γ_l is the free surface energy of the liquid, $mJ \cdot m^{-1}$.

Then according to the equation of Young, the formula is as follows:

$$\gamma_1(1 + \cos \theta) = 2\sqrt{\gamma_{sv}^d \gamma_{lv}^d} + \sqrt{\gamma_{sv}^p \gamma_{lv}^p} \tag{2}$$

Given that:

$$y = \frac{1}{2}(1 + \cos \theta) \frac{\gamma_l^p}{\sqrt{\gamma_l^d}}, x = \sqrt{\frac{\gamma_l^p}{\gamma_l^d}} \tag{3}$$

Based on the above test results, a relationship diagram was established between y and x , where the square of the slope is the polar force component of the measured interface, and the square of the intercept is the dispersion force component of the measured interface. The dispersion force component

of Gan he di (200 mesh) is calculated to be $19.85 \text{ mJ}\cdot\text{m}^{-2}$, the polar force component is $24.13 \text{ mJ}\cdot\text{m}^{-2}$, and the final surface energy is $43.98 \text{ mJ}\cdot\text{m}^{-2}$.

Similarly, experiments and calculations were carried out on the Gan he di (300 mesh, 400 mesh, 500 mesh), as well as on the Xiao he bian and Shi wu biao. Finally, the surface energy parameters of three kinds of limestone aggregates with different particle sizes are shown in Figure 9.

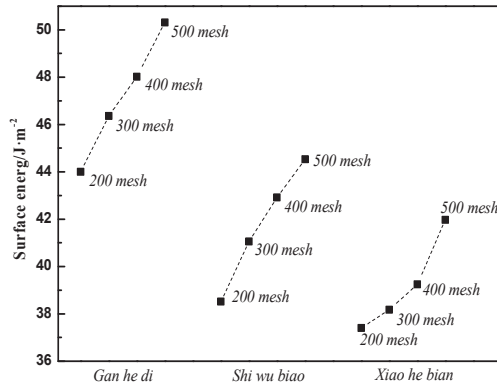


Figure 9. Surface energy of three kinds of aggregates.

3.2. Determination of Specific Surface Area of Aggregate

Based on the basic principle of BET adsorption, the research measured specific surface area for three limestone with particle sizes of 200 mesh, 300 mesh, 400 mesh, 500mesh, and 600mesh, respectively by using ASAP2020M+C physical adsorption instrument (made in Shanghai China by the corp. of Micromeritics).

Take Gan he di as an example, the specific surface area result is shown in Figure 10.

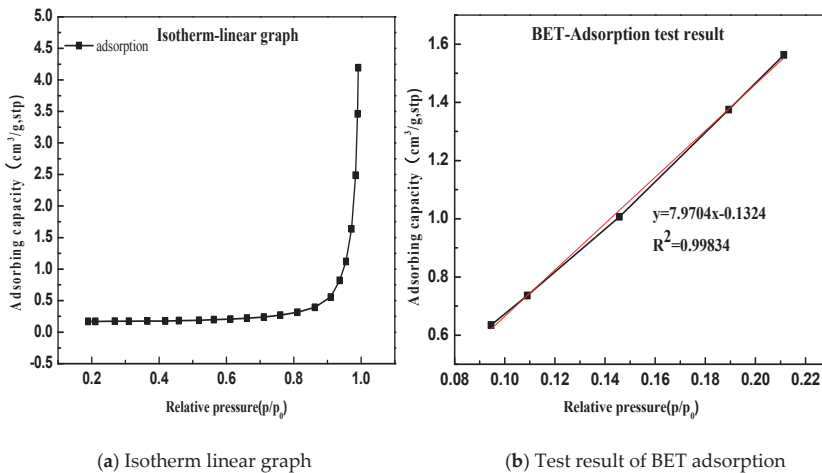


Figure 10. Determination of specific surface area of limestone. (a) Isotherm linear graph; (b) BET adsorption test result.

According to the BET equation, the Gan he di (200 mesh) has a specific surface area of 0.339 m²/g. The test and calculation methods for the remaining samples are similar, and the calculation results are summarized in Table 4.

Table 4. Summary of SSA calculation (m²/g).

Specimen	200 mesh	300 mesh	400 mesh	500 mesh	600 mesh
<i>Gan he di</i>	0.3388	0.6369	1.0296	1.3669	1.8751
<i>Xiao he bian</i>	0.1334	0.3987	0.8579	0.9422	1.8429
<i>Shi wu biao</i>	0.2667	0.5935	1.1000	1.1770	1.7493

The relationship between the specific surface area of the limestone aggregates and the particle size is established, as shown in Figure 11.

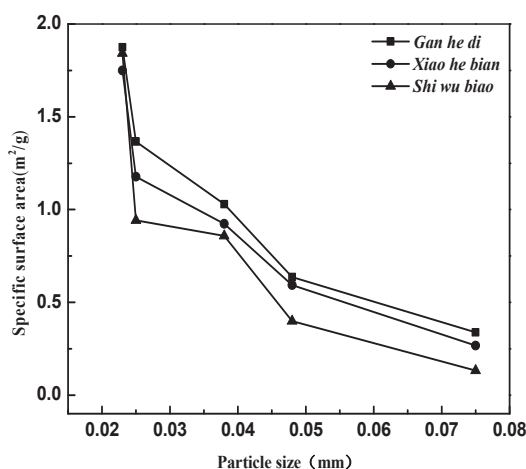


Figure 11. The specific surface area of three kinds of aggregates with different particle sizes.

As shown in Figure 11, the specific surface area of the three aggregates decreases with particle size increasing. For the three limestone aggregates selected in the test, the specific surface area of the Gan he di is the largest, and the specific surface area of Shi wu biao is the smallest as the grain size exceeds 600 mesh; While the particle size is reduced to 600 mesh, the specific surface area of the three types of aggregates remains basically consistent.

4. Results and Discussion

4.1. Orthogonal Design

It is well known that the specific surface area and surface energy are directly related to the material properties of the aggregate and the particle size of the aggregate [32,33]. On the other hand, the demulsification speed of the emulsified asphalt also has an objective relationship with the selection of the mixing ratio and the demulsification time node. Therefore, the experiment adopts orthogonal test design to select three different particle size limestone aggregates with different performance and composition and the effects of surface energy and specific surface area of the aggregate on the emulsion breaking speed of emulsified asphalt were investigated from the time factor, material factor, mixing ratio factor and particle size factor. The experimental method is the ultraviolet spectrometry obtained in Section 2.2. The factor level table as shown in Table 5.

Table 5. Factor levels table.

Factor \ Level	A Time (min)	B Material	C Mixing Ratio (%)	D Particle Size (mesh)
1	25	Gan he di	5	300
2	30	Shi wu biao	10	500
3	20	Xiao he bian	20	200

Note: In order to minimize the random errors that occur in the test, the ordering of the horizontal numbers here adopts random sorting.

Select the L9 (3⁴) orthogonal table, seven times for each test condition, average the results, and fill in the data in Table 6.

Table 6. Test plan and test result analysis.

TEST PLAN						Test Results
Factor Test Number	A 1	B 2	C 3	D 4	Absorbance(A)	
Index	1	1(25 min)	1(Gan he di)	1(5%)	1(300 mesh)	1.0961
	2	1	2(Shi wu biao)	2(10%)	2(500 mesh)	1.2338
	3	1	3(Xiao he bian)	3(20%)	3(200 mesh)	1.2219
	4	2(30 min)	1	2	3	0.9129
	5	2	2	3	1	1.1697
	6	2	3	1	2	0.8732
	7	3(20 min)	1	3	2	0.9632
	8	3	2	1	3	0.9792
	9	3	3	2	1	0.8243
Emulsified asphalt Demulsification speed	K ₁	2.9722	3.5518	2.9485	3.0801	T = K ₁ + K ₂ + K ₃
	K ₂	3.3827	2.9058	2.9610	3.1140	
	K ₃	2.8594	2.7567	3.3548	3.0022	
	$\bar{K}_1(K_1/3)$	0.990733	1.1838667	0.98283	1.0267	
	$\bar{K}_2(K_2/3)$	1.127567	0.9683	0.987	1.038	
	$\bar{K}_3(K_3/3)$	0.953133	0.9189	1.11827	1.0007	
	R	0.174437	0.264967	0.13544	0.0373	

Figure 12 shows the relationship between indicators and factors.

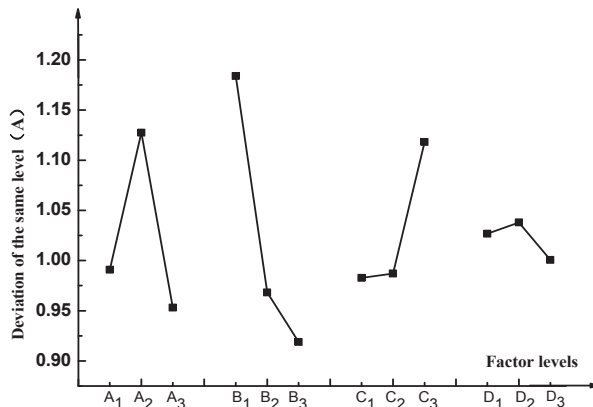


Figure 12. Factors and indexes.

As can be seen from Figure 12:

(1) The factor A (time) and factor B (material) had large deviations, therefore, this factor was the main factor influencing the breaking speed of emulsified asphalt. For factor C (mixing ratio),

the deviation is barely noticeable difference at level 1 (5%) and level 2 (10%), while the deviation was obvious when level 3 (20%) was reached, which reveals the effect of emulsified asphalt on the rate of demulsification is not obvious when the mixing is relatively low. But when the mixing ratio is increased to a certain value, the demulsification speed will change significantly.

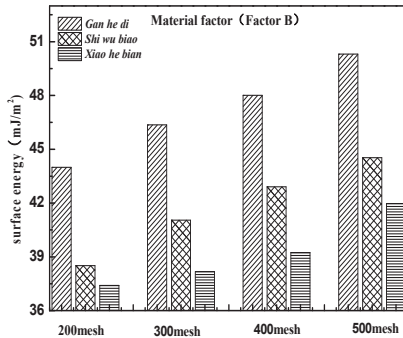
(2) From the Figure 12, the deviation of the factor D (particle size) was the smallest, which indicates that the particle size factor had a lower impact on the breaking speed of the emulsified asphalt. The reason for the analysis may be due to the small difference in the particle size of the aggregates selected in this experiment.

Next, factors B (material factor) and D (particle size factor) were used to analyze the influence of surface energy and the specific surface area of the aggregate on the breaking speed of the emulsified asphalt.

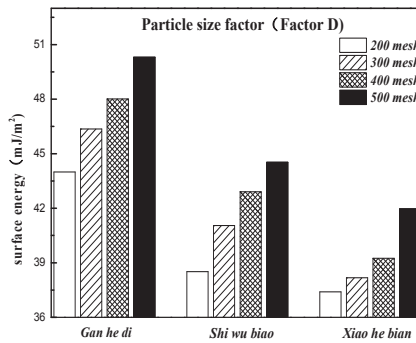
4.2. Effect of Aggregate Surface Energy on Demulsification Rate of Emulsified Asphalt

In order to study the influence of the surface energy parameters of aggregate on the breaking speed of emulsified asphalt, correlation analysis was carried out according to Figure 12 from the factors of material and particle size.

According to the design conditions of the orthogonal experiment in the previous section, it can be seen that level 1 of factor B was Gan he di, level 2 was Shi wu biao, and level 3 was Xiao he bian. The surface energy parameters of three different aggregates were compared, as shown in Figure 13.



(a) Material factor for factor B



(b) Particle size factor for factor D

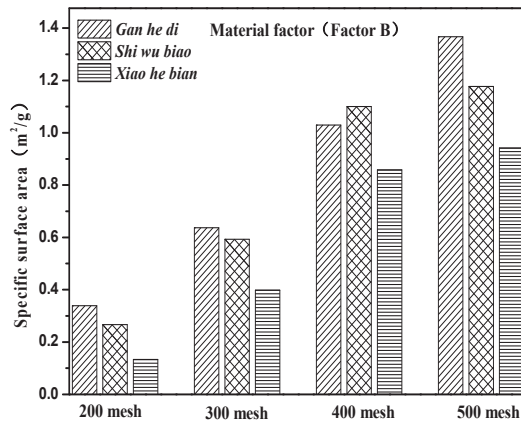
Figure 13. Material and particle size factors under the three kinds of aggregate surface energy parameters. (a)Material factor for factor B; (b) Particle size factor for factor D.

Figure 13 shows that the surface energy parameters of aggregates are related to the material itself and the particle size. For the three aggregates studied in this experiment, the surface energy parameters of the Gan he di aggregates are the largest, followed by the Shi wu biao and the minor ones Xiao he bian. In combination with Figure 12, under the material factor, level 1 (Gan he di) has the fastest demulsification rate, while level 3 (Xiao he bian) has the slowest rate of demulsification. Under the particle size factor, level 2 (500mesh) has the fastest demulsification rate and level 3 (200mesh) has the slowest rate of demulsification, which means that the greater the surface energy of the aggregate, the faster the breaking speed of emulsified asphalt. However, compared with the material factor, the influence of the particle size factor on the demulsification speed was less biased, which means that for the material factor, the surface energy parameter was not the only factor affecting the demulsification speed of emulsified asphalt. Combining with particle size analysis, it can be inferred that the influence of this unknown factor on the emulsion demulsification speed of emulsified asphalt should be larger than the surface energy parameters. The analysis of the unknown factors here is related to the structure, porosity, acid-base property of the material.

4.3. Influence of Specific Surface Area of Aggregate on Demulsification Speed of Emulsified Asphalt

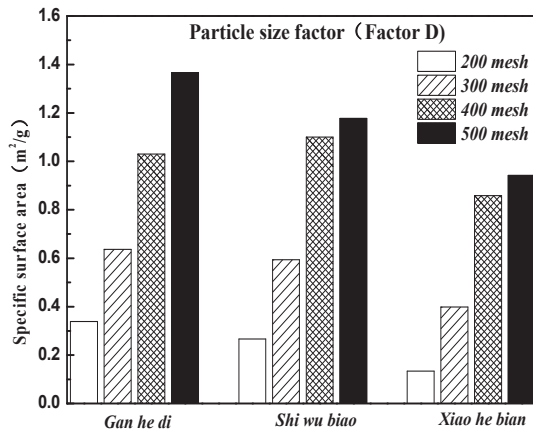
The specific surface area parameters of the three aggregates of different particle sizes studied in this paper were demonstrated in Section 3.2. The specific surface area parameters of the aggregates are compared with the correlation graphs of the factors and indicators in Figure 12, and results are shown in Figure 14.

It can be seen from Figure 14 that the specific surface area parameters of aggregates decreased with the increase of particle size, and the specific surface area parameters of different aggregates were not the same. The specific situation was 500 mesh > 400 mesh > 300 mesh > 200 mesh; Gan he di > Shi wu biao > Xiao he bian. The surface energy parameter of Shi wu biao, with a particle size of 400 mesh, was slightly larger than that of Gan he di, which may have been due to the random error generated by the experiment). In order to study the relationship between the specific surface area parameters of aggregates and the emulsion breaking speed of emulsified asphalt, the grey correlation was used for analysis. The results are shown in Table 7.



(a) Material factor for factor B

Figure 14. Cont.



(b) Particle size factor for factor D

Figure 14. Material and size factors under three kinds of aggregate surface parameters. (a) Material factor for factor B; (b) Particle size factor for factor D.

According to Table 7, Figures 13 and 14, the specific surface area of the aggregate was positively related to the emulsion breaking speed of the emulsified asphalt; that is, the larger the specific surface area is, the faster the emulsified asphalt breaks. From the gray correlation analysis in Table 7, it can be seen that the relationship between the specific surface area parameters of the aggregate and the breaking speed of emulsified was relatively low, indicating that the specific surface area parameter of the aggregate was not the dominant factor affecting the breaking speed of emulsified asphalt.

Table 7. The specific surface area of the aggregate and the demulsification of the emulsified asphalt speed of grey correlation analysis.

Gray correlation coefficient	Material Factors				Particle Size Factor		
	200 mesh	300 mesh	400 mesh	500 mesh	Gan he di	Shi wu biao	Xiao he bian
	0.3885	0.4490	0.7430	0.7088	0.5760	0.5500	0.4574

5. Conclusions

(1) The capillary rise method was used to determine the surface energy of aggregates, and results suggest that the specific surface energy parameters of aggregates are related to the particle size of aggregates. The larger the particle size, the smaller the surface energy, and vice versa. Besides, the surface free energy of the unit system is always proportional to the surface area A, as well as the density of the interface unit. The BET adsorption test illustrates the specific surface area of aggregates increases with the decrease of particle size; however, the specific surface area parameters of the three aggregates selected in this paper tend to be consistent when the particle size is reduced to 600 mesh.

(2) The influence of the surface energy and specific surface area of the aggregate on the breaking speed of emulsified asphalt was evaluated by UV spectroscopy. It was concluded that the surface energy and the specific surface area are exactly related to the emulsion breaking speed of the emulsified asphalt, and they are positively correlated. The larger the surface energy and the specific surface area of the aggregate, the faster the emulsion breaking speed of the emulsified asphalt.

(3) Gray correlation analysis shows that the correlation between the physical properties (surface energy, specific surface area, particle size) of the aggregate and the emulsified asphalt demulsification is relatively low when the aggregate size is small (mineral powder), and it indicates that physical

microscopic characteristics are not the main factor that affect the emulsion breaking speed. Instead, the material properties (excluding physical properties) of the aggregate itself, such as acid-base properties and chargeability, are the dominant factors affecting the emulsified asphalt demulsification.

(4) The effect of the characteristics of aggregates on the emulsion breaking speed of emulsified asphalt, in this article, is restricted to small particle size fine aggregates (as well as mineral powder). The effects of the relevant characteristics of coarse aggregates on the demulsification speed of emulsified asphalts are currently unable to be determined. Therefore, it has to be admitted that conclusions have certain limitations and further research is needed. Besides, for the coarse aggregates, a significant change, as revealed in the particle size, further study on the relationship between the aggregates and demulsification speed is necessary for.

Author Contributions: Investigation, F.T.; Methodology, T.M. and L.K.; Validation, T.M. and L.K.; Writing for original draft, F.T.; Writing for review & editing, G.X.

Funding: This research was funded by National Natural Science Foundation of China (No. 51878164 and No. 51378006), Natural Science Foundation of Jiangsu Province, China (BK20161421 and BK20140112), and Scientific Research Foundation of Graduate school of Southeast University (YBJJ 1843).

Acknowledgments: The authors would like to thank the fund from National Natural Science Foundation of China (No. 51508062 and No. 51378006), Natural Science Foundation of Jiangsu (BK20161421 and BK20140112), and the Open Fund of State Engineering Laboratory of Highway Maintenance Technology (Changsha University of Science & Technology, kfj160104).

Conflicts of Interest: The authors declare no conflict of interest.

References

1. Chen, D.; Jahren, C.T.; Lee, H.D.; Williams, R.; Kim, S.; Heitzman, M.; Kim, J. Effects of recycled materials on long-term performance of cold in-place recycled asphalt roads. *J. Perform. Constr. Facil.* **2009**, *2*, 270–280. [[CrossRef](#)]
2. Selvaratnam, S. Long Term Performance Evaluation of Cold in-Place Recycling (CIR) Technique in Nevada. Ph.D. Thesis, University of Nevada, Reno, NV, USA, 2013.
3. Liu, S.L. *Emulsified Asphalt and its Application in Road and Construction Engineering*; China Building Materials Press: Beijing, China, 2008. (In Chinese)
4. Wang, T.; Shen, D.Y.; Xu, T. Photocatalytic degradation properties of V-doped TiO₂ to automobile exhaust. *Sci. Total Environ.* **2017**, *586*, 347–354. [[CrossRef](#)] [[PubMed](#)]
5. Cherrington, M. The move to emulsions. *Earthmover Civil Contractor* **1992**, *30*, 33–36.
6. Mathews, D.H. Surface-active agents in bituminous road surfacing. *J. Appl. Chem.* **1962**, *12*, 56–64. [[CrossRef](#)]
7. He, H. Study on Properties of Modified Emulsified Asphalt and Micro Surface. Master's Thesis, Chang'an University, Xi'an, China, 15 June 2006. (In Chinese)
8. Hung, K.; Xu, T.; Li, G.F. Heating effects of asphalt pavement during hot in-place recycling using DEM. *Constr. Build. Mater.* **2016**, *115*, 62–69. [[CrossRef](#)]
9. Redelius, P. A novel system for delayed breaking control of bitumen emulsions. In Proceedings of the First World Congress on Emulsion, Paris, France, 19–22 October 1993.
10. Shaw, D. *Introduction to Colloid and Surface Chemistry*; Butterworths: Oxford, UK, 1992.
11. Shi, H.Q.; Xu, T.; Jiang, R.L. Combustion mechanism of four components separated from asphalt binder. *Fuel* **2017**, *192*, 18–26. [[CrossRef](#)]
12. Marchal, J.L.; Julien, P.; Boussad, N. A new approach to cold mix design and performance. In Proceedings of the 5th Eurobitume Congress, Stockholm, Sweden, 16–18 June 1993.
13. Marchal, J.L.; Julien, P.; Boussad, N. Bitumen emulsions testing: Towards a better understanding of emulsion behavior. In Proceedings of the 5th Eurobitume Congress, Stockholm, Sweden, 16–18 June 1993.
14. Xie, L.B.; Yang, J.X.; Ling, C. Discussion on storage stability of emulsified asphalt. *J. Highway Transp. Res. Dev.* **2006**, *9*, 87–89. (In Chinese)
15. Gorman, J.L.; Crawford, R.J.; Stannard, P.; Harding, I.H. The role of surface chemistry in bitumen emulsion-aggregate interactions. *Road Transp. Res.* **1998**, *7*, 3.

16. Hagen, A.P.; Lee, D.W.; Jones, T.M. AspHalt-aggregate interactions characterised by zeta potential and retained strength measurements for natural and organosilane-treated aggregates. *Transp. Res. Rec.* **1996**, *1535*, 111–116. [CrossRef]
17. Lyklema, J. Adsorption at solid-liquid interfaces with special reference to emulsion systems. *Colloids Surf. A* **1994**, *91*, 25–38. [CrossRef]
18. Castillo, G.L.; Poirier, P.A.J.; Bourrell, M. Breaking of an asphalt emulsion on a mineral aggregate: phenomenology, modelling and optimization. In Proceedings of the First World Congress on Emulsion, Paris, France, 19–22 October 1993.
19. Whiteoak, D.; Read, J.; Hunter, R.N. *The Shell Bitumen Handbook*; Shell Bitumen: London, UK, 1990.
20. Yuliestyan, A.; Garcia-morales, M.; Moreno, E. Assessment of modified lignin cationic emulsifier for bitumen emulsions used in road paving. *Mater. Des.* **2017**, *131*, 242–251. [CrossRef]
21. Zhang, Q.Q. Study on the Influence of Emulsification on the Properties of SBS Modified Asphalt. Ph.D. Thesis, China University of Petroleum, Qingdao, China, 24 May 2012. (In Chinese)
22. Highway science research institute of transportation department, ministry of transportation. In *Test Procedures for Asphalt and Asphalt Mixtures for Highway Engineering*; China Communications Press: Beijing, China, 2011. (In Chinese)
23. Asphalt Institute. Superpave Performance Graded Asphalt Binder Specifications and Testing. Available online: <https://trid.trb.org/view/661578> (accessed on 13 August 2018).
24. Tang, N. System and Process for Preparing Large-Particle Potassium Chloride by Cold-Decomposition Crystallization and Flotation Method with High-Sodium Potassic Salt Ore. WO 2014161248 A1, 9 October 2014.
25. Wu, H.J.; Li, Y.N.; Yang, K.Y. The Quartering Cup. CN 202420902, 15 March 2012.
26. Marin, T.W.; Janik, I.; Bartels, D.M. Vacuum ultraviolet spectroscopy of the lowest-lying electronic state in subcritical and supercritical water. *Nat. Commun.* **2016**, *8*, 15435. [CrossRef] [PubMed]
27. Tanabe, I.; Kawasaki, Y. Far-ultraviolet spectral changes of titanium dioxide with gold nanoparticles by ultraviolet and visible light. *Spectrochim. Acta Part A* **2018**, *197*, 103–106. [CrossRef] [PubMed]
28. Kong, L.Y.; Tang, F.L.; Xu, Y. The demulsification of emulsified asphalt evaluation based on UV spectrum velocity. *J. Chang'an Univ.* **2013**, *37*, 17–23. (In Chinese)
29. Biliński, B.; Holysz, L. Some theoretical and experimental limitations in the determination of surface free energy of siliceous solids. *Powder Technol.* **1999**, *102*, 120–126. [CrossRef]
30. Kong, L.Y.; Cao, H.P.; Zhang, Y.Z. External factors for contact angle of mineral fill with capillary rise method and solutions. *J. Harbin Inst. Technol.* **2017**, *46*, 85–89.
31. Fries, N.; Odic, K.; Dreyer, M. Wicking of Perfectly Wetting Liquids into a Metallic Mesh. In Proceedings of the 2nd International Conference on Porous Media and its Applications in Science and Engineering ICPM2, Kauai, HI, USA, 17–21 June 2007.
32. Cheng, D.X.; Little, D.N.; Lytton, R.L. Surface free energy measurement of aggregates and its application to adhesion and moisture damage of asphalt-aggregate systems. In Proceedings of the International Center for Aggregates Research 9th Annual Symposium: Aggregates—Concrete, Bases and Fines, Washington, DC, USA, 24 February 2001.
33. Thommes, M.; Kaneko, K.; Neimark, A.V. Physisorption of gases, with special reference to the evaluation of surface area and pore size distribution (IUPAC Technical Report). *Chem. Int.* **2011**, *38*, 25.



© 2018 by the authors. Licensee MDPI, Basel, Switzerland. This article is an open access article distributed under the terms and conditions of the Creative Commons Attribution (CC BY) license (<http://creativecommons.org/licenses/by/4.0/>).

Article

Improvement of Asphalt-Aggregate Adhesion Using Plant Ash Byproduct

Zhuangzhuang Liu ^{1,2}, Xiaonan Huang ^{1,2}, Aimin Sha ^{1,2,*}, Hao Wang ^{3,*}, Jiaqi Chen ^{3,4} and Cheng Li ^{1,2}

¹ Key Laboratory of Special Area Highway Engineering, MOE, Xi'an 710064, China; zzliu@chd.edu.cn (Z.L.); xnh0202@163.com (X.H.); cli@chd.edu.cn (C.L.)

² School of Highway, Chang'an University, Xi'an 710064, China

³ Rutgers, The State University of New Jersey, Piscataway, NJ 08854, USA; chenjqiaqi@csu.edu.cn

⁴ School of Civil Engineering, Central South University, Changsha 410083, China

* Correspondence: hwang.cee@rutgers.edu (H.W.); ams@chd.edu.cn (A.S.)

Received: 17 December 2018; Accepted: 8 February 2019; Published: 18 February 2019

Abstract: The adhesion bonding between asphalt and aggregate significantly influences field performance and durability of asphalt pavement. Adhesion promoters are typically used to improve asphalt-aggregate bonding and minimize moisture-related pavement damage, such as cracking and raveling. This study evaluated the effectiveness of plant ash byproduct as adhesion promoter to improve asphalt-aggregate adhesion performance. Three commonly used aggregate types (granite, basic rock, and limestone) and two asphalt binder types were used in laboratory testing. A modified stripping test method was developed to evaluate test results with image analysis and measurement of asphalt film thickness. The contact angle test and scanning electron microscopy (SEM) with energy disperse spectroscopy (EDS) were conducted. Test results showed that plant ash lixivium significantly improved asphalt-aggregate adhesion. Among three aggregate types, granite yielded the worst asphalt-aggregate adhesion for both control and treated specimens. The effectiveness of adhesion promotion varied depending on the type of asphalt or aggregate and temperature. The SEM/EDS observations showed that the mesh-like crystalline was formed at the interface between asphalt binder and aggregate in the treated specimen, which was believed to enhance the interfacial bonding and prevent asphalt film peeling off from aggregate.

Keywords: asphalt-aggregate adhesion; plant ash lixivium; stripping test; contact angle; interfacial transition zone

1. Introduction

The adhesion strength of asphalt binders is an important parameter for durability of asphalt pavements. Poor bonding effect between asphalt binder and aggregate has long been identified as a major cause leading to accelerated damage of asphalt pavement [1]. When asphalt film starts peeling off from aggregates, the asphalt-aggregate adhesion strength is greatly reduced and results in debonding at the asphalt-aggregate interface [2,3]. Many previous studies have found that the damages of asphalt pavements including cracking, raveling, and permanent deformation are related to the degradation of asphalt-aggregate adhesion strength [4–7]. Therefore, to increase asphalt-aggregate adhesion strength and eventually improve the performance and durability of asphalt pavement systems, better understanding of the bonding mechanism and microstructure of asphalt-aggregate interface is needed [8,9].

The adhesion strength of asphalt-aggregate interface consists of three components: (1) physical bonding from mechanical interlocking, (2) physicochemical adhesion caused by surface free energy, and (3) bonding due to interfacial chemical reactions [10]. To improve asphalt-aggregate bonding, various

adhesion promoters (also called anti-peeling agents) have been evaluated, such as fatty amines, organic amines, and nano admixtures [6,11–13]. Previous studies have found that polymer materials such as Styrene-Butadiene-Styrene (SBS), Ethylene-Vinyl-Acetate (EVA), and crumb rubber can improve moisture susceptibility of asphalt mixtures [14,15]. The promoters enhance the adhesion strength by adjusting surface energy of aggregate or forming chemical bonds between asphalt and aggregate [16]. However, most interface bonding promoters are slaked lime-based products, which are strong alkaline materials and may have adverse effects on the performance of asphalt mixtures. The previous studies mainly focused on application and evaluation of asphalt antistripping promoters (SBS, EVA, etc.) [17]. However, relatively few studies focused on evaluation of the effectiveness aggregate-promoters.

Plant ashes are byproducts from burning wheat straw, rice straw, wood straw, and corn cobs. Recent literatures reported the utilization of plant ashes (e.g., rich husk ash) in asphalt [18,19], so that the plant ash modified asphalt-based materials achieved good engineering performance. If the plant ashes were immersed in water, a large amount of alkaline substances (i.e., KOH, Ca(OH)₂) could be released, which has the potential to enhance the asphalt-aggregate adhesion. The main chemical compositions of plant ashes are SiO₂, K₂O, CaO, SO₃, MgO, Na₂O, Fe₃O₄, Al₂O₃, and TiO₂ [20]. However, the exact chemical compositions of plant ash lixivium vary depending on different raw materials (i.e., wheat straw, rice straw, wood straw, and corn cobs) [21–24]. The alkaline lixivium has great potential to modify the interface between asphalt and aggregate. In this study, plant ash lixivium was proposed to improve the asphalt-aggregate interface adhesion, which is rarely reported in previous literatures.

The asphalt film stripping test (also called water-boiling test) is a conventional method used to evaluate the adhesion strength of asphalt [25,26]. The test is widely used due to its simple operation procedure. The specimens after boiling are visually classified based on five-level criteria, which are not quantified criteria and could be subjective. Recently, image analysis method was concerned to provide quantitative evaluation of rolling bottle test instead of visual observation only [27]. Hence, the image analysis was combined with the traditional test in this study to investigate the effectiveness of plant ash treatment on interface bonding. In addition, advanced tests including contact angle test, SEM, and EDS were conducted to evaluate how the plant ash lixivium influence asphalt-aggregate adhesion by directly observing the microstructures of asphalt-aggregate interface zone. The observations can help explain the physicochemical adhesion mechanism of asphalt-aggregate system.

2. Testing Materials

2.1. Asphalt Binder and Aggregate

Two petroleum asphalts binders were used in this study, which were classified as #90A and #110A according to penetration test values. The basic rheological properties of two binders are provided in Table 1. The penetration, softening point, and ductility were measured based on ASTM-D5, ASTM-D36, and ASTM-D113 standards, respectively [28–30].

Table 1. Basic rheological properties of two asphalt binders.

Asphalt Types	Penetration at 25 °C/0.1 mm	Softening Point/°C	Ductility at 15 °C/cm
#90 grade A petroleum asphalt	88.2	45.6	>100
#110 grade A petroleum asphalt	107	44.8	>200

In this study, three types of aggregates (i.e., granite, basic rock, and limestone) were selected. For different types of aggregates, the base number and surface electrical potential related to adhesion characteristics were reported in the literature [31], as shown in Table 2.

Table 2. The base number and surface potential of aggregates [31].

Aggregate Types	Granite	Limestone	Basic Rock
Base number	0.55	0.96	0.65
Surface potentials /mV	−0.31	0.62	0.04

2.2. Plant Ash Lixivium

The fresh plant ash used in this study was the remnant after burning rice straw, wheat straw, wood, or corn cob. The plant ash was sieved through 0.3-mm sieve and dried in oven. The dried plant ash was then mixed with deionized water (pH = 6.7 at 20 °C) and stirred for 2 mins. In the mixed suspension liquid, the plant ash released alkaline ions, which could change the pH value of the suspension. In this study, five testing specimens with different ash-to-water (A/W) mass ratios were prepared in 500-mL glass beakers, as shown in Figure 1. After 30 min defecation, the lixiviums as presented below are filtered with filter papers.

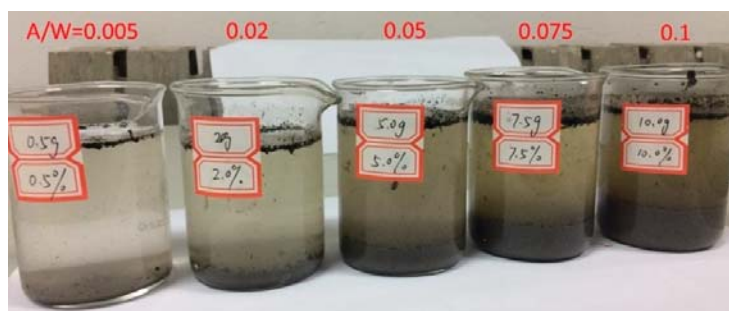


Figure 1. Plant ash lixivium suspensions with different ash-to-water (A/W) ratios.

The pH values of suspensions were measured at 0.5, 1, 2, 5, and 10 min after stirring with the beginning of pH = 6.7 (deionized water). Figure 2 presents the changes of suspension's pH value from stirring. The result indicated that the higher ash/water ratio yielded the higher final pH values as shown in Figure 2a. The changing trends of pH values for different suspensions were found to be similar, which showed rapid increase in the first 150 s and then remained with the relatively constant values. However, the pH value of the suspensions with high ash-water ratio increased at a faster rate than those with low ash-water ratios, and yielded higher final pH values.

In solutions, the H^+ and OH^- ions concentration can be calculated based on the pH value because $pH = -\lg(H^+) = 14 - \lg(OH^-)$. It seems the ions leaching from the plant ash could be calculated based on the pH data in Figure 2. However, in this study the solution contains K_2CO_3 , $KHCO_3$, KOH , KCl , and K_2SO_4 et al. It is hard to calculate the content of average ions released during the leaching, because KCl and K_2SO_4 rarely contributes to the pH value. However, the pH increasing must be linked to ion release, be they positive ions (K^+ , H^+) or negative ions (OH^- , Cl^- , CO_3^{2-} , HCO_3^- , SO_4^{2-}) in this study. Hence, the increased pH values were divided by time, as shown in Figure 2b. Thereby, the higher pH value increased means the higher ions releasing rate. The results declared that the leaching process of ions from plant ash could be divided into three stages: (1) Stage I: 0–60 s when a large amount of ions are released depending on the ash/water ratio; (2) Stage II: 60–300 s when the ion releasing rate is significantly slowed; and (3) Stage III: >300 s when fewer ions could be released in plant ash lixivium.

The relationship between the final pH values and the ash-water ratios of the suspensions was found to be nonlinear, as shown in Figure 3. The final pH value of the suspension greatly increased as the ash-water ratio increased from 0.02 to 0.075. Therefore, in this study, the plant ash lixivium

was prepared using the ash/water ratio of 0.075, and the solution was defecated for 30 mins and then filtered using filter papers with 120 μm opening.

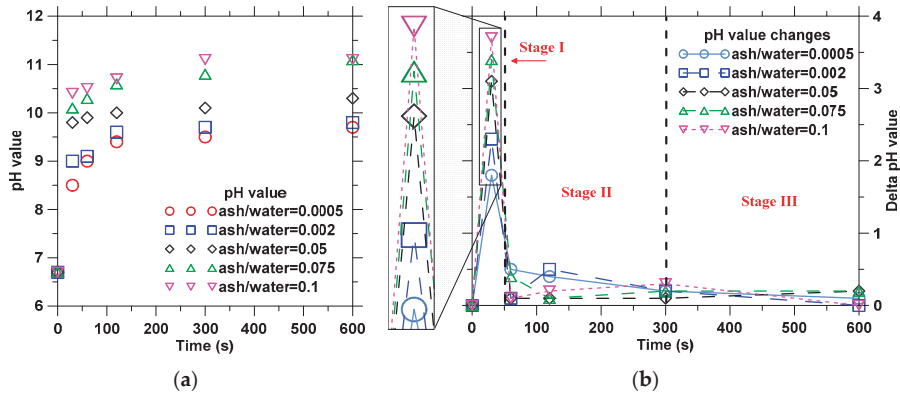


Figure 2. The pH value changes of suspensions with plant ash lixivium: (a) pH and (b) change of pH with time.

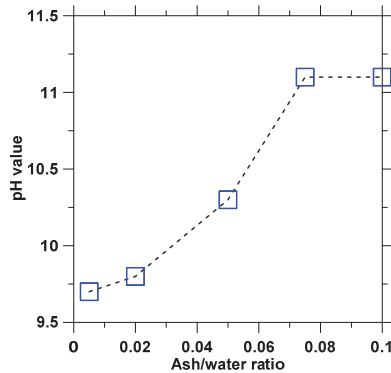


Figure 3. The relationship between final pH values and A/W ratios.

3. Adhesion Evaluation Using Conventional and Modified Stripping Tests

3.1. Conventional Stripping Test

The conventional stripping test (ASTM D3625) used to evaluate asphalt-aggregate adhesion was conducted on aggregates with particle sizes ranging from 13.2 mm to 19 mm. In this study, the stripping test was conducted on three types of aggregates (granite, limestone, and basic rock). The specimens were soaked in the plant ash lixivium for one hour and then dried in oven at 80 °C for two hours. The control specimens were prepared following the same procedure except that the aggregates were not soaked in the plant ash lixivium solution. To reduce the effect of asphalt film thickness, all the specimens were coated with asphalt binder by immersing aggregates in liquid asphalt for 45 seconds, and then hanged at room temperature for 15 mins to remove extra free binder. Then the specimens were boiled in water for 6 mins.

After boiling, the test specimens were visually classified based on the following criteria:

Level 1: The asphalt film is completely moved by water. The removed asphalt binder is floating on water surface, and the aggregate is barely covered.

Level 2: Most of asphalt film is moved by water. The area of exposed aggregate is more than 30% of the total surface area of the specimen.

Level 3: The asphalt film can be moved by water, but most of the asphalt binder is preserved on the surface of the aggregate. The area of exposed aggregate is less than 30% of the total surface area of the specimen.

Level 4: The asphalt film is barely moved by water, but the thickness of asphalt binder is uneven. The area of exposed aggregate is less than 10% of the total surface area of the specimen.

Level 5: The asphalt film is intact, and the area of exposed aggregate is close to 0% of the total surface area of the specimen.

The conventional test results showed that the lixivium treatment can increase the adhesion bonding of different types of aggregates by increasing the rating at least one level, as shown in Figure 4. For the #90 asphalt, the adhesion performance of asphalt-limestone and asphalt-basic rock were similar, but the asphalt-granite interface showed less adhesion bonding. For the #110 asphalt, basic rock showed the best anti-stripping performance as compared to granite and limestone. In general, basic rock and limestone have better anti-stripping performance as compared to granite. It is inconclusive on the effect of asphalt type on adhesion performance due to the unknown information on chemical components of asphalt and the complex nature of asphalt-aggregate adhesion. Regardless of the asphalt or aggregate type, the effectiveness of lixivium treatment on anti-stripping was found significant. The improvement in asphalt-aggregate adhesion can also be visually observed with the appearance of aggregate after the stripping test, as shown in Figure 5.

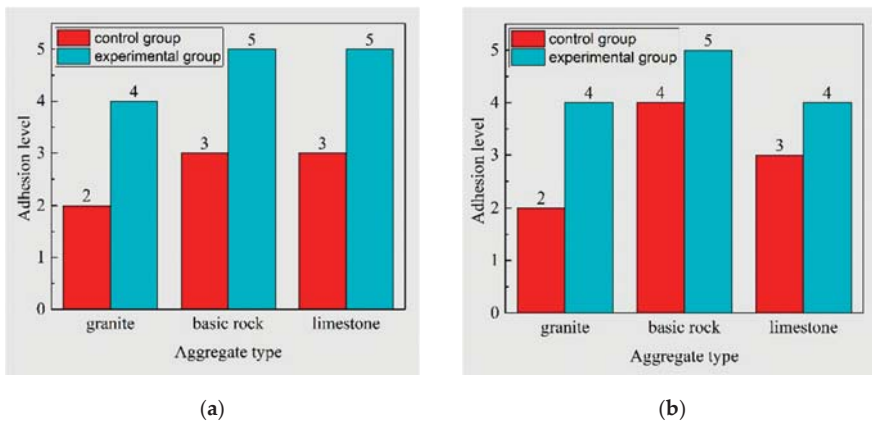


Figure 4. Asphalt-aggregate adhesion level based on stripping test: (a) #90 asphalt and (b) #110 asphalt (samples without treated were marked as control group, while the ones soaked with plant ash lixivium were marked as experimental group).

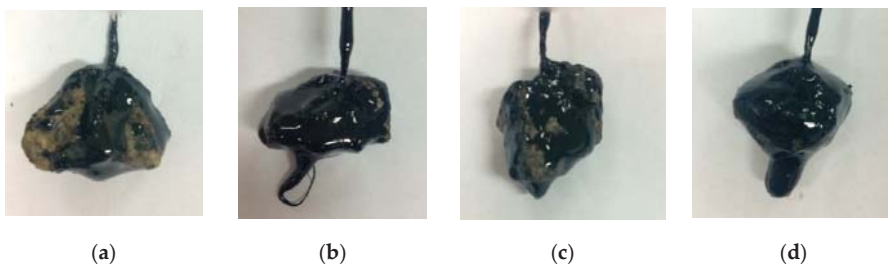


Figure 5. Visual observation of granite aggregates after stripping test: (a) #90 asphalt (control); (b) #90 asphalt (treated); (c) #110 asphalt (control); and (d) #110 asphalt (treated).

It is noted that the conventional stripping test results determined using the five-level criteria are influenced by subjective ranking and test procedure. The conventional stripping test does not provide further comparisons between the asphalt-aggregate interfaces having the same peeling-off grade.

3.2. Modified Stripping Test with Image Analysis

3.2.1. Adhesion Ratio and Asphalt Film Thickness

The conventional stripping test was modified by using image analysis to quantitatively analyze test results. The conventional stripping test requires that the aggregate size should be between 13.2 mm and 19 mm. In the modified stripping test, the asphalt binder was coated on the surface of flat rectangular specimens that were cut from larger aggregates. The surface areas of rectangular specimens were found to be close to those of the spheres with approximately 18.5-mm diameter. The ranges of surface areas and the calculated equivalent sphere diameters of aggregates are shown in Table 3.

Table 3. The surface area and equivalent particle size of used rectangular aggregates.

Aggregate	Calculated Surface Area/mm ²		Equivalent Sphere Diameter/mm
	Min	Max	Average
Granite	976.37	1172.78	18.48
Basic rock	965.66	1145.95	18.32
Limestone	1032.01	1168.71	18.71

To evaluate the specimens, two parameters were defined responding to two situations. For the specimens with aggregate surface exposure after boiling process, the adhesion ratio was defined as the ratio of the non-exposed area in the specimen surface to its total surface area, which could be determined using image analysis. For the specimens without aggregate surface exposure after boiling process, the thickness of asphalt film was used to evaluate the adhesion performance.

Figure 6 shows the appearances of testing specimens after the stripping test. It was found that more asphalt film was peeled off from the control specimens as compared to the treated specimens. To quantify the adhesion performance, photos were taken on the front and back surfaces after the stripping test. A series of image processing techniques, including contrast enhancement and thresholding, were performed to convert the original photos to binary images, as shown in Figure 7.

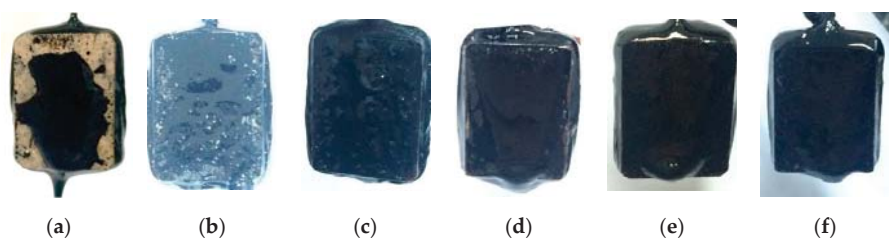


Figure 6. The specimens after modified stripping test: (a–c) control specimens with granite, basic rock, and limestone and (d–f) treated specimens with granite, basic rock, and limestone.



Figure 7. The image processing of test specimens with #110 asphalt and granite aggregate: (a) original image and (b) binary image.

Based on the binary images, the surface areas of asphalt binder (black) and the exposed area of aggregate specimen (white) can be determined. Therefore, the adhesion ratio was calculated using Equations (1) and (2).

$$\eta_s = \frac{\sum_{i=1}^n \eta_i}{n} \tag{1}$$

$$\eta_i = \frac{X_b}{X_w + X_b} \tag{2}$$

where η_s is the adhesion ratio (opposite to peeling off ratio); η_i is the adhesion ratio of surface i of the specimen; n is the total number of surfaces of the specimen ($n = 2$ for the specimens); and X_w and X_b are the total number of white and black pixels in the binary image, respectively.

For the specimen without asphalt film peeling off, the average thickness of coated aggregate was measured by the caliper and glass slides, as show in Figure 8. The glass slides were slightly compressed until the asphalt film contacted with the glass slides completely. The asphalt film thickness (δ) on specimen could be calculated using Equation (3).

$$\delta = \frac{\delta_a - \delta_s - (\delta_{g1} + \delta_{g2})}{2} \tag{3}$$

where δ_a is the total thickness of specimen with glass slides (mm); δ_s is the thickness of the specimen without asphalt film (mm); and δ_{g1} and δ_{g2} are the thickness of the glass slides (mm).



Figure 8. Schematic of asphalt film thickness measurement.

3.2.2. Adhesion Performance Results

The test results show that the specimens with granite showed exposed aggregate surface after boiling process, while the specimens with basic rock and limestone were still fully covered by asphalt film. The image analysis results of the granite aggregate specimen with different asphalt binders are presented in Figure 9. The adhesion and stripping ratios clearly showed that the treatment using plant ash lixivium improved adhesion performance significantly for both #90 and #110 asphalt binder.

For instance, the stripping ratio of granite-asphalt (#90) was reduced from 27.95% to 2.67%. At the same time, the stripping ratio of granite-asphalt (#110) changed from 32.89% to 2.74%.

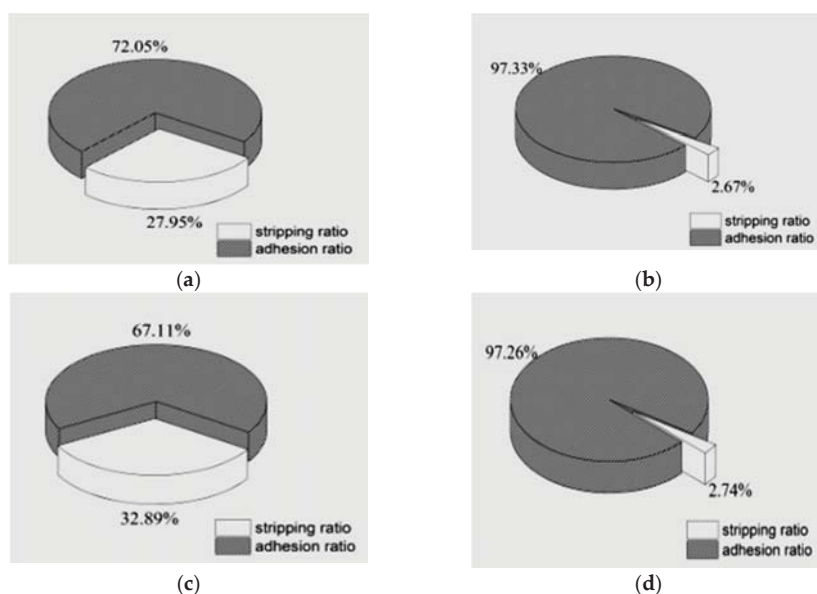


Figure 9. The adhesion and stripping ratios of granite specimen after modified stripping test: (a) control specimen with #90 asphalt; (b) treated specimen with #90 asphalt; (c) control specimen with #110 asphalt; and (d) treated specimen with #110 asphalt.

For specimens with basic rock and limestone, the conventional stripping test cannot compare the effects of treatment for basic rock and limestone specimens, because they both ranked at level 5. Hence, the modified stripping was developed providing quantitative index for adhesion performance evaluation in this case. In the modified stripping test, the thicknesses of asphalt film before and after the boiling process could be calculated. Table 4 presents the asphalt film thickness and the relative improvement for basic rock and limestone treated with plant ash lixivium, respectively. In general, the treatment of plant ash lixivium increased asphalt film thickness on aggregate surface after boiling. The treatment showed relatively higher effectiveness for the #110 asphalt in terms of the increasing ratio of asphalt film thickness. However, no consistent trend was observed for comparing the effectiveness of treatment on adhesion performance between basic rock and limestone. This is probably due to the complex mineral compositions of aggregates.

Table 4. The measured asphalt film thickness on aggregates and relative improvement.

Material	Average Thickness of Asphalt Film (mm)					
	#90 Asphalt			#110 Asphalt		
	Control	Treated Specimen	Improvement Ratio	Control	Treated Specimen	Improvement Ratio
Basic Rock	0.22	0.32	45.5%	0.18	0.30	66.7%
Limestone	0.20	0.30	50.0%	0.16	0.26	62.5%

4. Contact Angle Test

The contact angle test is typically used to determine the balance state of three phases (solid-gas, liquid-gas, and solid-liquid) based on surface free energy theory [29–34]. The asphalt-aggregate adhesion effect was evaluated using contact angle test in this study.

The interfacial intersection of solid-liquid surface and gas-liquid surface was defined as contact angle (θ), as shown in Young’s function defined in Equation (4). As shown in Equations (5)–(7), the work of adhesion (defined as W_a), work of infiltration (defined as W_i), and spreading coefficient (defined as S) increased with the reduction of contact angle (defined as θ), respectively. Hence, the contact angle can be used to indicate the adhesion performance between asphalt and aggregate.

$$\gamma_{s-g} - \gamma_{s-l} = \gamma_{l-g} \cos \theta \tag{4}$$

$$W_a = \gamma_{s-g} + \gamma_{l-g} - \gamma_{s-l} = \gamma_{l-g}(\cos \theta + 1) \tag{5}$$

$$W_i = \gamma_{s-g} - \gamma_{s-l} = \gamma_{l-g} \cos \theta \tag{6}$$

$$S = \gamma_{s-g} - \gamma_{s-l} - \gamma_{l-g} = \gamma_{l-g}(\cos \theta - 1) \tag{7}$$

where, γ_{s-g} is the interfacial tension of solid-gas interface; γ_{s-l} is the interfacial tension of solid-liquid interface; γ_{l-g} is the interfacial tension of liquid-gas interface, which is unknown but can be assumed as a unit because of the invariant air and liquid phases in this study; and θ is the contact angle.

In this study, the contact angle of asphalt-aggregate surfaces was measured using the device of OCA20 (produced by Dataphysics Group, Germany), as shown in Figure 10. The #90 asphalt was dropped onto the flat surface of rectangular-shape aggregate prepared using the same procedure described above, including washing and cutting to minimize the influences of aggregate surface roughness. The specimens were cured under 25 °C and 100 °C for 6 min, and then set under room temperature for 24 h before testing. In this study, a total of 12 aggregate specimens with 36 asphalt drops were tested.

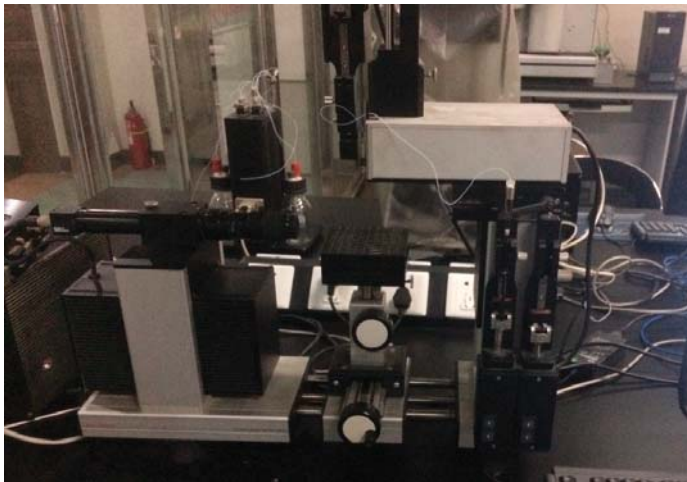


Figure 10. Optical video contact angle tester (OCA20).

The contact angle of each specimen was determined based on the images collected by the contact angle tester (OCA20, Dataphysics, Germany), as shown in Table 5. The results show that the contact angles of different specimens ranged between 90° and 180°, which indicates the weak adhesion at asphalt-aggregate interface in general. The smaller contact angle indicates the stronger adhesion at

asphalt-aggregate interface. The specimens treated with plant ash lixivium had smaller contact angle than the control specimens, especially at 100 °C.

Table 5. The test results of contact angles for different aggregates with #90 asphalt.

Aggregate Types	Control Samples		Treated Samples	
	100 °C	25 °C	100 °C	25 °C
Granite	128°	141°	109°	140°
Basic rock	114°	141°	100°	139°
Limestone	115°	143°	95°	136°

For the aggregate-asphalt interface, the greater adhesion work (W_a) needed for separating asphalt from aggregate indicates the stronger interfacial bonding between asphalt and aggregate. The calculated results of adhesion work for three aggregates with the #90 asphalt are presented in Figure 11. It is noted that the effect of plant ash lixivium should be based on the comparison of work of adhesion at the same temperature. The comparison of work of adhesion at different temperatures is not meaningful since the values of γ_{l-g} , γ_{s-l} , and γ_{s-g} in Equations (5)–(7) are dependent on temperature. Therefore, the improvement ratio after the treatment of plant ash lixivium were calculated and used to evaluate the effect of temperature on treatment effectiveness.

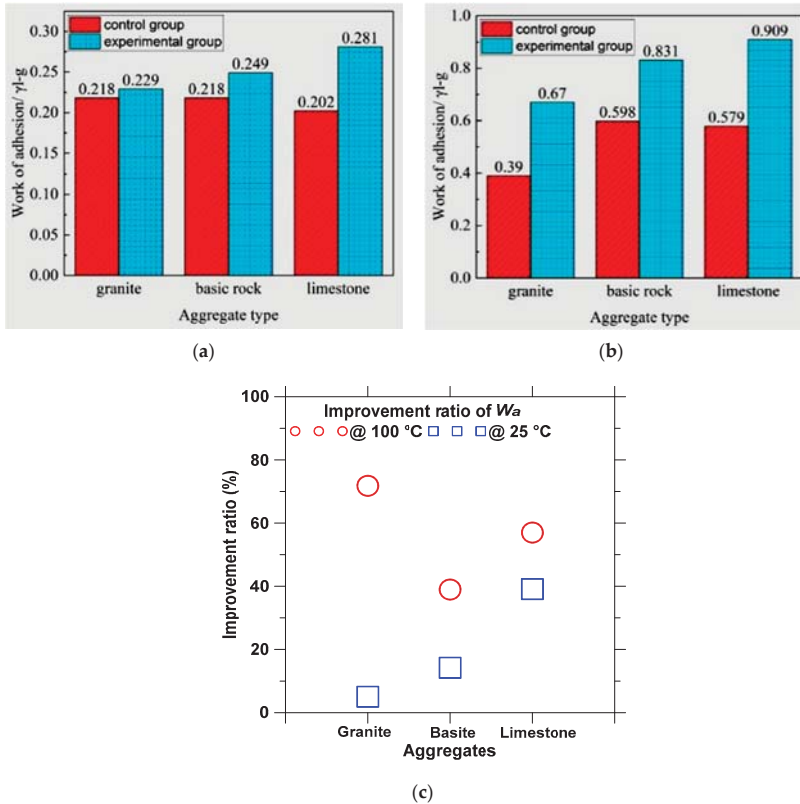


Figure 11. Adhesion work and improvement ratio by plant ash lixivium treatment for aggregates with #90 asphalt: (a) W_a at 25 °C; (b) W_a at 100 °C; and (c) improvement ratio.

The test results showed that the plant ash lixivium could increase adhesion work of asphalt-aggregate interface under both temperatures. For example, the adhesion work between limestone and asphalt increased from $0.202\gamma_{l-g}$ to $0.281\gamma_{l-g}$ at $25\text{ }^{\circ}\text{C}$, and from $0.579\gamma_{l-g}$ to $0.909\gamma_{l-g}$ at $100\text{ }^{\circ}\text{C}$. This means that the moisture invading process at the asphalt-aggregate interface could be delayed or prevented due to the stronger interface adhesion after treated by plant ash lixivium.

As compared to the control specimens, the improvement ratios of adhesion work for the treated specimens with granite, limestone, and basic rock were plotted in Figure 11c. It can be concluded from the improvement ratio that high temperature, i.e., $100\text{ }^{\circ}\text{C}$, can promote the modification of plant ash lixivium treatment. The reason could be that asphalt become softer at relative high temperatures, and thus can flow into minor cracks or surface cavities at aggregate surface and fully coat the aggregate. In the meanwhile, the chemical reaction between asphalt and aggregate might become stronger at higher temperatures; but more evidence is needed to support this point.

5. Microstructure Analysis with SEM and EDS

SEM was used to observe the microstructure and element composition at the asphalt-aggregate interface using the SEM device (JSM-6390A produced by JEOL, Japan). The flat rectangular specimens of the modified stripping test specimens were cut into smaller sized specimen for SEM analysis. The hot asphalt ($0.3\text{--}0.5\text{ }\mu\text{L}$) was dropped on the control and treated aggregates, and then dried at $135\text{ }^{\circ}\text{C}$ for 20 mins and cooled down to room temperature ($25\text{ }^{\circ}\text{C}$) to reach steady shape. Before SEM and EDS measurements, the upper surfaces of specimens were coated with a thin layer of platinum film (5 nm). The specimens with coated surfaces prepared for SEM/EDS analysis are shown in Figure 12.

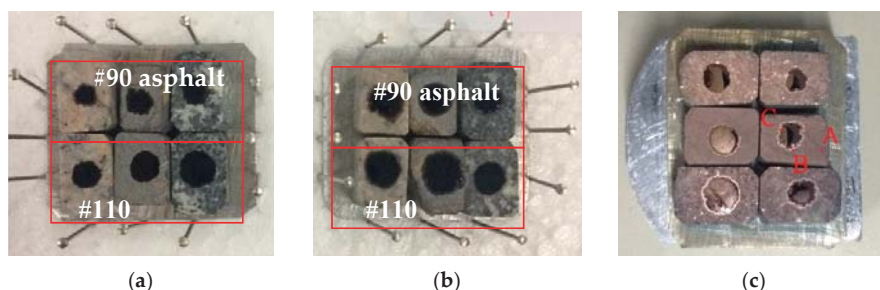


Figure 12. Specimens for scanning electron microscopy (SEM) with energy dispersive spectroscopy (EDS) measurements: (a) control; (b) treated specimen; and (c) observation locations at one specimen (A, B, C).

The boundaries between asphalt droplet and aggregate can be clearly identified, which was the light ring around the black asphalt droplet as shown in Figure 12c. For SEM/EDS analysis, the zone close to the asphalt-aggregate boundary was divided into three areas: Area A is the uncovered aggregate; Area B is the boundary between aggregate and asphalt; and Area C is the boundary between the light ring and the black asphalt droplet.

The comparison of aggregate surface images between the control and treated specimens are shown in Figure 13a,d, respectively, for A/B/C areas. It can be observed that the surface of treated aggregate has higher micro-texture that can increase surface area and thus enhance adhesion strength of asphalt-aggregate. Figure 13b and e show the clear boundary of interfacial transition zone (ITZ) between aggregate and asphalt after treatment. The thickness of ITZ was found in the range of $5\text{--}20\text{ }\mu\text{m}$ for asphalt mixture [35]. However, the ITZ of treated specimens was extended with the blurry zone, as shown in Figure 13e. The SEM images of asphalt binder surface in control specimens and treated specimens are shown in Figure 13c,f. A large amount of mesh crystallized substances were found in

the treated specimens, which could increase the physiochemical effect between asphalt and aggregates. Figure 13f showed that new crystalline products were observed.

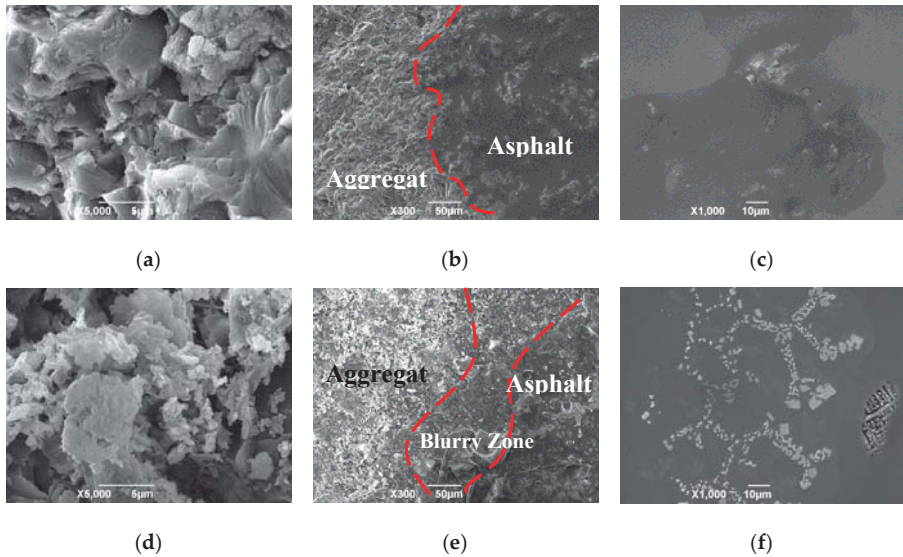
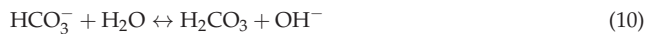


Figure 13. SEM images on aggregate surface, aggregate-asphalt interface, and asphalt surface of (a–c) control samples and (d–f) treated samples.

The SEM analysis showed that there were feather-like, needle-like, and square crystals on aggregate surfaces (Figure 14). In these images, the locations of 004, 022, and 023 at different crystals (as shown in Figure 14) were scanned by EDS, and the element composition was presented in Table 6. Although the component compositions of each burning plant ash were different, the main crystallizations of calcination were the same [22]. According to previous literature [21,22,24], the oxide compositions of the main chemical components of plant ash were SiO₂, K₂O and CaO, while the main crystalline compounds were generally K₂CO₃, KHCO₃, K₂SO₄, KCl, and SiO₂, et al. The SiO₂ is an insoluble component and K₂SO₄ and KCl are neutral salts. However, K₂CO₃ and KHCO₃ can be ionized following Equations (8)–(10), which can explain that the pH value of the suspensions with plant ash lixivium increased over leaching time (Figure 2).



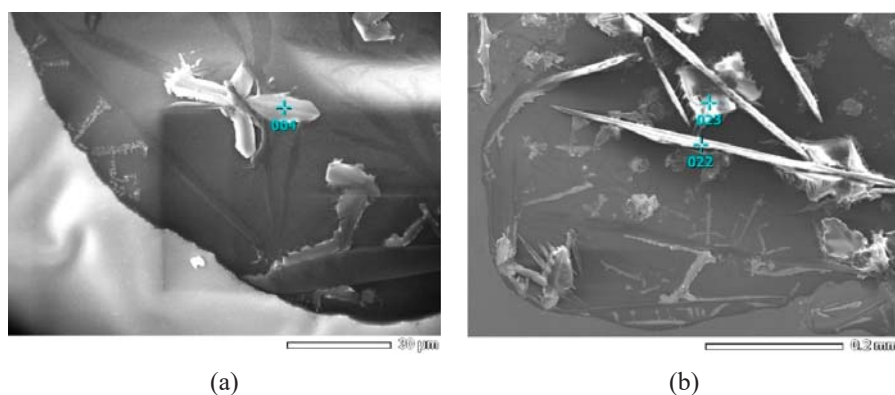


Figure 14. Observed crystal substances: (a) feather-like and (b) needle-like and square shape.

Table 6. The energy disperse spectroscopy (EDS) analysis results of different crystals on aggregate surface.

Location	Index	C	O	S	Cl	K
004 point	Mass/%	21.87	2.47	4.78	30.64	40.25
	Atom/%	45.32	3.84	3.71	21.51	25.62
022 point	Mass/%	5.59	26.33	17.39	–	50.69
	Atom/%	11.78	41.67	13.73	–	32.82
023 point	Mass/%	–	–	–	46.69	53.31
	Atom/%	–	–	–	49.14	50.86

At the observed positions (004, 022, and 023 point) in Figure 14, the atom fraction and mass fraction of elements of K, S, Cl, O, and C are shown in Table 6. It should be noted that the content of C and O could not be accepted because of the signal noise from air (including O_2 and CO_2). At the same time, there was no Ca element observed on specimen's surface. It indicates that in the lixivium solution the main positive ion is K^+ . The following reasons may explain this phenomenon: (1) the lower solubility of $Ca(OH)_2$ (1.65 g/L) than that of KOH (1120 g/L); (2) the CaO is sourced from $CaCO_3$ which is rarely dissolved in water; and (3) there may be no calcium salts in the ashes. The results suggest that in fact the alkalization of aggregates by the plant ash lixivium treatment is mainly contributed by the ionization of K_2CO_3 and $KHCO_3$. The alkalization promotes the higher adhesion between aggregate and asphalt binder.

Based on the distribution of K, S, and Cl elements, it was concluded that there was no KCl at 022 point and no K_2SO_4 at 023 point because S and Cl elements were not detected, respectively. Further, the element ratios of Cl/K and S/K detected by EDS were plotted in Figure 15, indicating the phase of KCl, K_2SO_4 , and $K_2CO_3/KHCO_3$. It was found that only KCl was present at point 023. The main phase at point 022 was K_2SO_4 , with small content of $K_2CO_3/KHCO_3$. At point 04, the mixture of KCl, K_2SO_4 , and $K_2CO_3/KHCO_3$ was found.

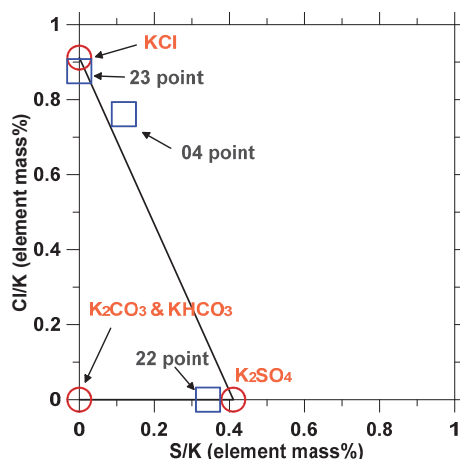


Figure 15. Element ratio based on analysis of EDS data.

6. Conclusions

In this study, plant ash lixivium was used to improve adhesion performance of three commonly used aggregates for asphalt mixtures. To evaluate the improvement of interface adhesion, the conventional stripping test was modified with image analysis of test results. The modified stripping test results showed plant ash lixivium can effectively prevent peeling of asphalt binder from aggregate. Among three aggregate types, granite yielded the worst asphalt-aggregate adhesion for both control and treated specimens. The treatment effectiveness of plant ash lixivium varied depending on the type of asphalt and aggregate.

The contact angle test and SEM/EDS analysis were conducted to analyze adhesion work and microstructure of aggregate-asphalt interfaces. The contact angle test revealed that plant ash lixivium increased work of adhesion of asphalt-aggregate interface, especially at high temperatures. The observations with SEM and EDS indicated that there were chemical interactions between asphalt and aggregate after the aggregate was treated with plant ash lixivium; three crystalline products were observed at the interface of asphalt and aggregate. The study findings prove the potential of using plant ashes to enhance the moisture resistance of asphalt mixtures in practical applications.

Author Contributions: Investigation, X.H. & Z.L.; Conceptualization, A.S. and H.W.; Methodology & Formal Analysis, X.H. and Z.L.; Data Curation, X.H.; Writing-Original Draft Preparation, Z.L. and X.H.; Writing-Review & Editing, H.W., J.C., and C.L.

Funding: This study was partially funded by the National Key R&D Program of China (2018YFB1600200) and National Natural Science Foundation of China (NSFC, No. 51708045).

Acknowledgments: The authors would like to acknowledge Sha Yaohua and Zou Xiaolong for their assistance in laboratory experiments.

Conflicts of Interest: The authors declare no conflict of interest. The funders had no role in the design of the study; in the collection, analyses, or interpretation of data; in the writing of the manuscript, and in the decision to publish the results.

References

1. Canestrari, F.; Cardone, F.; Graziani, A. Adhesive and Cohesive Properties of Asphalt-Aggregate Systems Subjected to Moisture Damage. *Road Mater. Pavement Des.* **2011**, *11*, 11–32. [[CrossRef](#)]
2. Xu, G.J.; Wang, H. Study of Cohesive and Adhesive Properties of Asphalt Concrete with Molecular Dynamics Simulation. *Comput. Mater. Sci.* **2016**, *112*, 161–169. [[CrossRef](#)]

3. Wang, H.; Lin, E.Q.; Xu, G.J. Molecular Dynamics Simulation of Asphalt-Aggregate Adhesion Strength with Moisture Effect. *Int. J. Pavement Eng.* **2017**, *18*, 414–423. [[CrossRef](#)]
4. Moraes, R.; Velasquez, R.; Bahia, H.U. Measuring the Effect of Moisture on Asphalt-Aggregate Bond with the Bitumen Bond Strength Test. *Transp. Res. Rec.* **2011**, *2209*, 70–81. [[CrossRef](#)]
5. Faramarzi, M.; Golestani, B.; Lee, K.W. Improving moisture sensitivity and mechanical properties of sulfur extended asphalt mixture by nano-antistripping agent. *Constr. Build. Mater.* **2017**, *133*, 534–542. [[CrossRef](#)]
6. Mo, L.T.; Huurman, M.; Woldekidan, M.F. Investigation into material optimization and development for improved ravelling resistant porous asphalt concrete. *Mater. Des.* **2010**, *31*, 3194–3206. [[CrossRef](#)]
7. Xu, T.; Wang, H.; Li, Z.D.; Zhao, Y.L. Evaluation of Permanent Deformation of Asphalt Mixtures Using Different Laboratory Performance Tests. *Constr. Build. Mater.* **2014**, *53*, 561–567. [[CrossRef](#)]
8. Xu, G.J.; Wang, H. Molecular Dynamics Study of Interfacial Mechanical Behavior between Asphalt Binder and Mineral Aggregate. *Constr. Build. Mater.* **2016**, *121*, 246–254. [[CrossRef](#)]
9. Yi, J.Y.; Pang, X.Y.; Feng, D.C.; Pei, Z.S.; Xu, M.; Xie, S.N.; Huang, Y.D. Studies on surface energy of asphalt and aggregate at different scales and bonding property of asphalt-aggregate system. *Road Mater. Pavement Des.* **2018**, *19*, 1102–1125. [[CrossRef](#)]
10. Bhasin, A.; Little, D.N.; Vasconcelos, K.L.; Masad, E.A. Surface Free Energy to Identify Moisture Sensitivity of Materials for Asphalt Mixes. *J. Transp. Res. Board* **2007**, *2001*, 37–45. [[CrossRef](#)]
11. Nejad, F.M.; Azarhoosh, A.R.; Hamed, G.H. Influence of using nonmaterial to reduce the moisture susceptibility of hot mix asphalt. *Constr. Build. Mater.* **2012**, *31*, 384–388. [[CrossRef](#)]
12. Arabani, M.; Roshani, H.; Hamed, G.H. Estimating Moisture Sensitivity of Warm Mix Asphalt Modified with Zycosoil as an Antistrip Agent Using Surface Free Energy Method. *J. Mater. Civil Eng.* **2012**, *24*, 889–897. [[CrossRef](#)]
13. Yusoff, N.I.; Breem, A.A.; Alattug, H.N. The effects of moisture susceptibility and ageing conditions on nano-silica/polymer-modified asphalt mixtures. *Constr. Build. Mater.* **2014**, *72*, 139–147. [[CrossRef](#)]
14. Gorkem, C.; Sengoz, B. Predicting stripping and moisture induced damage of asphalt concrete prepared with polymer modified bitumen and hydrated lime. *Constr. Build. Mater.* **2009**, *23*, 2227–2236. [[CrossRef](#)]
15. Nejad, F.M.; Aghajani, P.; Modarres, A. Investigating the properties of crumb rubber modified bitumen using classic and SHRP testing methods. *Constr. Building Mater.* **2012**, *26*, 481–489. [[CrossRef](#)]
16. Moreno, F.; Rubio, M.C. Effect of aggregate nature on the fatigue-cracking behavior of asphalt mixes. *Mater. Des.* **2013**, *47*, 61–67. [[CrossRef](#)]
17. Lesueur, D.; Petit, J.; Ritter, H. The mechanisms of hydrated lime modification of asphalt mixtures: A state-of-the-art review. *Road Mater. Pavement Des.* **2013**, *14*, 1–16. [[CrossRef](#)]
18. Han, Z.; Sha, A.; Tong, Z.; Liu, Z.; Gao, J.; Zou, X.; Yuan, D. Study on the optimum rice husk ash content added in asphalt binder and its modification with bio-oil. *Constr. Build. Mater.* **2017**, *147*, 776–789. [[CrossRef](#)]
19. Arabani, M.; Tahami, S.A. Assessment of mechanical properties of rice husk ash modified asphalt mixture. *Constr. Build. Mater.* **2017**, *149*, 350–358. [[CrossRef](#)]
20. Thompson, D.N.; Shaw, P.G.; Lacey, J.A. Post-harvest processing methods for reduction of silica and alkali metals in wheat straw. *Appl. Biochem. Biotechnol.* **2003**, *105*, 205–218. [[CrossRef](#)]
21. Yao, X.W.; Xu, K.L.; Yan, F. The Influence of Ashing Temperature on Ash Fouling and Slagging Characteristics during Combustion of Biomass Fuels. *Bioresources* **2017**, *12*, 1593–1610. [[CrossRef](#)]
22. Xiao, R.R.; Chen, X.L.; Wang, F.C. The physicochemical properties of different biomass ashes at different ashing temperature. *Acta Energ. Sol. Sin.* **2011**, *32*, 364–369. [[CrossRef](#)]
23. Grau, F.; Choo, H.; Hu, J. Engineering Behavior and Characteristics of Wood Ash and Sugarcane Bagasse Ash. *Materials* **2015**, *8*, 6962–6977. [[CrossRef](#)] [[PubMed](#)]
24. Thy, P.; Jenkins, B.M.; Grundvig, S. High temperature elemental losses and mineralogical changes in common biomass ashes. *Fuel* **2006**, *85*, 783–795. [[CrossRef](#)]
25. Guo, M.; Tan, Y.Q.; Zhou, S.W. Multiscale Test Research on Interfacial Adhesion Property of Cold Mix Asphalt. *Constr. Build. Mater.* **2014**, *68*, 769–776. [[CrossRef](#)]
26. Kim, Y.; Pinto, I.; Park, S. Experimental evaluation of anti-stripping additives in bituminous mixtures through multiple scale laboratory test results. *Constr. Build. Mater.* **2012**, *29*, 386–393. [[CrossRef](#)]
27. Lantieri, C.; Lamperti, R.; Simone, A.; Vignali, V.; Sangiorgi, C.; Dondi, G.; Magnani, M. Use of image analysis for the evaluation of rolling bottle tests results. *Int. J. Pavement Res. Technol.* **2017**, *10*, 45–53. [[CrossRef](#)]

28. ASTM Standard D5/D5M. *Standard Test Method for Penetration of Bituminous Materials*; ASTM International: West Conshohocken, PA, USA, 2013.
29. ASTM Standard D36/D36M. *Standard Test Method for Softening Point of Asphalt (Ring-and-Ball Apparatus)*; ASTM International: West Conshohocken, PA, USA, 2009.
30. ASTM D 113-99. *Standard Test Method for ductility Test*; ASTM International: West Conshohocken, PA, USA, 2002.
31. Zhang, K.; Zhang, Z.Q. Quantitative evaluation of the adhesion between asphalt and aggregate. *J. Hefei Univ. Technol.* **2015**, *6*, 810–815.
32. Arabani, M.; Hamed, G.H. Using the Surface Free Energy Method to Evaluate the Effects of Polymeric Aggregate Treatment on Moisture Damage in Hot-Mix Asphalt. *J. Mater. Civil Eng.* **2011**, *23*, 802–811. [[CrossRef](#)]
33. Rossi, C.O.; Caputo, P.; Baldino, N. Quantitative evaluation of organosilane-based adhesion promoter effect on bitumen-aggregate bond by contact angle test. *Int. J. Adhes. Adhes.* **2017**, *72*, 117–122. [[CrossRef](#)]
34. Ma, F.; Hao, J.X.; Fu, Z. Surface free energy analysis of asphalt modified with natural asphalt. *J. Traffic Transp. Eng.* **2015**, *15*, 18–24.
35. Zhu, X.Y.; Yuan, Y.; Li, L.H.; Du, Y.C.; Li, F. Identification of interfacial transition zone in asphalt concrete based on nano-scale metrology techniques. *Mater. Des.* **2017**, *129*, 91–102. [[CrossRef](#)]



© 2019 by the authors. Licensee MDPI, Basel, Switzerland. This article is an open access article distributed under the terms and conditions of the Creative Commons Attribution (CC BY) license (<http://creativecommons.org/licenses/by/4.0/>).

Article

Diffusibility Enhancement of Rejuvenator by Epoxidized Soybean Oil and Its Influence on the Performance of Recycled Hot Mix Asphalt Mixtures

Dongliang Kuang¹, Yuan Jiao¹, Zhou Ye¹, Zaihong Lu², Huaxin Chen¹, Jianying Yu^{3,*} and Ning Liu⁴

¹ School of Materials Science and Engineering, Chang'an University, Xi'an 710064, China; kuangdl@163.com (D.K.); 15114863419@163.com (Y.J.); joe_yezhou@163.com (Z.Y.); chenhx_paper@163.com (H.C.)

² Inner Mongolia Transportation Design Institute Co., Ltd., Huhhot 010000, China; luzaihongnm@163.com

³ State Key Laboratory of Silicate Materials for Architectures, Wuhan University of Technology, Wuhan 430070, China

⁴ Highway Researching and Designing Institute of Qinghai Province, Xining 810001, China; 1969ln@163.com

* Correspondence: jyyu@whut.edu.cn; Tel.: +86-027-5973-5080

Received: 26 March 2018; Accepted: 16 May 2018; Published: 18 May 2018

Abstract: Epoxidized soybean oil (ESO) was employed as a novel penetrant cooperating with a conventional rejuvenator (CR) for the recycling of reclaimed asphalt pavement (RAP). The influence of ESO on the diffusibility and the regenerating effects of CR on RAP were investigated. The diffusibility testing result shows that the diffusibility of CR is enhanced by the addition of ESO because the epoxy group in ESO can facilitate asphaltene dispersion due to its high polarity, which simultaneously reduces the viscosity and improves the fluidity of aged bitumen so as to allow diffusion of the rejuvenator into the aged bitumen. Road performance testing of a recycled hot mix asphalt mixture (RHMA) indicates that the fatigue and cracking resistance properties as well as the water stability of RHMA containing CR can be improved by the addition of ESO due to the diffusibility enhancement of CR, which boosts the regenerating effect of CR on aged bitumen in RAP. The fatigue and cracking resistance properties as well as the water stability of the recycled hot mix asphalt mixture containing CR with 7 wt % ESO approximate those of the hot mix asphalt mixture composed of the same virgin aggregates and bitumen. Taking into account the rutting resistance decline versus the addition of ESO, the content of ESO should not exceed 7 wt % of the conventional rejuvenator.

Keywords: reclaimed asphalt pavement; recycling; epoxidized soybean oil; rejuvenator; diffusing

1. Introduction

In the recycling of reclaimed asphalt pavement (RAP), the RAP is blended with virgin aggregate, virgin bitumen as well as a rejuvenator to fabricate recycled hot mix asphalt (RHMA), which can conserve natural resources and reduce environmental pollution [1–3].

RAP usually has lower road performance due to the aging of bitumen [4–6]. A rejuvenator that can reconstitute the chemical component and colloidal structure of aged bitumen to regenerate its performance [7,8] is crucial for the recycling of RAP. In previous studies, it was reported that the rejuvenator and aged bitumen were initially blended evenly, and then a series of testing, including the physical properties, rheological properties and chemical components, was conducted on the blends to investigate the influence of the rejuvenator on aged bitumen; the results indicate that the aged bitumen can reach the target performance grade if the appropriate amount of the rejuvenator is determined and added [9–12].

However, for the practical recycling process of RHMA, the rejuvenator is first sprinkled on the surface of RAP and then blended with virgin aggregate as well as virgin bitumen [13]. The processing time usually lasts 45 to 60 s, so it is impossible for the rejuvenator to be uniformly mixed with aged bitumen in RAP as well as added virgin bitumen [14]. Therefore, the regeneration of aged bitumen in RAP is essentially dependent on the diffusion of the rejuvenator [15]. Previous research has revealed that the hardness and viscosity of aged bitumen in RAP are higher than unaged bitumen [16], which decreases the movement of the bitumen molecule; therefore, the fluidity of aged bitumen is poor, and the diffusion of the rejuvenator into aged bitumen is obstructed [17]. In order to enhance the diffusibility of the rejuvenator into aged bitumen, some attempts such as decreasing the viscosity of the rejuvenator and increasing the preheating temperature of RAP have been made [18]; nevertheless, the improvement was finite. Therefore, it is necessary to develop new methods to enhance the diffusibility of the rejuvenator.

As mentioned above, the high hardness and viscosity of the aged bitumen make the rejuvenator diffusion into aged bitumen difficult, which can be ascribed to the high asphaltene content [19]. Therefore, the diffusibility of the rejuvenator can be enhanced by simultaneously reducing the asphaltene content and by increasing the fluidity of the aged bitumen.

Epoxidized soybean oil (ESO), a kind of plasticizer, has been widely applied in the production of plastic, rubber and paint due to good fluidity, penetrability and temperature stability [20]. Recently, ESO has been used for the modification of oxidized bitumen; the results indicate that ESO displays good compatibility with the oxidized bitumen due to the polar epoxy group in ESO [21] and can facilitate asphaltene dispersion [22], which benefits the colloidal structure transformation of the oxidized bitumen from gel to sol-gel; therefore, the fluidity of oxidized bitumen can be enhanced and the viscosity can be reduced [23].

In this paper, ESO was adopted as a novel penetrant with a conventional rejuvenator (CR), and these were applied together for the recycling of RAP. In addition, the effects of ESO on the diffusibility and regenerating effects of the conventional rejuvenator were investigated.

2. Materials and Methods

2.1. Materials

Bitumen, i.e., AH-70 paving bitumen, was supplied by China Offshore Bitumen Co., Ltd., Taizhou, China. The physical properties and chemical components of the bitumen are listed in Table 1.

CR was prepared in the laboratory, and its physical properties are shown in Table 2.

ESO was supplied by Tongxiang Chemical Co., Ltd. In Tongxiang, China. The properties of ESO are listed in Table 3.

RAP was obtained from Jingzhu Expressway in Hubei Province, China. The bitumen and aggregates in RAP were separated according to ASTM D2172 [24]. The asphalt-aggregate ratio of RAP was 3.8 wt %, determined according to ASTM D6307 [25]. The properties and chemical components of the aged bitumen and the gradation of the aggregates in RAP are displayed by Tables 4 and 5, respectively. Virgin aggregates, limestone coarse aggregate with a maximum sieve size of 19 mm and fine aggregate were supplied by Beishan Stone Factory in Chibi, China.

Table 1. Physical properties and chemical components of AH-70.

Items		Value
Physical properties	Softening point (°C)	47.2
	Ductility (15 °C, cm)	>150
	Penetration (25 °C, 0.1 mm)	70
	Viscosity (60 °C, Pa·s)	232
Chemical components	Saturates (%)	12.2
	Aromatics (%)	50.2
	Resins (%)	26.1
	Asphaltenes (%)	11.5

Table 2. Properties of CR.

Physical Properties	Items
Viscosity at 60 °C (cst)	1700
Flash point (°C)	>220
Viscosity ratio before and after TFOT	2.5
Weight loss after TFOT (%)	−2.6
Saturates content (%)	<30

Table 3. Properties of ESO.

Properties	Value
Molecular	1000
Viscosity (cps, 25 °C)	350
Acid value	0.45
Iodine value (%)	4.0
Flash point (°C)	280
Epoxy value (%)	6.1
Weight loss after heating (%)	0.08
Specific gravity (25 °C)	0.982

Table 4. Physical properties and chemical components of aged bitumen.

Items		Value
Physical properties	Softening point (°C)	58.3
	Ductility (15 °C, cm)	9.6
	Penetration (25 °C, 0.1 mm)	30
	Viscosity (60 °C, Pa·s)	410
Chemical components	Saturates (%)	11.2
	Aromatics (%)	31.3
	Resins (%)	29.1
	Asphaltenes (%)	28.4

Table 5. Gradation of aggregates in RAP.

Sieve (mm)	19	16	13.2	9.5	4.75	2.36	1.18	0.6	0.3	0.15	0.075
Passing (%)	100	99.2	98.3	90.9	68.4	50.3	34.1	26	17.4	14.3	4.7

2.2. Design and Preparation of RHMA

In this paper, AC-20 was selected as the objective gradation for RHMA. The Marshall Design procedure was used for the designing of RHMA of AC-20; the content of RAP was 30 wt %.

The designed gradation is presented in Table 6. The optimum asphalt aggregate ratio of 4.2 wt % was determined according to Marshall testing.

Table 6. Gradation of RHMA.

Sieve (mm)	19	16	13.2	9.5	4.75	2.36	1.18	0.6	0.3	0.15	0.075
Passing (%)	96.7	87.5	78.3	60.2	42.2	25.3	18.7	15.4	11.5	9.2	6.1

Preparation of RHMA: first, RAP was heated to 110 °C; then, the rejuvenator plus ESO heated to 100 °C as well as virgin coarse aggregates heated to 180 °C were placed in a stirrer at 180 °C and blended for 10 s. Then, virgin bitumen heated to 150 °C was added and blended for 90 s; finally, mineral powder was added and continuously blended for 90 s.

For comparison, a virgin hot mix asphalt (VHMA) mixture of AC-20 composed of the same virgin bitumen and virgin aggregates as RHMA was also prepared as the control sample; the optimum asphalt aggregate ratio was 3.8 wt %. The selected gradation is presented in Table 7. The performance of VHMA is described in Table 8.

Table 7. Gradation of VHMA.

Sieve (mm)	19	16	13.2	9.5	4.75	2.36	1.18	0.6	0.3	0.15	0.075
Passing (%)	97.1	87.5	76.6	55.7	38.2	27.5	18.8	16.2	12.7	10.2	5.1

Table 8. Performance of VHMA.

	Performance	VHMA
Rutting resistance	d ₆₀ (mm)	2.263
	DS (time/mm)	1300
Water stability	MS ₀ (%)	89
	TSR (%)	83
Fatigue property	N _f at 0.2 P (times)	10,350
	N _f at 0.3 P (times)	7951
	N _f at 0.4 P (times)	4642
	N _f at 0.5 P (times)	3617
Crack resistance	Failure strength (MPa)	7.3
	Failure strain (%)	2990
	Failure stiffness modulus (MPa)	2120

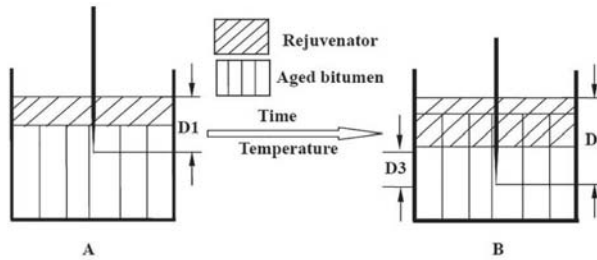
2.3. Diffusibility Testing Procedure of Rejuvenators

The diffusibility of the rejuvenators was tested according to the following procedure reported in previous research [26]:

- Aged bitumen heated to 140 °C was poured into penetration molds A and B, of which the inner diameter and height were 55 mm and 35 mm, respectively, and was then placed in an oven at a temperature of 110 °C for 30 min. Then, the rejuvenator heated to 110 °C was coated on the surface of the aged bitumen and maintained in an oven at 110 °C for 10 min to ensure the rejuvenator was uniformly scattered on the surface of the aged bitumen. The dosages of the aged bitumen and rejuvenator were 50 g and 5 g, respectively.
- Mold B was placed in an oven at a different temperature for a certain time or constant temperature for different times, and then continuously placed in an oven without power supply for 2.5–3 h, allowing the temperature to decrease to room temperature gradually to reduce the influence of interface contraction induced by a rapid decline in temperature on the flatness of the rejuvenator coat.

As observed in Scheme 1, the penetrations of aged bitumen with the rejuvenator coat before and after the diffusion experiment were D1 and D2, respectively. The difference (D3) between D1 and D2 was used to characterize the diffusibility of the rejuvenator. The larger the D3 value, the better the diffusibility.

The temperature and time of the diffusing experiment were 160 °C and 4 h, respectively. The aged bitumen was produced by artificial aging in the laboratory. The weight of aged bitumen and rejuvenator were 50 g and 5 g, respectively, and the ESO dosages were 1 wt %, 3 wt %, 5 wt % and 7 wt % of the rejuvenator weight.



Scheme 1. Synthesis of rejuvenator diffusion into aged bitumen by penetration testing.

2.4. Performance Testing of Asphalt Mixtures

The rutting depth at 60 min (d_{60}) and dynamic stability (DS) of the mixtures were tested according to ASTM D2172 [27]. The remnant stability (MS_0) and freeze-thaw strength ratio (TSR) of the mixtures were tested according to ASTM D4867 [28] and ASTM D1559 [29], respectively.

The beam fatigue experiments of the samples at 15 °C were performed by the UTM dynamic servo hydraulic produced by IPC Co., Ltd., Sydney, Australia according to ASTM D32 [30]. The experiment was conducted under a stress-control model with a speed of 50 mm/min and frequency of 10 Hz; the loading time and unloading time were 0.1 s and 0.9 s, respectively; the testing stress was selected as 0.2 P, 0.3 P, 0.4 P and 0.5 P (P is the failure stress of each kind of asphalt mixture).

Under the stress-control model, the fatigue properties can be depicted by the following fatigue equation.

$$\ln(N_f) = -n\ln(\sigma_0) + \ln(K) \quad (1)$$

where N_f is the cycle number to failure; σ_0 is the loading stress; K and n are constants. After linear simulation, the constants K and n can be obtained. The fatigue properties of the mixture can be evaluated by constants K and n .

The bending test was employed to characterize the crack resistance of the asphalt mixture under a minus temperature temperature, which was also conducted by the UTM dynamic servo hydraulic produced by IPC Co., Ltd., Sydney, Australia, according to ASTM D32 [30]. The experiment was performed at −10 °C, and the loading rate was 50 mm/min.

3. Results and Discussion

3.1. Effect of ESO on the Diffusibility of CR

Figure 1 reveals the penetration increment of aged bitumen covered by CR cooperating with ESO after being placed in an oven at 160 °C for 4 h. As observed from Figure 1, the penetration increment of aged bitumen covered by CR increased with the addition of ESO, which indicates the diffusibility of CR is enhanced by ESO. It can be explained as follows: the polar epoxy group included in ESO contributes to the asphaltene dispersion in the resin and aromatics, and then the viscosity

of aged bitumen is reduced and the fluidity of aged bitumen is improved, which are helpful for the enhancement of diffusibility.

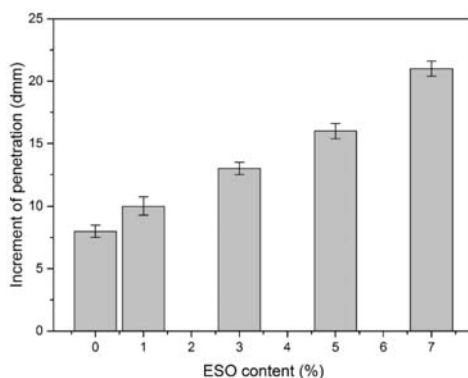


Figure 1. Penetration increment versus ESO.

Compared with the penetration increment of aged bitumen with a CR coat of 8 dmm, the penetration increment of the aged bitumen with the CR coat cooperating with 7 wt % ESO reaches 21 dmm, which is 2.6 times the penetration increment of aged bitumen with the CR coat.

3.2. Effect of CR on the Performance of RHMA

Table 9 displays the performance of RHMA with different contents of CR. It can be found that both cycle number to failure and water stability of RHMA increased with an increase in the CR content; when the CR content approaches 20 wt %, the water stability can meet the application requirements. It can be also observed from the table that the DS of the RHMA with 15 wt % and 20% CR are 1220 time/mm and 920 time/mm, respectively, which are 46% and 35% of that of the RHMA without CR, indicating the rutting resistance of the RHMA is sharply reduced by a high content of the rejuvenator. In view of this fact, the CR content is selected as 10 wt % in the following experiment in this paper.

Table 9. Performance of RHMA with different CR contents.

Performance		CR Content (%)				
		0	5	10	15	20
Rutting resistance	d_{60} (mm)	2.011	2.137	2.248	2.352	2.473
	DS (time/mm)	2650	2271	1753	1220	920
Water stability	MS ₀ (%)	67	70	72	78	82
	TSR (%)	61	64	68	73	79
Fatigue property	N _f at 0.2 P (times)	5860	6760	7145	8542	9350
	N _f at 0.3 P (times)	3155	3555	4153	6340	7620
	N _f at 0.4 P (times)	1375	2100	2600	3650	4100
	N _f at 0.5 P (times)	650	1000	1270	2005	2410
Crack resistance	Failure strength (MPa)	4.2	4.5	5.2	5.8	6.7
	Failure strain (%)	1400	1550	1800	2072	2300
	Failure stiffness modulus (MPa)	3020	2800	2605	2317	2150

3.3. Effect of ESO on the Performance of RHMA with CR

3.3.1. Fatigue Properties

The fatigue properties of RHMA with CR incorporated with different contents of ESO are shown in Figure 2 and Table 10. As displayed in Figure 2, the cycle number to failure of the RHMA with CR incorporated with ESO increases with the increase in ESO at different stress levels at 15 °C, indicating that the fatigue properties of the RHMA with CR can be improved by ESO. This can be explained as follows: CR containing ESO diffuses into aged bitumen more easily; therefore, the aged bitumen in RAP can be regenerated more effectively, which improves the fatigue properties of the RHMA.

Table 10 shows the parameters for the fatigue equation of RHMA with CR with different contents of ESO. It can be observed that the values of *K* and *n* of RHMA with CR increase with the addition of ESO, which also indicates that the RHMA containing the rejuvenator with ESO exhibits better fatigue properties [31]. The cycle number to failure of RHMA containing the CR with 7 wt % ESO is 9945, which nearly approaches the cycle number to failure of VHMA.

Furthermore, it can be also observed in Table 10 that the cycle number to failure of RHMA containing CR with 7 wt % ESO is 1.39 times that of RHMA containing CR without ESO under a 0.2 stress ratio; whereas, for the cycle number to failure of RHMA containing CR with 7 wt % ESO under the 0.5 stress ratio, it is 2.95 times that of RHMA containing CR without ESO under the 0.5 stress ratio, which indicates that ESO is more effective with respect to the fatigue property enhancement of RHMA containing CR under a high stress ratio.

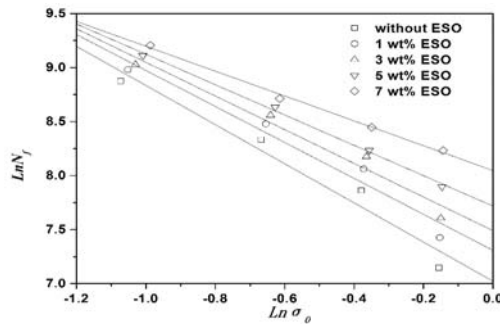


Figure 2. Fatigue curves of RHMA with CR incorporated with ESO.

Table 10. Parameters for the fatigue equation of RHMA with CR incorporated with ESO.

ESO Content (%)	<i>N_f</i>				Fatigue Equation	Equation Parameters	
	Stress Ratio					<i>K</i>	<i>n</i>
	0.2	0.3	0.4	0.5			
0	7145	4153	2600	1270	$LnN_f = -1.149Ln\sigma_0 + 7.022$	1121	1.149
1	7948	4810	3170	1680	$LnN_f = -1.405Ln\sigma_0 + 7.308$	1492	1.405
3	8327	5210	3550	2010	$LnN_f = -1.577Ln\sigma_0 + 7.491$	1791	1.577
5	9054	5620	3770	2690	$LnN_f = -1.665Ln\sigma_0 + 7.718$	2248	1.665
7	9945	6074	4660	3757	$LnN_f = -1.812Ln\sigma_0 + 8.047$	3124	1.812

3.3.2. Cracking Resistance Properties

Figure 3 reveals the failure strength, failure strain and failure stiffness modulus of RHMA containing CR incorporated with different contents of ESO at −10 °C. It can be observed in Figure 3 that, as ESO increases, the failure strength and failure strain increase, whereas the failure stiffness modulus declines at the same time, indicating that the cracking resistance properties of RHMA with

CR are improved by adding ESO. This can be ascribed to the chemical interaction between the epoxy groups which benefits the viscosity decline and molecule movement; therefore, the mixing between CR and aged bitumen as well as added virgin bitumen becomes more even. Consequently, the property restoration of aged bitumen is intensified, which significantly contributes to the enhancement of the cracking resistance of RHMA under a low temperature.

Furthermore, it can be also observed from Figure 3 that the failure strength and failure strain of RHMA containing CR with 7 wt % ESO can reach 7.3 MPa and 2767, respectively, i.e., 1.36 times and 1.54 times the failure strength and failure strain of RHMA containing only CR.

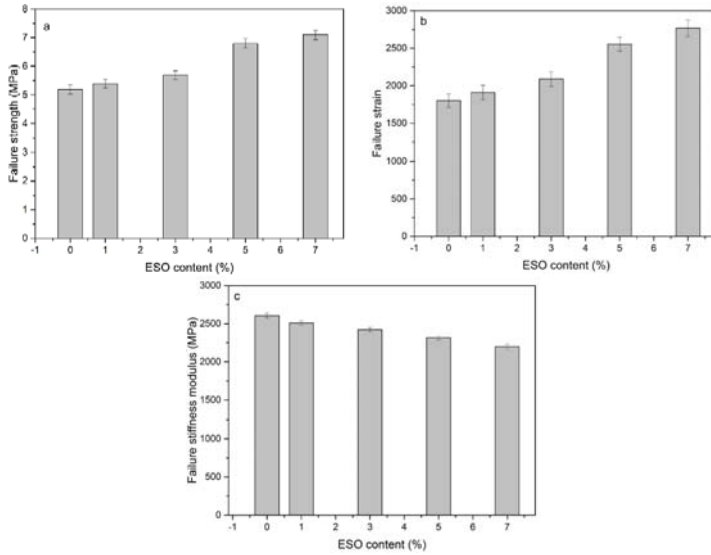


Figure 3. Beam bend results of RHMA with CR incorporated with ESO: (a) Failure strength; (b) Failure strain; (c) Failure stiffness modulus.

3.3.3. Water Stability

Figure 4 shows the MS_0 and TSR of RHMA containing CR incorporated with different contents of ESO. It can be seen from Figure 4 that the MS_0 and TSR of RHMA containing CR increase with the addition of ESO, indicating that the water stability of RHMA with CR is enhanced by ESO, which can be ascribed to the fact that ESO can facilitate CR diffusion into aged bitumen, wrapping around the surface of reclaimed aggregates by reducing the viscosity and increasing the fluidity of the aged bitumen, which benefits the compatibility between aged bitumen and CR as well as added virgin bitumen. Therefore the water stability of RHMA containing CR is improved by ESO. It can also be observed from Figure 4 that when the ESO content approaches 7 wt %, the MS_0 and TSR of the RHMA containing CR can reach 87% and 81%, respectively, which is close to those of the VHMA.

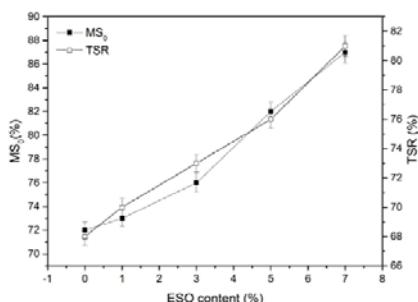


Figure 4. Water stability of RHMA with CR incorporated with ESO.

3.3.4. Rutting Resistance

Figure 5 shows the DS and d_{60} of RHMA containing CR incorporated with different contents of ESO. It can be found that with an increase in ESO, the d_{60} increases, whereas DS declines, which indicates the rutting resistance of RHMA-containing rejuvenators is reduced by ESO. This can be explained as follows: ESO facilitates rejuvenator diffusion into aged bitumen and intensifies the mixing between aged bitumen and the rejuvenator as well as added virgin bitumen, which adversely affects the rutting resistance of the RHMA under high temperature; therefore, the d_{60} increases, whereas DS declines. However, when the ESO content is between 5 wt % and 7 wt %, the DS of the RHMA-containing rejuvenator can still satisfy the application requirements.

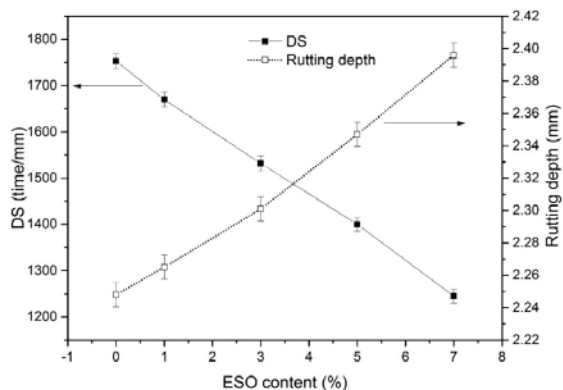


Figure 5. Rutting test result of RHMA with CR incorporated with ESO.

4. Conclusions

Epoxidized soybean oil was used as a penetrant to improve the diffusibility of a conventional rejuvenator and was applied for the recycling of reclaimed asphalt pavement together with a conventional rejuvenator. The influence of epoxidized soybean oil on the diffusibility of the conventional rejuvenator and the performance of a recycled hot mix asphalt mixture with the conventional rejuvenator were investigated. The conclusions were as follows:

1. The diffusibility of the conventional rejuvenator was significantly enhanced by ESO because the epoxy group included in ESO contributes to the asphaltene dispersion in resin and aromatics due to its high polarity. In addition, the fluidity of aged bitumen is improved and the viscosity is reduced, which are helpful for rejuvenator diffusion into aged bitumen.

2. The fatigue property, cracking resistance property as well as water stability of RHMA with the conventional rejuvenator were improved by ESO due to its facilitation of the diffusibility of the conventional rejuvenator. The fatigue property, cracking resistance property and water stability of the RHMA-containing conventional rejuvenator incorporated with 7 wt % approached those of the VHMA composed of the same virgin bitumen and virgin aggregates as RHMA.
3. The conventional rejuvenator with ESO improved the fatigue property, cracking resistance property as well as water stability of the RHMA at a lower content; thus, the negative effect of the high rejuvenator content on the rutting resistance of the RHMA was eliminated. Although the rutting properties of the RHMA-containing conventional rejuvenator incorporated with 7% ESO declined compared to RHMA with only the conventional rejuvenator, they still approached those of the VHMA and meet the application requirements.

Author Contributions: D.K. and J.Y. conceived and designed the experiments; Y.J. and Z.Y. performed the experiments; H.C. and Z.L. analyzed the data; N.L. contributed reagents/materials/analysis tools; D.K. wrote the paper.

Funding: This research was funded by [the key project of research and transformation of the Department of Science and Technology of Qinghai Province] grant number [Nos. 2018-SF-111 and 2018-ZJ-760], [projects of Transportation Department of Inner Mongolia Autonomous Region] grant number [Nos. NJ-2016-7 and NJ-2017-15], and [the Fund for Basic Scientific Research of Central Colleges of Chang'an University] grant number [Nos. 310831171015, 300102318401 and 300102318501].

Conflicts of Interest: The authors declare no conflicts of interest.

References

1. Shu, X.; Huang, B.S.; Vukosavljevic, D. Laboratory evaluation of fatigue characteristics of recycled asphalt mixture. *Constr. Build. Mater.* **2008**, *7*, 1323–1330. [[CrossRef](#)]
2. Xu, J.Z.; Hao, P.W.; Zhang, D.P. Investigation of reclaimed asphalt pavement blending efficiency based on micro-mechanical properties of layered asphalt binders. *Constr. Build. Mater.* **2018**, *163*, 390–401. [[CrossRef](#)]
3. Gao, L.; Li, H.; Xie, J.G.; Yu, Z.B. Evaluation of pavement performance for reclaimed asphalt materials in different layers. *Constr. Build. Mater.* **2018**, *159*, 561–566. [[CrossRef](#)]
4. Sivilevicius, H.; Braziunas, J.; Prentkovskis, O. Technologies and Principles of Hot Recycling and Investigation of Preheated Reclaimed Asphalt Pavement Batching Process in an Asphalt Mixing Plant. *Appl. Sci.* **2017**, *7*, 1104. [[CrossRef](#)]
5. Arshad, M.; Ahmed, M.F. Potential use of reclaimed asphalt pavement and recycled concrete aggregate in base/subbase layers of flexible pavements. *Constr. Build. Mater.* **2017**, *151*, 83–97. [[CrossRef](#)]
6. Vega-Zamanillo, A.; Calzada-Perez, M.A.; Lastra-Gonzalez, P.; Indacochea-Vega, I. Analysis of the use of cupola furnace slags, green sand and reclaimed asphalt pavement in asphalt concrete mixtures for low intensity traffic. *Inf. Constr.* **2017**, *16*, 229–237. [[CrossRef](#)]
7. Singh, D.; Girimath, S.; Ashish, P.K. Performance Evaluation of Polymer-Modified Binder Containing Reclaimed Asphalt Pavement Using Multiple Stress Creep Recovery and Linear Amplitude Sweep Tests. *J. Mater. Civ. Eng.* **2018**, *30*, 40–50. [[CrossRef](#)]
8. Elkashef, M.; Williams, R.C.; Cochran, E.W. Physical and chemical characterization of rejuvenated reclaimed asphalt pavement (RAP) binders using rheology testing and pyrolysis gas chromatography-mass spectrometry. *Mater. Struct.* **2018**, *51*, 11–19. [[CrossRef](#)]
9. Zhang, K.; Muhunthan, B. Effects of production stages on blending and mechanical properties of asphalt mixtures with reclaimed asphalt pavement. *Constr. Build. Mater.* **2017**, *149*, 679–689. [[CrossRef](#)]
10. Yang, S.H.; Lee, L.C. Characterizing the chemical and rheological properties of severely aged reclaimed asphalt pavement materials with high recycling rate. *Constr. Build. Mater.* **2016**, *111*, 139–146. [[CrossRef](#)]
11. Su, J.F.; Wang, Y.Y.; Yang, P. Evaluating and Modeling the Internal Diffusion Behaviors of Microencapsulated Rejuvenator in Aged Bitumen by FTIR-ATR Tests. *Materials* **2016**, *9*, 932. [[CrossRef](#)] [[PubMed](#)]
12. Chen, M.Z.; Leng, B.B.; Wu, S.P. Physical, chemical and rheological properties of waste edible vegetable oil rejuvenated asphalt binders. *Constr. Build. Mater.* **2014**, *66*, 286–298. [[CrossRef](#)]

13. Ma, T.; Huang, X.; Zhao, Y.; Zhang, Y. Influences of Preheating Temperature of RAP on Properties of Hot-Mix Recycled Asphalt Mixture. *J. Test. Eval.* **2016**, *26*, 43–46. [[CrossRef](#)]
14. Vislavicius, K.; Sivilevicius, H. Effect of reclaimed asphalt pavement gradation variation on the homogeneity of recycled hot-mix asphalt. *Arch. Civ. Mech. Eng.* **2013**, *13*, 345–363. [[CrossRef](#)]
15. Ding, Y.J.; Huang, B.S.; Shu, X. Use of molecular dynamics to investigate diffusion between virgin and aged asphalt binders. *Fuel* **2016**, *174*, 267–273. [[CrossRef](#)]
16. Xiao, Y.; Li, C.; Wan, M. Study of the Diffusion of Rejuvenators and Its Effect on Aged Bitumen Binder. *Appl. Sci.* **2017**, *7*, 397. [[CrossRef](#)]
17. Mokhtari, A.; Lee, H.D.; Williams, R.C. A novel approach to evaluate fracture surfaces of aged and rejuvenator-restored asphalt using cryo-SEM and image analysis techniques. *Constr. Build. Mater.* **2017**, *133*, 301–313. [[CrossRef](#)]
18. Anisimov, M.A.; Yudin, I.K.; Nikitin, V. Asphaltene Aggregation in Hydrocarbon Solutions Studied by Photon Correlation Spectroscopy. *J. Phys. Chem.* **1995**, *99*, 9576–9580. [[CrossRef](#)]
19. Karlsson, R.; Isacson, U. Application of FTIR-ATR to Characterization of Bitumen Rejuvenator Diffusion. *J. Mater. Civ. Eng.* **2003**, *15*, 157–165. [[CrossRef](#)]
20. Lee, S.; Park, M.S.; Shin, J. Effect of the individual and combined use of cardanol-based plasticizers and epoxidized soybean oil on the properties of PVC. *Polym. Degrad. Stab.* **2018**, *147*, 1–11. [[CrossRef](#)]
21. Calo, E.; Greco, A.; Maffezzoli, A. Effects of diffusion of a naturally-derived plasticizer from soft PVC. *Polym. Degrad. Stab.* **2011**, *96*, 784–789. [[CrossRef](#)]
22. Hashmi, S.M.; Firoozabadi, A. Self-assembly of resins and asphaltenes facilitates asphaltene dissolution by an organic acid. *J. Colloid Interface Sci.* **2013**, *394*, 115–123. [[CrossRef](#)] [[PubMed](#)]
23. Mangiafico, S.; Di Benedetto, H.; Sauzeat, C. Effect of colloidal structure of bituminous binder blends on linear viscoelastic behaviour of mixtures containing Reclaimed Asphalt Pavement. *Mater. Des.* **2016**, *111*, 126–139. [[CrossRef](#)]
24. ASTM D2172. *Standard Test Methods for Quantitative Extraction of Asphalt Binder from Asphalt Mixtures*; American Society for Testing Materials: West Conshohocken, PA, USA, 2001.
25. ASTM D6307. *Standard Test Method for Asphalt Content of Asphalt Mixture by Ignition Method*; American Society for Testing Materials: West Conshohocken, PA, USA, 2016.
26. Kuang, D.L.; Feng, Z.G.; Yu, J.Y. A New Approach for Evaluating Rejuvenator Diffusing into Aged Bitumen. *J. Wuhan Univ. Technol.* **2011**, *26*, 43–46. [[CrossRef](#)]
27. ASTM D3685. *Standard Method to Test Deformation Resistance by Asphalt Wheel Tracking Test*; American Society for Testing Materials: West Conshohocken, PA, USA, 2001.
28. ASTM D4867. *Standard Test Method for Effect of Moisture on Asphalt Concrete Paving Mixtures*; American Society for Testing Materials: West Conshohocken, PA, USA, 2009.
29. ASTM D1559. *Standard Test Method for Resistance to Plastic Flow of Bituminous Mixtures Using Marshall Apparatus*; American Society for Testing Materials: West Conshohocken, PA, USA, 1982.
30. ASTM D7460-2010. *Standard Test Method for Determining Fatigue Failure of Compacted Asphalt Concrete Subjected to Repeated Flexural Bending*; American Society for Testing Materials: West Conshohocken, PA, USA, 2010.
31. Wu, S.P.; Ye, Q.S.; Li, N. Investigation of rheological and fatigue properties of asphalt mixtures containing polyester fibers. *Constr. Build. Mater.* **2008**, *22*, 2111–2115. [[CrossRef](#)]



© 2018 by the authors. Licensee MDPI, Basel, Switzerland. This article is an open access article distributed under the terms and conditions of the Creative Commons Attribution (CC BY) license (<http://creativecommons.org/licenses/by/4.0/>).

Article

Effect of Rejuvenator Containing Dodecyl Benzene Sulfonic Acid (DBSA) on Physical Properties, Chemical Components, Colloidal Structure and Micro-Morphology of Aged Bitumen

Dongliang Kuang ^{1,*}, Zhou Ye ¹, Lifeng Yang ², Ning Liu ³, Zaihong Lu ⁴ and Huaxin Chen ^{1,*}

¹ Engineering Research Central of Pavement Materials, Ministry of Education, Chang'an University, Xi'an 710064, China; joe_yezhou@163.com

² School of Civil Engineering, Qinghai University, Xining 810016, China; qhyanglifeng@126.com

³ Highway Researching and Designing Institute of Qinghai Province, Xining 810001, China; 1969ln@163.com

⁴ Inner Mongolia Transportation Design Institute Co. LTD., Huhhot 010000, China; luzaihongnm@163.com

* Correspondence: kuangdl@163.com (D.K.); chenhx_paper@163.com (H.C.); Tel.: +86-029-82337246 (H.C.)

Received: 24 July 2018; Accepted: 14 August 2018; Published: 20 August 2018

Abstract: DBSA was used as a solubilizer together with conventional rejuvenator (CR) to produce a solubilized rejuvenator (SR), two kinds of aged bitumen involving TFOT aged bitumen and PAV aged bitumen were obtained by thin film oven test (TFOT) and pressurized aging vessel (PAV), respectively. Effects of CR and SR on the physical properties, chemical components, colloidal structure and micro-morphology of TFOT aged bitumen and PAV aged bitumen were investigated. Testing results of physical properties and chemical components indicated that CR and SR can replenish aged bitumen with necessary aromatics, TFOT aged bitumen that chemical component variation deteriorates its physical properties. With regard to PAV aged bitumen, of which the performance attenuation lies in chemical components variation and colloidal structure transformation, even if the content of CR reached up to 10 wt %, the regenerated bitumen cannot meet the regeneration requirement yet due to its definite influence on colloidal structure transformation, comparatively, sulfonic group in SR can react with the superficial atoms of asphaltenes to reform a solvation layer to facilitate the colloidal structure transformation of PAV aged bitumen, performance and beelike structure of regenerated PAV aged with bitumen with 10 wt % SR were approximated to that of virgin bitumen.

Keywords: aged bitumen; rejuvenator; solubilizer; colloidal structure; micro-morphology

1. Introduction

Bitumen has been widely applied in highway construction due to its excellent pavement performance [1,2]. As an organic binder, bitumen is subjected to aging as a consequence of heat and oxygen during storage, mixing, transportation and paving, as well as service period [3–5], which reduces the performance and service time of asphalt pavement [6,7]. Maintenances and reconstructions are practically necessary for the damaged asphalt pavement to dispose of the premature distresses [8]. In these processes, damaged asphalt pavement is firstly smashed and collected by road milling machine, which will produce huge amounts of reclaimed asphalt pavement (RAP) [9]. For the sake of resource conservation and environmental protection, recycling of RAP is an effective and sustainable technique to cope with the RAP [10]. Compared with virgin asphalt mixture, RAP has lower road performance due to bitumen aging [11], therefore the regenerating of aged bitumen is important for the recycling of RAP [12].

It has been reported in previous studies that aging of bitumen is the main factor resulting in the premature failure of asphalt pavement, which can be explained as following: The chemical components

proportions of bitumen are changed by aging [13,14], namely the asphaltenes content increases and aromatics content declines, which result in the decreasing in penetration and ductility as well as increasing in softening point and viscosity [15].

Aging not only damage the performance, but also affects the colloidal structure involving the type of colloidal structure and compatibility between chemical components. As it is known, the colloidal solution of bitumen is composed of asphaltenes covered by solvation layer acting as the micellar nucleus and malthene acting as the dispersing medium [16]. However, the solvation layer is subjected to be destroyed by aging, and then the asphaltenes will precipitate from the other chemical components [17], coupling with the increment in asphaltenes content induced by aging, the surface of bitumen becomes rough, which can be observed by Atomic Force Microscopy (AFM) [18]. The AFM testing conducted on bitumen indicates that the bitumen exhibits bee-like structure [19], and the dimension of bee-like structures of bitumen as well as the roughness of bitumen surface are increased after aging [20].

The aged bitumen can be classified as mild aged bitumen and severe aged bitumen according to the residual penetration of aged bitumen [21]. For mild aged bitumen, its chemical components variation after aging dominantly influences the performance attenuation of bitumen, thus it can be effectively regenerated by replenishing with necessary amount of aromatics, however, with regard to severe aged bitumen, its performance attenuation is attributed to both chemical components variation and colloidal structure transformation [22], therefore replenishing aromatics and recovering colloidal structure are both necessary for regeneration of severe aged bitumen.

Rejuvenators consisting of high proportion of aromatics have been widely applied for recycling of RAP [23], which can replenish aged bitumen with necessary aromatics, thus it can regenerate mild aged bitumen effectively. However, for severely aged bitumen, of which the colloidal structure has changed, the regeneration effect of rejuvenators including high proportion of aromatics is definite due to its little influence on recovering of colloidal structure [24].

Dodecyl benzene sulfonic acid (DBSA) as a surfactant has been widely used in synthesis of detergent. The sulfonic group in DBSA can react with superficial atoms of removed substance by hydrogen-bond interaction and reform a spatial stability layer to facilitate the dissolving of removed substance [25]. In this paper, the DBSA was used as a solubilizer together with conventional rejuvenator (CR) to produce a solubilized rejuvenator (SR). Effects of DBSA on the physical properties, chemical components, colloidal structure and micro-morphology of different aged bitumen were investigated.

2. Materials and Methods

2.1. Materials

Bitumen, with penetration of 70 grade, was supplied by Shaanxi Guolin Hi-Tech Material Co., Ltd., Xi'an, China, its physical properties and chemical component involving saturates (Sa), aromatics (Ar), resin (Re) and asphaltenes (As), were listed in Table 1. Fluid catalytic cracking slurry (FCC) heated to 100 °C and bitumen with penetration of 70 grade heated to 130 °C was initially blended in an iron container (Shaanxi Jingbo Hi-Tech Co., Ltd., Xi'an, China) for 15 min at a speed of 500 rpm to produce conventional rejuvenator (CR). For preparation of solubilized rejuvenator (SR), 1.5 wt % DBSA by weight of CR heated to 60 °C was added into CR heated to 110 °C and blended for 15 min at a speed of 500 rpm. The physical properties and chemical components of SR and CR are listed in Table 2.

Table 1. Physical properties and chemical components of virgin bitumen.

	Items	Value
Physical properties	Softening point (°C)	45.2
	Penetration (25 °C, dmm)	74
	Ductility (10 °C, cm)	22
	Viscosity (135 °C, cp)	420
Colloidal structure	Penetration index ^a	1.2
Chemical components	Saturates (%)	15.3
	Aromatics (%)	44.6
	Resins (%)	28.8
	Asphaltenes (%)	11.3

^a Penetration index was calculated according to [26].

Table 2. Physical properties and chemical components of SR and CR.

	Items	SR	CR
Physical properties	Flash point (°C)	>220	>220
	Viscosity (60 °C, Pa·s)	0.95	1.52
	Viscosity ratio after TFOT	1.7	2.1
	Weight loss after TFOT (%)	−1.5	−2.2
Chemical components	Saturates (%)	13.3	12.5
	Aromatics (%)	62.7	64.2
	Resins (%)	17.3	15.4
	Asphaltenes (%)	6.7	7.9

2.2. Preparation of Aged Bitumen

Two aged bitumens were obtained by thin film oven test (TFOT, aging at 163 °C for 5 h according to [27] and pressurized aging vessel (Prentex, San Francisco, CA, USA) (PAV, aging at 100 °C for 20 h under 2.1 MPa of air according to [28], respectively. The TFOT was employed to simulate the short-term aging including storage, transport, mixing and paving process of the bitumen, whereas the PAV was used to simulate the long-term aging of the bitumen in service period. The aged bitumen prepared by TFOT and PAV were denoted as TA and PA respectively.

2.3. Preparation of Regenerated Bitumen

SR (or CR) heated to 110 °C was firstly added into aged bitumen heated to 150 °C, and the blended at 150 °C with a speed of 500 rpm for 30 min to prepare regenerated bitumen, the content of SR (or CR) were 2, 4, 6, 8 and 10 wt % by weight of aged bitumen. The regenerated TA containing SR and CR were denoted as SR-TA and CR-TA respectively; and the regenerated PA containing SR and CR were denoted as SR-PA and CR-PA respectively.

2.4. Physical Properties Testing

Physical properties of virgin, aged, and regenerated bitumen, including softening point, penetration at 25 °C, ductility at 15 °C, and viscosity at 135 °C were tested according to the methods in [29], [30], [26] and [31], respectively.

2.5. Chemical Components Testing

Bitumen was dissolved in n-heptane (Shaanxi Jingbo Hi-Tech Co., Ltd., Xi'an, China), asphaltenes was firstly separated according to [32] and its content was determined. Residual n-heptane was evaporated and the residues were dissolved in toluene (Shaanxi Jingbo Hi-Tech Co., Ltd., Xi'an, China) to form a solution of 2% (w/v), then 1 µL sample solution was spotted on chromarods using a spotter.

Afterwards, the chromarods were expanded in n-heptane and toluene respectively. The contents of saturates, aromatics and resins were determined using Iatrosan MK-6 analyzer (Iatro Laboratories Inc., Tokyo, Japan).

2.6. Colloidal Structure Characterization

The colloidal structure can be characterized by Penetration Index (PI) [26] and Colloidal Stability Index (CSI) [24]. The CSI and PI are used for characterization of colloidal structure type and colloidal structure stability, respectively.

With respect to the PI of less than -2 , -2 to 2 and more than 2 , the corresponding colloidal structure of bitumen are Sol, Sol-Gel and Gel respectively [16]. The PI of virgin, aged, and regenerated bitumen were calculated according to [26] in this paper.

The CSI calculated based on the chemical components testing [24], is adapted to characterize the stability of colloidal structure of regenerated bitumen in this paper, the more the CSI of regenerated bitumen approximates that of virgin bitumen, the more the aged bitumen is regenerated. For obtaining the CSI, the chemical components of the samples were determined according to the methods mentioned in 2.5, and then the CSI were calculated according to the following equation:

$$CSI = \frac{ArC + ReC}{AsC + SaC} \quad (1)$$

where the ArC , ReC , AsC and SaC are the contents of aromatics, resin, asphaltenes and saturates, respectively.

2.7. Micro-Morphology Characterization

Atomic force microscopy (AFM) (BRUKER, New York, NY, USA) that is capable of measuring topographic features at nanometer-scale or even at atomic-scale resolution allows one to visualize precise details of surface topography of bitumen without special sample preparation [33]. In this paper, the AFM imaging was applied to characterize the microstructure of bitumen.

To obtain the samples for AFM observation, 1~1.5 g bitumen heated to $150\text{ }^{\circ}\text{C}$ was laid on a steel disk with the size of $10\text{ mm} \times 10\text{ mm} \times 1\text{ mm}$, and then self-cooled to ambient temperature (about $25\text{ }^{\circ}\text{C}$). All samples were stored in a container with a glass cap to prevent dust pick-up. The AFM images were observed after the samples were annealed for a minimum of 24 h. The topographic images were scanned in tapping mode with an etched silicon probe. The cantilever was $125\text{ }\mu\text{m}$ long with the curvature radius of 5–10 nm. The drive frequency and amplitude were 260 kHz and 56 mW, respectively. The scan rate was 0.8 Hz. The AFM images showed a $15\text{ }\mu\text{m} \times 15\text{ }\mu\text{m}$ region.

3. Results and Discussions

3.1. Characterization of TA and PA

Table 3 summaries the physical properties and chemical components of the TA and PA. Compared with virgin bitumen, the aged bitumen TA and PA exhibit lower penetration, ductility and aromatics content, but higher softening point, viscosity and asphaltenes content, which coincides with the results in previous studies.

It can be also observed from Table 3 that the PI of TA and PA are 1.7 and 3.5, indicate that the colloidal structure of TA and PA are Sol-Gel and Gel respectively, which manifests that the PAV aging influences the bitumen more severely and leads to colloidal structure transformation.

Table 3. Physical properties and chemical components of TA and PA.

	Items	TA	PA
Physical properties	Softening point (°C)	53.2	59.7
	Penetration (25 °C, dmm)	40	28
	Ductility (10 °C, cm)	7.8	3.2
	Viscosity (135 °C, cp)	630	2050
Colloidal structure	Penetration index	1.7	3.5
Chemical components	Saturates (%)	14.5	12.4
	Aromatics (%)	37.3	29.6
	Resins (%)	26.2	24.6
	Asphaltenes (%)	22.0	33.4

3.2. Physical Properties of Regenerated Bitumen

Figure 1a–d reveal the physical properties of regenerated TA and PA with different contents of CR and SR. It can be observed from the figure that the addition of CR and SR increases the penetration and ductility while decreases the softening point and viscosity.

Compared with CR, SR has more significant influence on the regeneration of aged bitumen. As the most important property of neat bitumen, the penetration of aged bitumen enhances rapidly with the increasing in SR content, comparatively, the influence of the CR content is more moderate. It can be seen from Figure 1a that the regenerated PA with 8 wt % SR owns a penetration of 62 dmm, which meets the requirement of regeneration, whereas the penetration of regenerated PA with 8 wt % CR is only 52 dmm, which is far from the requirement of regeneration. With continuous increasing in contents of SR and CR, the regenerated PA with 10 wt % SR owns a penetration of 72 dmm which is close to that of virgin bitumen, whereas the regenerated PA containing 10 wt % CR merely owns a penetration of 61 dmm which is merely 80 % of virgin bitumen.

The changing of ductility is similar to that of penetration, as shown in Figure 1b, the ductility increases linearly with the increasing in rejuvenator content, and the ductility of regenerated bitumen with SR is higher than that of regenerated bitumen with CR, the ductility of regenerated PA with 10 wt % SR can be extended from 3.2 cm to 20 cm, which is approximate that of virgin bitumen, whereas the value is 16 cm for regenerated PA with 10 wt % CR.

The softening point and viscosity show an opposite changing to that of penetration and ductility with the addition of rejuvenator. The softening point and viscosity are decreased with the increasing in rejuvenator content. As shown by Figure 1c,d, the SR also influences the softening point and viscosity more significantly than CR, regenerated bitumen with SR shows lower softening point and viscosity than regenerated bitumen with CR at the same rejuvenator content.

It can be also found from Figure 1 that 8 wt % CR and SR can effectively regenerate the physical properties of TA to satisfy the regeneration requirement. With regard to PA, the necessary content of SR for regenerating PA to satisfy the regeneration requirement is 10 wt %, but even if the content of CR reaches up to 10 wt %, the physical properties of PA cannot meet the regeneration requirement.

The result can be ascribed to that CR merely owns high proportion of aromatics, it can only regenerate aged bitumen by replenishing aromatics but can hardly restore the colloidal structure, therefore CR can effectively regenerate TA which maintains the same colloidal structure as virgin bitumen, whereas with regard to PA, its colloidal structure has transformed from Sol-Gel to Gel, thus CR cannot effectively regenerate the physical properties of PA due to its definite influence on colloidal structure restoration. Compared with CR, SR contains both high proportion of aromatics and sulfonic group, it can replenishing PA with necessary aromatics and react with the superficial atoms of asphaltenes to reform the solvation layer covering the surface of asphaltenes, which facilitates gathered asphaltenes stably disperse in colloidal solution at a smaller size and contributes the colloidal structure restoration of PA, therefore SR can regenerate PA more effectively than CR.

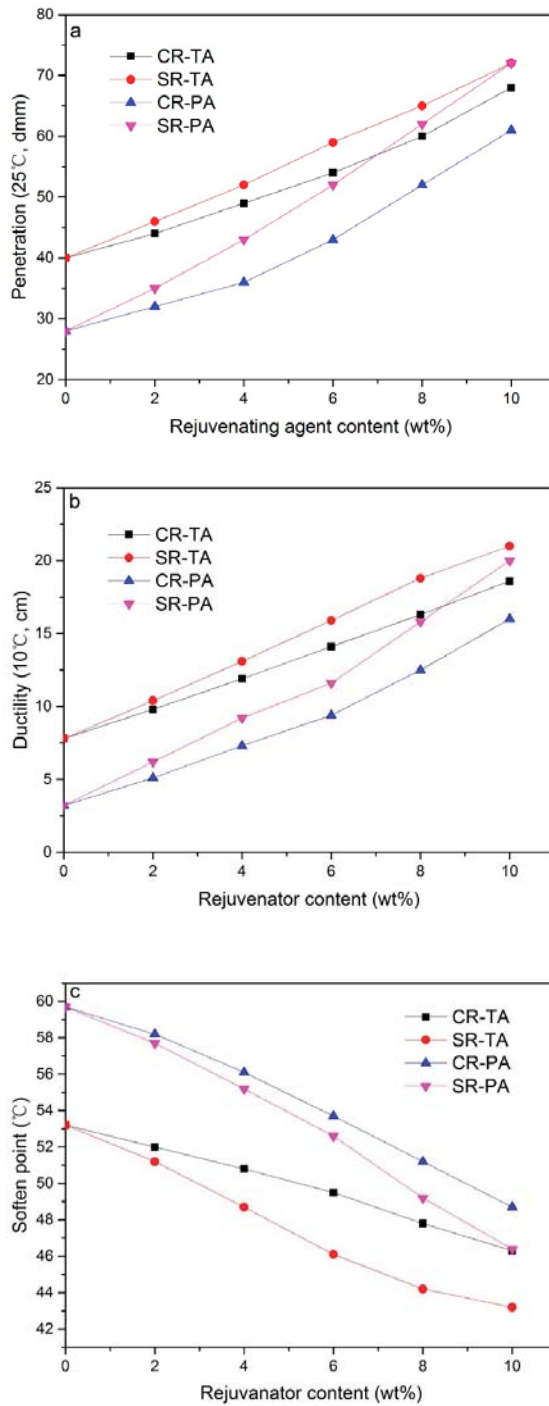


Figure 1. Cont.

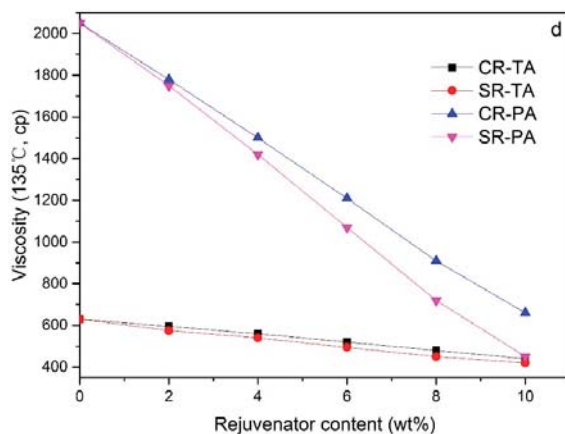


Figure 1. Physical properties of regenerated bitumen with different rejuvenators: (a) penetration, (b) ductility, (c) softening point, (d) viscosity.

3.3. Chemical Components of Regenerated Bitumen

Tables 4 and 5 show the chemical components of regenerated bitumen containing different contents of CR and SR. It can be found from that the Tables that with the increasing in contents of CR and SR, the aromatics content of regenerated asphaltens increases, whereas the asphaltens content declines, compared with relatively regular changing of aromatics content and asphaltens content, the resins content and saturates contents changed unregularly with the increasing in rejuvenator contents.

It can be found from Tables 4 and 5 that the chemical components of regenerated bitumen containing SR and CR are similar at the same rejuvenator content, which indicates that the SR and CR influence the chemical components reconstitution of TA and PA similarly.

Table 4. Chemical components of regenerated TA containing CR and SR.

Samples	Rejuvenator Content (wt %)	Weight of Chemical Components (wt %)			
		Sa	Ar	Re	As
CR-TA	0	14.5	37.3	26.2	22
	2	14.2	38.5	25.8	21.5
	4	14.4	38.9	26	20.7
	6	14.6	39.7	25.9	19.8
	8	15.4	40.7	25.5	18.4
	10	15.2	41.7	25.6	17.5
SR-TA	0	14.5	37.3	26.2	22
	2	14.1	38.1	26.5	21.3
	4	14.5	40.4	24.7	20.4
	6	14.2	41.9	24.7	19.2
	8	14.4	42.3	24.4	18.9
	10	14.1	43.5	25.1	17.3

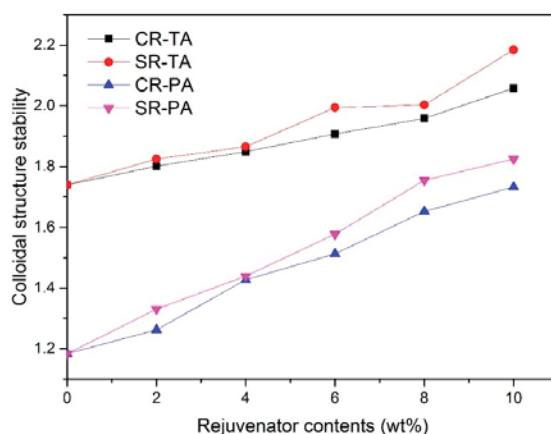
Table 5. Chemical components of regenerated PA containing CR and SR.

Samples	Rejuvenator Content (wt %)	Weight of Chemical Components (wt %)			
		Sa	Ar	Re	As
CR-PA	0	12.4	29.6	24.6	33.4
	2	11.8	31.3	24.5	32.4
	4	12.6	34.6	24.2	28.6
	6	12.5	36.4	23.8	27.3
	8	12.5	38.2	24.1	25.2
	10	13.1	40	23.4	23.5
SR-PA	0	12.4	29.6	24.6	33.4
	2	11.7	31.3	25.8	31.2
	4	11.4	33.7	25.3	29.6
	6	12.5	37.9	23.3	26.3
	8	12.2	39.8	23.9	24.1
	10	12.9	41	23.6	22.5

3.4. Colloidal Structure Stability of Regenerated Bitumen

Aging changes the chemical components of bitumen, and then negatively influence the compatibility between chemical components, which declines the colloidal structure stability of bitumen, therefore the regeneration effect of rejuvenator on aged bitumen can be investigated by characterization of colloidal structure stability index (CSI).

Figure 2 reveals the CSI of regenerated bitumen with different contents of CR and SR. It can be observed from Figure 2 that, the CSI of regenerated bitumen increase with the addition of rejuvenator, which indicates that the colloidal structure stability of aged bitumen can be improved by rejuvenator.

**Figure 2.** CSI of regenerated bitumen with different rejuvenators.

As described by Figure 2, regenerated bitumen containing SR displays high CSI than regenerated bitumen containing CR at the same rejuvenator content, for instance, 10 wt % SR and CR can regenerate the CSI of TA by increasing from 1.74 for TA to 2.03 and 2.27, respectively, which indicates that SR can enhance the CSI of aged bitumen more significantly than CR.

The result mentioned above can be explained as following: The CR contain high proportion of aromatics and low proportion of resins and asphaltenes (presented in Table 2), it can only improve the colloidal structure stability by replenishing aromatics to dilute content of asphaltenes, comparatively, the SR contains both high proportion of aromatics and active sulfonic group, it can on the one hand

replenish aromatics to reconstitute the chemical components of aged bitumen, and on the other hand can reform the solvation layer covering the surface of asphaltenes by sulfonic group reacting with the superficial atoms of asphaltenes in aged bitumen, therefore SR can improve the colloidal structure stability more effectively than CR.

3.5. Colloidal Structure Type of Regenerated Bitumen

Figure 3 shows the PI of regenerated bitumen with different contents of CR and SR. It can be observed from Figure 3 that the PI of regenerated bitumen declines with the addition of rejuvenator, as illustrated in Figure 3, 10 wt % SR and CR can decrease the PI from 2.8 for TA to 1.5 and 1.8, indicating that the colloidal structure of TA has transformed from Gel to Sol-Gel, which implies that both CR and SR equally influence the regeneration of TA, this result is coincident with the physical properties results of regenerated TA containing SR and CR.

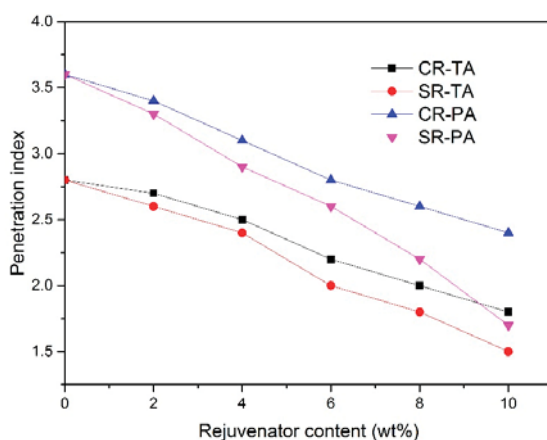


Figure 3. PI of regenerated bitumen with different rejuvenators.

It can be also observed from Figure 3 that the PI of regenerated PA containing SR is lower than that of regenerated PA containing CR at the same rejuvenator content, for example, 10 wt % SR can decrease the PI from 3.6 for PA to 1.7, indicating that the colloidal structure of regenerated PA containing 10 wt % SR has transformed from Gel to Sol-Gel, nevertheless the PI for regenerated PA containing 10 wt % CR is 2.4, indicating that the regenerated PA containing 10 wt % CR maintains Gel structure.

The result can be also ascribed to the chemical interaction between asphaltenes and SR. The active sulfonic group in SR can react with the superficial atoms of asphaltenes in PA, and then a solvation layer forms and covers on the surfaces of asphaltenes, which facilitate the asphaltenes to be uniformly re-dispersed in colloidal solution and contributes to the colloidal structure transformation from Gel to Sol-Gel. Compared with SR, CR can only replenish PA with aromatics, which can barely facilitate the colloidal structure transformation of PA, thus the regenerated PA maintains a colloidal structure of Gel even if the CR content reaches up to 10 wt %.

3.6. AFM Characterization

The bitumen displays a bee-like structure which can be observed by AFM images, and the dimension of the bee-like structures is increased with the asphaltenes precipitating from the other chemical components. As is known, the colloidal structure is subjected to be damaged by aging, which results in the asphaltenes precipitating from the other chemical components and increasing in dimension of the bee-like structures.

It can be inferred from the physical properties testing results in this paper that the SR can reconstitute the colloidal structure more effectively than CR, which was confirmed by penetration index testing results. In an effort to further assess the effect of CR and SR on colloidal structure restoration of different aged bitumen, AFM testing was performed on at multiple locations across the virgin bitumen, aged bitumen and regenerated bitumen.

Figure 4a–c show the surface micro-morphology of virgin bitumen, TFOT aged bitumen and PAV aged bitumen. It can be observed from Figure 4a that the surface of virgin bitumen is even and only a little bee-like structure is existed. However, the surface becomes rough after aging, which can be attributed to the damage of colloidal structure caused by aging, as shown in Figure 4b,c. In comparison with TFOT aged bitumen, PAV aged bitumen shows a rougher surface than TFOT aged bitumen, indicating that PAV aging damages the colloidal structure of virgin bitumen more severely than TFOT aging.

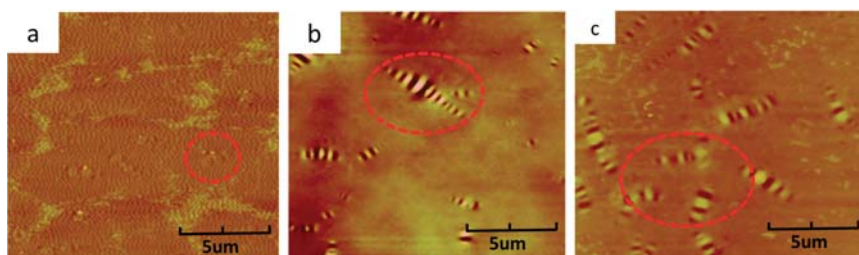


Figure 4. AFM images of virgin bitumen, TFOT aged bitumen and PAV aged bitumen: (a) virgin bitumen, (b) TFOT aged bitumen, (c) PAV aged bitumen.

The surface micro-morphology of regenerated TFOT aged bitumen by 10 wt % CR and SR is described in Figure 5a,b. It can be seen from Figure 5 that the surface of TFOT aged bitumen becomes smooth with introduction of 10 wt % CR and SR. Besides, it can be also observed that the surface micro-morphology of regenerated TFOT aged bitumen by 10 wt % CR share similarities with that of regenerated TFOT aged bitumen by 10 wt % SR, indicating that CR reconstitutes the colloidal structure of TFOT aged bitumen equally to SR, which is consistent with the physical properties and penetration index testing results of regenerated TFOT aged bitumen containing CR and SR.

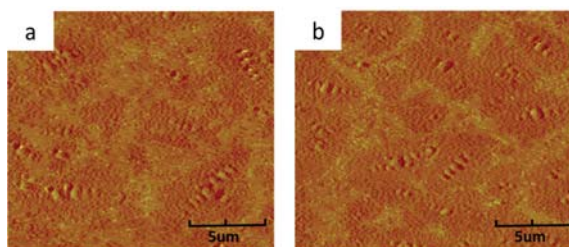


Figure 5. AFM images of regenerated TFOT aged bitumen: (a) regenerated TFOT aged bitumen with 10 wt % CR, (b) regenerated TFOT aged bitumen with 10 wt % SR.

Figure 6a,b demonstrate the micro-morphology of regenerated PAV aged bitumen by 10 wt % CR and SR. It can be found by comparing Figures 6a and 4c that, the regenerated PAV aged bitumen by 10 wt % CR maintains nearly the same surface micro-morphology as PAV aged bitumen, indicating that the CR can barely decrease the dimension of bee-like structure, however, the surface micro-morphology of regenerated PAV aged bitumen by 10 wt % SR shows similarities with that of virgin bitumen before

aging, indicating that the SR can effectively facilitate the re-dispersion of asphaltenes of PAV aged bitumen, which contributes to the colloidal structure restoration of PAV aged bitumen and performance improvement, this results is also in good agreement with the physical properties and penetration index testing results of regenerated PAV aged bitumen containing CR and SR.

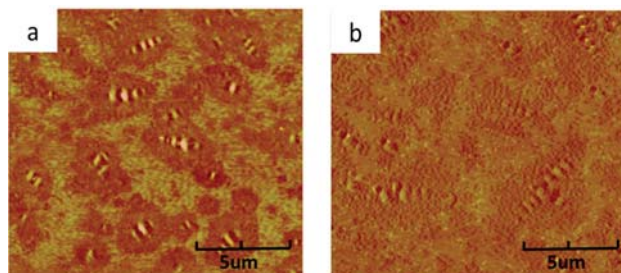


Figure 6. AFM images of regenerated PAV aged bitumen: (a) regenerated PAV aged bitumen with 10 wt % CR, (b) regenerated PAV aged bitumen with 10 wt % SR.

4. Conclusions

DBSA was adopted as a solubilizer together with conventional rejuvenator (CR) to produce a solubilized rejuvenator (SR). Effect of SR and CR on the physical properties, colloidal structure and micro-morphology of TFOT aged bitumen and PAV aged bitumen were investigated. The conclusions were as follows:

1. CR and SR influenced the chemical components of TFOT aged bitumen and PAV aged bitumen similarly, thus for TFOT aged bitumen that its physical properties attenuation were mainly attributed to the chemical component variation, can be effectively regenerated by 8 wt % of CR and SR. The physical properties of regenerated TFOT aged bitumen with 8 wt % of CR and SR can approximate to that of virgin bitumen before aging.

2. SR can replenish PAV aged bitumen with necessary amounts of aromatics and reconstitute the micellar nucleus dispersion in colloidal structure of PAV aged bitumen simultaneously, thus the physical properties of PAV aged bitumen can be recovered to the condition of virgin bitumen by 10 wt % of SR, comparatively, CR can barely influence the colloidal structure transformation of PAV aged bitumen, therefore the physical properties of PAV aged bitumen with 10 wt % of CR cannot meet the regeneration requirement yet.

3. The sulfonic group in DBSA can react with superficial atoms of asphaltenes to reform a solvation layer covering on the surface of asphaltenes, which contributes to colloidal structure transformation of aged bitumen, therefore PAV aged bitumen can be recovered from Gel to Sol-Gel by 10 wt % SR, and the dimension of beelike structure formed by asphaltenes can be approximate that of virgin bitumen.

Further research is required to confirm practical application and possibilities of DBSA incorporating with conventional rejuvenator road construction as well as the difference of regenerating effect on aged bitumen compared to conventional rejuvenator. For example, the road performance of recycled hot mix asphalt containing CR and SR as well as some other rejuvenators should be comparatively investigated.

Author Contributions: D.K. and H.C. conceived and designed the experiments; Z.Y. performed the experiments; L.Y. and Z.L. analyzed the data; N.L. contributed materials; D.K. wrote the paper.

Funding: This research was funded by [the project of Science and Technology of Qinghai Province] grant number [Nos. 2018-ZJ-760, 2018-SF-111 and 2018-SF-139], [projects of Transportation Department of Inner Mongolia Autonomous Region] grant number [Nos. NJ-2016-7 and NJ-2017-15], and [the Fund for Basic Scientific Research of Central Colleges of Chang'an University] grant number [Nos. 310831171015, 300102318401 and 300102318501].

Conflicts of Interest: The authors declare no conflicts of interest.

References

1. Elkashef, M.; Williams, R.; Cochran, E. Physical and chemical characterization of rejuvenated reclaimed asphalt pavement (RAP) binders using rheology testing and pyrolysis gas chromatography-mass spectrometry. *Mater. Struct.* **2018**, *51*, 11–19. [[CrossRef](#)]
2. Zhang, K.; Muhunthan, B. Effects of production stages on blending and mechanical properties of asphalt mixtures with reclaimed asphalt pavement. *Constr. Build. Mater.* **2017**, *149*, 679–689. [[CrossRef](#)]
3. Gao, L.; Li, H.; Xie, J.; Yu, Z. Evaluation of pavement performance for reclaimed asphalt materials in different layers. *Constr. Build. Mater.* **2018**, *159*, 561–566. [[CrossRef](#)]
4. Vegazamanillo, A.; Calzadaperez, M.; Lastragonzalez, P.; Indacocheavega, I.; Fernandezortega, J.A. Analysis of the use of cupola furnace slags, green sand and reclaimed asphalt pavement in asphalt concrete mixtures for low intensity traffic. *Revista de la Construcción* **2017**, *16*, 229–237. [[CrossRef](#)]
5. Chen, M.; Leng, B.; Wu, S.; Sang, Y. Physical, chemical and rheological properties of waste edible vegetable oil rejuvenated asphalt binders. *Constr. Build. Mater.* **2014**, *66*, 286–298. [[CrossRef](#)]
6. Shu, X.; Huang, B.; Vukosavljevic, D. Laboratory evaluation of fatigue characteristics of recycled asphalt mixture. *Constr. Build. Mater.* **2008**, *7*, 1323–1330. [[CrossRef](#)]
7. Sivilevicius, H.; Braziunas, J.; Prentkovskis, O. Technologies and principles of hot recycling and investigation of preheated reclaimed asphalt pavement batching process in an asphalt mixing plant. *Appl. Sci.* **2017**, *7*, 1104. [[CrossRef](#)]
8. Vislavicius, K.; Sivilevicius, H. Effect of reclaimed asphalt pavement gradation variation on the homogeneity of recycled hot-mix asphalt. *Arch. Civ. Mech. Eng.* **2013**, *13*, 345–363. [[CrossRef](#)]
9. Xu, J.; Hao, P.; Zhang, D.; Yuan, G. Investigation of reclaimed asphalt pavement blending efficiency based on micro-mechanical properties of layered asphalt binders. *Constr. Build. Mater.* **2018**, *163*, 390–401. [[CrossRef](#)]
10. Xiao, Y.; Li, C.; Wan, M.; Zhou, X.; Wang, Y.; Wu, S. Study of the diffusion of rejuvenators and its effect on aged bitumen binder. *Appl. Sci.* **2017**, *7*, 397. [[CrossRef](#)]
11. Arshad, M.; Ahmed, M. Potential use of reclaimed asphalt pavement and recycled concrete aggregate in base/subbase layers of flexible pavements. *Constr. Build. Mater.* **2017**, *151*, 83–97. [[CrossRef](#)]
12. Yang, S.; Lee, L. Characterizing the chemical and rheological properties of severely aged reclaimed asphalt pavement materials with high recycling rate. *Constr. Build. Mater.* **2016**, *111*, 139–146. [[CrossRef](#)]
13. Kuang, D.; Feng, Z.; Yu, J. A new approach for evaluating rejuvenator diffusing into aged bitumen. *J. Wuhan Univ. Technol.* **2011**, *26*, 43–46. [[CrossRef](#)]
14. Cavalli, M.; Zauamanis, M.; Mazza, E.; Partl, M.; Poulikakos, L. Effect of ageing on the mechanical and chemical properties of binder from RAP treated with bio-based rejuvenators. *Compos. Part B* **2018**, *141*, 174–181. [[CrossRef](#)]
15. Gamarra, A.; Ossa, E. Thermo-oxidative aging of bitumen. *Int. J. Pavement Eng.* **2018**, *19*, 641–650. [[CrossRef](#)]
16. Mangiafico, S.; Benedetto, H.; Sauzeat, C.; Olard, F.; Pouget, S.; Planque, L. Effect of colloidal structure of bituminous binder blends on linear viscoelastic behaviour of mixtures containing reclaimed asphalt pavement. *Mater. Des.* **2016**, *111*, 126–139. [[CrossRef](#)]
17. Zhang, H.; Wang, H.; Yu, J. Effect of aging on morphology of organo-montmorillonite modified bitumen by atomic force microscopy. *J. Microsc.* **2011**, *242*, 37–45. [[CrossRef](#)] [[PubMed](#)]
18. Jahromi, S.; Khodaii, A. Effects of nanoclay on rheological properties of bitumen binder. *Constr. Build. Mater.* **2009**, *23*, 2894–2904. [[CrossRef](#)]
19. Loeber, L.; Sutton, O.; Morel, J.; Valleton, J.; Muller, G. New direct observations of asphalts and asphalt binder by scanning electron microscopy and atomic force microscopy. *J. Microsc.* **2010**, *182*, 32–39. [[CrossRef](#)]
20. Baumgardner, G.; Masson, J.; Hardee, J.; Menapace, A.; Williams, A. Polyphosphoric acid modified asphalt: Proposed mechanisms. *J. Assoc. Asph. Paving Technol.* **2006**, *74*, 283–305.
21. Kuang, D.; Yu, J.; Cai, Z. Effect of rejuvenator on rejuvenation properties of aged bitumen of different aging degree. *Highway* **2011**, *5*, 153–157.
22. Lee, S.; Amirkhanian, S.; Park, N.; Kim, K. Characterization of warm mix asphalt binder containing artificially long-term aged binders. *Constr. Build. Mater.* **2007**, *23*, 2371–2379. [[CrossRef](#)]
23. Shen, J.; Amirkhanian, S.; Miller, J. Effects of rejuvenating agents on superpave mixtures containing reclaimed asphalt pavement. *J. Mater. Civ. Eng.* **2007**, *19*, 376–384. [[CrossRef](#)]


24. Kuang, D. Preparation of diffusible rejuvenator and its influence on performances of recycled bitumen and recycled asphalt mixture. Ph.D. Thesis, Wuhan University of Technology, Wuhan, China, 28 June 2012.
25. Zargar, G.; Gheysari, R.; Takassi, M.; Rostami, A.; Zadehnazari, A. Evaluation of a sulfanilic acid based surfactant in crude oil demulsification: An experimental study. *Oil Gas Sci. Technol.* **2018**, *73*, 176–182. [[CrossRef](#)]
26. ASTM D 5. *Standard Test Method for Penetration of Bituminous Materials*; American Society for Testing Materials: West Conshohocken, PA, USA, 2005.
27. ASTM D 1754. *Standard Test Method for Effects of Heat and Air on Asphaltic Materials*; American Society for Testing Materials: West Conshohocken, PA, USA, 2014.
28. ASTM D 6521. *Standard Practice for Accelerated Aging of Asphalt Binder Using a Pressurized Aging Vessel Lpar*; American Society for Testing Materials: West Conshohocken, PA, USA, 2013.
29. ASTM D 36. *Standard Test Method for Softening Point of Bitumen*; American Society for Testing Materials: West Conshohocken, PA, USA, 2006.
30. ASTM D 113. *Standard Test Method for Ductility of Bituminous Materials*; American Society for Testing Materials: West Conshohocken, PA, USA, 2016.
31. ASTM D 113. *Standard Test Method for Viscosity Determination of Asphalt at Elevated Temperatures Using a Rotational Viscometer*; American Society for Testing Materials: West Conshohocken, PA, USA, 2012.
32. ASTM D 4124. *Standard Test Method for Separation of Asphalt into Four Fractions*; American Society for Testing Materials: West Conshohocken, PA, USA, 2018.
33. Yu, X.; Burnham, N.; Tao, M. Surface microstructure of bitumen characterized by atomic force microscopy. *Adv. Colloid Interface Sci.* **2015**, *218*, 17–33. [[CrossRef](#)] [[PubMed](#)]



© 2018 by the authors. Licensee MDPI, Basel, Switzerland. This article is an open access article distributed under the terms and conditions of the Creative Commons Attribution (CC BY) license (<http://creativecommons.org/licenses/by/4.0/>).

Article

Evaluation of Thermal-Mechanical Properties of Bio-Oil Regenerated Aged Asphalt

Tianyuan Yang ^{1,*}, Meizhu Chen ¹, Xinxing Zhou ²  and Jun Xie ^{1,*}

¹ State Key Laboratory of Silicate Materials for Architectures, Wuhan University of Technology, Wuhan 430070, China; chenmzh@whut.edu.cn

² Key Laboratory of Highway Construction and Maintenance Technology in Loess Region of the Ministry of Transport, Shanxi Transportation Research Institute, Taiyuan 030006, China; zxx09432338@whut.edu.cn

* Correspondence: yangty2017@whut.edu.cn (T.Y.); xiejun3970@whut.edu.cn (J.X.)

Received: 9 October 2018; Accepted: 5 November 2018; Published: 8 November 2018

Abstract: Different proportions of bio-oil (5, 10, 15, and 20 wt%) were added into aged asphalt for its regeneration. Molecular dynamic simulations were used to measure the thermal and mechanical performances of bio-oil regenerated aged asphalt (BRAA). A new, simplified BRAA model was built to calculate the specific heat capacity, thermal expansion coefficient, elastic constant, shear modulus, bulk modulus, and Young's modulus. Simulation results showed that the thermal expansion coefficient (CTE α) of asphalt at 298 K decreased by 10% after aging. Bio-oil of 5 wt% could make the CTE α restore to the original level of base asphalt, while the addition of bio-oil would further decrease the specific heat capacity of aged asphalt. The shear modulus (G), Young's modulus (K) and bulk modulus (E) of asphalt increased after aging and decreased with the increasing amount of bio-oil. According to the calculated E/G value, the ductility of aged asphalt increased by 6.0% with the addition of 10 wt% bio-oil, while over 15 wt% bio-oil would make the ductility of BRAA decrease. In summary, the regeneration effects of bio-oil to the thermal expansion coefficient, flexibility, and ductility of aged asphalt had been proven, while excessive bio-oil would decrease the thermal stability of asphalt.

Keywords: thermal–mechanical properties; bio-oil; regeneration; aged asphalt; molecular dynamic simulation

1. Introduction

Asphalt mixture is a common pavement material. It provides a comfortable driving environment for vehicles. However, the pavement performance of asphalt mixture constantly decreases during service process. One of the key reasons is that asphalt, as a binder, is gradually aging under the influence of oxygen and ultraviolet [1–3]. In order to recycle and reuse the aged asphalt, a considerable amount of research has been done on the regeneration of aged asphalt. In 1915, asphalt recycling technology was first explored by American Warren Bother who reused the aged asphalt by heating waste asphalt mixture [4]. After 1956, due to the initial formation of the US domestic high-grade road network, the price of petroleum crude oil rose rapidly [5]. During the period from 1970 to 1989, the global oil crisis occurred and crude oil price continued to rise. The cost of new asphalt pavement increased greatly, thus, people paid more attention to asphalt recycling technology. Regarding the recycling mechanism of aged asphalt, the regeneration of aged asphalt can be considered as the reverse process of asphalt aging. By means of adding specific substances, the composition of asphalt is adjusted to reverse its performance and return to an appropriate state that can be reused [6–8]. Not only rheological properties but also changes in structure were considered as the indicators for the evaluation of asphalt regeneration effect. More testing methods, such as NMR, were used to investigate the additive's effects on aged asphalt [9].

Bio-oil is extracted from waste wood under 500 °C through thermal pyrolysis [10–12]. It has been a recently considered modifier applied to asphalt [13,14]. The main ingredient of bio-oil is close to petroleum asphalt, which makes bio-oil compatible with asphalt. Extensive research has been done to investigate the properties of bio-oil modified asphalt [15–17]. Williams [18] studied the physical and chemical properties of bio-oil and the physico-chemical behavior during thermal cracking. Yang [19] prepared the bio-oil modified asphalt and evaluated its properties. Guarin [20] investigated the rheological and chemical characterization of bio-oil modified asphalt and compared effects of several bio-oil materials in modification. The indices of viscosity, rutting and fatigue factors of bio-asphalt were investigated [21] and the optimal bio-asphalt production process was eventually determined by orthogonal experimental method. It has been proven that bio-oil could improve the diffusion and rheological properties of asphalt. Although research has been done with respects to the rheological, chemical or constructional properties of bio-asphalt [22,23], there is little in the way of literature introducing the regeneration effect of bio-oil recycled aged asphalt.

In this research, bio-oil was added into aged asphalt. Thermal-mechanical properties were studied to evaluate its rejuvenating effects on aged asphalt by means of molecular dynamics (MD) simulation. MD is a computer simulation method used to study the physical motion of atoms and molecules. Atoms and molecules are allowed to interact for a fixed period of time, so that the dynamic evolution of the system can be seen. In the most common version, the trajectories of atoms and molecules are determined by numerically solving Newton's equations of motion for a system of interacting particles, where the forces between the particles and their potential energies are usually calculated using the inter-atomic potential or the molecular mechanics field. This method was originally developed in the field of theoretical physics in the late 1950s [24,25], but is now mainly used in chemical physics, materials science, and bio-molecules modeling. Molecular models and simulation techniques can be used to study the interaction between asphaltenes, resins, saturates, and aromatics in asphalt, and to analyze the relationship between composition, structure, and performance [26–28]. Computers are used to calculate the model, predict the performance of the asphalt, and guide the design of the asphalt material. The molecular model of asphalt is divided into three categories: (1) One-component asphalt model; (2) three-component model (asphaltenes, soft asphalt, and resins) [29–31]; (3) four-component model (asphaltenes, aromatics, resins, and saturates) [32]. The physical properties, rheological properties, thermodynamic properties, and dissolution properties of asphalt can be predicted, in order to guide asphalt production.

In this research, molecular models of base asphalt, aged asphalt, and bio-oil regenerated aged asphalt (BRAA) were constructed. These models were simulated in a range of temperature. After that, the thermal-mechanical properties, including thermal expansion coefficient, heat capacity, elastic constant, shear modulus, Young's modulus, and bulk modulus were calculated. Among these properties, the thermal expansion coefficient and heat capacity reflect the performance of the asphalt during heating, which both determine the applicable temperature of the asphalt. The moduli affect the mechanical performances of asphalt, related to its resistance to damage.

2. Molecular Models and Methods

2.1. Modeling and Simulations Details

The components of asphalt include four main classes of fractions: Asphaltenes, resins, saturates and, aromatics. Asphaltenes consist of high molecular weight phenols and heterocyclic compounds. Resins consist of high molecular weight phenols and carboxylic acids produced by partial oxidation of the material. Saturates correlate with softening point of asphalt. Aromatics consist of partially hydrogenated polycyclic aromatic compounds. In Figure 1, the molecules were selected to represent asphaltenes, resins, saturates, and aromatics to construct the asphalt model. Moreover, the aged asphalt was selected by aging 50 h [33,34].

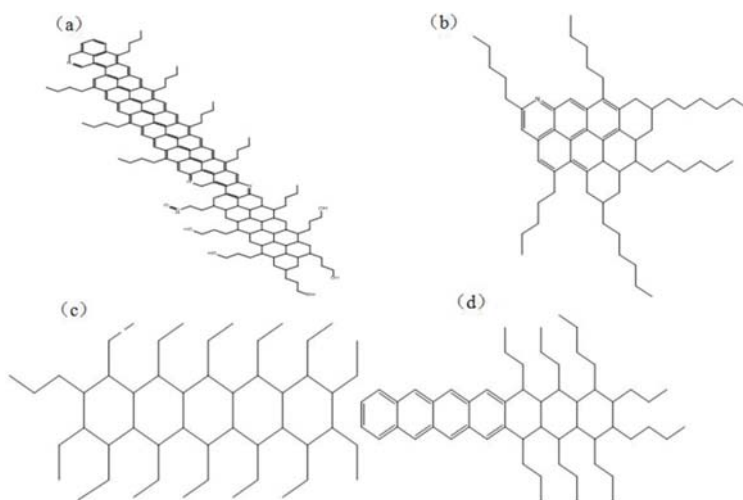


Figure 1. Components of asphalt: (a) asphaltenes; (b) resins; (c) saturates; (d) aromatics.

The main components of bio-oil extracted from waste wood were acetic acid, 1-carboxy-2-propanone, and methanol [35]. Bio-oil was mixed with aged asphalt to prepare BRAA by the mass fraction of 5%, 10%, 15%, and 20% to asphalt, respectively. Finally, six asphalt systems were obtained. Their compositions are shown in Table 1.

Table 1. Components of asphalt systems.

	Saturates	Aromatics	Resins	Asphaltenes	Acetic Acid	1-Carboxy-2-Propanone	Methanol
base asphalt	13.20%	51.70%	26.90%	8.20%			
aged asphalt	11.60%	37.20%	28.00%	23.20%			
5 wt% BRAA	11.05%	35.43%	26.67%	22.10%	2.86%	1.20%	0.70%
10 wt% BRAA	10.55%	33.82%	25.45%	21.09%	5.47%	2.28%	1.34%
15 wt% BRAA	10.09%	32.35%	24.35%	20.17%	7.84%	3.28%	1.92%
20 wt% BRAA	9.67%	31.00%	23.33%	19.33%	10.02%	4.19%	2.46%

The simulations were performed using Materials Studio, the software for simulating and modeling materials. Firstly, 3D models of the molecules showed above were constructed. Then, amorphous cell module was used to mix the components and to build the asphalt systems. The initial densities were set to be 1.0 g/cm³. Pressure was set at 101.325 kPa (1.0 atm). The asphalt systems were first relaxed to induce the system energy using the geometry optimization tool of Forcite module, then relaxed to state equilibrium using the dynamic tool with the parameters set to be isobaric-isothermal ensemble (NPT), 1.0 fs time step and 200 ps simulation time. After that, the systems were relaxed to state equilibrium with canonical ensemble (NVT), 1.0 fs time step and 200 ps simulation time. Condensed-phase optimized molecular potentials for atomistic simulation studies (COMPASS) force field were chosen in all molecular simulations and minimization processes in this research. The following processes were performed to simulate the physical state of asphalt systems and to calculate the thermal-mechanical properties. Simulation temperature ranged from 223 to 448 K. The six asphalt systems are shown in Figure 2.

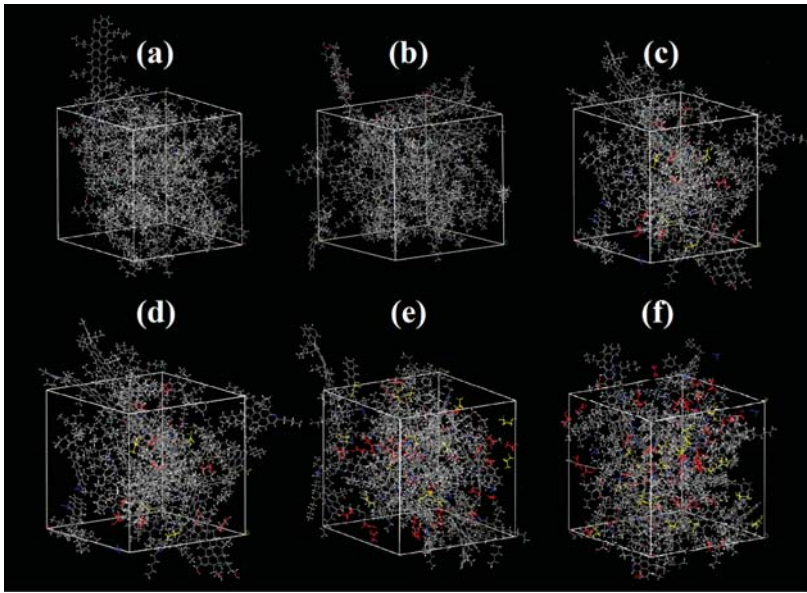


Figure 2. Models of asphalt systems: (a) asphalt; (b) aged asphalt; (c) 5% BRAA; (d) 10% BRAA; (e) 15% BRAA; (f) 20% BRAA.

2.2. Methods (Calculation Details)

2.2.1. Specific Heat Capacity

Specific heat capacity (C_p) is a measurable physical quantity equal to the ratio of the heat added to (or removed from) an object to the resulting temperature change [36]. During the heating process, the higher specific heat capacity slowed the asphalt temperature rise more slowly, which means that more energy will be consumed during asphalt heating. Otherwise, asphalt with higher specific heat capacity will be less susceptible to ambient temperature.

In this research, asphalt systems were relaxed to state equilibrium at the same pressure (1.0 atm) and different temperatures (223 to 448 K). The systems would have different properties at different temperatures. The specific heat capacity of asphalt could be analyzed by comparing the enthalpies of asphalt systems at different temperatures, as follows:

$$C_p = \frac{H}{T_p} = \frac{(E + PV)}{T_p} = \frac{1}{k_B T^2} (\langle (E + PV)^2 \rangle - \langle E + PV \rangle^2) \quad (1)$$

where C_p is specific heat; E is energy; P , V , and T are pressure, volume, and temperature, respectively; and k_B is Boltzmann constant. The E , P , V , and T could be obtained from result texts after dynamic simulations.

2.2.2. Thermal Expansion Coefficient

Thermal expansion is the tendency of matter to change in shape, area, and volume in response to a change in temperature [37]. In this research, asphalt systems were relaxed to state equilibrium at different temperature (223 to 448 K) to simulate the heating process of asphalt. With the change in temperature, the volumes of asphalt systems simultaneously changed. The volumetric thermal expansion coefficient (CTE α) could be calculated by the following equation:

$$\alpha = \frac{1}{V} \left(\frac{\partial V}{\partial T} \right)_P \quad (2)$$

where V , T , and P are volume, temperature, and pressure, respectively. The V , T , and P could be obtained from result texts after dynamic simulations.

2.2.3. Elastic Constant

After the asphalt systems relaxed to state equilibrium, the elastic constants of systems were calculated by Mechanical Property tool of Forcite module. A GPa of 0.03 was chosen to be the maximum strain applying to the asphalt systems in this simulation. For elastic materials, the elasticity could be evaluated by Hook's law:

$$\sigma_i = C_{ij}\epsilon_j \tag{3}$$

where $i, j = 1, 2, 3$. σ_i is the stress vector, while ϵ_j is the strain vector; C_{ij} is the six-dimensional stiffness matrix. The stress components could be calculated as follows:

$$\sigma_{ij} = -\frac{1}{V} \sum_k \left[m^k (u_i^k u_j^k) + \frac{1}{2} \sum_{l \neq k} (r_i^{kl}) f_j^{lk} \right] \tag{4}$$

where V is the volume; m^k and u^k are the mass and velocity of the k th particle, respectively; r is the distance between the k th and the first particles; f is the force exerted on the first particle by the k th particle. Lamé coefficient λ and μ can be calculated by the following:

$$\lambda = \frac{1}{6}(C_{12} + C_{13} + C_{21} + C_{23} + C_{31} + C_{32}) \approx \frac{1}{3}(C_{12} + C_{23} + C_{13}) \tag{5}$$

$$\mu = \frac{1}{3}(C_{44} + C_{55} + C_{66}) \tag{6}$$

$$\lambda + 2\mu = \frac{1}{3}(C_{11} + C_{22} + C_{33}) \tag{7}$$

2.2.4. Young's Modulus, Shear Modulus, and Bulk Modulus

Young's modulus, denoted by K , is a mechanical property of linear elastic solid materials, measuring the stiffness of a solid material. It defines the relationship between stress and strain in the material, which will be more or less dependent on temperature. Shear modulus, always denoted by G , is defined as the ratio of shear stress to the shear strain [38]. Bulk modulus, denoted by E , is defined as the ratio of the infinitesimal pressure increase to the resulting relative decrease of the volume. They could be calculated as follows:

$$K = \frac{\mu(3\lambda + 2\mu)}{\lambda + \mu} \tag{8}$$

$$G = \mu \tag{9}$$

$$E = \lambda + \frac{2}{3}\mu \tag{10}$$

where K , G , and E are Young's modulus, shear modulus, and bulk modulus, respectively; λ and μ are Lamé coefficients.

3. Results and Discussions

3.1. Thermal Properties of BRAA

The parameters of asphalt, aged asphalt, and BRAA were calculated by molecular dynamic simulations at different temperatures. As shown in Figure 3, the specific heat capacity (C_p) of asphalt systems showed an upward trend with temperature rises. Moreover, it decreased with aging condition and the addition of the bio-oil. The results indicated that the bio-oil renders asphalt more sensitive to

temperature. Furthermore, aging would weaken the temperature sensitive of asphalt binder, and the relationship between C_p and temperature is linear.

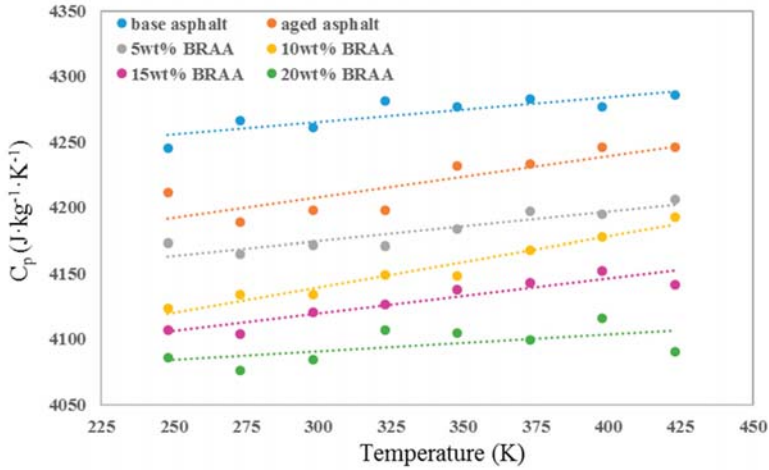


Figure 3. Specific heat capacities of asphalt systems.

Figure 4 showed the thermal expansion coefficient (CTE α) of asphalt, aged asphalt, and BRAA at different temperatures. As can be seen, the aged asphalt had the lowest CTE α , while the 20 wt% BRAA showed the highest. The CTE α of asphalt at 298 K decreased by 10.0% after aging. The addition of 5 wt% bio-oil could increase the CTE α of aged asphalt by 13.4% and make it even higher than that of base asphalt. Excessive bio-oil would further increase the CTE α of asphalt. However, when the mass fraction of bio-oil is more than 10%, the CTE α of BRAA would significantly increase over 350 K. The results indicated that the rejuvenating effect of bio-oil on aged asphalt shows an optimum dosage of 10% regarding the CTE α . Excessive bio-oil would decrease the thermal stability of asphalt and induce thermal expansion.

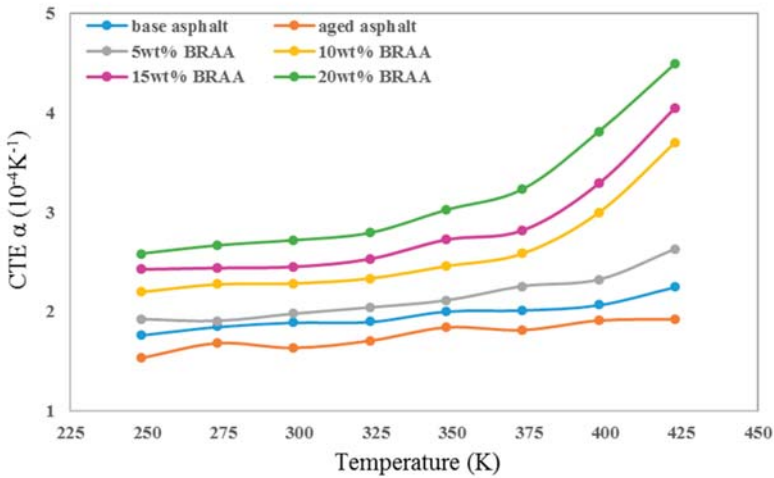


Figure 4. Thermal expansion coefficients of asphalt systems.

As conclusions, the CTE α of aged asphalt could be improved and the C_p would be decreased with the addition of bio-oil. Bio-oil of 5 wt% would be the suitable choice to regenerate the aged asphalt. CTE α of aged asphalt could restore the original level with the addition of 5 wt% bio-oil, while the thermal stability of asphalt would decrease when the amount of bio-oil was over 10 wt%.

3.2. Mechanical Properties of BRAA

As shown in Figure 5, the lame coefficient λ of asphalt decreased with the increasing temperature. It is demonstrated that temperature could have an influence on the mechanical properties and change the asphalt internal structure. The lame coefficient λ of aged asphalt was the highest, and the λ of BRAA reduced with the increasing bio-oil content, exhibiting that aging could improve the stiffness of asphalt. But bio-oil would also weaken the resistance to elastic deformation. The lame coefficient λ of base asphalt, aged asphalt, 5 wt% BRAA, 10 wt% BRAA, and 15 wt% BRAA at 298 K were 2.60, 3.04, 2.96, 2.84, and 2.02, respectively. The lame coefficient λ of 10 wt% BRAA could decrease by 6.6%, while the lame coefficient λ of 15 wt% BRAA could decrease by 33.6%. The results indicated that the effect of bio-oil on the lame coefficient λ of asphalt was not linearly taking place. Over 15 wt% bio-oil would significantly reduce the resistance of asphalt to elastic deformation.

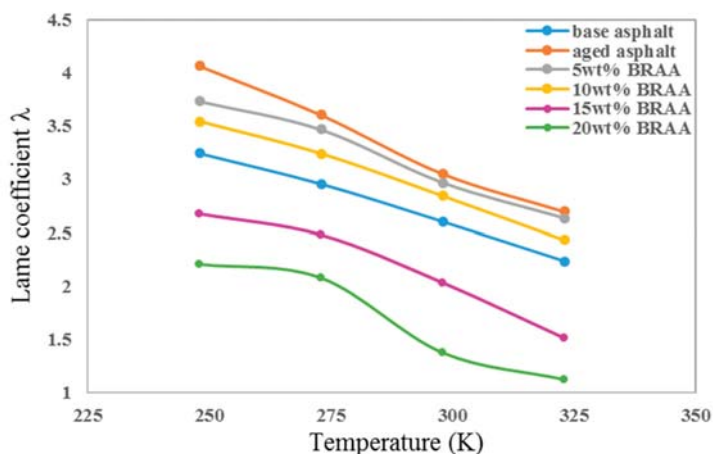


Figure 5. Lame coefficients of asphalt systems.

As can be seen in Figure 6, the shear moduli (G) increased after asphalt aging, while the G decreased with the increasing bio-oil addition amount. It indicated that the aging and bio-oil would have influence on the shear moduli. In addition, the G decreased with the increasing temperature, and the bio-oil also decreased the shear moduli of asphalt binder. As can be seen, shear moduli reduced in the order of aged asphalt, 5 wt% BRAA, 10 wt% BRAA, and base asphalt. It indicated that the flexibility of the asphalt decreased after aging, and the bio-oil could recover this change to some extent. The shear moduli of BRAA were close to those of base asphalt when the content of bio-oil reached 15 wt%. The G of 20 wt% BRAA was even lower than that of base asphalt.

As shown in Figure 7, the Young's moduli (K) were calculated according to λ and G at different temperatures. The Young's moduli of aged asphalt were highest, and decreased with the addition of bio-oil, while the K of 5 wt% BRAA and 10 wt% BRAA were bigger than that of base asphalt. The results showed that Young's modulus of asphalt increased by 35.2% after aging at 298 K, and adding 5 wt% bio-oil could decrease the Young's modulus of aged asphalt by 10.0%. Bio-oil of 15 wt% could restore the K of aged asphalt restore to its original level.

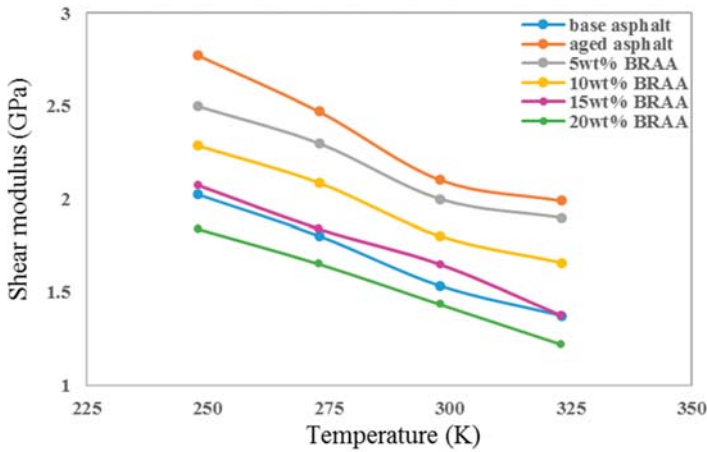


Figure 6. Shear moduli of asphalt systems at different temperatures.

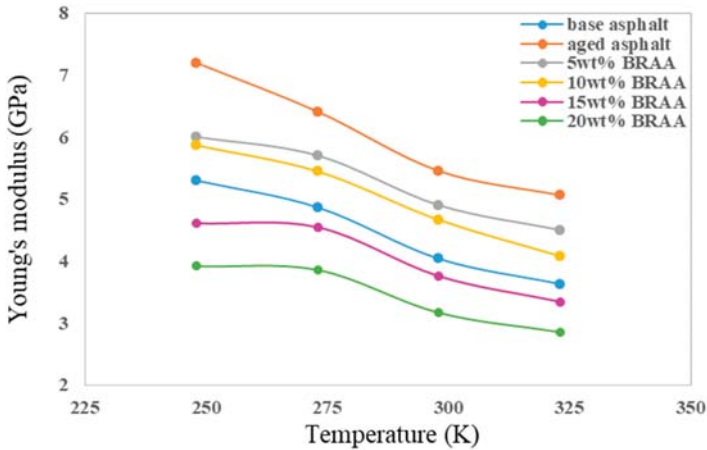


Figure 7. Young's moduli of asphalt systems at different temperatures.

As shown in Figure 8, the bulk moduli (E) at different temperatures were calculated from λ and G. The bulk moduli of asphalt increased after aging. Moreover, the bulk moduli decreased with the additional amount of bio-oil. It indicated that aging and bio-oil could affect the bulk moduli of asphalt. The E of base asphalt increased by 26.2% after aging, and 5 wt% bio-oil could decrease the E of aged asphalt by 4.8%. In addition, when the amount of bio-oil was more than 15 wt%, the BRAA had lower bulk moduli than base asphalt.

The ratio of bulk modulus to shear modulus (E/G) was used to estimate the brittle or ductile behavior of the material. High E/G values represent ductility, while low E/G values represent brittleness. The critical value for separating tough and brittle materials is about 1.75. As shown in Figure 9, calculated E/G value indicated that the base asphalt was ductile. The E/G value of asphalt decreased after aging. The addition of 5 wt% or 10 wt% of bio-oil could recover the ductility of aged asphalt to some extent. The E/G values of base asphalt, aged asphalt, 5 wt% BRAA, and 10 wt% BRAA were 2.361, 2.116, 2.159, and 2.244, respectively. The results showed that the ductility of asphalt decreased by 10.4% after aging, and 10 wt% bio-oil could improve the ductility of aged asphalt by 6.0%. However, 15 wt% bio-oil would further decrease the ductility of aged asphalt. On the other hand,

base asphalt had the highest E/G value at 298 K. With the addition of bio-oil, the highest E/G value temperature reduced, which indicated that bio-oil would decrease the temperature stability of asphalt.

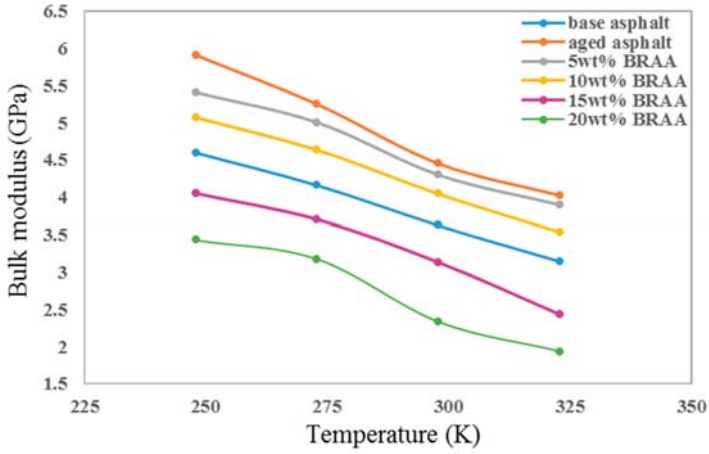


Figure 8. Bulk moduli of asphalt systems at different temperatures.

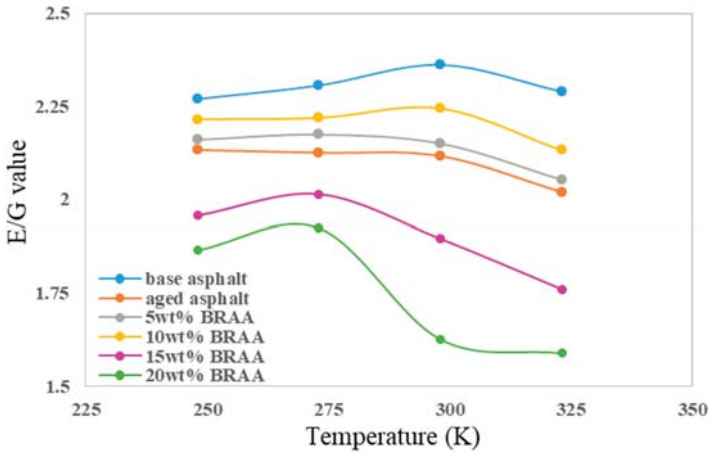


Figure 9. The E/G value of asphalt systems.

4. Conclusions

Molecular dynamic simulations were performed in order to investigate the thermal-mechanical properties of bio-oil regenerated aged asphalt (BRAA). Some conclusions were drawn:

- (1) The aging process had a significant impact on the thermal properties of asphalt. Aged asphalt had lower specific heat capacity and thermal expansion coefficient than base asphalt. The addition of 5 wt% bio-oil could make the thermal properties of aged asphalt restore to the original level. When the amount of bio-oil was over 10 wt%, the thermal stability of asphalt would be affected, which made the performance of asphalt decrease rapidly with temperature rising.
- (2) The aged asphalt had higher elastic constants, Young’s modulus, and bulk modulus than base asphalt, which meant asphalt hardened after aging. The addition of bio-oil would soften the aged asphalt, which reduced the possibility of asphalt cracking. 5 wt% of bio-oil could increase the

ductility of aged asphalt by 6.0%. As the amount of bio-oil increased, the structure of asphalt would be affected. When the addition of bio-oil was over 15 wt%, the ductility of aged asphalt would decrease instead.

It should be noticed that the model constructed in this study chose only one kind of molecule to represent each component of asphalt. The results of the simulation could only reflect the actual law to some extent, because asphalt is a complex mixture. The three molecules used to represent bio-oil are the three most abundant in bio-oil. Whether the other ingredients have an influence on the regeneration performance of bio-oil is not certain. Approaching the actual simulation, a more complex system should be built and more components need to be considered.

5. Further Research Work

The thermal-mechanical properties of bio-oil regenerated aged asphalt (BRAA) were evaluated, but the data were only based on computer simulations. More work should be done to further verify the rejuvenating effect of bio-oil. The specific heat capacity can be measured by differential scanning calorimetry (DSC), and the thermal expansion coefficient can be tested by Michelson interferometry or quartz dilatometry. Dynamic shear rheological test (DSR) and Dynamic thermomechanical analysis (DMA) can be carried out to measure the shear modulus (G) and bulk modulus (E) of BRAA. A ductility test can be done to verify the relationship between ductility and E/G value. The testing results will be compared to the simulation results. The results of the two may be different in value but have the same trend. Introducing coefficients and increasing the number of samples can improve the accuracy of the simulation. When the accuracy of the model is verified multiple times, the simulation will become the guiding basis for material design.

Author Contributions: Data curation: T.Y.; formal analysis: T.Y., X.Z.; project administration: J.X.; writing—original draft: T.Y.; writing—review and editing: X.Z., M.C.

Funding: This research was funded by National Natural Science Foundation of China (No. 51778515, 51708437), National Key Research and Development Program of China (No. 2017YFE0111600), Technological Innovation Major Project of Hubei Province (No. 2016AAA023), and Science and Technology Department of Shanxi Province International Cooperation (No. 201603D421027).

Conflicts of Interest: The authors declare no conflicts of interest. We declare that we do not have any commercial or associative interest that represents a conflict of interest in connection with the work submitted.

References

1. Wu, J.; Airey, G. The influence of aggregate interaction and aging procedure on asphalt aging. *J. Test. Eval.* **2009**, *37*, 402–409.
2. Wu, S.; Pang, L.; Liu, G.; Zhu, J. Laboratory study on ultraviolet radiation aging of asphalt. *J. Mater. Civ. Eng.* **2010**, *22*, 767–772. [[CrossRef](#)]
3. Mazzoni, G.; Bocci, E.; Canestrari, F. Influence of rejuvenators on asphalt ageing in hot recycled asphalt mixtures. *J. Traffic Transp. Eng.* **2018**, *5*, 157–168.
4. National Asphalt Pavement Association. *Hot Recycling of Yesterday*; Recycling Report; National Asphalt Pavement Association: Lanham, MD, USA, 1977; Volume 1.
5. Hamilton, J. *Historical Oil Shocks*; National Bureau of Economic Research: Cambridge, MA, USA, 1 February 2011.
6. Shen, J.; Amirkhanian, S.; Miller, J. Effects of rejuvenating agents on superpave mixtures containing reclaimed asphalt pavement. *J. Mater. Civ. Eng.* **2007**, *19*, 376–384. [[CrossRef](#)]
7. Xiao, F.; Amirkhanian, S.; Juang, C. Rutting resistance of rubberized asphalt concrete pavements containing reclaimed asphalt pavement mixtures. *J. Mater. Civ. Eng.* **2007**, *19*, 475–483. [[CrossRef](#)]
8. Mallick, R.; Kandhal, P.; Bradbury, R. Using marm-mix asphalt technology to incorporate high percentage of reclaimed asphalt pavement material in asphalt mixtures. *Transp. Res. Rec. J. Transp. Res. Board* **2008**, *2051*, 71–79. [[CrossRef](#)]
9. Rossi, C.; Caputo, P.; Loise, V.; Ashimova, S.; Teltayev, B.; Sangiorgi, C. A New Green Rejuvenator: Evaluation of Structural Changes of Aged and Recycled Bitumens by Means of Rheology and NMR.

- In RILEM 252-CMB-Symposium on Chemo Mechanical Characterization of Bituminous Materials; Springer: Arcavacata di Rende, Italy, 2018; pp. 177–182.
10. Xiu, S.; Shahbazi, A. Bio-oil production and upgrading research: A review renewable and sustainable. *Energy Rev.* **2012**, *16*, 4406–4414.
 11. Fini, E.; Kalberer, E.; Shahbazi, A.; Basti, M.; You, Z.; Ozer, H.; Aurangzeb, Q. Chemical characterization of biobinder from swine manure: Sustainable modifier for asphalt binder. *J. Mater. Civ. Eng.* **2011**, *23*, 1506–1513. [[CrossRef](#)]
 12. Prakash, R.; Singh, R.; Murugan, S. Experimental investigation on a diesel engine fueled with bio-oil derived from waste wood-biodiesel emulsions. *Energy* **2013**, *55*, 610–618. [[CrossRef](#)]
 13. Yang, X.; You, Z. High temperature performance evaluation of bio-oil modified asphalt binders using the DSR and MSCR tests. *Constr. Build. Mater.* **2015**, *76*, 380–387. [[CrossRef](#)]
 14. Gao, J.; Wang, H.; You, Z.; Mohd Hasan, M.R. Research on properties of bio-asphalt binders based on time and frequency sweep test. *Constr. Build. Mater.* **2018**, *160*, 786–793. [[CrossRef](#)]
 15. Yang, X.; You, Z.; Dai, Q. Performance Evaluation of asphalt binder modified by bio-oil generated from waste wood resources. *Int. J. Pavement Res. Technol.* **2013**, *6*, 431–439.
 16. Yang, X.; You, Z.; Dai, Q.; Mills-Beale, J. Mechanical performance of asphalt mixtures modified by bio-oils derived from waste wood resources. *Constr. Build. Mater.* **2014**, *51*, 424–431. [[CrossRef](#)]
 17. Cuadri, A.; Garcia-Morales, M.; Navarro, F.; Partal, P. Processing of bitumens modified by a bio-oil-derived polyurethane. *Fuel* **2014**, *118*, 83–90. [[CrossRef](#)]
 18. Williams, A.; Jones, J.; Ma, L.; Pourkashanian, M. Pollutants from the combustion of solid biomass fuels. *Prog. Energy Combust. Sci.* **2012**, *38*, 113–137. [[CrossRef](#)]
 19. Yang, S.; Suciptan, T.; Chang, Y. Investigation of rheological behavior of Japanese cedar based bio-binder as partial replacement for bituminous binder. In Proceedings of the Transportation Research Board 92nd Annual Meeting, Washington, DC, USA, 13–17 January 2013.
 20. Guarin, A.; Khan, A.; Butt, A.; Birgisson, B.; Kringos, N. An extensive laboratory investigation of the use of bio-oil modified bitumen in road construction. *Constr. Build. Mater.* **2016**, *106*, 133–139. [[CrossRef](#)]
 21. Sun, Z.; Yi, J.; Feng, D.; Kasbergen, C.; Scarpas, A.; Zhu, Y. Preparation of bio-bitumen by bio-oil based on free radical polymerization and production process optimization. *J. Clean. Prod.* **2018**, *189*, 21–29. [[CrossRef](#)]
 22. Sun, B.; Zhou, X. Diffusion and rheological properties of asphalt modified by bio-oil regenerant derived from waste wood. *J. Mater. Civ. Eng.* **2017**, *119*, 1–11. [[CrossRef](#)]
 23. Yang, X.; Mills-Beale, J.; You, Z. Chemical characterization and oxidative aging of bio-asphalt and its compatibility with petroleum asphalt. *J. Clean. Prod.* **2017**, *142*, 1837–1847. [[CrossRef](#)]
 24. Alder, B.; Wainwright, T. Studies in molecular dynamics. I. General method. *J. Chem. Phys.* **1959**, *31*, 459–466. [[CrossRef](#)]
 25. Rahman, A. Correlations in the motion of atoms in liquid argon. *Phys. Rev.* **1964**, *136*, A405. [[CrossRef](#)]
 26. Boek, E.; Yakovlev, D.; Headen, T.F. Quantitative molecular representation of asphaltenes and molecular dynamics simulation of their aggregation. *Energy Fuels* **2009**, *23*, 1209. [[CrossRef](#)]
 27. Pan, T.; Yu, Q.; Lloyd, S. Quantum-chemistry based study of beechwood lignin as an antioxidant of petroleum asphalt. *J. Mater. Civ. Eng.* **2013**, *10*, 1477–1488. [[CrossRef](#)]
 28. Allen, M.; Tildesley, D. *Computer Simulation of Liquids*; Oxford University Press: Oxford, UK, 22 August 2017.
 29. Zhang, L.; Greenfield, M. Effects of polymer modification on properties and micro-structure of model asphalt systems. *Energy Fuels* **2008**, *22*, 3363–3375. [[CrossRef](#)]
 30. Zhang, L.; Greenfield, M. Molecular orientation in model asphalts using molecular simulation. *Energy Fuels* **2007**, *21*, 1102–1111. [[CrossRef](#)]
 31. Groenzin, H.; Mullins, O. Molecular size and structure of asphaltenes from various sources. *Energy Fuels* **2000**, *14*, 677–684. [[CrossRef](#)]
 32. Li, D.; Greenfield, M. Chemical compositions of improved model asphalt systems for molecular simulations. *Fuel* **2014**, *115*, 347–356. [[CrossRef](#)]
 33. Bai, A.; Zhou, X. Self-healing Properties of Bio-oil Regenerated Asphalt. *J. Chongqing Jiaotong Univ. (Nat. Sci.)* **2018**, *8*, 29–33.
 34. Nie, Y.; Zhang, Y.; Yu, J.; Kuang, D.L.; Zhang, X.P. Research on aging mechanism and recycling mechanism based on asphalt four components analysis. *Appl. Mech. Mater.* **2012**, *204–208*, 1659–1664. [[CrossRef](#)]

35. Zhang, R. *Fuels and Chemicals Derived from Biomass*; Zhengzhou University Press: Zhengzhou, China, September 2004.
36. Halliday, D.; Resnick, R. *Fundamentals of Physics*; John Wiley & Sons: Hoboken, NJ, USA, 1981.
37. Tipler, P.; Mosca, G. *Physics for Scientists and Engineers*; Macmillan: London, UK, 2007.
38. McNaught, A. *Compendium of Chemical Terminology*; Blackwell Science: Oxford, UK, 1997.



© 2018 by the authors. Licensee MDPI, Basel, Switzerland. This article is an open access article distributed under the terms and conditions of the Creative Commons Attribution (CC BY) license (<http://creativecommons.org/licenses/by/4.0/>).

Article

A Comprehensive Evaluation of Rejuvenator on Mechanical Properties, Durability, and Dynamic Characteristics of Artificially Aged Asphalt Mixture

Pan Pan ^{1,2,3}, Yi Kuang ^{3,4}, Xiaodi Hu ^{3,*} and Xiao Zhang ^{1,2,*}

¹ Key Laboratory of Highway Construction and Maintenance Technology in Loess Region, Ministry of Transport, Taiyuan 030006, China; panp@wit.edu.cn

² Key Laboratory of Highway Construction and Maintenance Technology in Loess Region, Shanxi Transportation Research Institute, Taiyuan 030006, China

³ School of Civil Engineering and Architecture, Wuhan Institute of Technology, Wuhan 430205, China; kuangyi1992@hotmail.com

⁴ State Key Laboratory of Silicate Materials for Architectures, Wuhan University of Technology, Wuhan 430070, China

* Correspondence: huxiaodi625@hotmail.com (X.H.); xiaozhang2008@gmail.com (X.Z.); Tel.: +86-027-87194823 (X.H.); +86-0351-7585750 (X.Z.)

Received: 29 July 2018; Accepted: 27 August 2018; Published: 29 August 2018

Abstract: In this study, the aged asphalt binder and mixture were laboratory prepared through short-term ageing testing and long-term ageing testing. Firstly, the effect of rejuvenator on physical properties of aged asphalt binders was investigated. In addition, a series of laboratory tests were performed to evaluate the influence of ageing and rejuvenator content on the mechanical properties, durability and dynamic characteristics of asphalt mixtures. Physical test results of asphalt binder testified that rejuvenator used can efficiently recover the aged asphalt binder. However, the effect of ageing and rejuvenator content exhibits different trends depending on the physical property tests conducted. Moreover, artificially aged asphalt mixture with rejuvenator has better ability to resist moisture damage and ravelling. In addition, the ITSR value is more suitable to evaluate the moisture susceptibility for asphalt recycling. Although rejuvenator improves the thermal cracking resistance and fatigue property of aged asphalt mixture, rejuvenated mixture shows greater modulus and inferior ability to resist reflective cracking than the unaged mixture. Moreover, rejuvenated mixture shows less dependence on frequency at high temperature regions and stronger dependence at low temperature regions compared to unaged and long-term aged mixtures.

Keywords: artificially aged asphalt mixture; rejuvenator; durability; dynamic characteristics; overlay tester

1. Introduction

Asphalt mixture is widely used as a common road material for structural layers of pavement worldwide. During the service period, weather conditions and repeated load would deteriorate the mechanical performance and durability of the asphalt mixture, and then lead to some irreversible pavement distresses such as ravelling, rutting, cracking, etc. Removal of old pavement structure consequently produces a large amount of reclaimed asphalt pavement (RAP). For instance, more than 60,000,000 t of RAP material can be obtained annually in China [1]. To reduce the construction cost and generate environmental benefits, different countries have launched a series of experimental and practical researches on application of RAP material in new pavement construction [2,3].

Previous studies have confirmed that ageing of asphalt binder is the main cause of durability failure of asphalt pavement [4–6]. The ageing processes of asphalt pavement consists of short-term

ageing during the mixing and construction phase, and long-term ageing during the service life in the field. There are many reasons that can lead to asphalt binder ageing including oxidation, volatilization, absorption by aggregate, thermal polymerization, etc. [7]. According to the molecular characteristics, asphalt binder can be divided into four fractions: saturates, aromatics, resins, and asphaltenes. From the chemical composition point of view, ageing effect increases resins and asphaltenes while reduces aromatics in RAP binder, compared to the virgin asphalt binder [8]. Due to the aged RAP binder, recycling asphalt pavement is prone to ravelling and low temperature cracking [9–11]. Based on the component control theory of asphalt recycling, soft binder is needed to reduce the asphaltene content and increase the aromatic content of the aged RAP binder, in order to minimize the negative impact of using RAP material in recycling asphalt pavement.

Rejuvenators, including plant oils, waster derived oils and engineered products, can provide an alternative method to restore the aged asphalt for hot asphalt recycling [12–14]. Many research studies have been conducted to evaluate the effectiveness of different types of rejuvenators on artificially aged asphalt binder or/and aged RAP binder. In this case, the aged binder is heated and blended with the rejuvenator. Chen et al. investigated the effect of waste edible vegetable oil on artificially aged asphalt binder. They concluded that waste edible vegetable oil can be used as a rejuvenator in recycling asphalt pavement [8]. Based on Superpave design specification, Zaumanis et al. developed a procedure to determine the optimum rejuvenator content for modifying RAP binder [15]. It is highlighted that considering ageing effect is helpful for better understanding the effect mechanism of rejuvenator on RAP binder [16]. Although the rejuvenator can recover the physical and rheological properties of aged asphalt binder to some extent, the rejuvenated asphalt binder is more prone to ageing than the virgin binder [17]. Moreover, both experimental and simulation results testified that the diffusion and distribution of rejuvenator play an important role in affecting the engineering performance of recycling asphalt mixture [18,19]. In a study conducted by Wang et al., the mortar transfer ratio (MTR) test was employed to study the diffusion characteristics of rejuvenator in aged asphalt [20].

By summarizing the present recycled asphalt techniques, Moghaddam et al. found that the most common way to use rejuvenator is mixing them with aged asphalt mixture at high temperature [2]. According to Chinese Specification, the rejuvenator is added and mixed with the reclaimed asphalt mixture, new aggregate and virgin asphalt to obtain the recycling asphalt mixture [21]. Therefore, it is worth noting that the actual production of hot asphalt recycling is quite different from that of the rejuvenated asphalt binder. Im et al. compared three different rejuvenators on engineering performance of asphalt mixtures containing recycled materials. They concluded that the effectiveness of rejuvenators prepared by different sources on recycled asphalt mixture depends on the engineering properties concerned [22].

For proper field usage of rejuvenator, it is of high priority to balance the cracking and rutting performance of recycled asphalt mixture. The rejuvenator should reduce fatigue and low temperature cracking potential whilst maintaining stability to rutting [23,24]. Therefore, it is necessary to obtain a comprehensive understanding of the engineering properties for rejuvenated asphalt mixture. Moreover, there is also a need for sufficient understanding of the dynamic characteristics of recycled hot mix asphalt. These problems of recycled hot mix asphalt with rejuvenator provide the motivation to undertake this research.

In this study, a series of laboratory tests were conducted to investigate the influences of rejuvenator content on mechanical properties, durability and dynamic characteristics of artificially aged asphalt mixture. By studying the effect of using different amounts of a rejuvenator in recycled HMA and in aged binders subjected to different ageing times, this paper can not only clarify the effect of ageing process and rejuvenator content on the concerned properties of asphalt binder and HMA, but also demonstrate the suitability of available test or indicator to evaluate the performance of rejuvenated asphalt mixture. The finding of this study could help to gain a comprehensive understanding of rejuvenated asphalt mixture, and therefore contributes to proper usage of rejuvenator in recycled asphalt pavement.

2. Materials and Experimental

2.1. Materials

AH-90 paving asphalt with a penetration of 96 dmm (deci-millimetre, 25 °C), a softening point of 48.6 °C and a ductility of 156 cm was obtained from the Hubei Guochang Hi-tech Material Co., Ltd., Wuhan, China. The crushed diabase aggregate has a density of 2.953 g/cm³ and a particle size less than 16 mm. The limestone filler (LF) with a density of 2.699 g/cm³ was used as the mineral filler. The rejuvenator in this study was petroleum derived product, which was obtained from market. Table 1 illustrates the technical parameters of rejuvenator.

Table 1. Technical parameters of rejuvenator.

Properties	Rejuvenator	Test Method
Form	Liquid	
Color	Brown	
pH	5.6	pH test paper
Viscosity (25 °C), SFS	15	ASTM D-244
Solute component (wt %)	60	ASTM D-244
Regeneration component (wt %)	8	ASTM D-2006-70
Asphaltene component (wt %)	0.75	

2.2. Sample Preparation

For asphalt binder, aged samples were prepared by the thin film oven test, TFOT (ASTM D1754) and the pressurized ageing vessel, PAV test (ASTM D6521). The detailed TFOT and PAV test procedures were described in a previous research work [25]. For the standard PAV test, asphalt binder sample is needed to be placed in the PAV for 20 h ± 10 min. To simulate different long-term ageing history, TFOT aged asphalt binders were treated by PAV test within 5 h, 10 h, 15 h and 20 h, respectively. Generally, 20 h of PAV ageing approximates 2 to 3 years of asphalt pavement in service. Another TFOT aged binder without PAV test was employed as a control sample. Then, four dosages of rejuvenator (2.0%, 4.0%, 6.0% and 8.0%, by weight of binder) were added into each TFOT and PAV aged asphalt binder. The rejuvenated binder was blended using the propeller mixer at a constant speed of 800 rpm for 20 min at 135 °C. All the aged and rejuvenated asphalt binders were used for physical properties tests in Section 2.3.

Figure 1 shows the gradation curve of asphalt mixture with the nominal maximum size of 13 mm. The upper and lower limits of gradation followed to the Chinese Specification of JTG F40-2004 [26]. The content of mineral filler was 4% by weight of aggregate and the optimum asphalt content was 4.7% by weight of asphalt mixture. Aged asphalt mixtures were prepared by short-term ageing (STA) test and long-term ageing (LTA) test according to JTG E20 T0734 [27]. During the STA test, the incompact asphalt mixture was firstly spread to a height of 50 mm on a metal pan and placed in a force draft oven at 135 °C for 4 h. Then the compacted samples were prepared by STA aged mixture to perform LTA test, which were placed in the oven at 85 °C for 5 days. Finally, heated LTA aged sample was broken apart and then mixed with rejuvenator to prepare rejuvenated sample. All the unaged, LTA aged, and rejuvenated samples were used for mechanical properties, durability and dynamic modulus tests in Section 2.4.

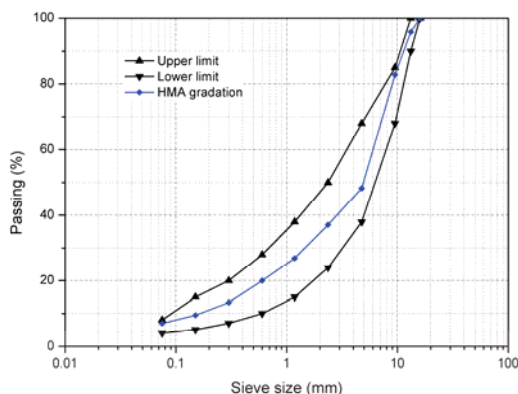


Figure 1. Chart of aggregate gradation.

2.3. Physical Properties Test of Asphalt Binder

The physical properties of the aged and rejuvenated asphalt binders, including softening point temperature, penetration (25 °C), ductility (15 °C), and rotation viscosity (135 °C) were studied in accordance with ASTM D36 [28], D5 [29], D113 [30] and D4402 [31], respectively.

2.4. Performance Test of Asphalt Mixture

2.4.1. Moisture Susceptibility Test

Considering the soaking and frost effect, Marshall stability (MS) and indirect tensile strength (ITS) tests were conducted to evaluate the moisture susceptibility of aged and rejuvenated asphalt mixtures according to JTG E20 T0709 and T0729, respectively [27]. The detailed test protocols for Marshall stability and indirect tensile are shown in Table 2. Four repetitions were prepared for each group of the MS and the ITS tests. The loss of strength due to the impact of the exposure condition were defined as a ratio of the corresponding test result of conditioned samples to the control samples. The Marshall strength ratio (MSR) and indirect tensile strength ratio (ITSR) can be calculated as Equations (1) and (2):

$$MSR = \frac{MS \text{ of conditioned samples}}{MS \text{ of control samples}} \times 100\% \tag{1}$$

$$ITSR = \frac{ITS \text{ of conditioned samples}}{ITS \text{ of control samples}} \times 100\% \tag{2}$$

Table 2. Summary of moisture susceptibility test protocols used.

	Marshall Stability Test	Indirect Tensile Strength Test
Control	Soaking for 0.5 h at 60 °C	Soaking for 2 h at 25 °C
Conditioned	Soaking for 48 h at 60 °C	Freezing at −18 °C for 16 h + Thawing at 60 °C for 24 h + Soaking for 2 h at 25 °C

2.4.2. Cantabro Abrasion Test

Since ravelling is a typical distress for rejuvenated mixture, the Cantabro abrasion test was performed to evaluate the resistance to particle loss of the aged and rejuvenated asphalt mixtures according to JTG E20 T0733 [27]. The compacted aged and rejuvenated samples were divided into control and conditioned groups. Before testing, the conditioned samples were kept in a water bath of

20 °C for 20 h. Then, four repetitions for each group were individually put in the Los Angeles abrasion device without steel balls. The abrasion test would be stopped when Los Angeles drum rotated for 300 revolutions at a speed of 30–33 revolutions per minute. After testing, the loose particles broken off from the surface of the testing sample were discarded. The mass loss ratio of sample before and after the test was adopted to evaluate the resistance to particle loss of mixture, which can be calculated as Equation (3):

$$\text{Massloss} = \left(1 - \frac{\text{sample mass after test}}{\text{sample mass before test}} \right) \times 100\% \quad (3)$$

2.4.3. Wheel Tracking Test

The wheel tracking test was employed to evaluate the resistance to permanent deformation of the aged and rejuvenated asphalt mixtures under dry condition. The size of test sample is 300 mm in length, 300 mm in width and 50 mm in height. Before testing, the aged and rejuvenated samples were kept in the test device of 60 °C for 6 h. The repeated load was 0.7 MPa at 60 °C and the wheel speed was 42 passes per minute. The rutting depth of samples during the testing process was recorded. Dynamic stability can be calculated by the rutting depth of 45 min and 60 min as Equation (4) according to JTG E20 T0719 [27].

$$\text{DS} = \frac{15 \times 42}{\text{RD}_{60} - \text{RD}_{45}} \quad (4)$$

where DS is dynamic stability, times/mm; RD_{45} and RD_{60} are the rutting depth at 45 and 60 min respectively, mm.

2.4.4. Dynamic Uniaxial Compression Test

Dynamic uniaxial compression test was also carried out to assess the high temperature stability of the aged and rejuvenated asphalt mixtures according to BS EN 12697-25 [32]. Test samples with a diameter of 100 mm and a height of 110 mm were prepared by coring and cutting the SGC samples. Before testing, the aged and rejuvenated samples were kept in the test device of 60 °C for 4 h. A haversine load with a peak stress of 0.7 MPa was applied on the sample for 3600 s at 60 °C.

2.4.5. Three-Point Bending Test

Three-point bending test was employed to evaluate the low temperature performance of the aged and rejuvenated asphalt mixtures according to JTG E20 T0715 [27]. The beam samples with 250 mm in length, 30 mm in width and 35 mm in height, were tested by a loading of 50 mm/min at -10 °C. Before testing, the samples were kept in the test device of -10 °C for 8 h. Four test repetitions were prepared for each mixture and the average value was used. The flexural strength, flexural strain, and flexural stiffness modulus were calculated by following equations:

$$R_B = \frac{3LP_B}{2bh^2} \quad (5)$$

$$\varepsilon_B = \frac{6hd}{L^2} \quad (6)$$

$$S_B = \frac{R_B}{\varepsilon_B} \quad (7)$$

where P_B is peak load at failure, kN; R_B is flexural strength, MPa; ε_B is flexural strain; S_B is flexural stiffness modulus, MPa; L , b and h are length, width and height of sample, respectively, mm.

2.4.6. Overlay Tester

The Overlay Tester (OT) was conducted to evaluate the reflective cracking resistance of the aged and rejuvenated asphalt mixtures according to TxDOT standard specification Tex-248F [33].

In this study, the OT samples were placed vertically and tested by UTM-100 at 25 °C. OT samples with 150 mm in length, 75 mm in width and 38 mm in thickness were prepared by cutting the SGC samples. The triangular load with a constant maximum displacement of 0.625 mm was applied for 10 s, including a loading time of 5 s and a rest time of 5 s.

2.4.7. Four-Point Bending Fatigue Test

Four-point bending test was carried out to evaluate the fatigue performance of the aged and rejuvenated asphalt mixtures according to JTG E20 T0739 [27]. The beam samples, with 380 mm in length, 65 mm in width and 50 mm in height were tested at four strain levels, including 400 $\mu\epsilon$, 500 $\mu\epsilon$, 600 $\mu\epsilon$ and 700 $\mu\epsilon$. For each strain level, four test repetitions were prepared for each mixture and the average value was used. The frequency of cyclic loading was 10 Hz and the test temperature was 25 °C. The loading cycles is defined as fatigue life when the stiffness modulus was decreased by 50% compared to the initial modulus. Previous studies found that fatigue life of asphalt mixture to strain follows the power function, which is shown as Equation (8) [34,35].

$$N_f = A(1/\epsilon)^n \quad (8)$$

where N_f is the fatigue life of asphalt mixture, ϵ is the strain level, A and n are the regression coefficients.

2.4.8. Dynamic Modulus Test

The dynamic modulus test was performed to study the viscoelastic characteristics of the aged and rejuvenated asphalt mixtures according to AASHTO TP62-07 [36]. The samples were tested by a haversine axial compressive stress with six frequencies ranging from 0.1 to 25 Hz at five temperatures including -10 °C, 4.4 °C, 21.1 °C, 37.8 °C and 54.4 °C. In accordance with a previous study, generalized logistic sigmoidal function was adopted to obtain the master curve of the dynamic modulus, which is shown as below in Equation (9) [37].

$$\log|E^*| = \delta + \frac{\alpha}{(1 + \lambda \times e^{\beta + \gamma \log f_r})^{\frac{1}{\lambda}}} \quad (9)$$

where $|E^*|$ is the dynamic modulus, MPa; f_r is reduced frequency, Hz; δ is minimum modulus value; α is span of modulus values; β , γ and λ are shape parameters. The reduced frequency f_r is defined as Equation (10):

$$f_r = f \times \alpha_T \quad (10)$$

where f is the loading frequency, Hz; α_T is the shift factor, which can be defined by Williams-Landel-Ferry (WLF) equation as follows [38].

$$\log \alpha_T = \frac{-C_1(t - t_0)}{C_2 + (t - t_0)} \quad (11)$$

where C_1 and C_2 are the model coefficients; t_0 and t are the reference temperature and the test temperature, °C.

3. Result and Discussion

3.1. Effect of Rejuvenator on Physical Properties of Aged Asphalt Binder

Figure 2 illustrates the effect of ageing process and rejuvenator content on penetration of asphalt binders. For the samples without rejuvenator, penetration of asphalt binders decreased with prolonging the ageing time. Since the PAV aged samples suffered longer ageing time compared to TFOT aged sample, penetration of four PAV aged asphalt binders were smaller than that of TFOT aged binder. For instance, penetration of TFOT aged binder was 76 dmm, while the corresponding results for 5 h

and 20 h PAV aged binders were 62 dmm and 31 dmm, respectively. Penetration implies the stiffness of asphalt binder. The results indicate that ageing would make asphalt binders become much harder.

For each aged asphalt binder, penetration increased with increasing the addition of rejuvenator. When the rejuvenator was 8% by weight of asphalt binder, the penetration of 20 h PAV aged asphalt binder increased from 31 dmm to 61 dmm. The obtained result implies that rejuvenator can efficiently soften and recover the aged asphalt binder. It is also confirmed by the test result of ductility, which is shown in Figure 3. Incorporation of rejuvenator linearly increased the ductility of TFOT and PAV aged asphalt binders. Ductility is generally used to evaluate the resistance to low temperature cracking of asphalt binder. The greater ductility means the asphalt binder is more flexible. Therefore, rejuvenator helps the aged asphalt binder to be less susceptible to cracking in cold weather condition.

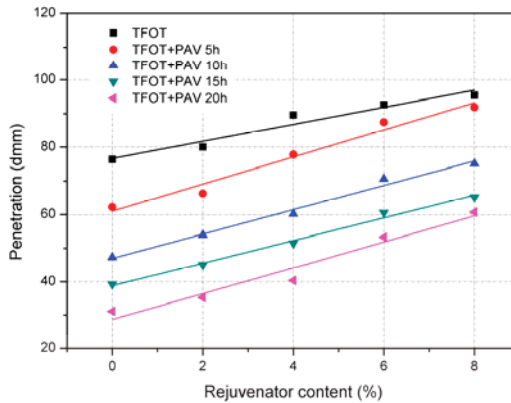


Figure 2. Penetration of TFOT and PAV aged asphalt binders with rejuvenator.

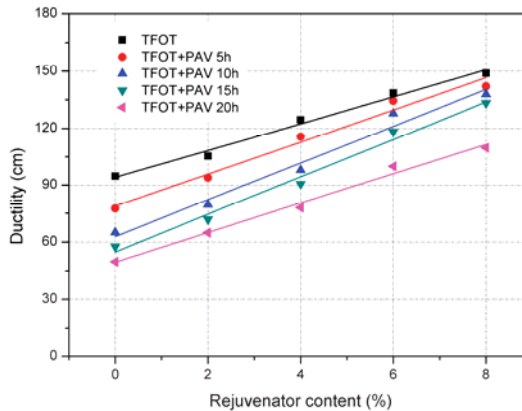


Figure 3. Ductility of TFOT and PAV aged asphalt binders with rejuvenator.

Figures 4 and 5 show the effect of rejuvenator on softening point temperature and viscosity of aged asphalt binders, respectively. Since asphalt binder would be harder after ageing, both the softening point temperature and viscosity increased due to the ageing effect. It can be assumed that aged asphalt mixture is less prone to permanent deformation at high temperature. For each aged asphalt binders, softening point temperature and viscosity shows a clear decline trend with increasing

the rejuvenator content. It indicates that rejuvenator softened the aged asphalt binders, which is in accordance with the results of penetration and ductility.

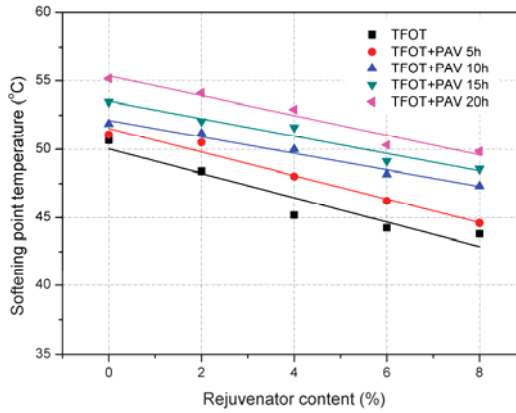


Figure 4. Softening point temperature of TFOT and PAV aged asphalt binders with rejuvenator.

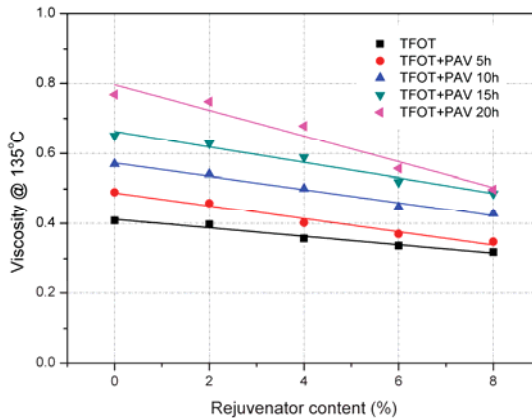


Figure 5. Viscosity of TFOT and PAV aged asphalt binders with rejuvenator.

Results of physical properties confirmed that rejuvenator used in this study can restore the aged asphalt binder. Since rejuvenator modifies the flexibility of aged asphalt binder, the recycled asphalt mixture is expected to have a stronger ability to resist temperature cracking and fatigue cracking. Moreover, the addition of rejuvenator would decrease the softening point temperature and viscosity of aged asphalt binder. For instance, the softening point temperature of 5 h PAV asphalt binder with 8% rejuvenator was 44.6 °C, which was smaller than the Chinese specification of 48 °C. It is worth noting that there is a risk of permanent deformation of recycled asphalt mixture with improper content of rejuvenator. Therefore, optimum rejuvenator content should be determined for obtaining recycled asphalt mixture with sufficient ability to resist both cracking and rutting.

Furthermore, it is noted that the changes in different physical properties of asphalt binder are quite different even after the same ageing process or adding the same content of rejuvenator into the aged asphalt binder. Compared to virgin asphalt binder, the penetration of 20 h PAV aged binder decreased 67.7% from 96 dmm to 31 dmm, while the corresponding softening point temperature increased 13.6%

from 48.6 °C to 55.2 °C. By adding 8% rejuvenator, the penetration of 20 h PAV aged asphalt binder increased 96.8% from 31 dmm to 61 mm, and the softening point temperature accordingly decreased 9.8% from 55.2 °C to 49.8 °C. It can be concluded that the effect of ageing and rejuvenator content will exhibit different trends depending on the physical property test conducted. Future study is also suggested to examine the asphalt binder grade change due to the penetration and the softening point.

3.2. Effect of Rejuvenator on Engineering Properties and Durability of Aged Asphalt Mixture

3.2.1. Moisture Susceptibility Test

Figure 6 shows the Marshall stability results of the unaged, long-term aged (LTA) and rejuvenated asphalt mixtures. Rejuvenated mixture was prepared by LTA mixture and rejuvenator. According to the aforementioned results in Section 3.1, the rejuvenator dosage was determined as 8% by weight of asphalt binder used in LTA mixture. The Marshall stability of control group for unaged and LTA samples were 11.43 kN and 14.04 kN, respectively. It indicates that long-term ageing process increased the stiffness of asphalt mixture. After soaking in a water bath of 60 °C for 48 h, the Marshall stability of unaged sample decreased to 11.04 kN, which was only a little lower the LTA sample of 11.89 kN. The Marshall stability ratio (MSR) greater than 80% is used as a critical indicator for hot mix asphalt. Although the MSR of LTA mixture was 84.7%, it is still quite lower than the unaged mixture of 96.6%. This implies LTA process makes asphalt mixture to be more susceptible to moisture. With incorporation of rejuvenator, rejuvenated asphalt mixture showed comparable Marshall stability and MSR value to the unaged mixture. It can be concluded that rejuvenator improves the resistance of aged asphalt mixture to moisture by the results obtained from Marshall stability test.

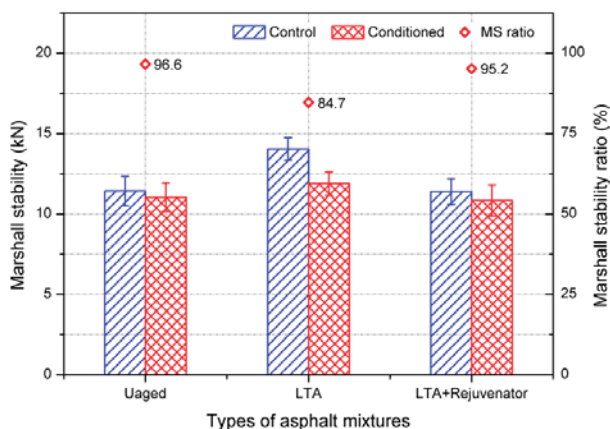


Figure 6. Marshall stability results of aged and rejuvenated asphalt mixtures.

In addition, indirect tensile strength test was also conducted to evaluate the moisture susceptibility of asphalt mixture, and the results are shown in Figure 7. Similar to MSR results, the indirect tensile strength ratio (ITSR) of rejuvenated sample was comparable to the unaged sample and greater than the LTA sample. ITSR results also confirmed the effectiveness of rejuvenator on aged asphalt mixture in term of moisture susceptibility. However, the indirect tensile strength of the control and conditioned rejuvenated samples were 1.36 MPa and 1.09 MPa, which were obviously greater than the corresponding results of unaged samples. Although the rejuvenator can recover the ability of aged asphalt mixture to resist freezing and thawing effect, it cannot enable the aged binder in LTA asphalt mixture to have a comparable stiffness with the unaged mixture at the test temperature of ITS.

The reason might be that the softening effect of rejuvenator on aged mixture at low temperature for ITS test becomes less significant compared to that at high temperature condition for Marshall stability test.

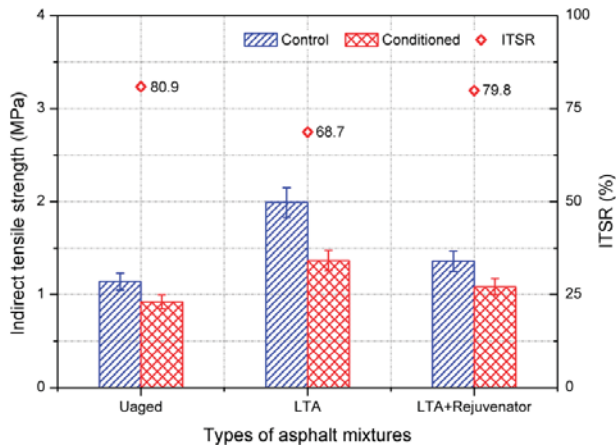


Figure 7. Indirect tensile strength test results of aged and rejuvenated asphalt mixtures.

Moreover, the ITSr value of LTA sample was 68.7%, which was lower than the performance requirement of 75% for hot mix asphalt according to the Chinese Specification of JTG F40-2004 [26]. For the indirect tensile strength test, freezing and thawing tests were performed on the asphalt mixture samples. Volume expansion and cracking would occur and lead to bonding failure between the asphalt binder and aggregate. The sample conditioning procedure is more efficient and serious than the Marshall stability test. Therefore, it is recommended to consider the ITSr value as a critical indicator for evaluating the moisture susceptibility, in order to reduce the risk of moisture damage for field usage of recycling hot mix asphalt.

3.2.2. Cantabro Abrasion Test

In asphalt mixture, asphalt binder serves as a glue to bond aggregate. Ageing would degrade the bonding strength of asphalt binder and make asphalt mixture to be more prone to ravelling. Therefore, the Cantabro test, which is usually applied in open graded mixture, was performed to evaluate the effect of long-term ageing and rejuvenator on abrasion loss of asphalt mixture. Generally, lower abrasion loss indicates the tested sample has better resistance to ravelling. The results obtained from Cantabro abrasion test are shown in Figure 8. For the control samples, the abrasion losses for unaged and LTA were 3.82% and 5.69%. It implies that long-term ageing makes asphalt mixture more susceptible to ravelling. Moreover, the corresponding result of rejuvenated samples was 4.14%, which was lower than that of LTA mixture and comparable to the unaged mixture. It testified that the resistance to ravelling was enhanced by incorporation with rejuvenator into aged mixture. This might be attributed to the improvement of bonding strength between rejuvenated asphalt binder and aggregate, which is in accordance with the results in Section 3.2.1.

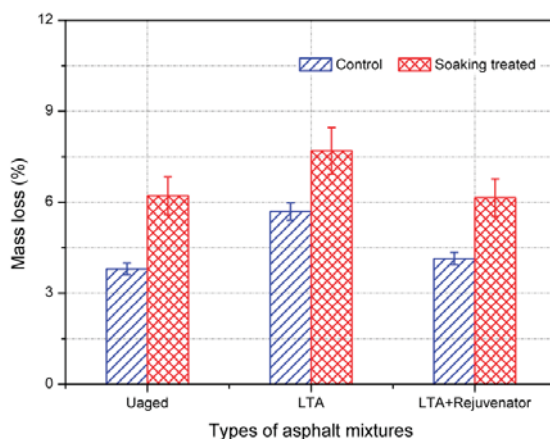


Figure 8. Cantabro abrasion test results of aged and rejuvenated asphalt mixtures.

For the same asphalt mixture, the abrasion loss of soaking treated samples was greater than that of the control group. There were similar increments in abrasion loss for the tested asphalt mixtures. After soaking treated, the increments of abrasion loss were 2.41%, 1.99% and 2.01% for unaged, LTA and rejuvenated samples, respectively. It is noted that the abrasion loss of rejuvenated samples after soaking treated was 6.15%, which was comparable to the corresponding result of control unaged mixture of 6.21%. In this circumstance, the result confirmed rejuvenator as an efficient additive to restore the resistance to particle loss of aged asphalt mixture.

3.2.3. High Temperature Performance

Figure 9 illustrates the obtained results for the wheel tracking test. For the same testing time, rutting depth of LTA sample was the lowest, followed by the rejuvenated and the unaged samples. According to Equation (4), dynamic stability results of unaged, long-term aged (LTA) and rejuvenated asphalt mixtures were 1165 times/mm, 3088 times/mm, and 1898 times/mm, respectively. Greater dynamic stability means better high temperature performance of asphalt mixture. Due to the stiffening effect of ageing, LTA asphalt mixture after ageing has better ability to resist permanent deformation under repeated loading, compared to the unaged mixture. Since rejuvenator softens the aged asphalt binder, the rutting resistance of rejuvenated mixture was midway between the unaged and the LTA mixtures, which can be attributed to the combined effect of rejuvenator and ageing.

Moreover, based on the test results the fitting equations of rutting depth and loading cycles were generated and are shown in Figure 9 as well. The equation parameters indicate that repeated loading is the least easily to induce the rutting for LTA mixtures, followed by the rejuvenated and unaged mixture. It can be concluded that softening effect of rejuvenator degrades the high temperature stability of asphalt mixture. It is noticeable that incorporation of rejuvenator into reclaimed asphalt mixture would increase the risk of permanent deformation for recycled asphalt pavement.

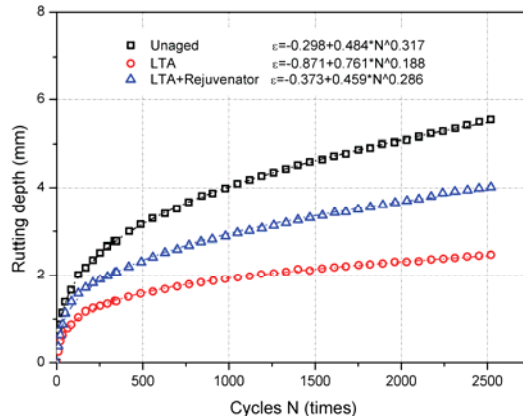


Figure 9. Wheel tracking test results of aged and rejuvenated asphalt mixtures.

To simulate the actual traffic load, the dynamic uniaxial compression test was performed to assess the high temperature performance of asphalt mixtures and the results are shown in Figure 10. The samples were tested at 60 °C and 0.7 MPa stress. For the same loading cycles, the permanent deformation of rejuvenated mixture was greater than the LTA mixture and lower than the unaged mixture, which was in accordance with the results of wheel tracking test. By using differential method, the deformation slope for each mixture was calculated and is presented in Figure 10 as well. Lower slope means the asphalt mixture is less susceptible to permanent deformation. The deformation curves for the asphalt mixture can be divided into two stage: initial stage and stable stage. The deformation slope of rejuvenated sample was slightly lower than the unaged sample during the whole test period, and their deformation curves were almost parallel in the stable stage. Moreover, the deformation slope of LTA sample was obviously lower than the rejuvenated sample. It also implies that rejuvenator softens the aged asphalt binder and lowers the ability of LTA mixture to resist permanent deformation.

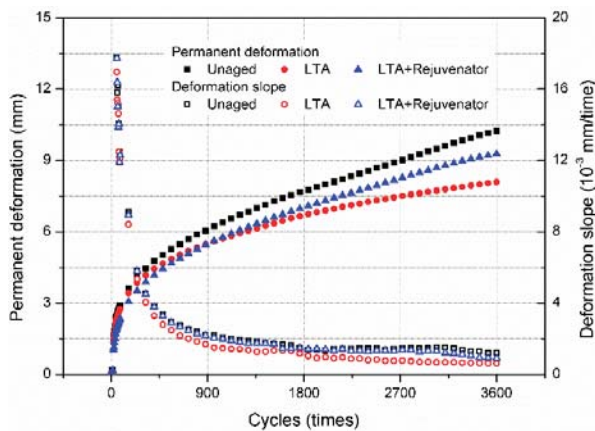


Figure 10. Dynamic uniaxial compression test results of aged and rejuvenated asphalt mixtures.

3.2.4. Cracking Resistance

Figure 11 illustrates the flexural strain and stiffness modulus of unaged, LTA and rejuvenated asphalt mixtures. Greater flexural strain means asphalt mixture has better ability to resist thermal cracking at low temperature. Compared to the unaged asphalt mixture, the flexural strain of LTA mixture decreased from $1724 \mu\epsilon$ to $1066 \mu\epsilon$ while the stiffness modulus correspondingly increased from 3467 MPa to 7095 MPa . It indicates that long-term ageing stiffened the asphalt mixture, resulting in inferior flexibility to low temperature cracking. Therefore, it is needed to improve the resistance to low temperature cracking of recycled asphalt pavement. By incorporating rejuvenator into LTA mixture, the flexural strain of rejuvenated asphalt mixture increased from $1066 \mu\epsilon$ to $1695 \mu\epsilon$, which was comparative to the unaged mixture. The result indicates the rejuvenator could improve the ability to resist low temperature cracking for reclaimed asphalt pavement in term of flexural strain. However, it should be noticed that the stiffness modulus of rejuvenated asphalt mixture was still greater than that of unaged mixture. In the present study, the stiffness modulus of rejuvenated and unaged asphalt mixtures were 5748 MPa and 3647 MPa , respectively. From this point of view, the rejuvenator cannot fully restore the stiffness modulus of concerned LTA mixture to the same level of unaged mixture, although they have similar flexural strains.

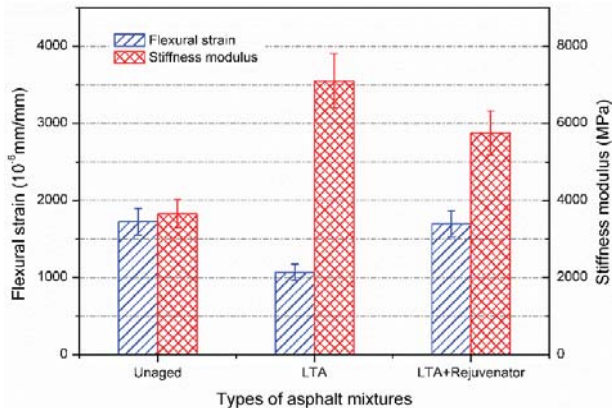


Figure 11. Three point bending test results of aged and rejuvenated asphalt mixtures.

Overlay tester was also employed to investigate the cracking resistance at intermediate temperature of $25 \text{ }^\circ\text{C}$ for aged and rejuvenated asphalt mixtures and the obtained results are shown in Figure 12. The tensile force was applied to the sample and recorded for each load cycle. The peak load is strongly dependent on the modulus of asphalt mixture. Generally, OT samples with high modulus requires greater tensile force to keep the constant tensile displacement. As seen in Figure 11, the stiffness modulus of LTA mixture was the greatest, followed by the rejuvenated and unaged samples, respectively. Therefore, the peak load of LTA, rejuvenated and unaged sample presents the similar trend for the same loading cycle.

Moreover, the peak load decreased dramatically before almost 50 cycles and then changes little for all the asphalt mixtures concerned in this study. During the testing period, reduction of peak load was the result of a decrease in modulus of asphalt mixture, which contributes to the cracking formation and propagation in the tested sample. In term of this view, the decrement of peak load after 1000 cycles can be also adopted to evaluate the cracking resistance of asphalt mixtures. Greater reduction means the asphalt mixture is more prone to reflective cracking. After OT test, the reductions of peak load were 43.2%, 86.3% and 58.1% for unaged, LTA and rejuvenated samples, respectively. Rejuvenator can recover the reflective cracking resistance of LTA mixture, which was in accordance with the results

in Figure 11. However, rejuvenated mixture showed slightly inferior resistance to reflective cracking compared with the unaged mixture. This might be attributed to the difference in stiffness modulus of rejuvenated and unaged mixtures.

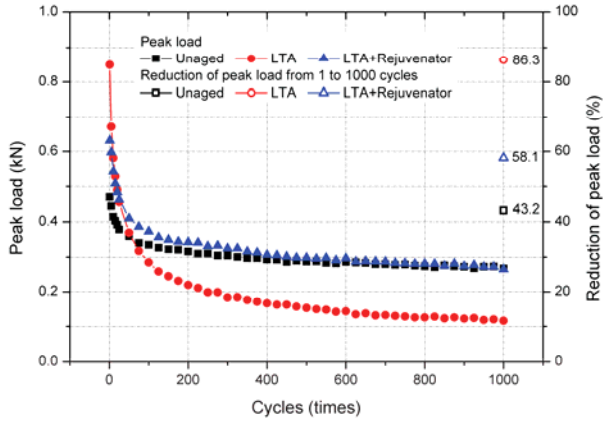


Figure 12. OT test results of aged and rejuvenated asphalt mixtures.

3.2.5. Fatigue Property

Fatigue damage of asphalt pavement is caused by repeated stresses and strains due to traffic load. Figure 13 presents the fatigue life of unaged, LTA and rejuvenated asphalt mixtures under different strain levels including 400 $\mu\epsilon$, 500 $\mu\epsilon$, 600 $\mu\epsilon$ and 700 $\mu\epsilon$, respectively. Compared to the fatigue life of unaged sample, there was significant improvement of fatigue life by incorporating rejuvenator into LTA asphalt mixture. Unlike the results in Section 3.2.4, rejuvenated mixture showed the most superior fatigue property within the whole testing strain levels. For OT test, a 2 mm gap between two bottom blocks was below the center of the sample. During the test period, stress concentration would induce the formation and propagation of reflective cracking. Compared to OT test result, the unexpected results of fatigue test might be attributed to their different test mechanisms and load patterns applied. Nevertheless, it can be concluded that rejuvenator prolongs the durability of recycled asphalt pavement in terms of fatigue life.

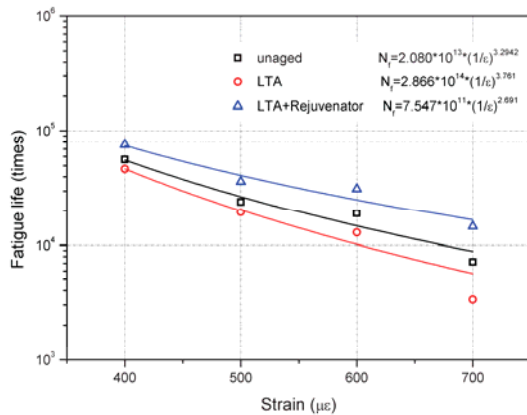


Figure 13. Four point bending fatigue test results of aged and rejuvenated asphalt mixtures.

According to Equation (8), power function was used to analyze the test data and the fitting results are shown in Figure 13. Generally, greater n value represents stronger strain dependency of fatigue life. The n value of rejuvenated samples was 2.691, which was lower than the unaged and LTA samples. It indicates that the fatigue life of rejuvenated mixture changes less due to the strain variation compared to the unaged and LTA mixtures. For instance, the fatigue life of rejuvenated mixture decreased by 78.7% when the strain increased from $400 \mu\epsilon$ to $700 \mu\epsilon$. The corresponding results for unaged and LTA mixture were 87.3% and 90.9%, respectively. It implies that rejuvenator leads the asphalt mixture to be less sensitive to strain level for the present fatigue test.

3.3. Dynamic Characteristics

Master curves of dynamic modulus for unaged, LTA and rejuvenated asphalt mixtures are shown in Figure 14. The generalized logistic sigmoidal function can be fitted well with the test data of dynamic modulus. The dynamic modulus of rejuvenated mixture was greater than that of unaged mixture and lower than the LTA mixture within the whole reduced frequency region. This is attributed to the combined effect of long-term ageing and rejuvenator on asphalt mixture. Long-term ageing enhances the stiffness of asphalt mixture, while the rejuvenator softens the aged asphalt mixture. Although the addition of rejuvenator decreases the modulus of LTA mixture, rejuvenated mixture still showed greater dynamic modulus than the unaged mixture. This was also confirmed by the stiffness modulus results obtained in Section 3.2.4.

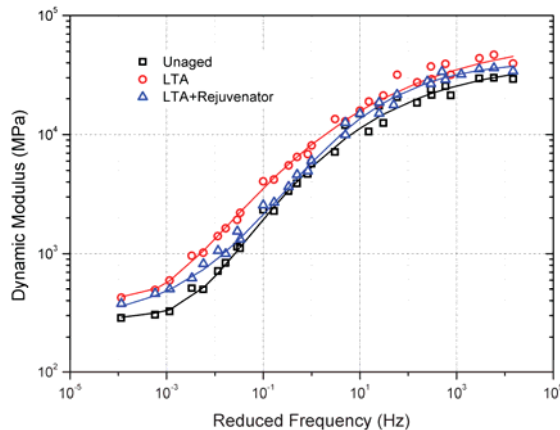


Figure 14. Master curves of dynamic modulus of aged and rejuvenated asphalt mixtures.

It is interesting to note that rejuvenated mixture has similar dynamic modulus with LTA mixture at low frequency (high temperature) and at high frequency (low temperature) regions. In addition, the master curves for rejuvenated and unaged mixtures almost overlapped when the reduced frequency ranged from 0.1 Hz to 1 Hz. The result indicates that rejuvenated mixture shows less dependence on load frequency at relatively high temperature than both the unaged and LTA mixtures, and the corresponding dependence for low temperature condition is just the opposite. Further study is recommended to be conducted on the effect mechanism of rejuvenator on frequency or temperature dependence of recycling asphalt mixture.

4. Conclusions

Laboratory ageing procedures were employed to prepare artificially aged asphalt binder and mixture. The effect of ageing and rejuvenator on asphalt binder and mixture was investigated by

a series of laboratory tests in this study. Based on the research results, conclusions could be drawn as follows.

- (1) Aged asphalt binder can be recovered to some extent by incorporating with rejuvenator. However, the effect of ageing and rejuvenator on asphalt binder differs from the physical properties concerned.
- (2) Rejuvenated asphalt mixture has comparable resistance to moisture damage and ravelling. ITSR value is recommended as an indicator for evaluating the moisture susceptibility for recycling asphalt pavement.
- (3) With similar flexural strain, rejuvenated asphalt mixture has greater modulus and inferior ability to resist reflective cracking than the unaged mixture.
- (4) Rejuvenated asphalt mixture, which is less sensitive to strain level, shows better fatigue property than unaged mixture.
- (5) Compared to unaged and LTA mixtures, rejuvenated mixture shows less dependence on frequency at high temperature regions and stronger dependence at low temperature regions.

The study compared the mechanical properties, durability, and dynamic characteristics of unaged, long-term aged, and rejuvenated asphalt mixtures by a series of available laboratory tests. Further study could be conducted on clarifying the rejuvenating mechanisms and effectiveness of different types of rejuvenators for reclaimed asphalt pavement. In addition, anti-ageing properties of rejuvenated asphalt mixture should be examined by both laboratory and field studies. Furthermore, critical indicators of rejuvenated asphalt mixture should be proposed to ensure the durability of recycled asphalt pavement.

Author Contributions: Data curation, Y.K.; Formal analysis, X.H.; Funding acquisition, X.H. and X.Z.; Investigation, P.P.; Methodology, X.H.; Writing—Original Draft, Y.K.; Writing—Review & Editing, P.P.

Funding: The authors acknowledge the support provided by the Open Fund of Key Laboratory of Highway Construction and Maintenance Technology in Loess Region, Ministry of Transport and Key Laboratory of Highway Construction and Maintenance Technology in Loess Region, Shanxi (No. KLTLR-Y14-6), the Science and Technology Project of Department of Transportation of Hubei Province (No. 2017-538-1-10), the Science Foundation of Wuhan Institute of Technology (No. K201846) and Open Fund of State Key Laboratory of Silicate Materials for Architectures, Wuhan University of Technology (SYSJ2018-22). Authors are very grateful for their financial support.

Acknowledgments: We would like to express our gratitude to the editors and the reviewers for their constructive and helpful review comments. The authors also wish to thank Shaopeng Wu and Yue Xiao (Wuhan University of Technology) for their help in providing the material used for experiments.

Conflicts of Interest: The authors declare no conflicts of interest.

References

1. Lin, J.; Hong, J.; Xiao, Y. Dynamic characteristics of 100% cold recycled asphalt mixture using asphalt emulsion and cement. *J. Clean. Prod.* **2017**, *156*, 337–344. [[CrossRef](#)]
2. Moghaddam, T.B.; Baaj, H. The use of rejuvenating agents in production of recycled hot mix asphalt: A systematic review. *Constr. Build. Mater.* **2016**, *114*, 805–816. [[CrossRef](#)]
3. Dinis-Almeida, M.; Castro-Gomes, J.; Sangiorgi, C.; Zoorob, S.E.; Afonso, M.L. Performance of warm mix recycled asphalt containing up to 100% RAP. *Constr. Build. Mater.* **2016**, *112*, 1–6. [[CrossRef](#)]
4. Bell, A. Summary report on the ageing of asphalt-aggregate system. *Transp. Res. Board* **1989**, *10*, 1–121.
5. Airey, G.D. State of the art report on ageing test methods for bituminous pavement materials. *Int. J. Pavement Eng.* **2003**, *4*, 165–176. [[CrossRef](#)]
6. Zaumanis, M.; Mallick, R.B. Review of very high-content reclaimed asphalt use in plant-produced pavements: state of the art. *Int. J. Pavement Eng.* **2015**, *16*, 39–55. [[CrossRef](#)]
7. Chen, M.; Leng, B.; Wu, S.; Sang, Y. Physical, chemical and rheological properties of waste edible vegetable oil rejuvenated asphalt binders. *Constr. Build. Mater.* **2014**, *66*, 286–298. [[CrossRef](#)]
8. Chen, M.; Xiao, F.; Putman, B.; Leng, B.; Wu, S. High temperature properties of rejuvenating recovered binder with rejuvenator, waste cooking and cotton seed oils. *Constr. Build. Mater.* **2014**, *59*, 10–16. [[CrossRef](#)]

9. Daniel, J.S.; Lachance, A. Mechanistic and volumetric properties of asphalt mixtures with recycled asphalt pavement. *Transport. Res. Rec.* **2005**, *1929*, 28–36. [[CrossRef](#)]
10. Molenaar, A.A.A.; Hagos, E.T.; van de Ven, M.F.C. Effects of ageing on the mechanical characteristics of bituminous binders in PAC. *J. Mater. Civ. Eng.* **2010**, *22*, 779–787. [[CrossRef](#)]
11. Xiao, F.; Airkhanian, S.N.; Wu, B. Fatigue and stiffness evaluations of reclaimed asphalt pavement in hot mix asphalt mixtures. *J. Test. Eval.* **2011**, *39*, 234–242.
12. Zaumanis, M.; Mallick, R.B.; Frank, R. Evaluation of different recycling agents for restoring aged asphalt binder and performance of 100% recycled asphalt. *Mater. Struct.* **2015**, *48*, 2475–2488. [[CrossRef](#)]
13. Ma, T.; Hussain, B.U.; Enad, M.; Hajj, E.Y. Estimating allowable RAP in asphalt mixes to meet target low temperature PG requirements. *J. Assoc. Asphalt Paving Technol.* **2010**, *79*, 473–495.
14. Kuang, D.; Jiao, Y.; Ye, Z.; Lu, Z.; Chen, H.; Yu, J.; Liu, N. Diffusibility enhancement of rejuvenator by epoxidized soybean oil and its influence on the performance of recycled hot mix asphalt mixtures. *Materials* **2017**, *10*, 574. [[CrossRef](#)] [[PubMed](#)]
15. Zaumanis, M.; Mallick, R.B.; Frank, R. Determining optimum rejuvenator dose for asphalt recycling based on superpave performance grade specifications. *Constr. Build. Mater.* **2014**, *69*, 159–166. [[CrossRef](#)]
16. Cavalli, M.C.; Zaumanis, M.; Mazza, E.; Partl, M.N.; Poulikakos, L.D. Ageing effect on rheology and cracking behaviour of reclaimed binder with bio-based rejuvenators. *J. Clean. Prod.* **2018**, *189*, 88–97. [[CrossRef](#)]
17. Ongel, A.; Hugener, M. Impact of rejuvenators on ageing properties of bitumen. *Constr. Build. Mater.* **2015**, *94*, 467–474. [[CrossRef](#)]
18. Ma, T.; Huang, X.; Zhao, Y.; Zhang, Y. Evaluation of the diffusion and distribution of the rejuvenator for hot asphalt recycling. *Constr. Build. Mater.* **2015**, *98*, 530–536. [[CrossRef](#)]
19. Zhang, Y.; van de Ven, M.F.C.; Molenaar, A.A.A.; Wu, S. Assessment of effectiveness of rejuvenators on artificially aged mortar. *J. Mater. Civ. Eng.* **2016**, *28*, 04016079. [[CrossRef](#)]
20. Wang, F.; Wang, Z.; Li, C.; Xiao, Y.; Wu, S.; Pan, P. The Rejuvenating Effect in Hot Asphalt Recycling by Mortar Transfer Ratio and Image Analysis. *Materials* **2017**, *10*, 574. [[CrossRef](#)] [[PubMed](#)]
21. *JTG F41—Technical Specification for Highway Asphalt Pavement Recycling*; Ministry of Transport of the People’s Republic of China: Beijing, China, 2008. (In Chinese)
22. Im, S.; Zhou, F.; Lee, R.; Scullion, T. Impacts of rejuvenators on performance and engineering properties of asphalt mixtures containing recycled materials. *Constr. Build. Mater.* **2014**, *53*, 596–603. [[CrossRef](#)]
23. Im, S.; Karki, P.; Zhou, F. Development of new mix design method for asphalt mixtures containing RAP and rejuvenators. *Constr. Build. Mater.* **2016**, *115*, 727–734. [[CrossRef](#)]
24. Zaumanis, M.; Mallick, R.B.; Poulikakos, L.; Frank, R. Influence of six rejuvenators on the performance properties of reclaimed asphalt pavement (RAP) binder and 100% recycled asphalt mixtures. *Constr. Build. Mater.* **2014**, *71*, 538–550. [[CrossRef](#)]
25. Pan, P.; Wu, S.; Hu, X.; Liu, G.; Li, B. Effect of material composition and environmental condition on thermal characteristics of conductive asphalt concrete. *Materials* **2017**, *10*, 218. [[CrossRef](#)] [[PubMed](#)]
26. *JTG F40—Technical Specifications for Construction Highway Asphalt Pavements*; Ministry of Transport of the People’s Republic of China: Beijing, China, 2004. (In Chinese)
27. *JTG E20—Ministry of Transport of the People’s Republic of China. Standard Test Methods of Bitumen and Bituminous Mixtures for Highway Engineering*; Ministry of Transport of the People’s Republic of China: Beijing, China, 2011. (In Chinese)
28. *ASTM D36/D36M-14e1—Standard Test Method for Softening Point of Bitumen (Ring-and-Ball Apparatus)*; ASTM International: West Conshohocken, PA, USA, 2014.
29. *ASTM D113-17—Standard Test Method for Ductility of Bituminous Materials*; ASTM International: West Conshohocken, PA, USA, 2017.
30. *ASTM D5/D5M-13—Standard Test Method for Penetration of Bituminous Materials*; ASTM International: West Conshohocken, PA, USA, 2013.
31. *ASTM D4402/D4402M-15—Standard Test Method for Viscosity Determination of Asphalt at Elevated Temperatures Using a Rotational Viscometer*; ASTM International: West Conshohocken, PA, USA, 2015.
32. *BS EN 12697-25—Bituminous Mixtures Test Methods: Cyclic Compression Test*; British Standard Institute: London, UK, 2016.
33. *Tex-248-F—Test Procedure for Overlay Test*; Texas Department of Transportation: Austin, TX, USA, 2009.

34. Hu, X.; Wang, N.; Pan, P.; Bai, T. Performance evaluation of asphalt mixture using brake pad waste as mineral filler. *Constr. Build. Mater.* **2017**, *138*, 410–417. [[CrossRef](#)]
35. Modarres, A.; Hamed, H. Developing laboratory fatigue and resilient modulus models for modified asphalt mixes with waste plastic bottles (PET). *Constr. Build. Mater.* **2014**, *68*, 259–267. [[CrossRef](#)]
36. AASHTO TP 62-07—Standard Test Method for Determining Dynamic Modulus of Hot-Mix Asphalt (HMA); American Association of State Highway and Transportation Officials: Washington, DC, USA, 2007.
37. Ruan, L.; Luo, R.; Hu, X.; Pan, P. Effect of bell-shaped loading and haversine loading on the dynamic modulus and resilient modulus of asphalt mixtures. *Constr. Build. Mater.* **2018**, *161*, 124–131. [[CrossRef](#)]
38. Pellinen, T.; Zofka, A.; Marasteanu, M.; Funk, N. Asphalt mixture stiffness predictive models. *J. Assoc. Asphalt Paving Technol.* **2007**, *76*, 575–625.



© 2018 by the authors. Licensee MDPI, Basel, Switzerland. This article is an open access article distributed under the terms and conditions of the Creative Commons Attribution (CC BY) license (<http://creativecommons.org/licenses/by/4.0/>).

Article

Assessment on Physical and Rheological Properties of Aged SBS Modified Bitumen Containing Rejuvenating Systems of Isocyanate and Epoxy Substances

Zhelun Li ¹, Xiong Xu ^{2,*}, Jianying Yu ^{1,*} and Shaopeng Wu ¹

¹ State Key Laboratory of Silicate Materials for Architectures, Wuhan University of Technology, Wuhan 430070, China; lizhelun@whut.edu.cn (Z.L.); wusp@whut.edu.cn (S.W.)

² School of Civil Engineering and Architecture, Wuhan Institute of Technology, Wuhan 430074, China

* Correspondence: xxucea@wit.edu.cn (X.X.); jyyu@whut.edu.cn (J.Y.);
Tel.: +86-158-7171-9331 (X.X.); +86-133-6728-9333 (J.Y.)

Received: 1 January 2019; Accepted: 13 February 2019; Published: 19 February 2019

Abstract: Styrene–butadiene copolymer (SBS)-modified bitumen (SMB) is widely applied in pavement construction. With yearly services, many SMB wastes urgently need to be reclaimed for repaving roads based on the objectives of environmental protection, landfill saving, as well as resource utilization. The present work is focused on the investigation of the physical and rheological properties of aged SMB incorporated with rejuvenating systems consisting of fluid catalytic cracking slurry (FCC slurry), C12–14 aliphatic glycidyl ether (AGE), diphenylmethane diisocyanate (MDI), and other additives. The rejuvenating systems containing the main components of 10% FCC slurry, 10%FCC/3%AGE, and 10%FCC/3%AGE/1% MDI were respectively recorded as R_a , R_b , and R_c . The results indicate that both R_b and R_c have obvious workability that make contributions for improving comprehensive physical properties while slightly reducing the softening point, which were also proven to be effective for the re-rejuvenation of re-aged binder. The higher viscous-elastic temperature caused by the agglomeration of binder molecules in aged SMB could be dropped to a lower value with rejuvenating systems, while improving the low-temperature crack resistance. With the use of the R_b and R_c rejuvenating systems, the high-temperature deformation resistance of aged SMB fell, approaching the performance of fresh SMB. Vibration noise consumption could be improved for aged SMB incorporated with R_b and R_c in the form of viscous loss, while the effects for re-aged SMB containing the same rejuvenating systems were weakened but still effective.

Keywords: SBS-modified bitumen; rejuvenating systems; physical properties; viscous-elastic temperature; rutting factor; vibration noise consumption

1. Introduction

Along with the booming development of highway construction in China, tri-block styrene–butadiene copolymer (SBS)-modified bitumen is widely applied in high-class pavement due to its advantageous high- and low-temperature performance, driving comfort, smooth surface, and abrasive resistance [1–4]. Despite that, during the in-service period, a series of physical and chemical changes resulting in the performance deterioration of SBS-modified bitumen (SMB) occur under the comprehensive effect of the natural environment such as heat, UV, oxygen, and rainwater [5–8]. Furthermore, a great deal of waste SMB is constantly produced and causes huge resource and landfill waste as well as environmental hazards [9,10]. Accordingly, the problem of high-quality rejuvenation for waste SMB urgently needs to be solved.

The aging of SMB includes not only oxidation and poly-condensation of base bitumen, but also the oxidative degradation of SBS, which differs from the aging of base bitumen [11]. Owing to the oxidative degradation of SBS, the road performances of SMB after long-term aging significantly drop to hardly meet standardized requirements [12–15]. Thus, the consideration regarding the comprehensive performance recovery of SMB should be taken for both aged bitumen and aged SBS. As of now, some publications have reported that the rejuvenation of aged SMB can be realized by adding fresh SMB and/or rich aromatic oils [16–20]. For instance, Gong et al. investigated the physical and chemical properties of aged SMB mixed with bio-oil derived from biodiesel residue, and discovered that the bio-oil could be used to achieve the goal of rejuvenating aged SMB and enhance its physical properties, while mitigating the highly-oxidized components aggregated and dispersing the asphalt molecules [21]. Chen et al. conducted a study using waste edible vegetable oil to rejuvenate aged asphalt binder containing SBS by testing the physical and rheological properties, and found that waste edible vegetable oil is suitable for the recycling of aged SBS modified asphalt with the result of better performance recovery [22].

Although these kinds of physical components have some advantages in restoring most of the properties of aged SMB, the performance recovery is only for aged bitumen binder and not aged polymer. In fact, some publications have reported that the oxidation and degradation of SBS would simultaneously occur during the oxidative aging step, with the destructed polymer pieces forming with oxygen-containing groups such as hydroxyl and carbonyl groups [23–26]. Considering the use of those groups, we propose an in-situ chemical reaction to amend the molecular structure of SBS polymer in order to improve the properties of bitumen binder. In view of this emerging idea, the novelty differs from other reports in trying to use the reactive components to make a partial connection among degraded polymer, and the high aromatic mixtures to adjust the chemical composition of aged virgin bitumen are both involved.

This present work aims to solve the issue of high-quality recycling of aged SMB by using the selected rejuvenating system consisting of fluid catalytic cracking slurry (FCC slurry), C12–14 aliphatic glycidyl ether (AGE), diphenylmethane diisocyanate (MDI), and other additives. The physical and rheological properties of aged SMB incorporating the rejuvenating systems were systematically investigated, and the re-rejuvenation effects of the selected rejuvenating system are discussed and analyzed.

2. Experimental

2.1. Raw Materials

The used SBS modified bitumen (SBS/bitumen, 5/100) was obtained in the laboratory by mixing linear SBS (1301, S/B = 30/70) and base bitumen (SK-70). FCC slurry was selected to improve the chemical components of aged bitumen binder. The relative mass percentages in saturates, aromatics, resins, and asphaltenes were 8.82%, 75.23%, 7.93%, and 8.02%, respectively. AGE is a low-viscosity end-epoxy molecule that can penetrate into the binder and disperse the agglomeration formed from aging. MDI was selected to limit the dropping high-temperature properties of rejuvenated SMB through the chemical consolidation reaction.

2.2. Aging Procedure of SMB

The evenly dispersed SMB specimens were standardly prepared for pressure aging vessel (PAV) aging. The aging experiments were as follows in order of the thin film oven test (TFOT, referring to ASTM D1754) and the PAV test (referring to ASTM D6521) [27], the lab conditions of which were 163 °C × 5 h and 100 °C × 2.1 MPa × 20 h (in air atmosphere) to simulate the short-term mixing and paving process and the long-term working aging of SMB, respectively.

2.3. Rejuvenation for Aged SMB

The aged SMB specimens above were quantitatively weighed and shifted to an agitated vessel for hot mix rejuvenation. Until the stable temperature of 150 °C was reached, the low-speed agitation started, while 10% FCC slurry, 3% AGE and other low amounts of additives with or without 1% MDI were respectively mixed into the binder for 20 min to prepare three kinds of rejuvenated SMB. The rejuvenating systems containing the main components of 10% FCC slurry, 10%FCC/3%AGE, and 10%FCC/3%AGE/1% MDI are respectively abbreviated as R_a , R_b , and R_c for reference in this manuscript.

2.4. Tests for Physical Properties

The physical properties of various SMB specimens as mentioned above, included viscosity at 135 °C, softening point, penetration at 25 °C, and ductility at 5 °C were measured according to ASTM D4402, ASTM D36, ASTM D5, and ASTM D113, respectively [28–31]. Additionally, the experimental results of the primary physical properties of fresh and PAV-aged SMB are presented in Table 1.

Table 1. Primary physical properties of styrene–butadiene copolymer modified bitumen (SMB) before and after pressure aging vessel (PAV) aging.

Technical Index	Fresh SMB	PAV-Aged SMB
Ductility at 5 °C (cm)	36.8	1.2
Softening point (°C)	70.5	63.1
Viscosity at 135 °C (Pa·s)	2.56	2.85
Penetration at 25 °C (dmm)	48	17

2.5. Tests for Rheological Properties

The rheological characteristics of the various SMB specimens mentioned above were tested using a dynamic shear rheometer (DSR, MCR101, Anton Paar, Graz, Austria). The tests for rheological properties were conducted under strain-controlled conditions at 10 rad/s with the heat rate of 2 °C/min between the temperature ranges of −10 and 80 °C. During the test, plates with an 8 mm diameter and a 2 mm gap below 30 °C and plates with a 25 mm diameter and a 1 mm gap above 30 °C were respectively used. According to the manufacturing specifications, related rheological parameters such as elastic modulus (G'), viscous modulus (G''), complex modulus (G^*), phase angle (δ), and rutting factor ($G^*/\sin \delta$) were simultaneously obtained to assess the rheological properties of rejuvenated SMB.

3. Results and Discussion

3.1. Effect of Rejuvenating Systems on the Physical Properties of Aged SMB

Table 2 presents the related experimental results regarding the physical properties and recovery rates of aged SMB incorporating rejuvenating systems. From the table, with rejuvenating systems, the improvement on the ductility and penetration of aged SMB was clearly visible, while the softening point and viscosity both dropped to some extent. The differences in the physical properties of rejuvenated SMB containing R_a , R_b , and R_c were easily observed in that R_b and R_c had significant advantages in making contributions to the ductility recovery, penetration recovery, and viscosity reduction of aged SMB—except for the softening point—in comparison with R_a . The explanation for the results is that the epoxy components play a vital effect in diffusing and dispersing the agglomerated substances of the aged binder. Meanwhile, compared with R_b , the slight weakness of R_c for improving the physical properties is the reaction consolidation caused between MDI and aged SMB.

Furthermore, the data show that the use of R_b and R_c for aged SMB promoted ductility recovery rates approaching 76.6% and 67.1%, penetration recovery rates of 112.5% and 95.9%, the viscosity indexes were 37.5% and 49.2%, and the softening point retention rates were 71.6% and 79.1% while the

results of rejuvenated SMB containing R_a were respectively 37.0%, 70.8%, 44.9%, and 79.7%. The data shown here indicate that the rejuvenating systems containing AGE with or without MDI can work better to both restore the physical properties of aged SMB and obtain rejuvenated SMB with various behaviors suitable for re-application.

Table 2. Physical properties and recovery rates of aged SMB incorporating rejuvenating systems.

Technical Index	Aged SMB	Rejuvenated SMB			Equation
		R_a	R_b	R_c	
Ductility at 5 °C (cm)	1.2	13.6	28.2	24.7	-
Softening point (°C)	63.1	56.2	50.5	55.8	-
Penetration at 25 °C (dmm)	17	34	54	47	-
Viscosity at 135 °C (Pa·s)	2.85	1.15	0.96	1.26	-
Ductility recovery rate (%)	-	37.0	76.6	67.1	$PCR = \frac{P_R}{P_F} \times 100\%$
Softening point retention rate (%)	-	79.7	71.6	79.1	
Penetration recovery rate (%)	-	70.8	112.5	95.9	
Viscosity recovery rate (%)	-	44.9	37.5	49.2	
Viscosity index (%)	-	-	-	-	

Note: In the equation, PCR refers to the performance recovery ratio for rejuvenated binder; P_R refers to the value for physical properties of rejuvenated binder; and P_F refers to the value for the physical properties of fresh binder.

3.2. Effect of Rejuvenating Systems on the Physical Properties of Second Aged SMB

Figures 1–4 display the physical properties of ductility, softening point, penetration, and viscosity of aged SMB containing R_b and R_c , respectively. It is clear that rejuvenated SMBs containing R_b or R_c , after second aging, almost lost their low-temperature ductility, accompanied by a rise in the softening point. When R_b and R_c were selected again for the rejuvenation of second-aged SMB, the ductility increased by 23.7 and 20.2 cm with the recovery rates of 67.7% and 57.6%, while the softening point decreased by 5.1 °C and 3.4 °C with retention rates of 74.5% and 80.6%. The results indicate that the rejuvenating system can, to some degree, restore the low-temperature properties of second-aged SMB and depress the significant deterioration of high-temperature properties.

Meanwhile, the penetration increased by 25 dmm and 21 dmm with recovery rates of 97.9% and 83.3%, which illustrates that the use of these kinds of rejuvenating systems was still effective in restoring the penetration of second-aged SMB. Lastly, the results of the viscosity index (46.1% and 65.2%) show that the viscous behavior of second-aged SMB were improved using R_b , and increased with the addition of MDI. In other words, the use of R_c was effective in restoring the low-temperature properties and limited the sharp fall of high-temperature properties for the second-aged SMB. To conclude, both R_b and R_c had good working abilities for recycling re-aged SMB in order to achieve better properties.

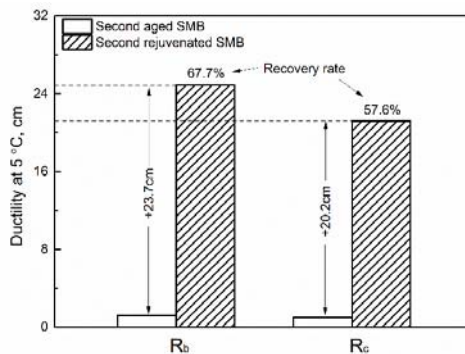


Figure 1. Effect of rejuvenating systems on the ductility of second-aged SMB.

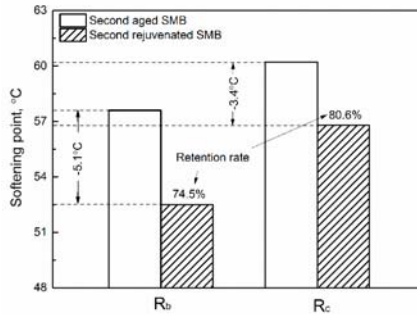


Figure 2. Effect of rejuvenating systems on the softening point of second-aged SMB.

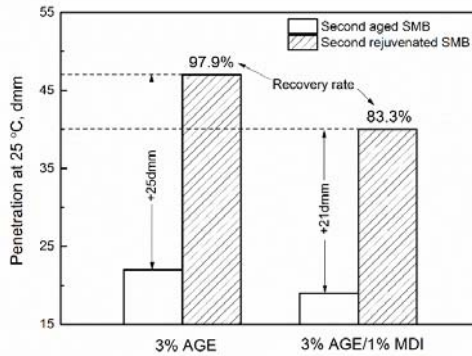


Figure 3. Effect of rejuvenating systems on the penetration of second-aged SMB.

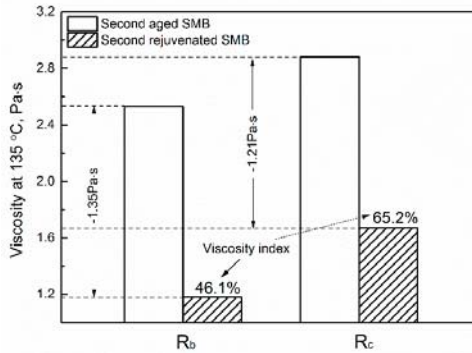


Figure 4. Effect of rejuvenating systems on the viscosity of second-aged SMB.

3.3. Effect of Rejuvenating Systems on the Viscous-Elastic Behavior of Aged SMB

The viscous-elastic characteristics of aged SMB with incorporated rejuvenating systems are presented in Figure 5. As depicted in Figure 5a, the values of G' and G'' of fresh SMB after aging increased, and the viscous-elastic temperature shifted to a higher level from 14.6 °C to 24.2 °C, indicating that the deformation resistance of fresh SMB increased during the aging period, causing the viscous portion (G'' after 14.6 °C) of fresh SMB to tend to the harder portion before 24.2 °C. From Figure 5b, it can be clearly seen that the values of G' and G'' of rejuvenated SMB were to some extent lower than the aged one, and the viscous-elastic temperature of aged SMB decreased with the addition of rejuvenators. Compared with R_a , the exhibited viscous behaviors of R_b - and

R_c -rejuvenated SMB were more obvious, the viscous-elastic temperatures of which decreased to 8.1 °C and 12.1 °C, respectively. The findings illustrate that rejuvenating systems such as R_b and R_c provide the benefit of activating the hard components in aged SMB to the viscous components, and improve the low-temperature crack resistance. The reason for the higher viscous-elastic temperature of rejuvenated SMB containing R_c depends upon the chemical reactions between the isocyanate groups and the formed reactive groups (e.g., $-OH$ and $-COOH$) in aged binder [9].

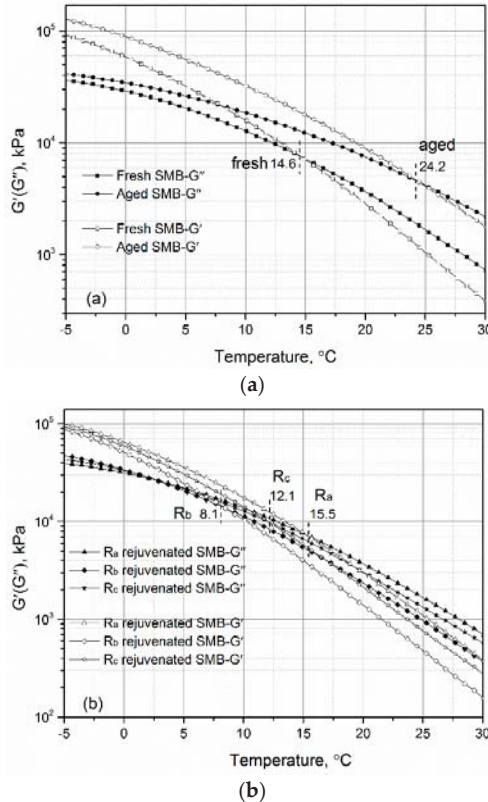


Figure 5. Viscous-elastic characteristics of (a) fresh and aged SMB and (b) rejuvenated SMB.

3.4. Effect of Rejuvenating Systems on the Physical Properties of Aged SMB

The loss tangent ($\tan \delta$) is a vital indicator used to depict the damping loss of materials. Figure 6 displays its tendency and changing law for various bitumen specimens containing fresh, aged, and rejuvenated types. Useful and interesting information obtained from the figure is that the loss tangent of fresh SMB decreased with aging, however, to a certain degree, the loss tangent of aged SMB increased with rejuvenation. In other words, with the hardening of fresh SMB during the aging period, the damping loss was reduced on the basis of elastic energy storage, and when the aged SMBs were rejuvenated with R_a , R_b , and R_c , the damping loss was recovered to a higher level. These results indicate that the vibration consumption of aged SMB containing rejuvenating systems may give them potential for use in reducing tire-ground noise. Differences in the damping loss of rejuvenated SMB incorporating R_b and R_c can mainly be attributed to the fact that the chemical reactions between isocyanate and aged SMB cause the partial hardening of the mixes, leading to a decrement of the viscous loss.

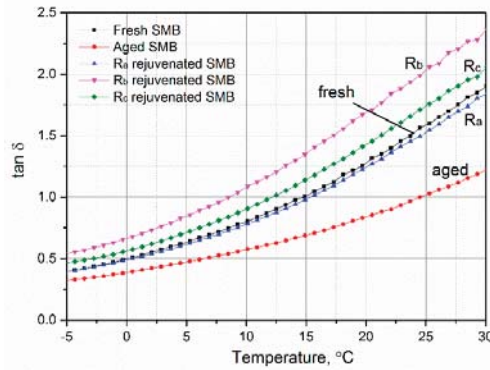


Figure 6. Effect of rejuvenating systems on the loss tangent of aged SMB.

3.5. Effect of Rejuvenating Systems on the Complex Modulus and Phase Angle of Aged SMB

The complex modulus and phase angle of aged SMB with rejuvenating systems are displayed in Figure 7. In the temperature region between -5 and 30 °C, the complex modulus and phase angle of fresh SMB respectively increased and decreased after aging. With rejuvenation, the complex modulus recovered to that of the original or lower level of fresh SMB, while the phase angle increased to near to or greater than the level of the fresh SMB. Compared with R_c , R_b had a more obvious role in promoting the temperature sensitivity of aged SMB. All of the results demonstrate that the rejuvenating systems, particularly R_b , can activate the transfer of the hard components to the soft components in aged SMB, allowing superior rheological characteristics to be obtained.

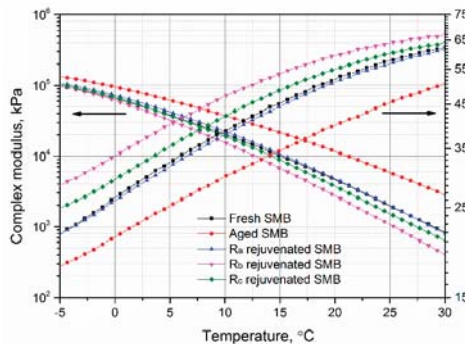


Figure 7. Effect of rejuvenating systems on the complex modulus and phase angle of aged SMB.

3.6. Effect of Rejuvenating Systems on Rutting Factor of Aged SMB

Figure 8 shows the rutting factors of aged SMB incorporating R_a , R_b , and R_c with increasing temperature. The temperature points inserted in this figure refer to the requirements of the SHRP specification. It can be seen that the rutting factor of fresh SMB visibly increased after aging, while the rutting factor reduced with rejuvenation, among which rejuvenated SMB containing R_b exhibited the greatest decrease. The results obtained indicate that the rejuvenation systems, especially R_b , had significant effects in decreasing the high-temperature characteristics of aged SMB. The findings show that depending upon the low-viscosity epoxy components in R_b , it can easily permeate into the aged binder and disperse the agglomerated substances formed by aging. Additionally, from the inserted figure, it can be seen that the rutting factor of rejuvenated SMB containing R_c was somewhat higher in comparison with that containing R_b , demonstrating that the chemical reaction between R_c and aged

SMB can cause an increase in the rutting factor, and thus improve the high-temperature deformation resistance of rejuvenated binder.

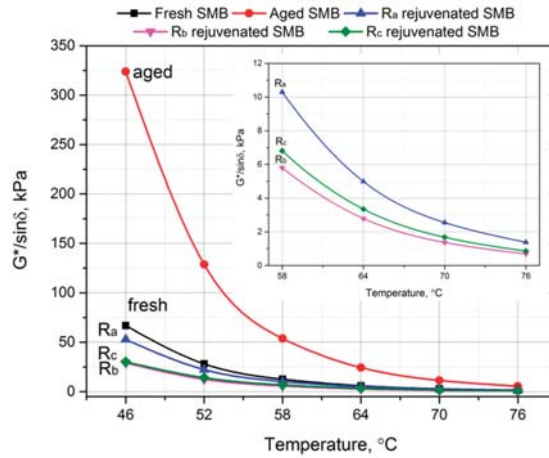


Figure 8. Rutting factor ($G^*/\sin \delta$) of fresh, aged, and rejuvenated SMB versus temperature.

3.7. Effect of Rejuvenation System on the Phase Angle of Second-Aged SMB

Due to better rejuvenation of aged SMB with R_c according to the discussions above, the research on the rheological properties of second-rejuvenated SMB is continued in this section. Figure 9 shows the effect of R_c on the phase angle of second-aged SMB. By comparing the phase angle trends of second-aged and rejuvenated SMB, it can be clearly obtained that the obvious differences of the phase angle were observed before approximately 50 °C (namely, the consistently higher phase angle of second-rejuvenated SMB), while the value of second-rejuvenated SMB was more similar to the fresh one. The results indicate that the flow behaviors of second-aged SMB can be restored by this kind of rejuvenation system. Regarding the first-rejuvenated SMB containing R_c , four phase angle-temperature points (−5, 5, 25, and 60 °C) were selected to comparatively analyze the rejuvenation ability of R_c . At these four positions, the second-rejuvenated SMB consistently exhibited a lower rheological characteristic when compared with the first-rejuvenated one, which indicates that the rejuvenation ability of R_c was weakened for second-aged SMB. To summarize, this type of rejuvenation system is still effective and useful to recover the rheological properties, and manifests better rejuvenation ability for second-aged SMB.

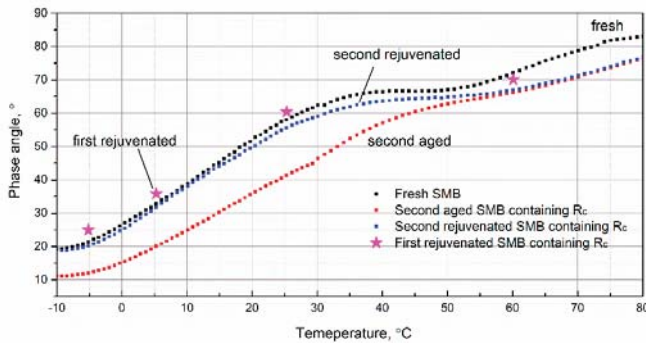


Figure 9. Effect of rejuvenating system on the phase angle of second-aged SMB.

3.8. Effect of Rejuvenation System on the Damping Loss of Second-Aged SMB

The two temperatures of 5 °C and 60 °C were selected as references to investigate the low- and high-temperature viscous damping loss of first- and second-rejuvenated SMB containing R_c , the data of which are presented in Table 3. As can be seen, regardless of whether the temperature was at 5 or 60 °C, the values of second-rejuvenated SMB were relatively lower when compared with the first-rejuvenated one. The results indicate that the viscous damping loss and deformation degree of second-rejuvenated SMB cannot recover to those of the first rejuvenation, but that second-rejuvenated SMB can also show relatively good rheological properties. The explanation for this is that the re-aging and re-rejuvenation bring about the agglomeration of higher-weight components and reaction-consolidation substances formed in the asphalt binder, and thus affect the consumption of vibration energy through the viscous loss of second-rejuvenated SMB.

Table 3. Loss tangent of first- and second-rejuvenated SMB containing 10%FCC/3%AGE/1% MDI (R_c) at 5 °C and 60 °C.

Samples	$\delta, ^\circ$		Tan δ	
	5 °C	60 °C	5 °C	60 °C
First-rejuvenated SMB containing R_c	35.8	70.1	0.72	2.76
Second-rejuvenated SMB containing R_c	31.8	66.9	0.62	2.34

4. Conclusions

This research aimed to achieve the high-quality performance recovery of aged SMB using rejuvenating systems consisting of FCC slurry, AGE, MDI, and other additives. The physical and rheological properties of rejuvenated SMB were systematically investigated and evaluated. Some worthy and interesting results are summarized below:

1. Both R_b and R_c rejuvenation systems of had significant advantages in contributing to improving the physical properties, including the ductility, penetration, and viscosity of aged SMB, while slightly reducing the softening point. Meanwhile, these kinds of rejuvenating systems were proved to still be applicable in the re-rejuvenation of re-aged binder.
2. The results of viscous-elastic temperatures indicate that oxidative aging promotes the hardening caused from the agglomeration of binder molecules for fresh SMB, which leads to a sharp increase of the viscous-elastic temperature. However, with the rejuvenating systems, particularly R_b , the viscous-elastic temperature of rejuvenated SMB could be somewhat reduced to improve the low-temperature crack resistance.
3. The obtained results on rutting factors indicate that the rejuvenating systems, especially R_b and R_c , are harmful to the high-temperature deformation resistance of rejuvenated SMB, but their performance level can still be close to that of fresh SMB with changing temperature.
4. The results of damping loss demonstrated that vibration consumption for noise was improved for aged SMB with incorporated R_b and R_c in the form of viscous loss, and furthermore, the effects for re-aged SMB using the same rejuvenating systems were weakened but still effective.
5. We recommend the use of rejuvenating systems containing epoxy—with or without isocyanate—for recycling aged SBS asphalt binder for application in the mid-temperature region. The disadvantage of rejuvenated binder lies in its poorer high-temperature workability. Despite that, more considerations regarding the performance restoration of degraded polymer in binder should be examined in future work.

Author Contributions: Z.L., X.X. and J.Y. conceived and designed the experiments; Z.L. and X.X. performed the experiments; Z.L., X.X., J.Y. and S.W. analyzed the data; J.Y. and S.W. contributed reagents/materials/analysis tools; Z.L. wrote this paper.

Funding: This research was funded by the Fundamental Research Funds for the Central Universities (2016-YB-010).

Acknowledgments: This work is supported by the Fundamental Research Funds for the Central Universities (2016-YB-010). The authors gratefully acknowledge the financial support. Thanks are also honestly due to my supervisor's responsibility for the experienced test and paper writing. We are very grateful for the help from our research project groups.

Conflicts of Interest: The authors declare no conflict of interest.

References

1. Zhao, X.Y.; Wang, S.F.; Wang, Q.; Yao, H.R. Rheological and structural evolution of SBS modified asphalts under natural weathering. *Fuel* **2016**, *184*, 242–247. [[CrossRef](#)]
2. Durrieu, F.; Farcas, F.; Mouillet, V. The influence of UV aging of a styrene/butadiene/styrene modified bitumen: Comparison between laboratory and on site aging. *Fuel* **2007**, *86*, 1446–1451. [[CrossRef](#)]
3. Cong, P.; Luo, W.; Xu, P.; Zhao, H. Investigation on recycling of SBS modified asphalt binders containing fresh asphalt and rejuvenating agents. *Constr. Build. Mater.* **2015**, *91*, 225–231. [[CrossRef](#)]
4. Xu, X.; Yu, J.Y.; Wang, R.Y.; Hu, J.X.; Xue, L.H. Investigation of road performances of reaction-rejuvenated SBS modified bitumen mixture. *Constr. Build. Mater.* **2018**, *183*, 523–533. [[CrossRef](#)]
5. Xiao, F.P.; Putman, B.; Amirhanian, S. Rheological characteristics investigation of high percentage RAP binders with WMA technology at various aging states. *Constr. Build. Mater.* **2015**, *98*, 315–324. [[CrossRef](#)]
6. Yan, C.Q.; Xiao, F.P.; Huang, W.; Quan, L. Critical matters in using Attenuated Total Reflectance Fourier Transform Infrared to characterize the polymer degradation in Styrene–Butadiene–Styrene-modified asphalt binders. *Polym. Test.* **2018**, *70*, 289–296. [[CrossRef](#)]
7. Xu, S.; Yu, J.Y.; Hu, C.B.; Qin, D.F.; Xue, L.H. Laboratory evaluation of rejuvenation effect of reactive rejuvenator on aged SBS modified bitumen. *Mater. Struct.* **2017**, *50*, 233. [[CrossRef](#)]
8. Nian, T.F.; Li, P.; Wei, X.Y.; Wang, P.H.; Li, H.S.; Guo, R. The effect of freeze-thaw cycles on durability properties of SBS-modified bitumen. *Constr. Build. Mater.* **2018**, *187*, 77–88. [[CrossRef](#)]
9. Xu, X.; Yu, J.Y.; Xue, L.H.; He, B.Y.; Du, W.; Zhang, H.; Li, Y. Effect of reactive rejuvenating system on physical properties and rheological characteristics of aged SBS modified bitumen. *Constr. Build. Mater.* **2018**, *176*, 35–42. [[CrossRef](#)]
10. Poulidakos, L.D.; Santos, S.; Bueno, M.; Kuentzel, S.; Hugener, M.; Partl, M.N. Influence of short and long term aging on chemical, microstructural and macro-mechanical properties of recycled asphalt mixtures. *Constr. Build. Mater.* **2014**, *51*, 414–423. [[CrossRef](#)]
11. Xu, X.; Yu, J.Y.; Zhang, C.L.; Cao, Z.L.; Gu, Y.; Xue, L.H. Effect of reactive rejuvenators on structure and properties of UV-aged SBS modified bitumen. *Constr. Build. Mater.* **2017**, *155*, 780–788. [[CrossRef](#)]
12. Singh, S.K.; Kumar, Y.; Ravindranath, S.S. Thermal degradation of SBS in bitumen during storage: Influence of temperature, SBS concentration, polymer type and base bitumen. *Polym. Degrad. Stabil.* **2018**, *147*, 64–75. [[CrossRef](#)]
13. Wang, T.; Xiao, F.P.; Amirhanian, S.; Huang, W.D.; Zheng, M.L. A review on low temperature performances of rubberized asphalt materials. *Constr. Build. Mater.* **2017**, *145*, 483–505. [[CrossRef](#)]
14. Hao, J.T.; Cao, P.Y.; Liu, Z.H.; Wang, Z.X.; Xia, S.F. Developing of a SBS polymer modified bitumen to avoid low temperature cracks in the asphalt facing of a reservoir in a harsh climate region. *Constr. Build. Mater.* **2017**, *150*, 105–113. [[CrossRef](#)]
15. RRasool, T.; Yao, H.R.; Hassan, A.; Wang, S.F.; Zhang, H.Y. In-field aging process of high content SBS modified asphalt in porous pavement. *Polym. Degrad. Stabil.* **2018**, *155*, 220–229. [[CrossRef](#)]
16. Chen, M.Z.; Xiao, F.P.; Putman, B.; Leng, B.B.; Wu, S.P. High temperature properties of rejuvenating recovered binder with rejuvenator, waste cooking and cotton seed oils. *Constr. Build. Mater.* **2014**, *59*, 10–16. [[CrossRef](#)]
17. Zhu, H.; Xu, G.; Gong, M.; Yang, J. Recycling long-term-aged asphalts using bio-binder/plasticizer-based rejuvenator. *Constr. Build. Mater.* **2017**, *147*, 117–129. [[CrossRef](#)]
18. Qiu, Y.J.; Ding, H.B.; Rahman, A.; Wang, W.Q. Damage characteristics of waste engine oil bottom rejuvenated asphalt binder in the non-linear range and its microstructure. *Constr. Build. Mater.* **2018**, *174*, 202–209. [[CrossRef](#)]

19. Asli, H.; Ahmadinia, E.; Zargar, M.; Mohamed, R.K. Investigation on physical properties of waste cooking oil–rejuvenated bitumen binder. *Constr. Build. Mater.* **2012**, *37*, 398–405. [[CrossRef](#)]
20. Zargar, M.; Ahmadinia, E.; Asli, H.; Karim, M.R. Investigation of the possibility of using waste cooking oil as a rejuvenating agent for aged bitumen. *J. Hazard. Mater.* **2012**, *233*, 254–258. [[CrossRef](#)]
21. Gong, M.H.; Yang, J.; Zhang, J.Y.; Zhu, H.R.; Tong, T.Z. Physical-chemical properties of aged asphalt rejuvenated by bio-oil derived from biodiesel residue. *Constr. Build. Mater.* **2016**, *105*, 35–45. [[CrossRef](#)]
22. Chen, M.Z.; Leng, B.B.; Wu, S.P.; Sang, Y. Physical, chemical and rheological properties of waste edible vegetable oil rejuvenated asphalt binders. *Constr. Build. Mater.* **2014**, *66*, 286–298. [[CrossRef](#)]
23. Xu, X.; Yu, J.Y.; Xue, L.H.; Zhang, C.L.; Zha, Y.G.; Gu, Y. Investigation of Molecular Structure and Thermal Properties of Thermo-Oxidative Aged SBS in Blends and Their Relations. *Materials* **2017**, *10*, 768. [[CrossRef](#)] [[PubMed](#)]
24. Xu, X.; Yu, J.Y.; Zhang, C.L.; Xu, S.; Xue, L.H.; Xie, D. Investigation of aging behavior and thermal stability of styrene-butadiene-styrene tri-block copolymer in blends. *Polymer (Korea)* **2016**, *40*, 947–953. [[CrossRef](#)]
25. Wu, S.P.; Pang, L.; Mo, L.T.; Chen, Y.C.; Zhu, G.J. Influence of aging on the evolution of structure, morphology and rheology of base and SBS modified bitumen. *Constr. Build. Mater.* **2009**, *23*, 1005–1010. [[CrossRef](#)]
26. Singh, R.P.; Desai, S.M.; Solanky, S.S.; Thanki, P.N. Photodegradation and stabilization of styrene-butadiene-styrene rubber. *J. Appl. Polym. Sci.* **2000**, *75*, 1103–1114. [[CrossRef](#)]
27. *Standard Practice for Accelerated Aging of Asphalt Binder Using a Pressurized Aging Vessel (PAV)*; ASTM D6521; ASTM International: West Conshohocken, PA, USA, 2018.
28. *Standard Test Method for Viscosity Determination of Asphalt at Elevated Temperatures Using a Rotational Viscometer*; ASTM D4402; ASTM International: West Conshohocken, PA, USA, 2015.
29. *Standard Test Method for Softening Point of Bitumen (Ring-and-Ball Apparatus)*; ASTM D36; ASTM International: West Conshohocken, PA, USA, 2014.
30. *Standard Test Method for Penetration of Bituminous Materials*; ASTM D5; ASTM International: West Conshohocken, PA, USA, 2013.
31. *Standard Test Method for Ductility of Asphalt Materials*; ASTM D113; ASTM International: West Conshohocken, PA, USA, 2017.



© 2019 by the authors. Licensee MDPI, Basel, Switzerland. This article is an open access article distributed under the terms and conditions of the Creative Commons Attribution (CC BY) license (<http://creativecommons.org/licenses/by/4.0/>).

Article

Investigation of the Potential Use of Calcium Alginate Capsules for Self-Healing in Porous Asphalt Concrete

Shi Xu ^{1,*}, Xueyan Liu ¹, Amir Tabaković ^{1,2,3}  and Erik Schlangen ¹ 

¹ Civil Engineering and Geosciences, Delft University of Technology, Delft 2628CN, The Netherlands; x.liu@tudelft.nl (X.L.); amir.tabakovic@dit.ie (A.T.); Erik.Schlengen@tudelft.nl (E.S.)

² Research Enterprise and Innovation, Dublin Institute of Technology, Dublin D07 EWW4, Ireland

³ School of Civil Engineering, University College Dublin, Dublin D04 K3H4, Ireland

* Correspondence: s.xu-1@tudelft.nl; Tel.: +31(0)-15-27-85944

Received: 21 November 2018; Accepted: 29 December 2018; Published: 7 January 2019

Abstract: Improving the healing capacity of asphalt is proving to be an effective method to prolong the service life of an asphalt pavement. The calcium alginate capsules encapsulating rejuvenator have been developed and proved to provide successful localized crack healing in asphalt mastic. However, it is not known whether this self-healing asphalt system will improve healing capacity of a full asphalt mix. To this aim, this paper reports on study which investigate effect of the calcium alginate capsules onto self-healing capacity of the porous asphalt mix. X-ray computed tomography (XCT) was used to visualize the distribution of the capsules in porous asphalt. The effect of the capsules on fracture resistance of porous asphalt concrete was studied by semi-circular bending (SCB) tests. A semi-circular bending and healing programme was carried out to evaluate the healing effect of these capsules in porous asphalt concrete. Indirect Tensile Stiffness Modulus (ITSM) tests were employed in order to investigate the influence of the capsules on the stiffness of the porous asphalt concrete. The results indicate that incorporating calcium alginate capsules significantly improve the healing capacity of porous asphalt concrete without compromising its performance.

Keywords: self-healing; asphalt; rejuvenation; calcium alginate capsules

1. Introduction

The asphalt healing phenomenon was first reported by Bazin in 1967 [1], since then, it captured attention of road engineers and material scientists. Self-healing became a hotspot in the research field of bituminous materials [2]. The healing mechanism can be explained as interpenetration and bonding, which means the cracking interface will disappear as a function of time that the cracking surfaces are brought in contact, and this phenomenon can be accelerated with a temperature increase [3]. In the life cycle of an asphalt pavement, the self-healing capacity of asphalt plays an important role against the fatigue damages, which is considered by pavement engineers in predicting the performance of asphalt pavement [2]. However, the intrinsic healing capacity of asphalt pavement itself is not sufficient to provide an efficient healing and significant life extension. Aimed to prolong the service life of asphalt pavement with self-healing technologies, more researches focused on the development of extrinsic healing methods in asphalt.

The induction healing methods, including induction heating and microwave heating, have been intensively investigated in the past ten years [4]. The concept lies on the induction heating of the embedded conductive particles to improve the healing capacity of a pavement [5–8]. The research findings indicate that the induction healing method has significant healing effect on the micro cracks in asphalt pavement. However, this technology could not reduce the ageing of asphalt or even accelerate the ageing with high temperature, which might results in a stiffer asphalt binder which leads to increased cracking and pavement failure.

Embedded rejuvenator encapsulation method provides an alternative extrinsic solution for self-healing asphalt. The concept is to add encapsulated healing agent (rejuvenator) in the asphalt mix, allowing the release of encapsulated healing agent on demand (upon cracking) and healing the crack by softening the aged binder allowing it flow which in turn closes the crack and repairs the damage [9]. To this aim, several encapsulation methods are developed, including epoxy capsules [10], Melamine-formaldehyde (MMF) modified capsules [11], calcium alginate capsules [9] and alginate fibres [12]. Among them, the calcium alginate capsules have the advantages of simple production process, low cost, environmental friendly and ability to encapsulate higher amounts of rejuvenator, which shows great potential for the application in self-healing asphalt [9,13].

Porous asphalt (PA), the open graded asphalt mix with a void content above 20%, was first designed and applied in 1972 in Netherlands [14]. The advantages of a PA include noise reduction, comfortable driving and reducing of splash and providing good water draining preventing water accumulation on the surface of the pavement. As a result, PA was implemented quickly in the asphalt pavement design in Netherlands and worldwide [15–17]. However, the high void content structure of porous asphalt concrete is prone to clogging, stripping, and accelerated aging [18,19]. Raveling of porous asphalt concrete, which is a failure at the surface of the pavement occurring within the stone-to-stone contact regions and causes the loss of aggregate particles from the road surface, is the main defect of porous asphalt [19]. It is caused by an increase of stiffness, reduction of relaxation capacity and formation of micro-cracks in the binder due to aging [20]. If the micro-cracks can be healed in the early stage, the problem of raveling can be prevented or delayed, as such the service life of porous asphalt will be prolonged [21].

In a previous paper, Xu et al. [9] successfully prepared calcium alginate capsules Figure 1. The X-ray tomography image of the capsule indicates that the calcium alginate capsules have a special porous structure instead of a traditional core-shell structure, which small rejuvenator droplets are encapsulated by porous media within the shell. The capsules thermal stability and compressive resistance were tested through thermogravimetric analysis (TGA) and micro-compressive tests. Xu et al. [9] showed that the calcium alginate capsules are able to survive the asphalt production and compaction process. Furthermore, the healing effect of these capsules were investigated with a three-point-bending testing and healing programme on asphalt mastic beams. The results indicated that the healing capacity of asphalt mastic beams with calcium alginate capsules are significantly higher than reference beams.

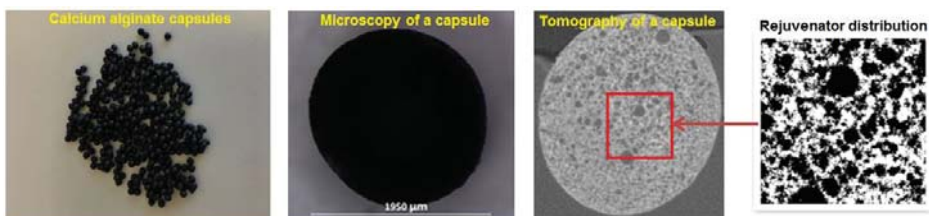


Figure 1. Calcium alginate capsules prepared by Xu et al. [9].

Xu et al. [9] explored general potential use of calcium alginate capsules in self-healing asphalt by investigating the capsule properties and the healing effect in mastic. However, the efficiency of the calcium alginate capsule encapsulating rejuvenator healing system in a full asphalt mix is unknown. Tabaković et al. [22] reported that self-healing rejuvenation process using compartmented alginate fibre encapsulating rejuvenator has very small effect on improvement of fatigue properties of PA mix. However, alginate capsules have ability to deliver higher amount of healing agent to the damaged area and as such have a better ability to repair the damage and restore asphalt pavement physical and mechanical properties. Therefore, the objective of this study was to investigate how calcium alginate capsules encapsulating rejuvenator affect the mechanical properties and the healing capacity of porous

asphalt concrete. To this aim, a porous asphalt mix with capsules was designed and compacted. A porous asphalt mixture without capsules was used as reference mixture. The distribution of the calcium alginate capsules was investigated by XCT. The healing capacity of the porous asphalt mix was evaluated by a testing and healing programme based on SCB tests. The standard ITSM tests were employed to investigate how these capsules influence the stiffness of porous asphalt concrete. The fluorescence characteristics of the rejuvenator was used to track the transportation of rejuvenator on fractured surface.

2. Experimental Method

2.1. Materials

2.1.1. Calcium-Alginate Capsules

Chemicals including sodium alginate, poly(ethylene-alt-maleic-anhydride) (PEMA) and CaCl_2 were used to prepare these capsules. Since the calcium alginate capsules were manufactured following the same procedures as the previous research, as shown in Figure 1, the prepared capsules have a uniform diameter of 1.95 mm and a honey-comb like porous structure [9]. These capsules also possessed the same mechanical resistance and thermal stability as previous research [9]. The industrial rejuvenator R20 encapsulated in these capsules was provided by Latexfalt B.V., Koudekerk aan den Rijn, Netherlands. The other chemicals used in this research were purchased from Sigma Aldrich, St. Louis, MO, USA.

Figure 2 shows the rejuvenator used in this research. The rejuvenator named as R20 is black under normal visible light (Figure 2a), which makes it very hard to distinguish the rejuvenator from asphalt mastic (Figure 2b). However, the fluorescent component of the rejuvenator turns into brown color under ultraviolet (UV) light (Figure 2c), which allows the rejuvenator being tracked once released via the fracture of capsules.

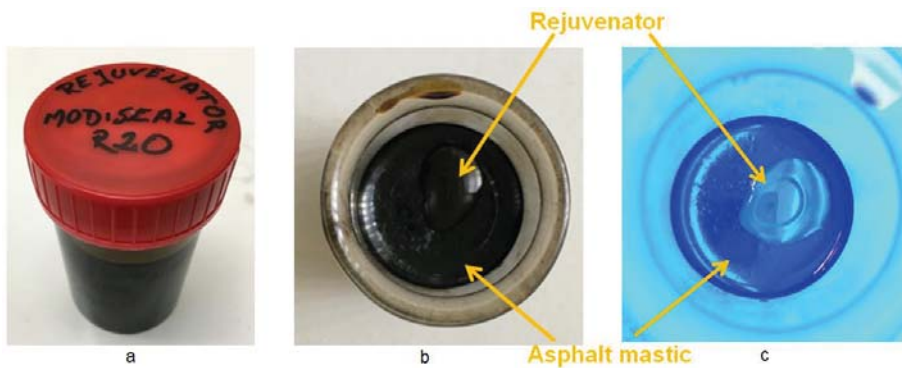


Figure 2. Rejuvenator R20: (a) normal appearance; (b) on asphalt mastic under visible light and (c) on asphalt mastic under UV light.

2.1.2. Porous Asphalt Mix and Test Specimens

The porous asphalt mix used in this study was based on the standard mix PA 0/11 (Table 1). Two types of mixtures were designed for the study, including a porous asphalt mix with capsules and a reference mix without capsules. According to the previous research, using calcium alginate capsules to replace 7% the volume of bitumen (8% by weight) possesses a higher healing efficiency. Thus, in this paper, the capsules were added in the porous asphalt mix by replacing 7% volume of the bitumen [9]. The bitumen used in the mix was the standard paving grade bitumen 70–100 provided by Vitol, London, UK. All the aggregates were Bestone (a kind of limestone widely used in PA construction

in Netherlands, Bontrup, Amsterdam, Netherlands) or byproduct of Bestone. The porous asphalt test samples used in this study include cylinders for Indirect Tensile Stiffness Modulus (ITSM) tests and semi-circular samples for Semi Circular Bending (SCB) tests. All the samples were drilled from 50 cm × 50 cm × 5 cm asphalt slabs.

Table 1. Mix composition of Porous Asphalt Concrete.

Mix Constituent	% Content in Mix	
	7% Capsules	Without Capsules
16 mm	8.5	8.5
11.2 mm	66.1	66.1
8 mm	8.5	8.5
5.6 mm	1.9	1.9
2 mm	6.9	6.9
500 μm	2.2	2.2
180 μm	0.7	0.7
125 μm	0.7	0.7
63 μm	4.5	4.5
Bitumen (70/100)	4.092	4.4
Capsules	0.363	0

The asphalt slabs were prepared in Rosmalen Heijmans infra BV (Heijmans Infra, Rosmalen, Netherlands). To prepare a slab, the designed pre-heated materials were carefully mixed in the laboratory rotating drum mixer (Figure 3a). Then, the mixed materials were collected and weighed to meet the required amount of an asphalt slab (Figure 3b). Subsequently, the weighed asphalt mix was poured into a mold and compacted with a manual roller compactor (Figure 3c). After a series of compaction cycles, the porous asphalt slab was produced (Figure 3d).

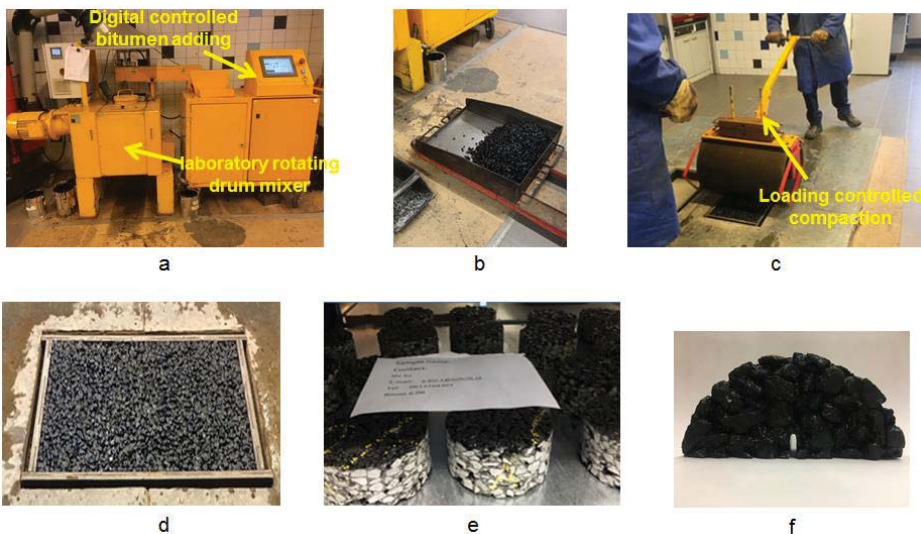


Figure 3. Porous asphalt slab preparation procedure: (a) mixing in laboratory rotating drum mixer; (b) weighing the mixture; (c) compaction with manually roller compactor; (d) prepared porous asphalt slab; (e) cylinder samples for ITSM tests and (f) semi-circular sample for SCB tests.

For the ITSM tests, cylinder samples (Figure 3e) were drilled from the slabs and at least 6 cylinder samples were tested for each group. For the SCB tests, the semi-circular samples (Figure 3f) were

acquired by sawing the asphalt cylinders in half and a notch was inserted in each SCB specimen and at least 6 SCB samples were tested for each group. For the XCT test, a small cylinder with 33.5 mm in diameter and 48.5 mm in height was drilled from mixture.

2.2. Testing Methods

2.2.1. XCT

The aim of using X-ray computed tomography (XCT) was to visualize the calcium alginate capsules within the porous asphalt mix. In this way, whether the capsules could survive the real asphalt production process and how they were distributed could be investigated. In this paper, the XCT was performed using a Phoenix Nanotom CT scanner (Baker Hughes, Wunstorf, Germany) (Figure 4). To fit the lateral dimension of the small porous asphalt cylinder, the resolution was set as 20 μm between each computed voxels.

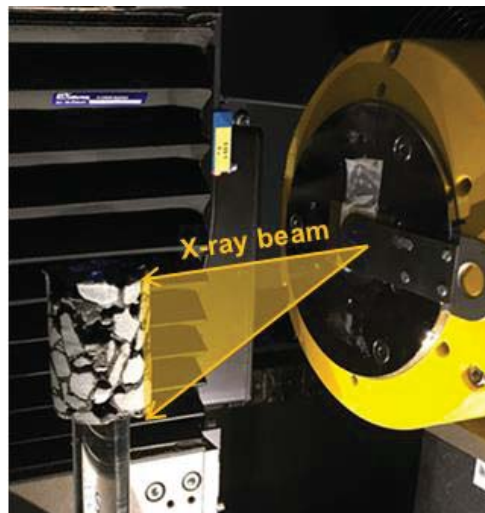


Figure 4. XCT scanning system for porous asphalt specimen.

2.2.2. ITSM Tests

ITSM test, according to the standard EN 12697-26:2012 [23], was employed to investigate the effect of the alginate capsules encapsulating rejuvenator on the stiffness modulus of the Porous Asphalt mix. The porous asphalt cylinder specimens used in the ITSM tests had a diameter of 100 ± 2 mm and height of 50 ± 1 mm. A Universal Testing Machine (Industrial process controls LTD, Melbourne, Australia) with a maximum load of 5 kN (UTM 5) with a temperature chamber was employed in the ITSM tests. The ITSM tests were performed at 20 °C at four different frequencies (8 Hz, 4 Hz, 2 Hz and 1 Hz). The Poisson's ratio of 0.22 was assumed for this porous asphalt concrete [21].

2.2.3. SCB Tests

The SCB tests were performed according to EN 12697-44:2010 [24]. Figure 5a shows the schematic diagram of the semicircular test samples. The SCB samples had a diameter of 100 ± 2 mm, thickness of 50 ± 1 mm and radius of 50 ± 1 mm. A notch was placed in the middle of each sample, with a notch length of 10 ± 0.2 mm and width of 3 ± 0.1 mm. The loading speed was set as 5 mm/min. In order to achieve a brittle fracture from the notch throughout the test specimen, the SCB tests were performed in a temperature controlled chamber (Industrial process controls LTD, Melbourne, Australia) at 0 °C.

A load vs displacement curve acquired from SCB tests is presented in Figure 5b. It indicated that the SCB tests were able to generate brittle fracture in the porous asphalt specimens.

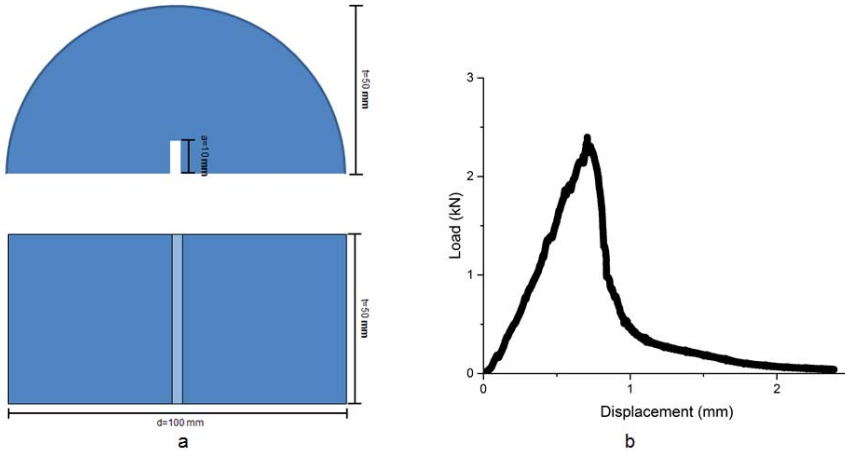


Figure 5. (a) Geometry information of the semi-circular porous asphalt specimens and (b) load vs displacement curve from SCB tests.

A UTM 15 testing system with temperature chamber was employed to perform the SCB tests (Figure 6). The support span for the SCB tests was set as 80 mm, which was 80% of the diameter of the specimen (Figure 6a). Figure 6b shows a fractured specimen after the SCB test, which indicates that the SCB tests allow crack initiate from the notch, propagate throughout the depth and finally lead to fracture.

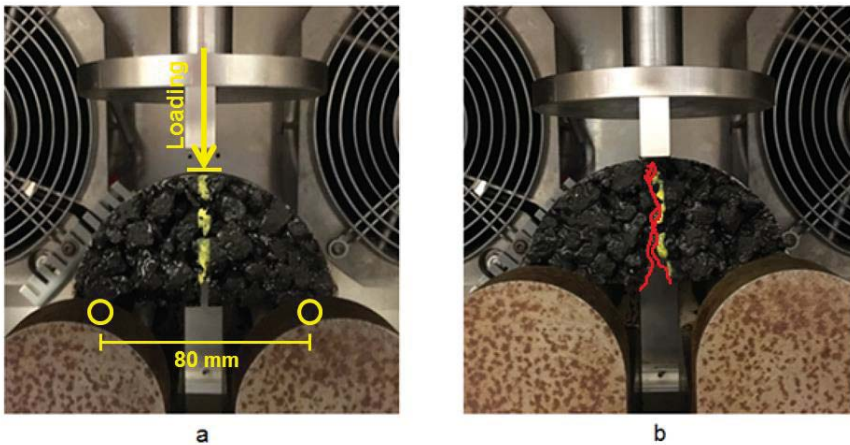


Figure 6. (a) SCB tests setup and (b) Fractured specimen after test.

In order to evaluate the fracture resistance of the specimens, the peak load, fracture toughness and fracture energy were also calculated from the SCB tests results.

The fracture toughness (K_{Ic}) and fracture energy (G_{Ic}) were calculated following the NCHRP09-46 (for straight line notch), and using Equations (1) and (4), respectively:

$$K_{Ic} = Y_{Ic(0.8)} \sigma_o \sqrt{\pi a} \tag{1}$$

where:

K_{Ic} = Fracture Toughness ($\text{Pa} \cdot \text{m}^{1/2}$)

$$\sigma_o = \text{Stress (N/m}^2\text{)}, \frac{P}{2rt} \quad (2)$$

P = Applied load (N)

r = Specimen radius (m)

t = Specimen thickness (m)

Y_{Ic} = Normalised Stress intensity factor,

$$Y_{Ic(0.8)} = 4.782 + 1.219 \left(\frac{a}{r} \right) + 0.63e^{7.045 \left(\frac{a}{r} \right)} \quad (3)$$

$$G_{Ic} = \frac{W_f}{A_{lig}} \quad (4)$$

where:

G_{Ic} = Fracture Energy (J/m^2),

W_f = Work of the fracture–area under the load displacement curve (J),

$$W_f = \int P du \quad (5)$$

P = Applied load (N),

u = load line displacement (m),

$$A_{lig} = \text{Ligament area (m}^2\text{)}, A_{lig} = (r - a) \times t \quad (6)$$

r = Specimen radius (m),

t = Specimen thickness (m),

a = Notch length (m).

2.2.4. Healing Efficiency Evaluation

In this research, evaluation of the healing efficiency was conducted with a testing and healing programme based on SCB tests. To evaluate the healing efficiency of a SCB specimen:

1. First, the initial peak load of the specimen were measured by the first SCB test;
2. Second, the fractured specimen was spliced to close the fracture face and conditioned at 23 °C for 20 h on a plain surface. In order to create a constant confinement to ensure the close of cracked surfaces, the specimens were carefully wrapped with tape during the healing process;
3. Subsequently, the second SCB test was performed to acquire the regained peak load of the specimen after healing. Afterwards, step 2 was repeated to perform another healing cycle following by the third SCB test.

Healing efficiency of the specimen was determined using healing index (HI), which was calculated with the peak load measured from three SCB tests, using equation (7):

$$HI = \frac{C_x}{C_1} \quad (7)$$

where:

HI = the healing index (%),

C_1 = original peak load of the sample;

C_x = fracture property after x cycles of healing.

3. Results and Discussion

3.1. XCT

Figure 7 shows the XCT scanning images of the porous asphalt sample. The XCT images clearly illustrate the porous structure and the material distribution of the porous asphalt mix. In both images, the calcium alginate capsules, which recognized as black round spots, are uniformly distributed in the porous structure together with asphalt mastic. The capsules within the structure preserve perfect round shape, which indicate that capsules are not damaged from the porous asphalt manufacture process. Meanwhile, the uniform distribution of capsules provides a higher chance to bring the capsules to the potential damaging sites, thus more comprehensive healing.

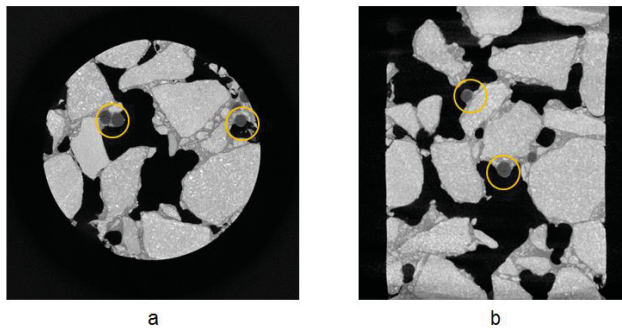


Figure 7. X-ray tomography images: (a) top view of the porous asphalt cylinder and (b) front view of porous asphalt cylinder.

3.2. Indirect Tensile Stiffness Modulus of Porous Asphalt Concrete

Figure 8 shows the stiffness modulus results at 20 °C. The results show that with calcium alginate capsules, the porous asphalt specimens have higher stiffness modulus than reference specimens in all loading frequency. It indicates that adding the alginate capsules encapsulating the rejuvenator in porous asphalt mix contributes to a higher stiffness, which means that the capsules have a reinforcing effect on the porous asphalt concrete, similarly as for the asphalt mastic mix [9].

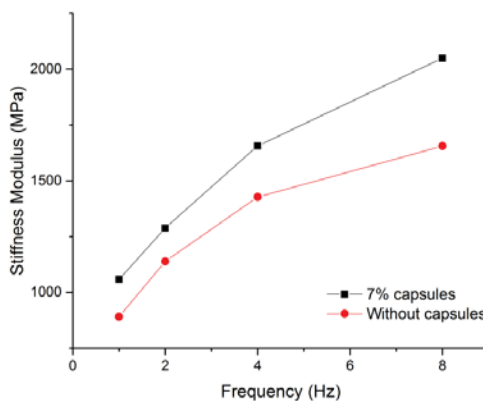


Figure 8. The stiffness modulus results at 20 °C.

3.3. Fracture Face of the Porous Asphalt Specimens after the SCB Test

The fracture surface of a SCB specimen with capsules is shown in Figure 9. As shown in Figure 9, broken capsules can be found on both sides of the fractured beams, which indicates that the capsules are

able to break upon propagation of cracks. On the other hand, presences of these capsules demonstrate that the calcium alginate capsules have not been crushed by mixing or compaction in this research, which indicates a huge potential for the application in field construction.

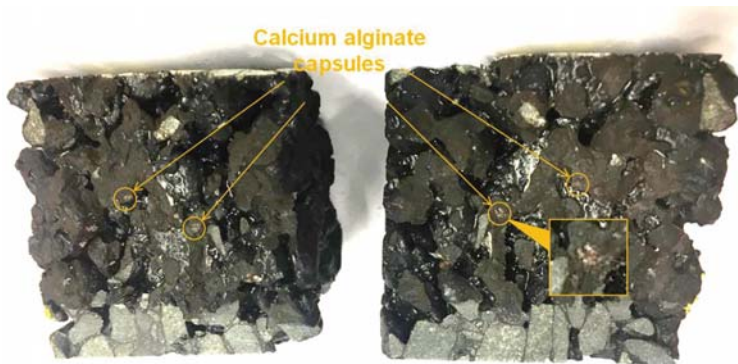


Figure 9. Fracture surface of a SCB specimen with 7% capsules.

In order to track the releasing of rejuvenator from the capsules which were broken in SCB tests, as shown in Figure 10, the sample on the right side of Figure 9 was exposed to UV light. Since the rejuvenator content of a single capsule is limited, there is no large area distribution of rejuvenator. However, following the locations of broken capsules in Figure 9, brown area can be found which refers to released rejuvenator under UV light.

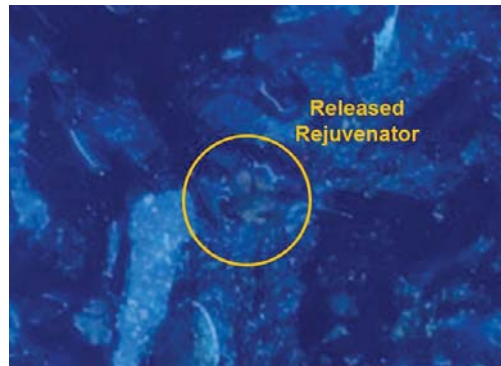


Figure 10. Released rejuvenator on fracture face.

3.4. Fracture Properties of the Porous Asphalt Concrete with Capsules

3.4.1. Peak Load

Figure 11 shows the peak load results from SCB tests. Generally, the porous asphalt specimens with capsules have relatively higher peak load than the reference specimens and the increase is more significant in the 2nd and the 3rd SCB tests. Which might be because of the reinforcing effect from capsules that contribute to the fracture resistance of the porous asphalt. The initial peak loads of both types of mix are much higher than the peak load from second and third SCB tests. Which means the 20 h healing period are not able to perform significant healing effect. It might because of the initial SCB test breaks the original arrangement of the aggregates of porous asphalt, and it is very hard to regain the interlocking effect between aggregates under room temperature and without any compaction.

The peak loads from the second time SCB tests for the same specimen are very close to the peak loads from the third time SCB tests. It indicates that except defects from first SCB tests, the second time SCB tests did not seriously defect the porous asphalt specimens, as such the healing effect plays a more important role. That is also the reason that specimens with capsules show much higher fracture resistance in the second and third time SCB tests.

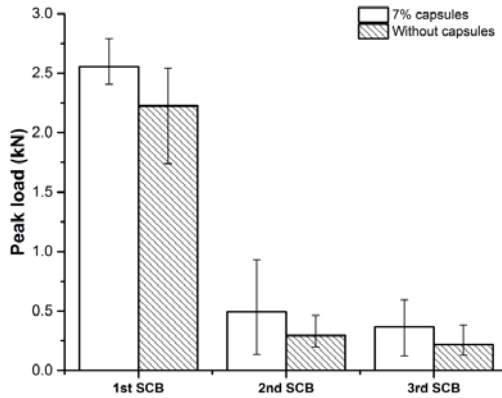


Figure 11. Peak load of SCB specimens.

3.4.2. Fracture Toughness

The fracture toughness of porous asphalt specimens, which directly represents the ability for the fracture resistance, are presented in Figure 12. As shown in Figure 12, due to the fracture damage, the initial toughness cannot be significantly healed in the following healing cycles, which is similar to the trend in Figure 11. However, SCB specimens with calcium alginate capsules show slightly higher toughness than reference specimens in all testing cycles. In the first time SCB tests, specimens with or without capsules does not show significant difference in toughness. While in the second time SCB tests, the specimens with capsules have an average toughness of $1.3 \times 10^5 \text{ Pa}\cdot\text{m}^{1/2}$, but specimens without capsules have only $8.4 \times 10^4 \text{ Pa}\cdot\text{m}^{1/2}$. Damages from the first time SCB tests have significant effect on the toughness of the SCB specimens and most of the toughness loss cannot be recovered. With calcium alginate capsules, the SCB specimens are able to achieve more healing in toughness.

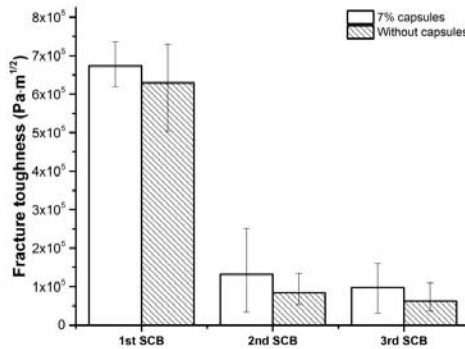


Figure 12. Fracture toughness of SCB specimens.

3.4.3. Fracture Energy

Figure 13 presents the fracture energy results from SCB tests. The fracture energy calculation considers the area beneath the load-displacement curve, which is indicative of fracture resistance in the

whole testing process that from the initiation of crack to the failure of sample. Similar to peak load and toughness, the first time SCB test results are very close, Nevertheless, SCB specimens with capsules consumes significantly higher energy than reference specimens. It indicates that the encapsulated rejuvenator released upon fracture, wet the fracture face and generate more bonds than reference specimens. Hence the SCB specimens with capsules accumulate more energy during the rest period and show much more healing than reference samples.

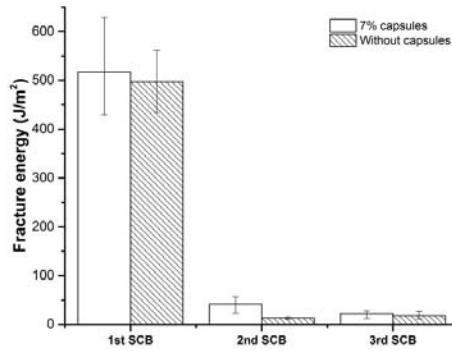


Figure 13. Fracture energy of SCB specimens.

3.4.4. Healing Efficiency

In this research, the healing efficiency was evaluated by the peak load healing ratio during rest periods. The healing results are presented in Figure 14. The results show that the SCB specimens with capsules are able to restore 19.3% of the initial peak force, which is 6% higher than the specimens without capsules. In the third time SCB tests, SCB specimens with capsules can still achieve a healing ratio of 14.3%. Without capsules, the healing effect is only 9.9%. Figure 14 also illustrates that even with calcium alginate capsules, the healing effect on such a serious fracture is very limited. Although the application of calcium alginate capsules largely improved the healing capacity, the limitation of these capsules as well as other rejuvenation methods lies on the damage level. The calcium alginate capsules are more capable of micro-crack healing, aimed to close crack at early stage thus preventing serious defect in asphalt pavement. In this way, the calcium alginate capsules possess a healing potential in the application in construction field.

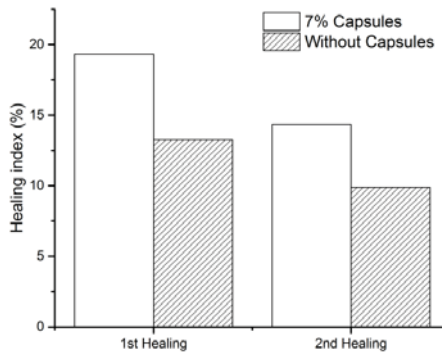


Figure 14. Healing index of SCB specimens.

This research demonstrates that addition of calcium alginate capsules with encapsulated rejuvenator increases the healing efficiency of porous asphalt mix. However, this healing effect will decrease if a damage is beyond the healing capacity.

4. Conclusions

This study explores the potential use of calcium alginate in porous asphalt and following conclusions are drawn:

- XCT is an effective method to analyze the structure and material distribution in porous asphalt mix. In XCT images, the presence of capsules in the porous asphalt mix demonstrate that calcium alginate capsules are able to survive asphalt manufacture process. The uniform distribution of capsules indicates a more comprehensive healing potential in porous asphalt;
- From the ITSM tests results, application of these calcium alginate capsules shows reinforcing effect by improving the stiffness modulus of the porous asphalt mix;
- After SCB tests, the presence of capsules on the fracture surfaces indicates that calcium alginate capsules are able to fracture upon the propagation of cracks. By this means, the encapsulated rejuvenator are able to release and heal the damage site;
- In the SCB testing and healing programme, samples with capsules are able to achieve a healing index that is 6% higher than the reference samples, which means addition of calcium alginate capsules improves the healing capacity of asphalt during the porous asphalt fracture and healing cycles;
- However, samples with capsules could only achieve a maximum healing index of 19% in the healing cycles, which indicates that if the damage beyond the healing capacity, the calcium alginate capsules are not able to recover all the losing properties especially interlocking effect between aggregates;
- The fluorescent component of rejuvenator allows tracking of the transportation of rejuvenator, which in turn could evaluate the healing effect.

Finally, this research initially explores the potential use of calcium alginate capsules in porous asphalt, the authors will continue the research on investigation of capsules on fatigue properties of PA and optimization of the calcium alginate capsules healing system. In comparison to the induction healing method, calcium alginate capsules show limited healing capacity of a PA. Thus, the future research will be focused on the development of a combined healing system which calcium alginate capsules are incorporated in induction healing to achieve an optimum healing which combines both effective crack healing and aged binder rejuvenation.

Author Contributions: S.X., X.L., A.T. and E.S. conceived and designed the experiments; S.X. performed the experiments and analyzed the data; S.X., X.L., A.T. and E.S. wrote the paper.

Funding: This research was funded by China Scholarship Council, grant number 201506950066.

Acknowledgments: The help of Heijmans in making all the porous asphalt specimens used in the research is greatly appreciated. We thank Latexfalt for providing the rejuvenator. Support from the technicians from the pavement engineering department and Microlab in TUDelft are also appreciated.

Conflicts of Interest: The authors declare no conflict of interest.

References

1. Bazin, P.; Saunier, J. Deformability, fatigue and healing properties of asphalt mixes. In Proceedings of the International Conference on the Structural Design of Asphalt Pavements, Ann Arbor, MI, USA, 7–11 August 1967.
2. Sun, D.; Sun, G.; Zhu, X.; Guarin, A.; Li, B.; Dai, Z.; Ling, J. A comprehensive review on self-healing of asphalt materials: Mechanism, model, characterization and enhancement. *Adv. Colloid Interface Sci.* **2018**, *256*, 65–93. [[CrossRef](#)] [[PubMed](#)]
3. Kim, Y.R.; Little, D.N.; Burghardt, R. SEM analysis on fracture and healing of sand-asphalt mixtures. *J. Mater. Civ. Eng.* **1991**, *3*, 140–153. [[CrossRef](#)]
4. Xu, S.; García, A.; Su, J.; Liu, Q.; Tabaković, A.; Schlangen, E. Self-healing asphalt review: From idea to practice. *Adv. Mater. Interfaces* **2018**, *5*, 1800536. [[CrossRef](#)]

5. García, Á.; Schlangen, E.; van de Ven, M.; van Vliet, D. Induction heating of mastic containing conductive fibers and fillers. *Mater. Struct.* **2011**, *44*, 499–508. [[CrossRef](#)]
6. Liu, Q.; Schlangen, E.; van de Ven, M. Induction healing of porous asphalt concrete beams on an elastic foundation. *J. Mater. Civ. Eng.* **2012**, *25*, 880–885. [[CrossRef](#)]
7. Gallego, J.; del Val, M.A.; Contreras, V.; Páez, A. Heating asphalt mixtures with microwaves to promote self-healing. *Constr. Build. Mater.* **2013**, *42*, 1–4. [[CrossRef](#)]
8. Norambuena-Contreras, J.; Garcia, A. Self-healing of asphalt mixture by microwave and induction heating. *Mater. Des.* **2016**, *106*, 404–414. [[CrossRef](#)]
9. Xu, S.; Tabaković, A.; Liu, X.; Schlangen, E. Calcium alginate capsules encapsulating rejuvenator as healing system for asphalt mastic. *Constr. Build. Mater.* **2018**, *169*, 379–387. [[CrossRef](#)]
10. García, Á.; Schlangen, E.; van de Ven, M.; Sierra-Beltrán, G. Preparation of capsules containing rejuvenators for their use in asphalt concrete. *J. Hazard. Mater.* **2010**, *184*, 603–611. [[CrossRef](#)] [[PubMed](#)]
11. Su, J.-F.; Qiu, J.; Schlangen, E. Stability investigation of self-healing microcapsules containing rejuvenator for bitumen. *Polym. Degrad. Stab.* **2013**, *98*, 1205–1215. [[CrossRef](#)]
12. Tabaković, A.; Post, W.; Cantero, D.; Copuroglu, O.; Garcia, S.; Schlangen, E. The reinforcement and healing of asphalt mastic mixtures by rejuvenator encapsulation in alginate compartmented fibres. *Smart Mater. Struct.* **2016**, *25*, 084003. [[CrossRef](#)]
13. Xu, S.; Tabaković, A.; Liu, X.; Schlangen, E. Preparation of calcium alginate capsules and the application in asphalt mastic. In Proceedings of the 6th International Conference on Self-Healing Materials, Friedrichshafen, Germany, 25–28 June 2017.
14. Van Der Zwan, J.T.; Goeman, T.; Gruis, H.; Swart, J.; Oldenburger, R. Porous asphalt wearing courses in the Netherlands: State of the art review. *Transp. Res. Rec.* **1990**, *1265*, 95–110.
15. McDaniel, R.; Thornton, W. Field evaluation of a porous friction course for noise control. In Proceedings of the Annual Meeting of the Transportation Research Board, Washington, DC, USA, 9–13 January 2005.
16. Bolzan, P.; Nicholls, J.; Huber, G. Searching for superior performing porous asphalt wearing courses. In Proceedings of the 80th Transportation Research Board Annual Meeting, Washington DC, USA, 7–11 January 2001.
17. Pasetto, M.; Baldo, N. Comparative performance analysis of bituminous mixtures with EAF steel slags: A laboratory evaluation. In Proceedings of the 2008 Global Symposium on Recycling, Waste Treatment and Clean Technology, Cancun, Mexico, 12–15 October 2008; pp. 565–570.
18. Kim, H.; Sokolov, K.; Poulidakos, L.; Partl, M. Fatigue evaluation of porous asphalt composites with carbon fiber reinforcement polymer grids. *Transp. Res. Re. J. Transp. Res. Board* **2009**, *2116*, 108–117. [[CrossRef](#)]
19. Klomp, A. *Life Period of Porous Asphalt*; Dutch Road and Hydraulic Engineering Institute Report: Rijkswaterstaat, The Netherlands, 1996.
20. Hagos, E.T. The Effect of Aging on Binder Properties of Porous Asphalt Concrete. Ph.D. Thesis, Delft University of Technology, Delft, The Netherlands, 2008.
21. Liu, Q.; García, Á.; Schlangen, E.; van de Ven, M. Induction healing of asphalt mastic and porous asphalt concrete. *Constr. Build. Mater.* **2011**, *25*, 3746–3752. [[CrossRef](#)]
22. Tabaković, A.; Schuyffel, L.; Karač, A.; Schlangen, E. An evaluation of the efficiency of compartmented alginate fibres encapsulating a rejuvenator as an asphalt pavement healing system. *Appl. Sci.* **2017**, *7*, 647. [[CrossRef](#)]
23. Bituminous Mixtures. *Test Methods for Hot Mix Asphalt, Part 26: Stiffness*; EN 12697-26; CEN: Brussel, Belgium, 2004.
24. Bituminous Mixtures. *Test Methods for Hot Mix Asphalt, Part 44: Crack Propagation by Semi-Circular Bending Test*; EN 12697-44; CEN: Brussel, Belgium, 2010.



Article

Microfluidic Synthesis of Ca-Alginate Microcapsules for Self-Healing of Bituminous Binder

Benan Shu ¹, Shaopeng Wu ^{1,*}, Lijie Dong ², Qing Wang ² and Quantao Liu ¹

¹ State Key Laboratory of Silicate Materials for Architectures, Wuhan University of Technology, Wuhan 430070, China; shuba@whut.edu.cn (B.S.); liuqt@whut.edu.cn (Q.L.)

² State Key Laboratory of Advanced Technology for Materials Synthesis and Processing, School of Materials Science and Engineering, Wuhan University of Technology, Wuhan 430070, China; lijie@whut.edu.cn (L.D.); 254546@whut.edu.cn (Q.W.)

* Correspondence: wusp@whut.edu.cn; Tel./Fax: +86-(0)27-87054920

Received: 11 April 2018; Accepted: 17 April 2018; Published: 19 April 2018

Abstract: This work aims to develop an original alginate micro-emulsion combining with droplets microfluidic method to produce multinuclear Ca-alginate microcapsules containing rejuvenator for the self-healing of bituminous binder. The sizes of the Ca-alginate microcapsules could be easily controlled by tuning flow rates of the continuous and dispersed phases. The addition of a surfactant Tween80 not only improved the stability of the emulsion, but it also effectively reduced the size of the microcapsules. Size predictive mathematical model of the microcapsules was proposed through the analysis of fluid force. Optical microscope and remote Fourier infrared test confirmed the multinuclear structure of Ca-alginate microcapsules. Thermogravimetric analysis showed that the microcapsules coated with nearly 40% rejuvenator and they remained intact during the preparation of bitumen specimen at 135 °C. Micro self-healing process of bituminous binder with multinuclear Ca-alginate microcapsules containing rejuvenator was monitored and showed enhanced self-healing performance. Tensile stress-recovery test revealed that the recovery rate increased by 32.08% (in the case of 5% microcapsules), which meant that the Ca-alginate microcapsules containing rejuvenator could effectively enhance the self-healing property of bituminous binder.

Keywords: Ca-alginate microcapsules; microfluidic; self-healing; bitumen

1. Introduction

Self-healing materials as a kind of intelligent material have attracted increasing interest because it can automatically repair the internal structural damage of the material [1–6]. Bitumen-a is widely used material in pavements has a limited service life. The bituminous pavement would produce micro cracks under the action of load, temperature, ultraviolet light, and so on. Although it has a certain self-healing ability, it will develop into a macro crack under the action of continuous traffic load [7–10]. In view of this, bitumen containing various capsules with self-healing property to prolong its service life has been widely investigated [11–15]. However, synthesis of those capsules generally has some disadvantages: limited encapsulation, high cost, and complex synthesis process. Sodium alginate, for its low cost, ease of use, and non-toxicity has been intended to be used to prepare microcapsules for the self-healing of bitumen. Garcia et al. [16,17] reported on the fabrication of porous calcium alginate spheres containing sunflower oil for the self-healing of bitumen mixture. The oil content of the capsules prepared by this method was limited and the particle size was too large to repair the micro cracks in the bitumen. Size distribution would influence self-healing performance of microcapsules in bitumen [18,19]. In view of this, different-sized and high rejuvenator loading calcium alginate microcapsules are badly needed.

At present, there are two mechanisms for the synthesis of alginate microcapsules: forward gelation and reverse gelation. For the forward gelation, Ren et al. [20] reported using oil/water/oil (O/W/O) double emulsions as templates to synthesize alginate microcapsules with oil core by a microfluidic device. The effect of the inner and outer diameters of quartz glass tube on the size of Ca-alginate microcapsules was analyzed. Kuan-Wen Yeh et al. [21] reported that Ca-alginate microcapsules with tea-tree oil were synthesized after the addition of calcium chloride solution to the sodium alginate solution in the flask with mixing and the release model was studied. The microcapsules had a large particle size distribution. Romanowsky et al. [22] have demonstrated a parallelized microfluidic design by making double emulsions of water/octanol/water (W/O/W) to prepare various encapsulation like Ca-alginate microcapsules with oil cores. Supaporn et al. [23] synthesized the Ca-alginate microcapsules containing eucalyptus oil with a narrow size distribution via Shirasu porous glass (SPG) membrane. The concentration of alginate solution, temperature, and release model were investigated. Chew et al. [24] proposed that Kenaf seed oil was encapsulated using co-extrusion technology with a high methoxyl pectin (HMP)-enhanced alginate shell. Schmit et al. [25] showed that the oil droplets were pumped into alginate/CaCO₃ solution and the formed O/W emulsion was added drop wise to the oil–acetic acid bath through a co-flow junction microfluidic device. However, the distribution and dissolution of CaCO₃ limited the morphology of the capsules. Marquis et al. [26] described two-step approach allowing the encapsulation of several oil micro-droplets within alginate micro-gels. Cotton cellulose nanocrystals and calcium carbonate was used to prepare Pickering emulsion in the first step, oil micro-droplets resulting from the Pickering emulsion were encapsulated within alginate micro-gels using microfluidics. Evandro Martins et al. [27,28] proposed a technique of oil encapsulation in Ca-alginate microcapsules by inverse gelation. The oil containing calcium ions dropped into the sodium alginate solution, and the calcium ions diffused from inside to outside to obtain capsules. The reverse gelation mechanism has also been extensively studied by other researchers [29–32]. However, those methods usually either involved multiple fluids to be controlled simultaneously in the process of experiments, or cumbersome preparation which makes mass production difficult. Furthermore, the diffusion of calcium ions makes it easy for alginate solution to form a whole block of hydrogel and the secondary dissolution of capsules in reverse gelation makes it difficult to produce separable capsules. Moreover, the formation mechanism of droplets in microfluidic devices has not been deeply studied.

To the best of our knowledge, it seems there is no published paper concerning the synthesis of using alginate micro-emulsion combining droplets microfluidic. In view of this, this paper performed a micro-emulsion of alginate and rejuvenator combining with droplets microfluidic method to produce Ca-alginate microcapsules. The size can be easily controlled and the formation mechanism of the emulsion droplets in microfluidic device was deeply studied from the point of view of the fluid force. Then a size predictive mathematical model of the microcapsules was proposed. In addition, the self-healing performance of bitumen containing the microcapsules was investigated. This research provides possibilities for industrial large-scale production of Ca-alginate microcapsules containing rejuvenators, extending the service life of bituminous materials—such as bitumen highways, bitumen waterproofing layers, and bitumen anticorrosive materials—and realizing development of a more sustainable and green construction industry related to bitumen materials.

2. Materials and Methods

2.1. Materials

Sodium alginate, Tween80, and anhydrous calcium chloride (CaCl₂·2H₂O) were purchased from Sinopharm Chemical Reagent Co., Ltd. (Beijing, China). 70A (70A is an abbreviation of bitumen with 60/80 pen grade) bitumen was supplied by KOCH Bitumen Co., Ltd. (Wuhan, China) and properties are shown in Table 1. Rejuvenator was obtained from Hubei Bo Run Chemical Technology Co., Ltd.

(Wuhan, China) and its properties are shown in Table 2. Oil was purchased from Jiali grain and Oil Co., Ltd. (Beijing, China). All of the reagents were used without further purification.

Table 1. Properties of the 70A bitumen binder.

Bitumen	Penetration/0.1 mm (20 °C)	Softening Point/°C	Ductility (15 °C)
70A	68.7	48.5	>100 cm

Table 2. Properties of the rejuvenator.

Apparent Viscosity/Pa s (60 °C)	Flash Point/°C	Saturates/%	Aromatics/%	Density/g·cm ⁻³ (15 °C)
0.285	240	21.07	67.4	0.935

2.2. Preparation of O/W Emulsions

300 mL deionized water, 3 g alginate, 100 mL rejuvenator, and different volume fractions of Tween80 (0–2.0%) were mixed and stirred for 10 min at 50 °C. Then the mixture was sheared for 15 min with a high-speed shearing mixer running at 8000 rpm.

2.3. Fabrication of Ca-Alginate Microcapsules by Microfluidic

A microfluidic device with a co-axial flow focusing geometry was designed as Figure 1. For the outer phase, oil was pumped (NE-1000, ERA Syringe Pump, New Era Pump systems Inc, Washington, WA, USA) through a fused silica capillary tube (interior diameter (ID) 0.8 mm and outside diameter (OD) 1.0 mm) with a rate of changing from 3 mL·h⁻¹ to 9 mL·h⁻¹. The inner phase, emulsion was pumped through a fused silica capillary tube (interior diameter (ID) 400 μm and outside diameter (OD) 600 μm) with a rate of changing from 3 mL·h⁻¹ to 9 mL·h⁻¹. Emulsion droplets with different diameters can be generated at the different flow rate of continuous phase and dispersed phase owing to the effect of fluid force. When the droplets were immersed in calcium chloride solution, the substitution of calcium ions to sodium ions causes the crosslinking of alginate ions into membrane, and finally microcapsules with different diameters can be synthesized. The microcapsules were retained in calcium chloride solution for 4 h, and the calcium chloride solution containing microcapsules was filtered and the Ca-alginate microcapsules with rejuvenator was left in oven at 110 °C for 12 h. The oil on the surface of calcium chloride solution could be repeatedly recycled by a separating liquid funnel.

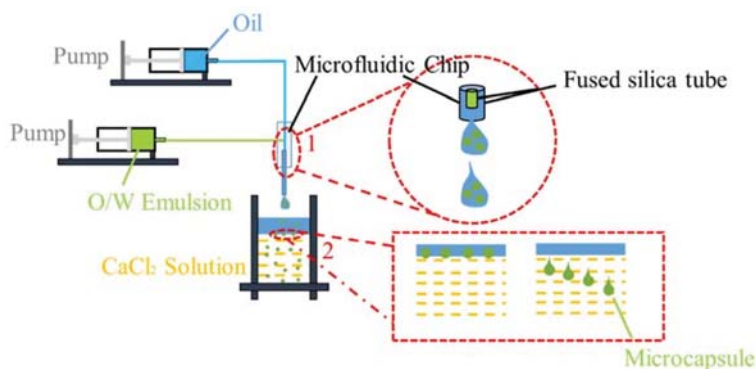


Figure 1. Schematic showing the droplets microfluidic device with a co-axial flow focusing geometry.

2.4. Characterization of Ca-Alginate Microcapsules

Polarizing microscope (ECLIPSE LV100N POL, Nikon, Tokyo, Japan) and fluorescence microscope (CX23, OLYMPUS, Wuhan, China) were used to image microcapsules.

A thermal analysis test with a working temperature range of 50–600 °C was conducted. TGA/DSC simultaneous thermal analyzer (STA449c/3/G, Berlin, Germany) was used in this paper. The heating rate was controlled at 10 °C/min with a maximum temperature of 600 °C. At the same time, high-purity nitrogen ambient gas was applied at a flow rate of 500 mL/min. During the pyrolysis process, the organic volatile substances of the polymers were decomposed to low molecular weight products. The relationship between the mass of the test sample and the temperature can be obtained from the TGA/DSC tests, which can be used to analysis the rejuvenator content in the microcapsules as well as the thermal stability of the microcapsules.

The FT-IR test can detect functional groups in a material which can be used to determine whether a chemical reaction occurs by comparing the differences in functional groups. The FT-IR test was conducted through an infrared spectrum instrument (Nexus, Thermo Nicolet Corporation, Washington, WA, USA) to confirm the successful synthesis of the microcapsule with wavelengths ranging from 400 cm⁻¹ to 4000 cm⁻¹.

2.5. Self-Healing Evaluation of Bitumen Containing Ca-Alginate Microcapsules

70# bitumen was aged for 5 h at 163 °C according to the standard JTG E20-2011 [33]. After that, different contents (i.e., by weight) Ca-alginate microcapsules was added slowly to the aged bitumen at 135 °C with a stirring speed of 200 rpm. Then the mixture was poured into the strips of 50 mm length, 10 mm width, and 2 mm height. These bitumen strips were kept at 0 °C for 1 h, and then fractures (approximately 20 μm) was made using a blade. Finally, the bitumen strips with fracture were transferred to the glass slide. Fracture morphology of samples with different content Ca-alginate microcapsules and self-healing time was observed by optical microscopy and fluorescence microscopy as well as tensile stress-recovery test to evaluate the self-healing property of bitumen containing Ca-alginate microcapsules.

3. Results and Discussion

3.1. Synthesis Mechanism of the Microcapsules

Micro-emulsion of rejuvenator in sodium alginate solution (O/W) was formed with high-speed shearing. The synthesis mechanism of Ca-alginate microcapsules containing rejuvenator is shown in Figure 2. Schematic in Figure 2a shows the formation of Ca-alginate microcapsules with rejuvenator core. Once in contact with the calcium chloride solution, the alginate ions on the surface of the droplets would cross-link to form a membrane under the substitution of sodium ions by calcium ions. As the reaction goes on, calcium ions continue to diffuse and invade the membrane because of the influence of calcium ions concentration difference between the inside and outside of the membrane. Thus micro-droplets of rejuvenator were in situ immobilized in the microcapsules. Some droplets will amalgamate to form large cores due to instability. Finally, multinuclear Ca-alginate microcapsules containing rejuvenator were successfully synthesized. The crosslinking mechanism of Ca-alginate is showed in Figure 2b.

Figure 3a shows the morphology of Ca-alginate microcapsules. The formation of the tail is a result of the forces that droplets subjected at the oil–water interface. When the droplets fall to the oil–water interface, they are subjected to gravity and a viscous force. One part of droplets in calcium chloride solution has formed membrane, but the other part was also emulsion. There was a central extrusion effect on this part generated by viscous force of the rejuvenator phase. It was deformed and form a tail during the drop of emulsion in the case of calcium ions. Figure 3b shows the fracture morphology of Ca-alginate microcapsules. It can be seen that there are many bright spots in the microcapsule center (the area black arrows pointed), which is the core of rejuvenator. Figure 3c shows the fluorescence

morphology of microcapsules. The whole microcapsules have a strong fluorescence effect, which is attributed to the rejuvenator with fluorescence effect.

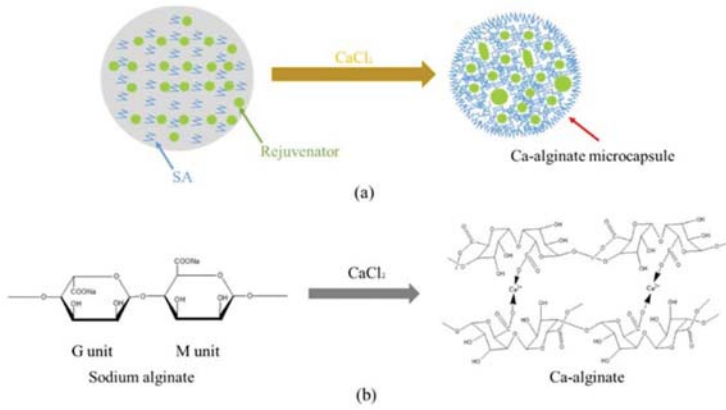


Figure 2. Schematic for the formation of Ca-alginate microcapsules with rejuvenator core (a) and crosslinking mechanism of Ca-alginate (b).

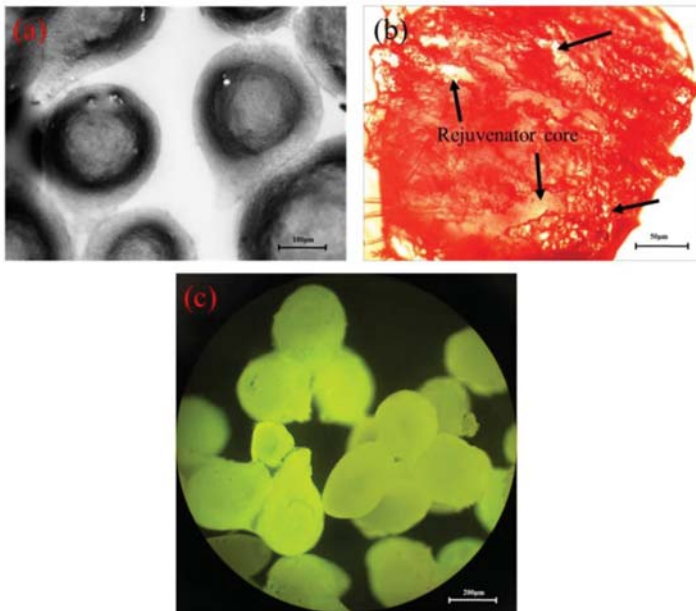


Figure 3. Morphology of the microcapsules (θ_o : 3 mL·h⁻¹, θ_e : 5 mL·h⁻¹): (a,b) by optical microscope; (c) by fluorescence microscope.

The successful synthesis of microcapsules rejuvenator core can be further confirmed by FT-IR test. From the comparison of alginate and microcapsules in Figure 4, it can be seen that 2851 cm⁻¹, 2925 cm⁻¹ is symmetric telescopic vibration and asymmetric expansion vibration of -CH₂-. 1634 cm⁻¹ is the telescopic vibration of carboxyl group. These absorption peaks did not appear in the test of

microcapsules. The infrared absorption peak from 1747 cm^{-1} to 1161 cm^{-1} moved to the lower wave number, and the intensity of all the absorption peaks became wider and weaker. This result is attributed to the addition of calcium ions made the carboxyl group into crosslinking. G began to fold the accumulation of seaweed ions, changing from the neat and orderly band structure to the curly cross-linking structure, eventually forming a three-dimensional network structure. Due to such steric effect, the intensity of all absorption peaks decreased and some absorption peaks moved to the lower wave number while some other peaks disappeared. For instance, comparison of the infrared spectra of rejuvenator and microcapsules shows that the peak 3470 , 3000 , 2854 , and 2679 cm^{-1} in rejuvenator disappeared after the synthesis of microcapsules; the infrared absorption peak from 1747 cm^{-1} to 1161 cm^{-1} moved to the lower wave number. These changes are because the calcium alginate membrane restricted the spatial displacement of the group in the rejuvenator and made the partial absorption peak disappeared, another partial absorption peak moved to the lower wave number, which indicated that the rejuvenator was coated in Ca-alginate shell.

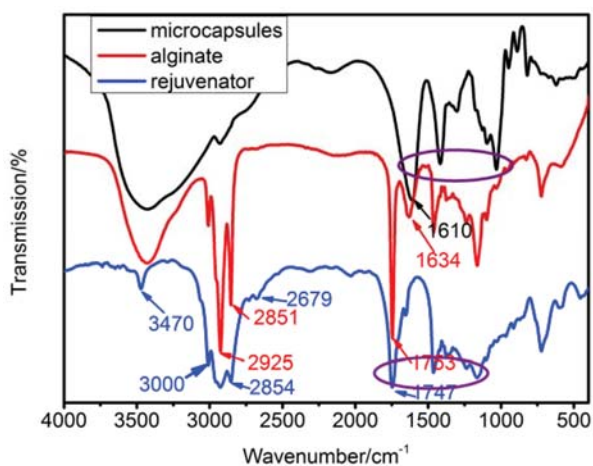


Figure 4. FT-IR test of microcapsules, alginate, and rejuvenator.

3.2. Effect of Surfactant on the Size of the Microcapsules

During the synthesis of the microcapsules by microfluidic droplets, there is a long retention time of micro-emulsion in the syringe. It is necessary to prepare highly stable emulsion to prevent its stratification in the syringe. The comparison of the micro-emulsion with different content Tween80 was conducted. Figure 5 shows the stability of micro-emulsion at room temperature. It can be seen that the emulsion without Tween80 showed obvious inhomogeneity. For example, there was a large variation in the size of emulsion and the emulsified droplets were unstable and they ruptured quickly. When 0.5% Tween80 was added, the size of emulsion had a significant decrease and there was only a few of the droplets coalesced. The size of emulsion with 1.0% Tween80 was further decreased and the stability was substantially improved and there was no obvious aggregation and fusion. When 2.0% Tween80 was added, the size of emulsion decreased and there was no significant change in stability as compared to the emulsion with 1.0 wt % of Tween80. In view of this, the content of 1.0% emulsion in this study was used. It also showed that the addition of Tween80 significantly reduced the size of the microcapsules (Figure 6). When 0.0, 0.5, 1.0, and 2.0% Tween80 was added, the size of microcapsules (θ_0 : $3\text{ mL}\cdot\text{h}^{-1}$, θ_e : $5\text{ mL}\cdot\text{h}^{-1}$) were about 610, 470, 420, and 400 μm respectively. The addition of surfactant like Tween80 can diminish the interfacial tension of the liquid [34–36], which affected the synthesis of Ca-alginate from two different ways. One is that water molecules can be fixed on the surface of the rejuvenator droplets by Tween80 to prevent the aggregation and fusion of the emulsion

droplets in alginate solution, thus improving the stability of the micro-emulsion. Another is that the smaller interfacial force makes the adhesive force between the emulsion and the outer surface of the quartz tube decreased. When the velocity of the continuous phase is not changed, the emulsion droplets are more easily formed which means that a smaller shear force generated by the continuous phase is needed to form the same size droplets after surfactant Tween80 is added. Thus, the size of alginate microcapsules decreased after adding Tween80.

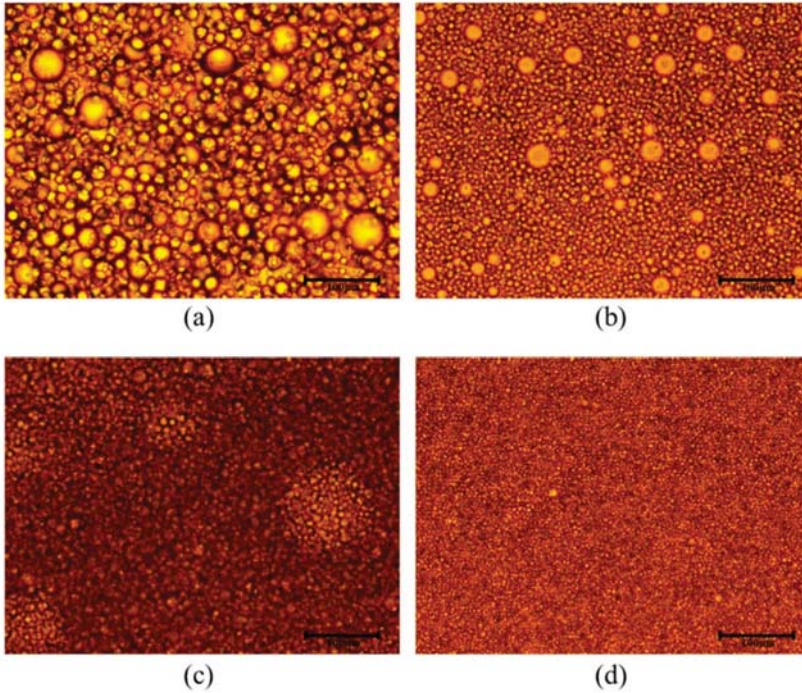


Figure 5. Optical microscopic image of emulsion with different content Tween80: (a) 0%; (b) 0.5%; (c) 1.0%; (d) 2.0%.

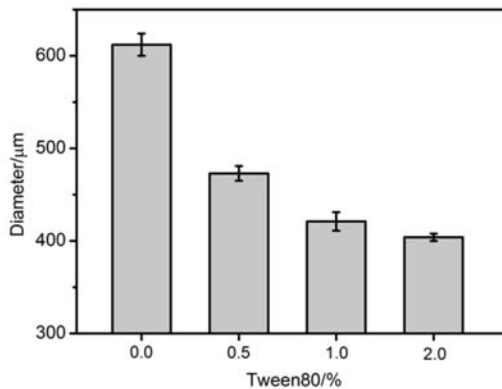


Figure 6. Size of microcapsules synthesized with different content Tween80 (θ_o : $3 \text{ mL}\cdot\text{h}^{-1}$, θ_e : $5 \text{ mL}\cdot\text{h}^{-1}$).

3.3. Effect of the Flow Rates of Continuous and Dispersed Phases on Microcapsules' Size

The control of morphology of the microcapsules was performed by tuning the flow rate of continuous (oil) and dispersed (O/W emulsion) phases. Table 3 shows the relation between the size of the microcapsules and the velocity of continuous and dispersed phase. It can be seen that when the flow rate of continuous and dispersed phase was changed between 3 mL·h⁻¹ and 9 mL·h⁻¹, the microcapsules with diameter from 139 ± 8 μm to 482 ± 16 μm were synthesized. It also revealed that by keeping constant flow rate of dispersed phases, the diameter of the microcapsules decreased with the increase of flow rate of the continuous phase. On contrary, using a constant flow rate for continuous phase, the diameter of the microcapsules increased with the increase of flow rate of the dispersed phase.

Table 3. Diameter of microcapsules versus flowrate of continuous (3 mL·h⁻¹–9 mL·h⁻¹) and dispersed phases (3 mL·h⁻¹–9 mL·h⁻¹).

$\vartheta_e/\text{mL}\cdot\text{h}^{-1}$	$\vartheta_o/\text{mL}\cdot\text{h}^{-1}$			
	3	5	7	9
3	385 ± 4 μm	221 ± 11 μm	172 ± 5 μm	139 ± 8 μm
5	421 ± 12 μm	272 ± 8 μm	203 ± 3 μm	159 ± 8 μm
7	460 ± 8 μm	290 ± 5 μm	218 ± 9 μm	161 ± 13 μm
9	482 ± 16 μm	311 ± 3 μm	232 ± 11 μm	169 ± 5 μm

3.4. Size Predictive Mathematical Model of the Microcapsules

The results can be explained through the interaction of the forces acting on the micro-emulsion droplets. In this experimental method, the formation and morphology of droplets was affected by the four different forces acting on the droplets. They are shear force (F_s) produced by continuous phase, interfacial force between dispersed phase and outer surface of quartz glass tube (F_i), thrust produced by the pump (F_t), and buoyancy force (F_b) produced by density difference between continuous and dispersed phase.

$$F_s = 3\pi \times \mu_o \times (\vartheta_o - \vartheta_e) \times r_e \quad (1)$$

$$F_i = 2\pi \times \gamma \times \sigma_e \quad (2)$$

$$F_t = \rho_e \times \varnothing_e \times \vartheta_e \quad (3)$$

$$F_b = \pi \times (\rho_e - \rho_o) \times g \times r^3/6 \quad (4)$$

μ_o represents viscosity of the continuous phase (oil), ϑ_o and ϑ_e are velocity of the continuous phase and dispersed phase, r_e means radius of emulsion droplets, γ is the wetting radius of the emulsion droplet at the inner quartz capillary tube, σ_e stand for the interfacial tension, \varnothing_e stands for flux of the emulsion, ρ_e and ρ_o are density of the emulsion and oil phase respectively. Bond number (B_o) was used to evaluate the relationship between buoyancy force and interfacial force

$$B_o = \Delta\rho g L^2 / \sigma \quad (5)$$

$\rho_o = 0.9318$, $\rho_e = 0.9832$. $B_o \ll 1$, so F_b could be ignored [37]. Replace the Formulas (1)–(3) into Formula (5)

$$F_i = F_t + F_s \quad (6)$$

$$r_e = [2\pi \times \gamma \times \sigma_e + \vartheta_e \times (2\pi\mu_o - \rho_e \times \varnothing_e)] / 3\pi \times \mu_o \times \vartheta_o. \quad (7)$$

γ , σ_e , μ_o , ρ_e , and \varnothing_e are determined by the physical properties of the micro-emulsion and microfluidic device. So it can be drawn that $r_e \propto \vartheta_e$, $r_e \propto 1/\vartheta_o$. When surfactant Tween80 was added, interfacial force of the emulsion was decreased namely σ_e decreased, thus r decreased when ϑ_e and ϑ_o were constant.

The experimental results conform to the law of the formula deduced. A three-dimensional experimental image of diameter of the microcapsules versus flow rate ($3 \text{ mL}\cdot\text{h}^{-1}$ – $9 \text{ mL}\cdot\text{h}^{-1}$) of continuous phase and dispersed phase is shown in Figure 7a and the fitting image is shown in Figure 7b. A fitting formula was proposed.

$$r_e = (1009.2 + 55.932 \times \vartheta_e) \times \vartheta_o^{-1} \times R^2 = 0.98578 \tag{8}$$

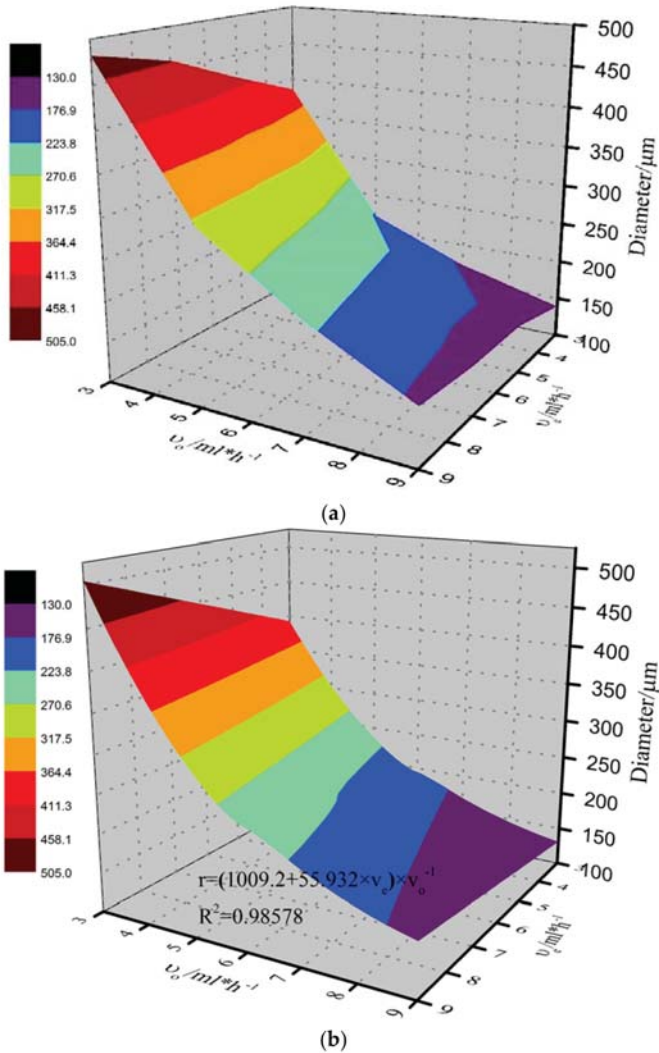


Figure 7. Three-dimensional experimental image (a) and fitting image (b) of diameter of the microcapsules versus flow rate of continuous phase (oil) and dispersed phase (alginate emulsion).

3.5. Self-Healing Property of Bitumen with Multinuclear Ca-Alginate Microcapsules

The effect of Ca-alginate microcapsules on the self-healing performance of bituminous binder was studied for the first time. The thermal stability of the microcapsules was investigated and showed in Figure 8. The thermogravimetry test in Figure 8a shows that thermogravimetric curves of the pure Ca-alginate sphere and microcapsules had similar characteristics. Nearly 40% rejuvenator was coated in Ca-alginate microcapsules. It also can be seen from Figure 8b that the initial decomposition temperature of the rejuvenator was 200 °C, the maximum decomposition temperature was 325 °C. The microcapsules and Ca-alginate sphere had slight mass loss at 100 °C, which was the evaporation of water. The maximum decomposition temperature of the microcapsules was 313.5 °C, and the maximum decomposition temperature of the Ca-alginate sphere was 256 °C which reveal that, when a bitumen specimen with multinuclear Ca-alginate microcapsules containing rejuvenator is prepared at 135 °C, the microcapsules probably keep intact.

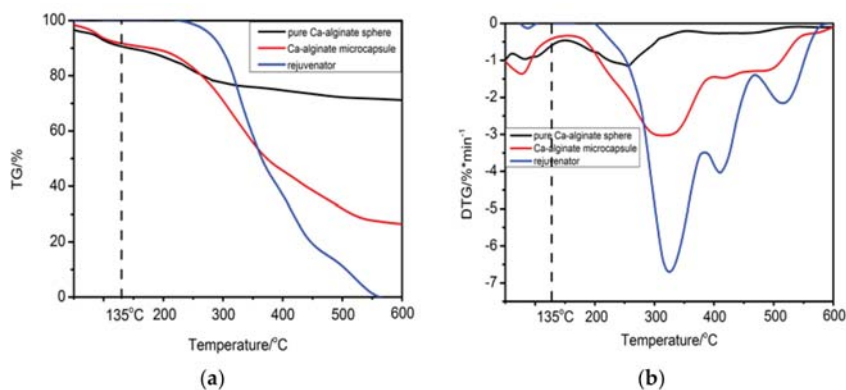


Figure 8. Thermal analysis of alginate, Ca-alginate microcapsules and rejuvenator: (a): TG vs. temperature, (b): DTG vs. temperature.

3.5.1. Micro Self-Healing Process of Bituminous Binder with Microcapsules

The self-healing mechanism of microcapsules for bitumen is that when the crack develops to meet microcapsules, the shell materials of microcapsules will be ruptured because of stress concentration at the tip of a crack. Then rejuvenator release and flow into the crack owing to capillary action. Rejuvenator will dissolve bitumen on both side of the crack. Then bituminous molecules spread quickly to the crack center under the effect of Brownian movement and concentration difference. In the case of the π -stacking of the aromatic rings and amphoteric character of aromatic molecules, the rejuvenator with high proportion of aromatic components can improve adhesion between bituminous molecules. Thus, the self-healing property of bitumen can be enhanced [38–40]. Micro self-healing process of bituminous binder containing multinuclear Ca-alginate microcapsules containing rejuvenator was monitored by optical microscope and fluorescence microscope and showed in Figure 6. A crack with a width of nearly 20 μm was produced in Figure 9a. Microcapsules were ruptured on the fracture surface of bitumen. After 30 s, it can be seen from Figure 9b that massive rejuvenator with intense fluorescence effect released and flowed into crack under the effect of capillary action. Part of the rejuvenator diffused into bituminous binder area surrounding those microcapsules. After 1 min, from Figure 9c, it can be seen that rejuvenator in the crack began to rapidly diffuse to the both sides of the crack. The asphalt on both sides of the crack was partly dissolved and diffused to the crack center rapidly because of concentration difference. After 4 h, it can be seen from Figure 9d that the crack disappeared. The microcapsules were partially embedded in the low intensity area. According to the self-healing

mechanism, low intensity fluorescence area (in Figure 9d) is the mixture of bitumen and rejuvenator, which was attributed to Brownian motion of bituminous molecules and rejuvenator molecules.

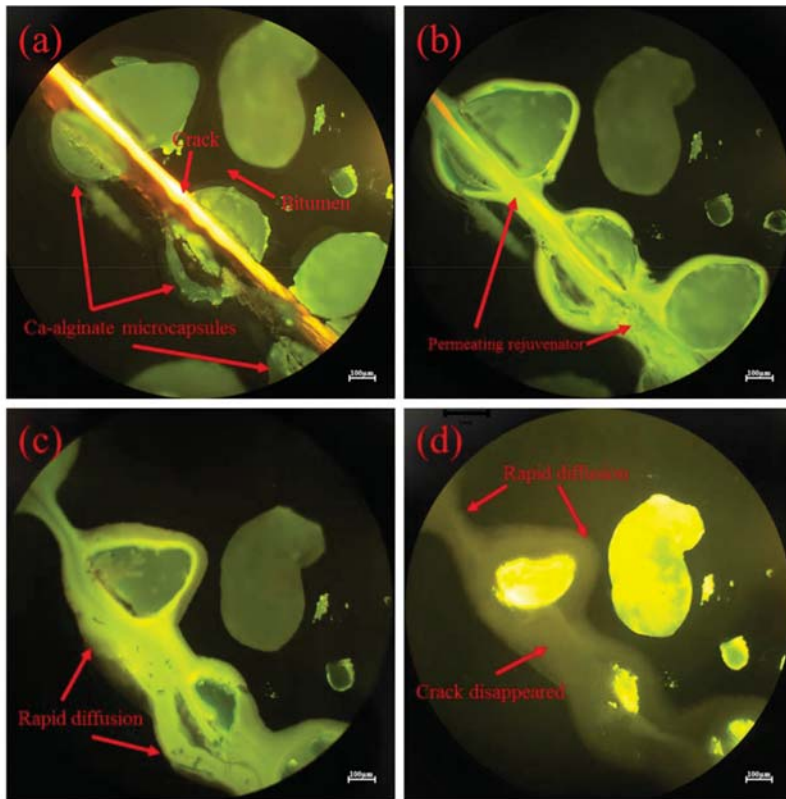


Figure 9. Micro self-healing process of bituminous binder with Ca-alginate microcapsules characterized by fluorescence microscope and optical microscope test (at 20 °C): (a) once a crack was produced; (b) after 30 s; (c) after 1 min; (d) after 4 h.

3.5.2. Tensile Stress-Recovery Test of Bituminous Binder with Microcapsules

Tensile stress-recovery test was conducted to evaluate self-healing property of bitumen containing Ca-alginate microcapsules (Figure 10). Bitumen mixing the microcapsules was poured in to the mold at 135 °C (Figure 10a). Then the specimen was kept for one hour at −10 °C. After that the specimen was snapped and the tensile stress was recorded (Figure 10b). Further, the two parts were contacted again and kept flat for one day at low temperature (10 °C). Finally, it can be seen from Figure 10c that the two parts were reconnected to a complete specimen, and the tensile stress was partially restored. The entire process was carried out under low temperature conditions because it guaranteed the brittle fracture of bitumen, and at the same time, the self-healing effect of rejuvenator on bitumen was better exhibited, and the effect of the self-repairing ability of the bitumen itself on the experimental results at low temperature could be minimized.

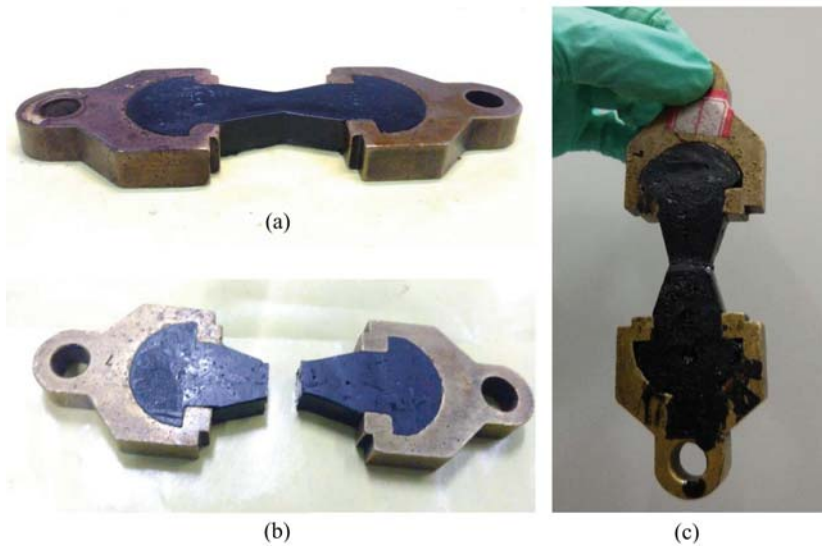


Figure 10. The process of tensile stress-recovery test: (a) ductility specimen at low temperature; (b) brittle fracture of specimen; (c) the two parts were connected again at low temperature.

The self-healing property of bituminous binder with multinuclear Ca-alginate microcapsules containing rejuvenator was evaluated by recovery rate of tensile stress and result was showed in Table 4 and Figure 11. It revealed that initial tensile stress of bitumen had a slight decrease, namely from 70.23 N to 61.48 N, with increase of the content of Ca-alginate microcapsules. The location of the microcapsules in bitumen structure is like a defect. With the increase of the content of Ca-alginate microcapsules, the defects in the bitumen structure also increased, which led to the decrease of mechanical properties of the bitumen specimens. After the self-healing time, the tensile stress of those samples got a different degree of recovery. Tensile stress increased from 33.58 N to 49.12 N with the addition of microcapsules. Furthermore, with the increase of the microcapsules content from 0% to 5%, the recovery rate of tensile stress was increased from 47.81% to 79.89%, which meant that the self-healing property of bitumen with multinuclear Ca-alginate microcapsules containing rejuvenator was enhanced.

Table 4. Tensile stress of bitumen specimens with different content Ca-alginate microcapsules.

Specimen	Tensile Stress (N)	Tensile Stress after Recovery (N)	Strength Recovery Rate (%)
0	70.23	33.58	47.81
1%	68.85	37.96	55.13
3%	65.93	44.68	68.81
5%	61.48	49.12	79.89

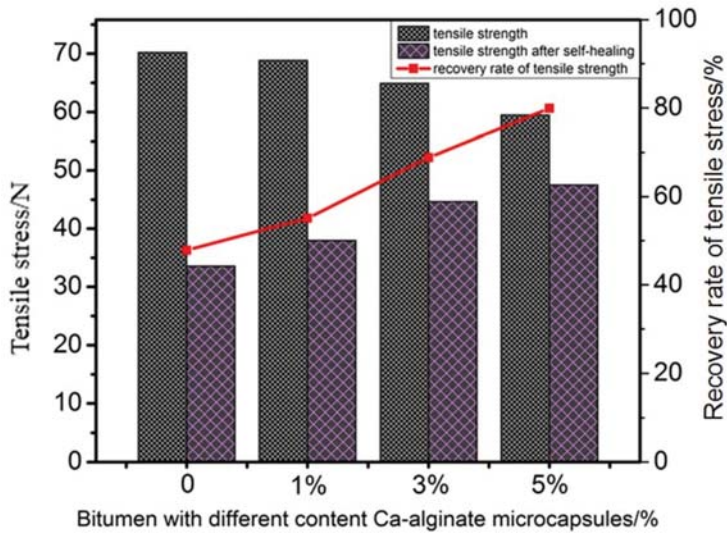


Figure 11. Tensile stress and recovery rate of bitumen with different content Ca-alginate microcapsules.

4. Conclusions

In this paper, we proposed a microfluidic method to synthesize multinuclear Ca-alginate microcapsules containing rejuvenator. The effect of surfactant and flowrate on the emulsion and the size of microcapsules was studied. Further, the self-healing properties of bituminous binder with those microcapsules was investigated. The following conclusions can be drawn:

1. Multinuclear Ca-alginate microcapsules containing rejuvenator were successfully synthesized by a microfluidic droplet device.
2. The microcapsules with size ranging from 139 μm to 482 μm has be synthesized. The addition of surfactant Tween80 could effectively improve stability of the emulsion and reduce the size of the microcapsules. The size could be easily controlled by changing the flow rates of continuous phase and dispersed phase.
3. The formation mechanism of the emulsion droplets in the microfluidic device was explained by force analysis of the droplets, and the prediction model of the microcapsules size was thus obtained.
4. Micro self-healing process of bituminous binder with those microcapsules was monitored and showed the enhanced self-healing performance. Tensile stress-recovery test revealed that the recovery rate increased by 32.08% (in the case of 5% microcapsules), which meant that the multinuclear Ca-alginate microcapsules containing rejuvenator we fabricated could effectively enhance the self-healing property of bituminous binder.

Acknowledgments: This research was supported by Natural Science Foundation of China (no. 51508433 and no. 51778515).

Author Contributions: Conceived and designed the experiments: B.S., S.W., L.D., Q.W. Performed the experiments: B.S. Analyzed the data: B.S., Q.L. Attributed reagents/materials/analysis tools: S.W. Wrote the paper: B.S.

Conflicts of Interest: There are no conflicts of interest regarding the publication of this paper.

References

- White, S.R.; Sottos, N.R.; Geubelle, P.H.; Moore, J.S.; Kessler, M.R.; Sriram, S.R.; Brown, E.N.; Viswanathan, S. Autonomic healing of polymer composites. *Nature* **2002**, *409*, 794–797.
- Blaiszik, B.J.; Caruso, M.M.; McIlroy, D.A.; Moore, J.S.; White, S.R.; Sottos, N.R. Microcapsules filled with reactive solutions for self-healing materials. *Polymer* **2009**, *50*, 990–997.
- Suryanarayana, C.; Rao, K.C.; Kumar, D. Preparation and characterization of microcapsules containing linseed oil and its use in self-healing coatings. *Prog. Org. Coat.* **2008**, *63*, 72–78.
- Wei, H.; Wang, Y.; Guo, J.; Shen, N.; Jiang, D.; Zhang, X.; Yan, X.; Zhu, J.; Wang, Q.; Shao, L. Advanced micro/nanocapsules for self-healing smart anticorrosion coatings. *J. Mater. Chem. A* **2014**, *3*, 469–480.
- Amendola, V.; Meneghetti, M. Self-healing at the nanoscale. *Nanoscale* **2009**, *1*, 74–88. [PubMed]
- Sun, D.; An, J.; Wu, G.; Yang, J. Double-layered reactive microcapsules with excellent thermal and non-polar solvent resistance for self-healing coatings. *J. Mater. Chem. A* **2015**, *3*, 4435–4444.
- Xu, G.; Wang, H. Molecular dynamics study of oxidative aging effect on asphalt binder properties. *Fuel* **2017**, *188*, 1–10.
- Petersen, J.C.; Harnsberger, P.M. Asphalt aging: Dual oxidation mechanism and its interrelationships with asphalt composition and oxidative age hardening. *Transp. Res. Rec. J. Transp. Res. Board* **1998**, *1638*, 47–55.
- Das, P.K.; Balieu, R.; Kringos, N.; Birgisson, B. On the oxidative ageing mechanism and its effect on asphalt mixtures morphology. *Mater. Struct.* **2014**, *48*, 1–15.
- Li, R.; Wang, C.; Wang, P.; Pei, J. Preparation of a novel flow improver and its viscosity-reducing effect on bitumen. *Fuel* **2016**, *181*, 935–941.
- Wang, Y.; Su, J.; Schlangen, E.; Han, N.; Han, S.; Li, W. Fabrication and characterization of self-healing microcapsules containing bituminous rejuvenator by a nano-inorganic/organic hybrid method. *Constr. Build. Mater.* **2016**, *121*, 471–482.
- Sun, D.; Pang, Q.; Zhu, X.; Tian, Y.; Lu, T.; Yang, Y. Enhanced self-healing process of sustainable asphalt materials containing microcapsules. *ACS Sustain. Chem. Eng.* **2017**, *5*, 9881–9893.
- Su, J.F.; Schlangen, E. Synthesis and physicochemical properties of high compact microcapsules containing rejuvenator applied in asphalt. *Chem. Eng. J.* **2012**, *198*, 289–300.
- Aguirre, M.A.; Hassan, M.M.; Shirzad, S.; Daly, W.H.; Mohammad, L.N. Micro-encapsulation of asphalt rejuvenators using melamine-formaldehyde. *Constr. Build. Mater.* **2016**, *114*, 29–39.
- Shirzad, S.; Hassan, M.M.; Aguirre, M.A.; Mohammad, L.N.; Daly, W.H. Evaluation of sunflower oil as a rejuvenator and its microencapsulation as a healing agent. *J. Mater. Civ. Eng.* **2016**, *28*, 4016116.
- Micaelo, R.; Al-Mansoori, T.; Garcia, A. Study of the mechanical properties and self-healing ability of asphalt mixture containing calcium-alginate capsules. *Constr. Build. Mater.* **2016**, *123*, 734–744.
- Al-Mansoori, T.; Micaelo, R.; Artamendi, I.; Norambuena-Contreras, J.; Garcia, A.; Al-Mansoori, T.; Micaelo, R.; Artamendi, I.; Norambuena-Contreras, J.; Garcia, A. Microcapsules for self-healing of asphalt mixture without compromising mechanical performance. *Constr. Build. Mater.* **2017**, *155*, 1091–1100.
- Zhang, M.; Xing, F.; Shi, K.Y.; Du, X.X. Study on organic microcapsule based self-healing cementitious composite. *Adv. Mater. Res.* **2011**, *239*, 764–767.
- Li, R.; Zhou, T.; Pei, J. Design, preparation and properties of microcapsules containing rejuvenator for asphalt. *Constr. Build. Mater.* **2015**, *99*, 143–149.
- Ren, P.W.; Ju, X.J.; Xie, R.; Chu, L.Y. Monodisperse alginate microcapsules with oil core generated from a microfluidic device. *J. Colloid Interface Sci.* **2010**, *343*, 392–395. [PubMed]
- Yeh, K.W.; Chang, C.P.; Yamamoto, T.; Dobashi, T. Release model of alginate microcapsules containing volatile tea-tree oil. *Colloids Surf. A Physicochem. Eng. Asp.* **2011**, *380*, 152–155.
- Romanowsky, M.B.; Abate, A.R.; Rotem, A.; Holtze, C.; Weitz, D.A. High throughput production of single core double emulsions in a parallelized microfluidic device. *Lab Chip* **2012**, *12*, 802–807. [PubMed]
- Noppakundilograt, S.; Piboon, P.; Graisuwan, W.; Nuisin, R.; Kiatkamjornwong, S. Encapsulated eucalyptus oil in ionically cross-linked alginate microcapsules and its controlled release. *Carbohydr. Polym.* **2015**, *131*, 23–33. [PubMed]
- Chew, S.C.; Tan, C.P.; Long, K.; Nyam, K.L. In-vitro evaluation of kenaf seed oil in chitosan coated-high methoxyl pectin-alginate microcapsules. *Ind. Crop. Prod.* **2015**, *76*, 230–236.



25. Schmit, A.; Courbin, L.; Marquis, M.; Renard, D.; Panizza, P. A pendant drop method for the production of calibrated double emulsions and emulsion gels. *RSC Adv.* **2014**, *4*, 28504–28510.
26. Marquis, M.; Alix, V.; Capron, I.; Cuenot, S.; Zykwinska, A. Microfluidic encapsulation of pickering oil microdroplets into alginate microgels for lipophilic compound delivery. *ACS Biomater. Sci. Eng.* **2016**, *2*, 535–543.
27. Martins, E.; Renard, D.; Davy, J.; Marquis, M.; Poncelet, D. Oil core microcapsules by inverse gelation technique. *J. Microencapsul.* **2015**, *32*, 86–95. [PubMed]
28. Martins, E.; Poncelet, D.; Rodrigues, R.C.; Renard, D. Oil encapsulation in core-shell alginate capsules by inverse gelation II: Comparison between dripping techniques using W/O or O/W emulsions. *J. Microencapsul.* **2017**, *34*, 522–534. [PubMed]
29. Abang, S.; Chan, E.S.; Poncelet, D. Effects of process variables on the encapsulation of oil in ca-alginate capsules using an inverse gelation technique. *J. Microencapsul.* **2012**, *29*, 417–428. [PubMed]
30. Celli, G.B.; Teixeira, A.G.; Duke, T.G.; Brooks, M.S.L. Encapsulation of lycopene from watermelon in calcium-alginate microparticles using an optimised inverse-gelation method by response surface methodology. *Int. J. Food Sci. Technol.* **2016**, *51*, 1523–1529.
31. Vandenberg, G.W.; De, L.N.J. Evaluation of protein release from chitosan-alginate microcapsules produced using external or internal gelation. *J. Microencapsul.* **2008**, *18*, 433–441.
32. Li, X.; Wu, Z.; He, Y.; Ye, B.C.; Wang, J. Preparation and characterization of monodisperse microcapsules with alginate and bentonite via external gelation technique encapsulating *Pseudomonas putida* Rs-198. *J. Biomater. Sci. Polym. Ed.* **2017**, *28*, 1556–1571. [PubMed]
33. *Standard Test Methods of Bitumen and Bituminous Mixtures for Highway Engineering: JTG E20-2011*; China Highway & Transportation Standards: Beijing, China, 2011.
34. Mirchi, V.; Saraji, S.; Goual, L.; Piri, M. Dynamic interfacial tension and wettability of shale in the presence of surfactants at reservoir conditions. *Fuel* **2015**, *148*, 127–138.
35. Nowak, E.; Xie, Z.; Kovalchuk, N.M.; Matar, O.K.; Mjh, S. Bulk advection and interfacial flows in the binary coalescence of surfactant-laden and surfactant-free drops. *Soft Matter* **2017**, *13*, 4616–4628. [PubMed]
36. Herdes, C.; Santiso, E.E.; James, C.; Eastoe, J.; Müller, E.A. Modelling the interfacial behaviour of dilute light-switching surfactant solutions. *J. Colloid Interface Sci.* **2015**, *445*, 16–23. [PubMed]
37. Neeson, M.J.; Chan, D.Y.; Tabor, R.F. Compound pendant drop tensiometry for surface tension measurement at zero Bond number. *Langmuir ACS J. Surf. Colloids* **2014**, *30*, 15388–15391.
38. Lee, H.J.; Kim, Y.R. Viscoelastic continuum damage model of asphalt concrete with healing. *J. Eng. Mech.* **1998**, *124*, 1224–1232.
39. Bonnaure, F.P. Laboratory investigation of the influence of rest periods on the fatigue characteristics of bituminous mixes. In Proceedings of the Asphalt Paving Technology, Kansas City, MO, USA, 1982. Available online: <https://trid.trb.org/view/725881> (accessed on 19 April 2018).
40. García, Á.; Schlagen, E.; van de Ven, M.; Sierra-Beltrán, G. Preparation of capsules containing rejuvenators for their use in asphalt concrete. *J. Hazard. Mater.* **2010**, *184*, 603–611. [PubMed]



© 2018 by the authors. Licensee MDPI, Basel, Switzerland. This article is an open access article distributed under the terms and conditions of the Creative Commons Attribution (CC BY) license (<http://creativecommons.org/licenses/by/4.0/>).

Article

Self-Healing Property of Ultra-Thin Wearing Courses by Induction Heating

Jiuming Wan ¹ , Yue Xiao ^{1,*} , Wei Song ¹, Cheng Chen ¹, Pan Pan ² and Dong Zhang ¹

¹ State Key Laboratory of Silicate Materials for Architecture, Wuhan University of Technology, Wuhan 430070, China; wanjm@whut.edu.cn (J.W.); songwei6695@whut.edu.cn (W.S.); chencc@whut.edu.cn (C.C.); pytmac@whut.edu.cn (D.Z.)

² School of Civil Engineering and Architecture, Wuhan Institute of Technology, Wuhan 430205, China; panpan8597@126.com

* Correspondence: xiaoy@whut.edu.cn; Tel: +86-027-8716-2595

Received: 29 June 2018; Accepted: 6 August 2018; Published: 9 August 2018

Abstract: Ultra-thin wearing course (UTWC) has been developed in pavement preventive maintenance for many years. However, how to prolong the service life of UTWC still requires further research. This study introduced AC-5 and SMA-5 asphalt mixtures, which can be induction heated. Steel fiber and steel slag were used in the mixtures as additives. Marshall Stability and induction heating property of mixtures were characterized. In addition, self-healing property of UTWC materials had been emphatically conducted. Adding steel fiber in mixtures led to higher Marshall Stability and lower flow value, while steel slag generally showed a negative effect. Induction heating property showed a positive relationship with the additives. Induction heating time was positively correlated to the healing ratio of the mixtures. Induction heating on the mixtures could recover the strength of mixtures to a certain degree. Mixtures with more steel fiber showed a higher healing ratio. Basalt-steel slag based mixtures showed better healing ratios than the basalt based mixtures. The healing ratios of mixtures illustrated a decreasing tendency as the healing cycle increased.

Keywords: ultra-thin wearing course; self-healing; induction heating; steel fiber; steel slag

1. Introduction

China has achieved a sharp development of civil highway transportation in the last decades, showing a positive influence on the national economy. However, pavements gradually fail due to long-time service, which reduces the traffic efficiency and driving safety. Therefore, prolonging the service life of pavement with adequate maintenance is urgently required. Preventive maintenance [1,2] is a strategy that conducting maintenance on pavement that has not been seriously damaged. It has been proven to effectively prolong the service life of pavement. In addition, preventive maintenance is more economical than reconstructing a new pavement. Paving ultra-thin wearing course (UTWC) [3,4] on pavement has been served as an effective approach for prolong the service life of pavement since many year ago. UTWC was initially developed in France [5]. It is asphalt mixture course whose thickness is between 15 and 25 mm. UTWC is usually paved on the top of surface course, performing as a new wearing course. Researchers had developed many materials for UTWC. Their results [6,7] and applications [8] proved that paving UTWC instead of reconstructing the entire pavement is both environmentally [9] and economically viable. The skid resistance [10] of the pavement can be also recovered. It has advantages of shorter construction time, fewer costs, and less resources consumption. However, how to prolong the service life of UTWC still requires further research.

Besides, recycling solid waste, such as steel slag [11], could also ease some environmental pressure. It has been applied to replace part of natural aggregate in mixture, which will reduce

the excessive exploitation of natural minerals. Previous studies [1,12,13] claimed that steel-slag based asphalt concrete showed acceptable performance. It proved that using steel slag to fabricate asphalt mixture was feasible. Thereby, this study also employed steel slag in UTWC to contribute to environmental protection.

On the other hand, induction heating is conducted on asphalt mixtures to melt ice and snow [14,15]. Some researchers [16,17] heal the pavement distress and prolong the service life of pavement through induction heating. Asphalt will show a great mobility when it is heated to a certain temperature since it is a viscoelastic material. The flow of asphalt binder into the crack within the asphalt mixture could help to achieve closure of the crack [18]. Thus, the cracks can be healed and the strength of mixture is recovered to a certain degree. Therefore, materials of UTWC with self-healing function were originally introduced in this study. Conducting self-healing on the asphalt pavement could effectively prolong the service life of UTWC. It could reduce both the cost and the consumption of natural resource. AC-5 and SMA-5 asphalt mixtures that can be induction heated were introduced. They were designed to be the materials of UTWC, which could be induction heated and therefore heal the crack. Steel fiber and steel slag had been used in the asphalt mixture as the heat source. Self-healing property of the UTWC materials through induction heating was emphatically investigated. In addition, the angularity and Form Two-Dimensional (2D) of aggregates, Marshall Stability, and induction heating property of the asphalt mixtures were also characterized. This study proposed the UTWC materials with self-healing function and provide the laboratory assessment was conducted. It could help to realize the self-healing of UTWC, and therefore contribute to the environmental pressure of the maintenance engineering.

2. Materials

Basalt and limestone filler were used as aggregate and filler in mixtures. Basalt was prepared in Hubei Province and filler was produced in Henan Province. Steel slag that was produced in Jiangxi Province were screened to the size of 2.36–4.75 mm in order to replace the basalt of same size with same volume. Table 1 presents the properties of aggregates and filler. A high viscosity asphalt binder was employed in the mixtures. Penetration of the high viscosity asphalt at 25 °C was 4.88 mm. Softening point was 86.9 °C and ductility at 5 °C was 720 mm.

Table 1. Properties of aggregates and filler.

Properties	Apparent Specific Gravity	Bulk Specific Gravity	Water Absorption (%)	Crushing Value (%)	Content of f-CaO (%)
Basalt	2.84	2.75	1.12	12.6	-
Steel slag	3.2	2.86	2.77	14.3	1.17
Limestone filler	2.67	2.67	-	-	-

Basalt and steel slag of 2.36–4.75 mm were also measured by Aggregate Image Measurement System. Cumulative distribution of corresponding angularity index and Form2D were characterized. Gradient angularity describes the variation at the particle boundary that influences the overall shape. The gradient angularity quantifies changes along a particle boundary with higher gradient values, indicating a more angular shape. Gradient angularity has a relative scale of 0 to 10,000 with a perfect circle having a small non-zero value. This index indicates the angularity, aggregates with higher angularity index prefer to show more obvious angularities. Equation (1) explains the calculation of gradient angularity:

$$GA = \frac{1}{\left(\frac{n}{3} - 1\right)} \sum_{i=1}^{n-3} |\theta_i - \theta_{i+3}| \quad (1)$$

where GA is the gradient angularity (Dimensionless), θ is the angle of orientation of the edge points, n is the total number of points, and subscript i denoting the i th point on the edge of the particle. Form2D (Dimensionless) applies to fine aggregate sizes only and quantifies the relative form from

two-dimensional images of aggregate particles. It has a relative scale of 0 to 20. Form2D indicates the sphericity of the aggregate. Aggregates of higher Form2D value show more obvious circle shape, and a perfect circular aggregate has a Form2D value of zero. The form index Form2D is expressed by Equation (2).

$$\text{Form2D} = \sum_{\theta=0}^{\theta=360-\Delta\theta} \left[\frac{R_{\theta+\Delta\theta} - R_{\theta}}{R_{\theta}} \right] \tag{2}$$

where, R_{θ} is the radius of the particle at an angle of θ , $\Delta\theta$ is the incremental difference in the angle. Angularity index and Form2D describe particle shape of aggregate. Figure 1 presents the gradient angularity of basalt and steel slag. The data points of steel slag were higher than that of basalt when the angularity index is below 3700. Conversely, it showed lower cumulative of particles when the angularity index is over 3700. Figure 2 expresses the Form2D of basalt and steel slag. The cumulative of particles of steel slag were higher than that of basalt when the value of Form2D is below 10. Tables 2 and 3 express the statistical result of particle number and proportion in different angularity range and Form2D range, which quantify the data more intuitively. The proportion of steel slag with angularity range of 5400–10,000 and 3750–10,000 were 7.39% and 29.06%, while that of basalt was 1.5% and 24%. The proportions of steel slag with high and extreme angularity were higher than basalt. According to Table 3, proportion of steel slag with Form2D range of 0–6.5 and 0–8 were 39.9% and 61.6%, while that of basalt were 23% and 55%. It suggested that proportion of steel slag with circular shape and moderate circular shape were higher than basalt. Therefore, steel slag that was used in this study had a more circular shape and higher angularity than basalt.

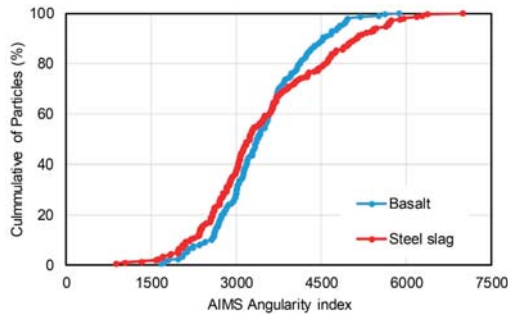


Figure 1. Gradient angularity of basalt and steel slag.

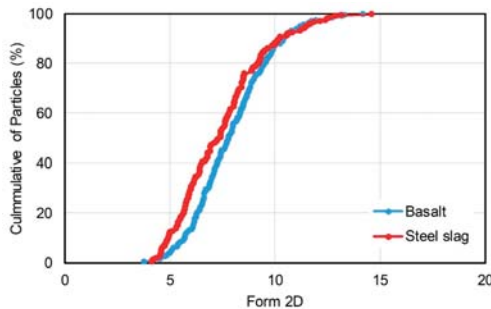


Figure 2. Form2D of basalt and steel slag.

Table 2. Particle number and proportion in different angularity range.

Angularity Range	Basalt		Steel Slag	
	Particle Number	Proportion	Particle Number	Proportion
Low (≤ 2100)	9	4.50%	18	8.87%
Moderate (2100–3975)	143	71.50%	126	62.07%
High (3975–5400)	45	22.50%	44	21.67%
Extreme (5400–10,000)	3	1.50%	15	7.39%

Table 3. Particle number and proportion in different Form2D range.

Form2D Range	Basalt		Steel Slag	
	Particle Number	Proportion	Particle Number	Proportion
Low (≤ 6.5)	46	23.0%	81	39.9%
Moderate (6.5–8)	64	32.0%	44	21.7%
High (8–10.75)	75	37.5%	62	30.5%
Extreme (10.75–20)	15	7.5%	16	7.9%

Steel fiber with length of 4.2–5.0 mm and equivalent diameter of 70–130 μm was used. The density and the melting point of the steel fiber were 7.85 g/cm^3 and 1530 $^\circ\text{C}$. It could help to realize the induction heating function of mixtures. Additionally, the lignin fiber was used as stabilizer in SMA-5 mixture, its length was of 4–6 mm and PH value was 7.5 ± 1.0 . The oil absorption rate of the lignin fiber was more than five times of the fiber mass, and the mass ratio of lignin fiber-aggregate was 0.3%.

3. Research Program

3.1. Mixture Design

AC-5 asphalt mixture had been designed according to the specification “JTG F40 2004”, which specifies the design method and the corresponding standards of asphalt mixture in China. SMA-5 asphalt mixture was designed according to AASHTO. Mixtures without steel slag were named as basalt based mixtures. Steel slag of 2.36–4.75 mm was proposed to replace the same size basalt as the same volume. Mixtures that contained steel slag were labelled as basalt-steel slag based mixtures. Figures 3 and 4 illustrate the gradations of AC-5 and SMA-5 mixtures. The replacement of steel slag does not change the corresponding designed gradations. For all AC-5 mixtures, the binder-aggregate mass ratio was 6.2%. The asphalt binder-aggregate mass ratio of all SMA-5 mixtures was 6.5%. The mixing temperature was 175 $^\circ\text{C}$, and the mold temperature was 165 $^\circ\text{C}$.

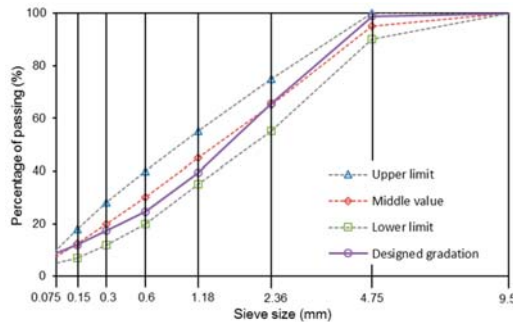


Figure 3. Gradations of AC-5 mixtures.

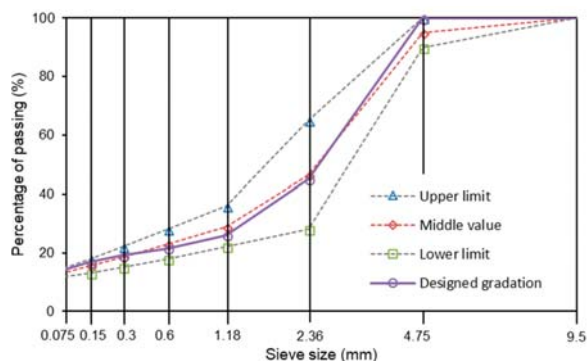


Figure 4. Gradations of SMA-5 mixtures.

On the other hand, steel fiber was added in the mixtures. Contents of steel fiber in each mixture were 0%, 1%, 2%, and 3%.

3.2. Testing and Characterization

Testing and characterization on materials consist of three parts, namely the Marshall Stability test, induction heating property, and self-healing property. The standard of this test is “JTG E20-2011”, which sets the standard experiment method in China. Marshall Stability test reflects the fracture strength of asphalt mixture. Four parallel Marshall specimens were tested for each mixture. These specimens were kept in a water bath with a temperature of $60\text{ }^{\circ}\text{C} \pm 0.5\text{ }^{\circ}\text{C}$ for 30 min. These specimens were then set on a Marshall Stability Apparatus, and corresponding Marshall Stability and flow value of Marshall specimens were determined after testing. The loading rate for this test was 50.0 mm/min, and it was stopped when the Marshall specimens failed.

Average temperature rising rate of the materials after induction heating was investigated to indicate induction heating property. Marshall specimens were introduced for induction heating. Induction heating equipment was employed to heat the Marshall specimens. A FLIR infrared camera was used to record the infrared image of specimens after induction heating. The distance between equipment and specimens was 15 mm. The power of equipment was 7.9 kilowatts and the frequency was 124 kHz. Induction heating time was 30 s. A software named FLIR Tool was used to calculate the average temperature of the Marshall specimens. Induction heating property of the materials was therefore concluded by testing the average temperature rising rate of the mixtures during the induction heating period.

The self-healing property was characterized by semi-circular bending test. Semi-circular bending test at $-10\text{ }^{\circ}\text{C}$ is a test that indicates the low temperature cracking resistance of asphalt mixture. The description of semi-circular specimens and infrared image after induction heating is shown in Figure 5. Semi-circular specimens were fabricated by cutting Marshall specimens. A notch with depth of 10 mm was made. Therefore, there would be a stress concentration along the notched part of the specimen when loading was applied. Figure 6 presents a complete cycle of self-healing analysis. Semi-circular specimens were stored at $-10\text{ }^{\circ}\text{C}$ for 5 h before test. A Universal Testing Machine (UTM-25) with an upper limit of 25 kN was used to exert loading on specimens as b stage of Figure 6. Testing temperature was $-10\text{ }^{\circ}\text{C}$ and loading rate was 0.5 mm/min. Loading stopped as force began to decrease, then the peak loading could be recorded. As shown in stage c, the broken specimens were put in a temperature control box at $25\text{ }^{\circ}\text{C}$ for 24 h. The last stage was illustrated in part d. Pieces of specimens were put together and induction heated. Consequently, pieces of specimens could be bonded together. Thus, specimens were self-healed. After that, the healed specimens were kept in a temperature control box

at 25 °C for 24 h and the self-healing circle was completed. Four self-healing circles were performed on each specimen to investigate the persistence of self-healing of the asphalt mixtures.

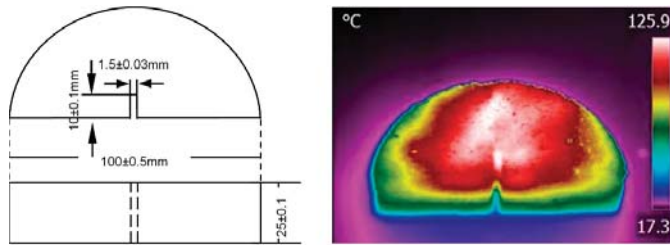


Figure 5. Description of the semi-circular specimen and infrared image after induction heating.

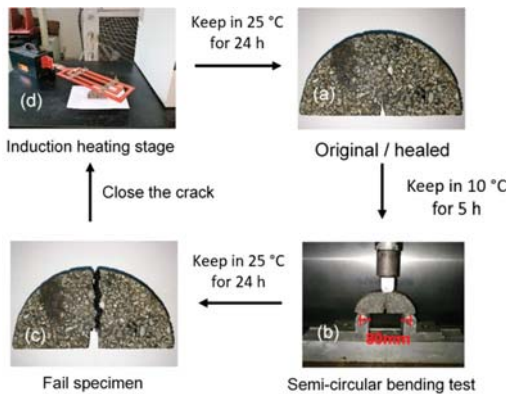


Figure 6. The self-healing cycle: (a) The original/healed specimen; (b) Semi-circular bending test in UTM-25; (c) The fail specimen; (d) Induction heating on specimen for healing.

4. Result and Discussion

4.1. Marshall Stability and Flow Value

Marshall Stability illustrates the high temperature fracture strength of a sample under loading. Flow value indicates the deformation that asphalt mixture can endure when fracture happens. These indicators are used as the important properties for asphalt mixture design and testing. Asphalt mixture with inadequate Marshall Stability and flow value is thought to have poor mechanical property. Figure 7 illustrates the Marshall Stability of the mixtures. Basalt-steel slag based AC-5 and SMA-5 asphalt mixture presented an increasing tendency as the content of steel fiber in mixture increased from 0 to 3%. Basalt based mixture also showed a rising tendency when the content of steel fiber increased from 0 to 2%. However, when the content of steel fiber went up to 3%, Marshall Stability of the specimens showed a decreasing tendency. Researchers had reported that the addition of fibers would reinforce asphalt mixture. Hence, Marshall Stability rises as the content of steel fiber increases. However, excessive addition of steel fiber may harm the structure of mixture and limit the effective asphalt binder. Consequently, the fracture strength will decrease when the content of steel fiber is added. Besides, basalt-steel slag based mixture presented lower Marshall Stability than corresponding basalt based mixture. It proved that the addition of steel slag would negatively affect the fracture strength of asphalt mixture. But, the reduction resulting from steel slag was acceptable since Marshall Stability of these mixtures met the specification of 8 kN. Figure 8 shows the flow

value of mixtures. Flow values of the specimens gradually decreased as the content of steel fiber raises. Addition of steel slag would raise flow value of both basalt based and basalt-steel slag based AC-5 mixtures.

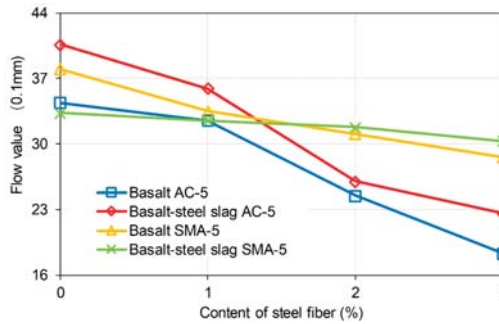


Figure 7. Marshall stability of the mixtures.

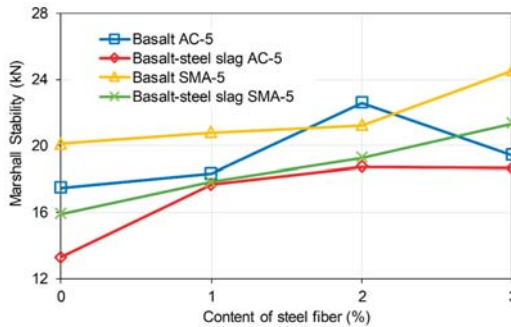


Figure 8. Flow value of the mixtures.

4.2. Induction Heating Property

UTWC that was introduced in this study is designed to have a self-healing function, so the average temperature rising rate of these materials during induction heating is important. Table 4 illustrates the average temperature rising rate of mixtures during induction heating time of 30 s. Mixtures without steel fiber showed no temperature change after induction heating. Average temperature rising rate of all the mixtures presented a rising tendency as the content of steel fiber increased. Rising rate of temperature of the basalt-steel slag based mixtures could even reach over 1 °C/s. Additionally, average temperature rising rate of basalt-steel slag based mixtures were higher than that of the corresponding basalt based mixtures. In summary, the addition of steel fiber and steel slag had a positive correlation to the induction heating property of UTWC.

Table 4. Average temperature rising rate of the mixtures during induction heating.

Description of Mixture	Content of Steel Fiber				
	0%	1%	2%	3%	
Average temperature rising rate (°C/s)	Basalt AC-5	0	0.31	0.61	0.99
	Basalt SMA-5	0	0.34	0.59	1.02
	Basalt-steel slag AC-5	0	0.37	0.70	1.11
	Basalt-steel slag SMA-5	0	0.36	0.74	1.25

4.3. Self-Healing Property

The influence of steel slag and steel fiber on self-healing property of asphalt mixtures was emphatically investigated. However, an excessive time of induction heating of specimens would excessively raise the temperature of the asphalt mixture. As Figure 9 shows, the excessive average temperature rising rate led to softening of asphalt binder, which resulted in the deformation or collapse of the asphalt mixtures. Therefore, induction heating time was controlled, and hence the average temperature rising rate of the asphalt mixture. It was noted that, the deformation of asphalt mixture initially happens when the highest temperature point of the specimen was between 120 and 130 °C. Thus, the upper limit of induction heating time of mixtures with 3%, 2%, and 1% steel fiber were controlled at 120 s, 140 s, and 200 s. Mixtures did not show deformation and collapse with these induction heating times and the corresponding cracks can be healed to a certain degree.

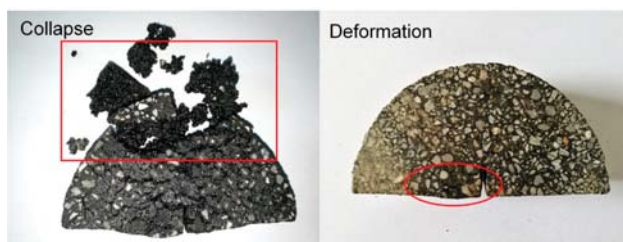


Figure 9. Collapse (left) and deformation (right) of the semi-circular specimens caused by excessive high temperature.

Gradient induction heating time and self-healing cycle were, respectively, conducted. Bending test at -10 °C was conducted on semi-circular specimens. Fracture toughness states the cracking resistance of asphalt mixtures at low temperature. Equations (3) and (4) illustrate the computation [19,20] of fracture toughness. Specimen with higher fracture toughness have better cracking resistance.

$$K_{IC} = Y_I \sigma_0 \sqrt{\pi a} \quad (3)$$

$$\sigma_0 = \frac{P_C}{2rt} \quad (4)$$

where

K_{IC} = fracture toughness ($\text{MPa} \times \text{m}^{0.5}$);

Y_I = the normalized stress intensity factor that is a constant in this study (Dimensionless);

P_C = the critical load (N);

r = radius of specimens (m);

t = the specimen thickness (m); and,

a = the notch length (m).

The same semi-circular bending tests were conducted on the initial/healed specimens after the induction heating. Healing ratio was used to indicate the self-healing property. It illustrates the degree that the specimens would recover after induction heating. It is determined according to Equation (5):

$$\text{HR} = \frac{K_{ICi}}{K_{IC}} \times 100\% \quad (5)$$

where HR is healing ratio (%), K_{ICi} ($\text{MPa} \times \text{m}^{0.5}$) is the fracture toughness of specimens that had been healed as cycle i , and K_{IC} ($\text{MPa} \times \text{m}^{0.5}$) is the initial fracture toughness of the specimens. Figure 10 illustrates the healing ratio of basalt based and basalt-steel slag based AC-5 mixtures with 3% steel

fiber by induction heating time and self-healing cycle dependencies. AC and SAC are the abbreviations of basalt based AC-5 mixture and steel slag-basalt based AC-5 mixture. SMA and SSMA are the abbreviations of basalt based SMA-5 mixture and steel slag-basalt based SMA-5 mixture. Steel fiber content and cycle times were also included in the abbreviation of specimens. The abbreviation is introduced as the format of mixture type-steel fiber content-cycle time. For instance, AC-3-1 means the first semi-circular bending test on basalt based AC-5 specimen, which contains 3% steel fiber. SSMA-3-2 means the second semi-circular bending test on steel slag-basalt based SMA-5 mixture that contains 3% steel fiber. Bars of the left side are the healing ratio of basalt based AC-5 asphalt mixtures, and the bars with small white dots are that of basalt-steel slag based AC-5 asphalt mixtures. Different colors distinguish induction heating time on specimens from 60 to 120 s. Information of abscissa axis shows the mixture type and corresponding self-healing cycle time. Basalt-steel slag based AC-5 mixtures showed higher healing ratio at the same induction heating time and cycle. Increase of induction heating time increased the healing ratio. The healing ratio of first cycle could even reach 80%. Healing ratio of specimens showed a decreasing tendency as the cycle time increase. Figures 11 and 12 present the healing ratio of AC-5 mixtures with 2% and 1% steel fiber. Basalt-steel slag based mixtures also showed higher healing ratio when compared to the corresponding basalt based mixture. Induction heating times are also correlated to the healing ratio of mixtures. Besides, the reduction of steel fiber in AC-5 asphalt mixture showed a negative effect on the healing ratio of mixture. The highest healing ratio of AC-5 mixtures with 2% and 1% steel fiber were 33.5% and 17.3%, which were far lower than that of AC-5 mixture with 3% steel fiber.

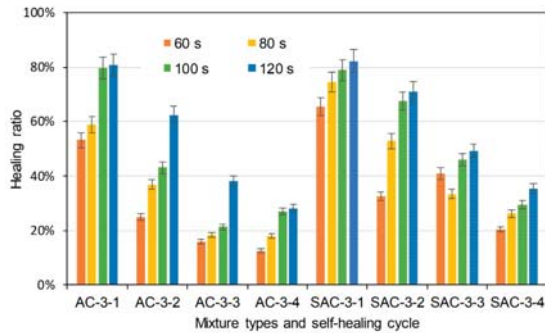


Figure 10. Healing ratio of basalt based and basalt-steel slag based AC-5 mixtures with 3% steel fiber by induction heating time and self-healing cycle dependency.

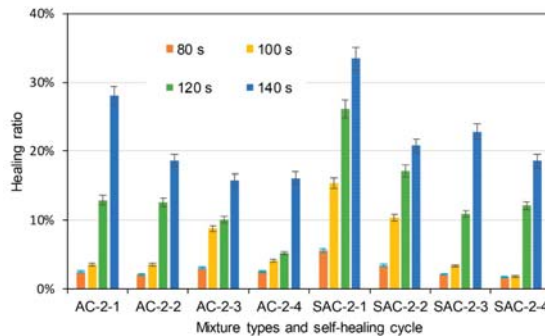


Figure 11. Healing ratio of basalt based and basalt-steel slag based AC-5 mixtures with 2% steel fiber by induction heating time and self-healing cycle dependency.

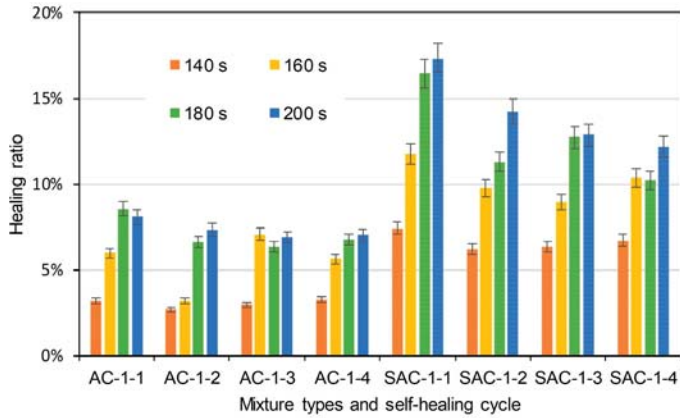


Figure 12. Healing ratio of basalt based and basalt-steel slag based AC-5 mixtures with 1% steel fiber by induction heating time and self-healing cycle dependency.

Figures 13–15 illustrate the healing ratio of SMA-5 mixtures. The effects of induction heating time, steel slag, and cycle were similar to that of AC-5 mixtures. Nevertheless, healing ratios of SMA-5 mixtures were very low when compared to AC-5 mixture. Healing behaviour of asphalt mixture is based on the flow of asphalt binder around crack. Asphalt binder in AC-5 mixture is supposed to easily bind the crack. However, lignin fiber in SMA-5 mixture can fix the asphalt binder, resulting in a poor mobility of the asphalt in healing time. Therefore, difference of asphalt mobility determines the healing ratio of AC-5 and SMA-5 mixtures. In summary, induction heating on the mixtures could recover the strength of the mixtures to a certain degree. Induction heating time was positively correlated to the healing ratios of mixtures. Within the adequate range, longer induction heating time will lead to better self-healing property. Basalt-steel slag based mixtures showed better healing ratios than basalt based mixtures. Mixtures with more steel fiber showed higher healing ratio in same induction heating time than mixtures with less steel fiber. It proved that the addition of steel slag could help to raise the self-healing property of mixtures. The healing ratio of mixtures illustrates a decreasing tendency as the number of cycle increase. The healing properties of SMA-5 mixtures were generally lower than that of AC-5 mixtures.

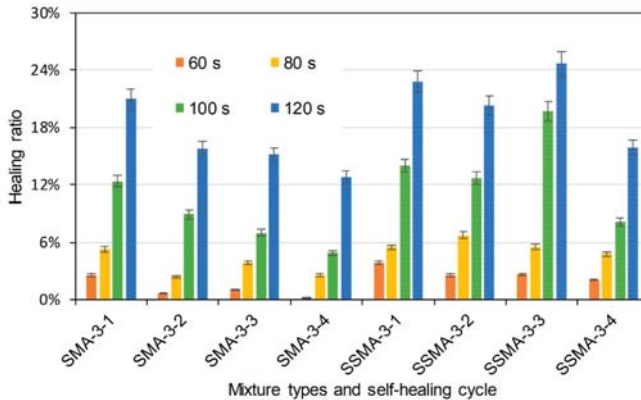


Figure 13. Healing ratio of basalt based and basalt-steel slag based SMA-5 mixtures with 3% steel fiber by induction heating time and self-healing cycle dependency.

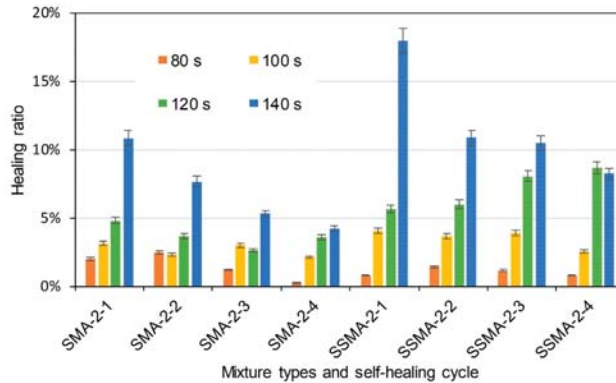


Figure 14. Healing ratio of basalt based and basalt-steel slag based SMA-5 mixtures with 2% steel fiber by induction heating time and self-healing cycle dependency.

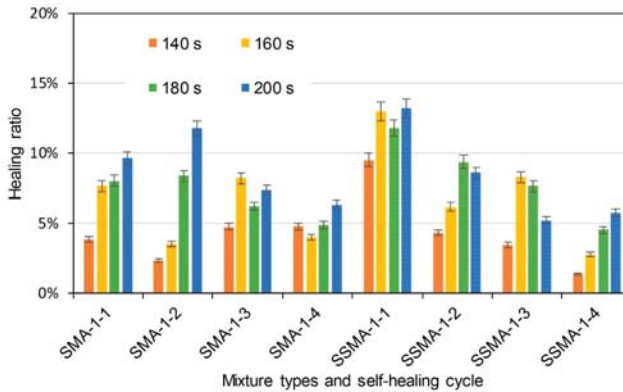


Figure 15. Healing ratio of basalt based and basalt-steel slag based SMA-5 mixtures with 1% steel fiber by induction heating time and self-healing cycle dependency.

5. Conclusions

SMA-5 and AC-5 asphalt mixtures were designed as ultra-thin wearing course materials that could be induction heated. Steel slag, as well as steel fiber, were employed as additives in corresponding asphalt mixtures, to accelerate the induction heating speed. Marshall Stability, induction heating property, and self-healing property of the materials were characterized. The following conclusions could be drawn.

(1) Steel slag lowers slightly the Marshall Stability of asphalt mixture, while steel slag presented positive effect. Marshall Stability of basalt–steel slag based AC-5 and SMA-5 asphalt mixture presented an increasing tendency with the increased content of steel fiber from 0 to 3%. Basalt based mixture also showed a rising tendency when the content of steel fiber increase from 0 to 2%. However, when the content of steel fiber goes up to 3%, the Marshall Stability of specimens showed a decreasing tendency. Flow values of specimens gradually decreased as the content of steel fiber raises. The addition of steel slag raised the flow values of both basalt based and basalt-steel slag based AC-5 mixtures. Basalt-steel slag based mixture presented lower Marshall Stability than the corresponding basalt based mixtures.

(2) Steel slag enhances the induction heating speed. The induction heated average temperature rising rate of all mixtures presented a rising tendency as the content of steel fiber increased. Average

temperature rising rate of basalt-steel slag based mixtures reached over 1 °C/s. Additionally, the average temperature rising rate of basalt-steel slag based mixtures were higher than that of corresponding basalt based mixtures.

(3) Mixtures with steel slag showed higher healing ratio than mixtures without steel slag. Adequate induction heating on mixtures could recover the strength to a certain degree. Within the adequate range, induction heating time was positively correlated to the healing ratios of mixtures. However, excessive heating time would deteriorate the mixture due to high temperature deformation. Mixtures with 3% steel fiber show a higher healing ratio within the same induction heating time than mixtures with 2% or 1% steel fiber. Basalt-steel slag based mixtures showed higher healing ratios than basalt based mixtures.

Author Contributions: Data curation, Y.X.; Formal analysis, P.P.; Funding acquisition, Y.X.; Investigation, J.W., Y.X., W.S. and D.Z.; Methodology, P.P.; Writing—original draft, J.W.; Writing—review & editing, Y.X.

Funding: This research was funded by the National Natural Science Foundation of China (No. U1733121 and 51778515). Authors are very grateful for their financial support.

Acknowledgments: The authors gratefully acknowledge Wuhan University of Technology for their materials and experimental instruments supports.

Conflicts of Interest: The authors declare no conflict of interest.

References

- Hunt, L.; Boyle, G. Steel Slag in Hot Mix Asphalt Concrete. Available online: <https://rosap.ntl.bts.gov/view/dot/33871> (accessed on 6 August 2018).
- Peshkin, D.G.; Hoerner, T.E.; Zimmerman, K.A. *Optimal Timing of Pavement Preventive Maintenance Treatment Applications*; Transportation Research Board: Washington, DC, USA, 2004.
- Geng, L.; Ma, T.; Zhang, J.; Huang, X.; Hu, P. Research on Performance of a Dense Graded Ultra-Thin Wearing Course Mixture. *Appl. Sci.* **2017**, *7*, 800. [CrossRef]
- Beyene, M.A.; Meininger, R.C.; Gibson, N.H.; Munoz, J.F.; Youtcheff, J. Forensic investigation of the cause(s) of slippery ultra-thin bonded wearing course of an asphalt pavement: Influence of aggregate mineralogical compositions. *Int. J. Pavement Eng.* **2016**, *17*, 887–900. [CrossRef]
- Luo, Y.L. Brief Introduction to Application of Maintenance Technology on Ultra-thin Wearing Course for Asphalt Pavement of Expressway. *Guangdong Highw. Commun.* **2011**, *1*, 005.
- Nan, X.F.; Tian, Z.F. Experimental research on ultra thin friction course interlayer bonding strength. *Int. J. Pavement Res. Technol.* **2009**, *2*, 176–180.
- Guan, Y.S.; An, F.W.; Han, C.; Zhang, Z.X. Design and Evaluation of Ultra Thin Friction Courses Asphalt Mixture Modified by Polyolefin. *Adv. Mater. Res.* **2013**, *723*, 41–49. [CrossRef]
- Hefer, A.; Horak, E.; Heathcote, H.; Hess, R.; Jeewan, A. Review of experiences with Ultra-Thin Friction Course Performance on airport runways. *Rehabilitation* **2008**, *204*, 758.
- Cui, P.; Wu, S.; Xiao, Y.; Wan, M.; Cui, P. Inhibiting effect of Layered Double Hydroxides on the emissions of volatile organic compounds from bituminous materials. *J. Clean. Prod.* **2015**, *108*, 987–991. [CrossRef]
- Xiao, Y.; Wang, F.; Cui, P.; Lei, L.; Lin, J.; Yi, M. Evaluation of Fine Aggregate Morphology by Image Method and Its Effect on Skid-Resistance of Micro-Surfacing. *Materials* **2018**, *11*, 920. [CrossRef] [PubMed]
- Chen, Z.; Wu, S.; Xiao, Y.; Zeng, W.; Yi, M.; Wan, J. Effect of hydration and silicone resin on Basic Oxygen Furnace slag and its asphalt mixture. *J. Clean. Prod.* **2016**, *112*, 392–400. [CrossRef]
- Wu, S.; Xue, Y.; Ye, Q.; Chen, Y. Utilization of steel slag as aggregates for stone mastic asphalt (SMA) mixtures. *Build. Environ.* **2007**, *42*, 2580–2585. [CrossRef]
- Ahmedzade, P.; Sengoz, B. Evaluation of steel slag coarse aggregate in hot mix asphalt concrete. *J. Hazard. Mater.* **2009**, *165*, 300. [CrossRef] [PubMed]
- Sun, Y.; Wu, S.; Liu, Q.; Hu, J.; Yuan, Y.; Ye, Q. Snow and Ice Melting Properties of Self-healing Asphalt Mixtures with Induction Heating and Microwave Heating. *Appl. Therm. Eng.* **2017**, *129*, 871–883. [CrossRef]
- Pan, P.; Wu, S.; Xiao, Y.; Liu, G. A review on hydronic asphalt pavement for energy harvesting and snow melting. *Renew. Sustain. Energy Rev.* **2015**, *48*, 624–634. [CrossRef]

16. Gómez-Mejjide, B.; Ajam, H.; Lastra-González, P.; Garcia, A. Effect of air voids content on asphalt self-healing via induction and infrared heating. *Constr. Build. Mater.* **2016**, *126*, 957–966. [[CrossRef](#)]
17. Menozzi, A.; Garcia, A.; Partl, M.N.; Tebaldi, G.; Schuetz, P. Induction healing of fatigue damage in asphalt test samples. *Constr. Build. Mater.* **2015**, *74*, 162–168. [[CrossRef](#)]
18. Liu, Q.; Wu, S.; Schlangen, E. Induction heating of asphalt mastic for crack control. *Constr. Build. Mater.* **2013**, *41*, 345–351. [[CrossRef](#)]
19. Lim, I.L.; Johnston, I.W.; Choi, S.K. Stress intensity factors for semi-circular specimens under three-point bending. *Eng. Fract. Mech.* **1993**, *44*, 363–382. [[CrossRef](#)]
20. Li, X.; Marasteanu, M. Evaluation of the low temperature fracture resistance of asphalt mixtures using the semi circular bend test. *J. Assoc. Asphalt Paving Technol.* **2004**, *73*, 401–426.



© 2018 by the authors. Licensee MDPI, Basel, Switzerland. This article is an open access article distributed under the terms and conditions of the Creative Commons Attribution (CC BY) license (<http://creativecommons.org/licenses/by/4.0/>).

Article

Effect of Healing Agents on Crack Healing of Asphalt and Asphalt Mortar

Changluan Pan ¹, Ping Tang ¹, Martin Riar ^{1,2}, Liantong Mo ^{1,*}, Mingliang Li ³ and Meng Guo ⁴

¹ State Key Lab of Silicate Materials for Architectures, Wuhan University of Technology, Wuhan 430070, China; panchangluan@whut.edu.cn (C.P.); tangping@whut.edu.cn (P.T.); m.m.riara@whut.edu.cn (M.R.)

² Department of Physics and Electronics, South Eastern Kenya University, 170-90200 Kitui, Kenya

³ Research Institute of Highway Ministry of Transport, Beijing 100088, China; ml.li@rioh.cn

⁴ College of Architecture and Civil Engineering, Beijing University of Technology, Beijing 100124, China; gm@bjut.edu.cn

* Correspondence: molt@whut.edu.cn; Tel.: +86-27-8729-2641

Received: 19 June 2018; Accepted: 2 August 2018; Published: 7 August 2018

Abstract: This study investigated the effect of seven healing agents on crack healing ability of long-term aged asphalt and its mortar. Different healing agents including sunflower oil, aromatic oil, bitumen emulsion, and maltene-based emulsions were used. The crack healing of asphalt made use of two asphalt disk samples and healing was evaluated using direct tensile tests. For asphalt mortar, notched semi-circular samples were used. Test results indicated that the crack healing of asphalt and its mortar depended strongly on the type of healing agent. In general, asphalt healed faster than its mortar. Asphalt healing could be well improved by using oil agents, while asphalt mortar could be well healed with maltene-based emulsions. The crack healing of asphalt mortar developed rapidly followed by a steady state of increase. Initial crack healing using healing agents could be contributed by the diffusion and softening effects, which resulted in low strength recovery. Long term healing could lead to the bonding reconstitution in the cracks, which were decisive for the final strength gain. The promising healing agent should be able to achieve maximum strength recovery to resist cracking as well as a sufficient re-healing ability to deal with crack opening and closing.

Keywords: asphalt; asphalt mortar; healing agents; crack healing; healing model

1. Introduction

Asphalt mixture usually consists of coarse aggregate, fine sand, filler, and bitumen. Asphalt pavements paved with hot asphalt mixture are safe, economic, and durable. Their design life is about 16 years for highways and freeways in China [1]. During the long period of service life, fatigue cracks, thermal cracks, and reflective cracks occur in asphalt pavements due to traffic loads and environmental conditions [2–4]. Cracks give easy access to water and moisture permeation in asphalt concrete, as well as pavement structure. As a result, water-induced damage could happen under the dynamic water pressure and pumping effect of repeated wheel loadings [5]. The premature distresses including stripping bleeding and pothole significantly affects the driving safety and comfort, as well as the service life of asphalt pavement. It is, thus, necessary to fill and seal the cracks in due course to prevent progressive water damage.

Bituminous materials have self-healing property, which is helpful for crack healing to recover stiffness, extend fatigue life and regain strength [6–9]. It was reported that induction heating and embedding microcapsules containing rejuvenator agents could promote crack healing [10–17]. Magnetic induction heating and microwave heating technology could heat bituminous materials and heal cracks [18–23]. Asphalt mixtures containing microcapsules were found to promote crack healing by release the rejuvenator agents into the cracks [24–27]. These technologies are effective in healing

micro-cracks, while for macro-cracks, additional materials are needed to fill in the gap and promote crack healing [28,29].

Asphalt mortar is a composite material consisting of fine aggregates, fillers, and bitumen. It is an important binding material in asphalt concrete to hold coarse aggregates together and form the skeleton for loading support. Since asphalt mortar is rich of bitumen, it was found to significantly affect the performance of recycled asphalt mixtures [30]. Asphalt, asphalt mortar, and asphalt mixtures all have an important role on the crack resistance and healing of asphalt pavements. Some studies indicated that the self-healing properties of bituminous materials reduced at the direction of scale from bitumen, asphalt mastic, asphalt mortars, and asphalt mixtures. The addition of filler, fine sand, and coarse aggregates could significantly decrease the self-healing ability of bituminous materials [6–9]. It was found that the healing strongly depends on the crack size. Cracks at the meso scale and macro scale might hardly heal completely. It becomes necessary to introduce heat or healing agents to promote the healing of open cracks.

This study aims at a better understanding of the crack healing ability of asphalt and asphalt mortar containing healing agents. Different healing agents including sunflower oil, aromatic oil, bitumen emulsion, and maltene-based emulsion were used to promote the crack healing. The healing agents were applied on the fractured surfaces of long-term aged asphalt sample, as well as its mortar samples. The crack healing of asphalt samples was tested after healing for 1 day, 2 days, and 4 days by means of the strength recovery. For the mortar healing, longer healing time was considered for 1–60 days to improve healing. Mortar specimens were tested and the recovery of stiffness, strength, and fracture energy was used as healing indicators. Effects of various agents on crack healing were investigated and a model was proposed to predict the development of mortar healing over time.

2. Materials and Methods

2.1. Materials

Long-term aged asphalt and asphalt mortar which contained basalt aggregate, limestone mineral filler and SBS (Styrene Butadiene Styrene) modified asphalt was used in this study. Table 1 gives the aggregate gradation of the studied mortar. The gradation was determined from the fine fraction (smaller than 4.7 mm sieve size) of AC-13 mixture gradation specified in Chinese Standard of Highway Asphalt Pavement Design, JTG D20-2017 [1]. An SBS-modified asphalt binder that was commonly used in the surface wearing course was employed. Its main properties are as follows: penetration of 73 mm, ductility of 52.1 at 5 °C, and softening point of 68 °C. Long-term aged asphalt was obtained after subjected to RTFOT (Rolling Thin Film Oven Test) aging and PAV (Pressure Aging Vessel) aging according ASTM D6521-18 [31]. The used basalt aggregate had a Los Angeles abrasion value of 7.8%, a crushed stone value of 12.0%, a flakiness and elongation index of 8.5%, and a specific gravity of 2.961 g/cm³. Limestone mineral filler with a density of 2.83 g/cm³ and chemical composition of 51.8% CaO, 3.49% SiO₂ and 1.29% Al₂O₃ was used. The asphalt content of asphalt mortar was determined by 9.2% by taking into account the optimum asphalt content of 4.7% for AC-13 asphalt mixture and the percentage of fine aggregate in the total mixed aggregate.

Seven different healing agents were used in this study and their origins are briefly described below. These healing agents used could be classified into sunflower oil, aromatic oil, bitumen emulsion, and maltene-based emulsion. The use of renewable bio-oil as a modifier for petroleum asphalt has recently been getting more attention [32–34]. Sunflower oil was, thus, to represent a renewable bio-oil as the healing agent. Aromatic oil was chosen because it is part of bitumen's composition and was proven to have a significant effect on asphalt rejuvenation [35,36]. The content of aromatic hydrocarbon of the used aromatic oil employed was 78% according to ASTM D2140 [37]. The smoke point of sunflower cooking oil was 227 °C, while the flash point was 315 °C.

Table 1. Aggregate gradations for the AC-13 mortar.

Sieve Size (mm)	Upper Limitation (%)	Lower Limitation (%)	Passing Percent (%)
4.75	100	100	100
2.36	100	48	66.8
1.18	76	30	50.2
0.6	56	20	32.8
0.3	40	14	22.5
0.15	30	10	14.5
0.075	16	8	9.6

In order to compare the crack healing ability between these two types of oil and their emulsions, sunflower oil and aromatic oil were emulsified by using 60% oil, 2.5% cationic emulsifier, 0.3% stabilizer, and 37.2% water. The solution was controlled at 60–70 °C, while the oil was heated up to 110–120 °C. The oil emulsion was prepared by a high shear colloid mill for 2 min in the laboratory.

Two maltene-based emulsions, named HA-2, and HA-3 were commercial pavement maintenance agents. Both of them were cationic emulsions with a high content of aromatics. For the purpose of comparison, one base asphalt emulsion, named BBE was used. The related technical requirements of the used BBE meet with those for PC-1 base asphalt emulsion according to Technical Specification for Construction of Highway Asphalt Pavements, JTG F40-2004 [38].

In total, seven healing agents were used in this study, which are listed as follows: sunflower oil (KY), sunflower oil emulsion (KR), aromatic oil (FY), aromatic oil emulsion (FR), two commercial maltene-based emulsions (HA-2 and HA-3), and base asphalt emulsion (BBE). Table 2 gives the test results on the measured viscosity and the four components (saturates, aromatics, resins, and asphaltenes) determined by means of thin-layer chromatography (TLC) interfaced with flame ionization detection (FID) (IATROSCAN MK-6, LSI Medience Corporate, Tokyo, Japan) [39]. The particle size of the healing emulsions including KR, FR, HA-2, HA-3, and BBE agents was observed by an XSP-16A biological microscope produced by Nanjing Jiangnan Yongxin Optical Co., Ltd. (Nanjing, China) Almost all of particles are less than 10 µm and more than 80% of them were less than 5 µm.

Table 2. Chemical composition and viscosity of the healing agents.

Healing Agents	Chemical Composition (%)				Viscosity	
	Saturates	Aromatics	Resins	Asphaltenes	Residue at 60 °C (Pa s)	Emulsion at 25 °C (cp)
KY	1.5	86.3	10.0	2.2	0.5–5	–
FY	7.3	84.5	3.3	4.9	30–50	–
KR	1.5	86.3	10.0	2.2	0.5–5	30–50
FR	7.3	84.5	3.3	4.9	30–50	40–60
HA-2	18.1	48.6	22.2	11.1	140–160	50–70
HA-3	12.2	70.1	11.2	6.5	100–120	45–65
BBE	14.1	29.6	43.5	12.8	210–230	150–170

Note: KY = sunflower oil; KR = sunflower oil emulsion; FY = aromatic oil; FR = aromatic oil emulsion; HA-2 and HA-3 = two commercial agents; BBE = base asphalt emulsion.

2.2. Sample Fabrication

The asphalt sample was prepared by using two pieces of asphalt disks as indicated by Figure 1. To prepare the asphalt disk, a small drop of asphalt was placed on the surface of a round nail 14 mm in diameter and pressed to obtain a thick asphalt film around 0.4–0.6 mm. Two nails coated with asphalt films were put together with or without applying healing agents on the surface of asphalt disks. After applying the healing agent, the two disks were adhered together vertically and compressed by the weight of the top nail. In order to determine the asphalt tensile strength, a similar asphalt sample, but with one asphalt disk of 1 mm thickness to adhere two nails was prepared. The tensile strength obtained on this asphalt sample that only consists of one asphalt disk is defined as the original strength.

Figure 2 presents an illustration for the semi-circular bending test setup on the asphalt mortar sample. Semi-circular bending test (SCB) specimens were prepared by taking into account the effect of long-term aging. Long-term aging was simulated by placing loose asphalt mortar in an oven at 100 °C for 96 h [40,41]. Marshall specimens of 100 mm diameter and 63 mm height were prepared using 75 blows per face. Notched SCB samples of 100 mm diameter with a notch 4 mm thick and 10 mm deep at the midpoint were carefully sawn from Marshall specimens according to AASHTO TP105 [42].

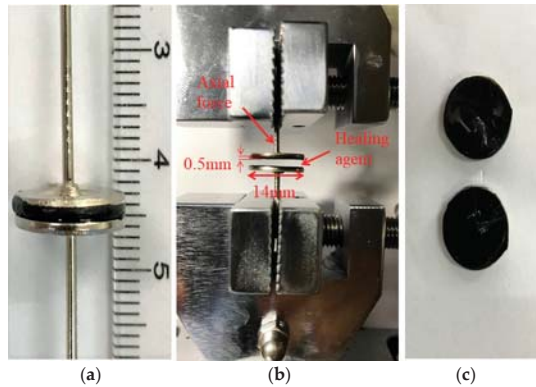


Figure 1. Asphalt sample (a), test setup (b), and the fractured surfaces (c).

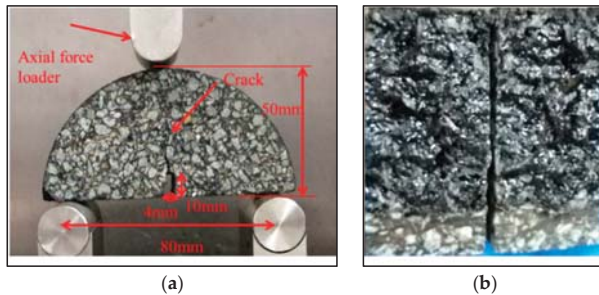


Figure 2. Semi-circular bending test setup (a) for mortar sample and the fractured surfaces (b) after testing.

2.3. Test Procedures

A tensile testing machine (ZQ-990A, Zhiqiu Precision Instruments Co., Ltd., Dongguan, China) was used to carry out the asphalt sample test. The blank asphalt sample was referred to the one without applying healing agents. It was prepared by adhering the two asphalt disks directly together. The other samples were prepared by applying various healing agents on one surface of each pair of asphalt disks. The healing agent was applied by using a soft brush and the application rate was carefully controlled at 0.2–0.3 kg/m². After that, the pair of asphalt disks were adhered together and healed for different periods of time (1, 2, and 4 days) at room temperature around 25 °C. After reaching the desired healing time, a direct tensile test was performed at –10 °C with a load rate of 50 mm/min. Before starting the test, the samples were kept in an environmental cabinet at –10 °C for 1 h to ensure the test samples reached the required test temperature. The effects of 1, 2, and 4 days on asphalt healing were investigated. In this test, three replicate samples in each group were conducted, and the mean value of test result was used for data analysis. Similarly, the asphalt sample that only consists of

one asphalt disk was subjected to direct tensile testing under the same test conditions. The obtained results was defined as the original strength, which was used as the unique reference to determine the healing index from the asphalt samples consisting a pair of asphalt disks.

A universal testing machine (UTM-25, IPC Global, Victoria, Australia) was used to artificially make asphalt mortar cracks. This test was divided into three steps:

- Initial fracture of the SCB samples: The test was conducted at $-10\text{ }^{\circ}\text{C}$ with a load rate of 0.5 mm/min . Before starting the test, the samples were kept in an environmental cabinet at $-10\text{ }^{\circ}\text{C}$ for 4 h to ensure the test specimens reach the required test temperature. Each sample was loaded until completely broken. The fractured sample was moved to room temperature for at least 2 h to raise the temperature of the sample to around $25\text{ }^{\circ}\text{C}$.
- Application of the healing agents: A soft brush was used to apply the healing agents on the cracked surfaces at a spreading rate ranging from 0.3 to 0.7 kg/cm^3 . This rate was appropriate to ensure that the healing agents were fully wetted in the cracked surface without excessive outflow. After the healing agents were applied, the samples were carefully placed together and excess healing agents were wiped. Then they were placed vertically at room temperature.
- After 1 day of healing, the samples were tested again. In order to avoid moisture attachment on the cracked surfaces, which would affect the healing of the samples, when they were completely broken, they were put at room temperature for 2 h. The same fractured samples were then put together carefully without the re-application of the healing agents. After 2 days of healing, the same specimen was tested. By the fracture and re-heal method, the effect of 4, 8, 30, and 60 days on crack healing was evaluated. In this test, at least three replicate samples in each group were conducted, and the mean value of test result was used for data analysis.

2.4. Healing Indicators

The healing of asphalt materials is usually evaluated by the recovery of the material's mechanical properties, such as stiffness, tensile strength, fatigue life, and dissipative energy [7,11,20]. The commonly used healing index is the ratio of the material strength after healing to the original strength. In this case, a higher ratio indicates a better healing performance.

In this study, the healing index obtained from the recovery of strength was used to measure the healing ability of asphalt. In order to get more insight into the crack resistance after healing, healing indices including the recovery of strength, stiffness, and fracture energy as indicated in Figure 3 were used to explore the crack healing of asphalt mortar. In this paper, the three healing indices mentioned above were determined according to AASHTO TP105 [42] and are shown in Equations (1)–(6).

Strength healing index (FI) is the strength recovery ratio calculated by:

$$FI = \frac{F_{ah}}{F_{ai}} \times 100\% \quad (1)$$

where the subscripts "i" and "h" indicates the peak force F_a tested initially and after the healing, respectively.

Stiffness Index (SI) is the stiffness recovery ratio determined by:

$$SI = \frac{S_{ph}}{S_{pi}} \times 100\% \quad (2)$$

The subscripts "i" and "h" presents the mortar stiffness S_p tested initially and after the healing, respectively.

Fracture Energy Index (EI) is the fracture energy ratio:

$$EI = \frac{E_h}{E_i} \times 100\% \quad (3)$$

$$E_{i/h} = \frac{W_f}{A_{lig}} \tag{4}$$

where “i” and “h” are fracture energy tested initially and after the healing, respectively. Ligament area (A_{lig}) and the work of fracture (W_f) are determined by Equations (5) and (6), respectively.

$$A_{lig} = (r - a)t \tag{5}$$

where r , a and t are sample radius, notch length and specimen thickness, respectively.

$$W_f = \sum_i^n \frac{1}{2}(F_{i+1} + F_i)(d_{i+1} - d_i) \tag{6}$$

where F_i and F_{i+1} present applied load at i and $i + 1$ load step application, respectively, and d_i and d_{i+1} are the displacement at the i -th and $i + 1$ position.

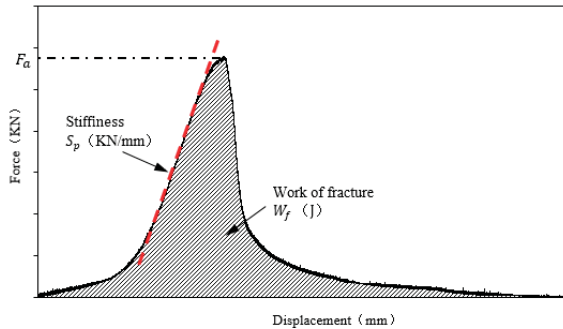


Figure 3. Illustration of determination on peak strength, stiffness, and fracture energy based on the load-displacement curve.

3. Results and Discussion

3.1. Effect of Healing Agents on Asphalt

Figure 4 shows the results obtained from direct tensile testing on blank asphalt samples and those treated with various healing agents. Data obtained from the one-disk asphalt sample were also added for the purpose of reference. Different healing periods of time including 1, 2, and 4 days were involved. Based the force-displacement curves, the peak forces of healed asphalt samples were determined. Furthermore, the original bitumen tensile strength obtained from the one-disk asphalt sample was determined as 383 N. By comparing the peak forces with the original bitumen tensile strength, the healing index of strength recovery were presented in Figure 5.

As indicated in Figure 4, different healing agents displayed distinct behavior on the force-displacement curves. The healing effect of each agent was well distinguished from the peak force. For better interpretation of the healing ability of asphalt, the healing index (FI) shown in Figure 5 will be used for the following discussion. As can be seen, the blank asphalt sample had an obvious healing ability. The healing index was 46% for one day of healing and extended healing time could result in an increased healing index. When the healing time reached 4 days, up to 76% strength recovery could be obtained. Among the seven healing agents, the category of non-emulsion agents, for example, FY and KY showed the highest values of healing index. The emulsion type of the healing agents tended to show a complex healing behavior due to the presence of water. It was expected that the evaporation of water between two asphalt disks significantly affected the gain of strength. This was well observed by comparing KY with KR. Similar results could also be seen between FY and FR. The application of traditional bitumen emulsion (BBE) could improve the crack

healing, especially at the initial phase when compared with the blank asphalt sample. Two maltene-based emulsions (HA-2 and HA-3) did not show a consistent trend on the improvement of crack healing. HA-2 had a higher healing index before 2 days of healing compared to the blank asphalt sample, while a lower value was found for HA-3. This indicated that HA-3 and KR did not promote the healing of asphalt during 4 days of healing. The data presented in Figure 5 shows that the asphalt could have a considerable healing ability even after long-term aging. Oil healing agents could really promote the healing of asphalt. This is attributed to the dissolution and wetting effects of this type of agent. Some emulsion agents showed limited effect on healing because the presence of water between the two asphalt disks evaporated slowly and, thus, impeded the emulsion breaking. This resulted in low strength gain, especially at the initial phase.

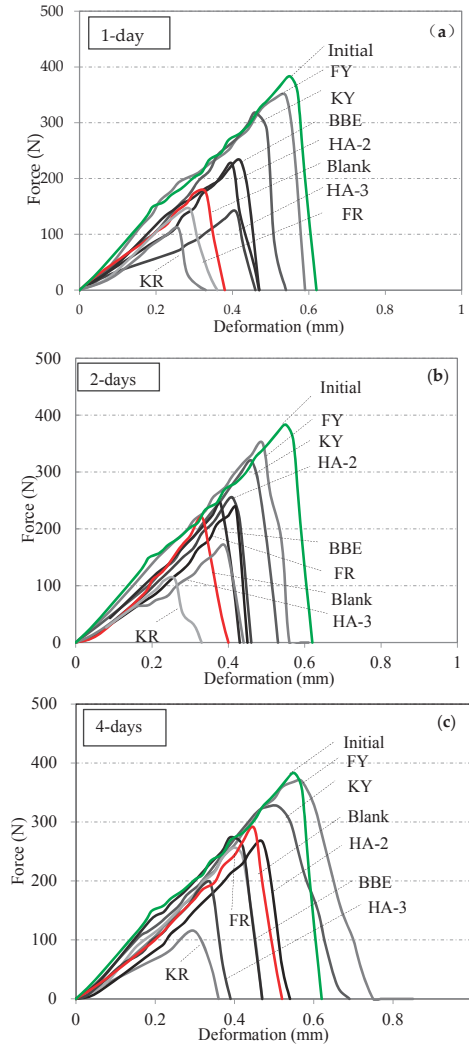


Figure 4. Direct tensile testing results on asphalt samples treated with various healing agents and healed for 1 day (a), 2 days (b), and 4 days (c).

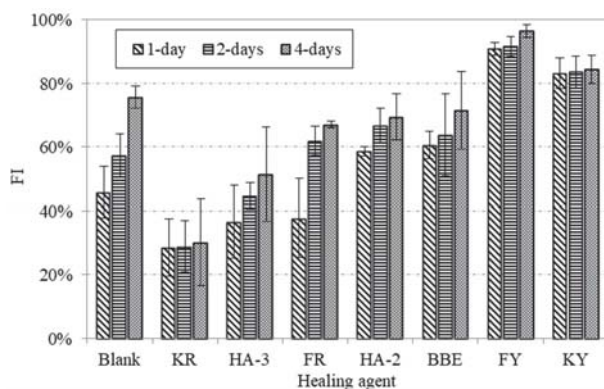


Figure 5. Healing index of strength recovery (FI) for various healing agents determined by taking into account the original bitumen tensile strength of 383 N.

3.2. Appearance of Fractured Surface for Asphalt

Figure 6 shows the fractured surfaces of asphalt samples healed by various healing agents. It should be noted that the direct tensile testing was performed at -10°C . At such a low temperature, asphalt, especially after long term aging, tended to have a brittle failure. When the pair of asphalt disks was adhered together, the crack interface could be the weak link for fracture if the crack was not completely healed. For this reason, the observation of the fracture surfaces could be very useful for evaluation of failure mode, as well as the diffusion of the healing agents. Three failure modes could be expected: failure within the crack interface, failure through the asphalt disks, and adhesive failure between asphalt disk and the nail. After inspection of all the fractured samples, it was found that all of the nails were covered with black asphalt binder and the adhesive failure between the asphalt disk and the nail was hardly seen. This indicated that the adhesive strength between the asphalt disk and the nail was much higher than the cohesive strength of the asphalt, as well as the crack healing strength. Among the seven healing agents, sunflower oil (KY) and aromatic oil (FY) provided strong healing effects for asphalt cracks. For this reason, the fracture surfaces tended to occur within the asphalt disks, but not the crack surfaces. However, sunflower oil emulsion (KR) exhibited the lowest healing effect. Therefore, the failure was concentrated on the crack interface between two asphalt disks. This was proven by the observation of sticky residue on both surfaces of the fractured sample. When the healing time was increased to 4 days, the same failure mode happened, but drier and harder fracture surfaces were observed. This indicated that the healing agent was gradually diffused in the asphalt disks and, thus, led to increased healing strength. When the healing index was higher than 70%, the failure was likely changed from the crack interface to the asphalt disks, or a mixed failure of both could be observed. The above discussion indicates that some of the used healing agents could really improve the crack healing of asphalt and prevent crack failure. The strength gain depended on the interaction between the asphalt and the used healing agents. Extended healing time, thus, improved the healing strength. The failure mode and the hardness of the fracture surfaces could be an indicator for the interaction between asphalt and the healing agent.

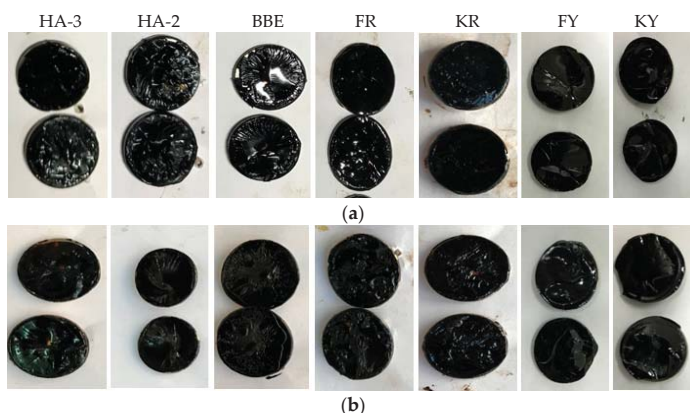


Figure 6. Fracture surfaces for various asphalt samples after (a) 1 day and (b) 4 days of healing.

3.3. Healing of Asphalt Mortar

Tables 3 and 4 present a summary of test results obtained on the strength, stiffness, and fracture energy of asphalt mortar treated with and without healing agents. It should be noted that the initial strength, stiffness, and fracture energy stand for the original mechanical properties. When the mortar specimens were cracked and healed without treating with healing agents, the recovery of strength, stiffness, and fracture energy was very low. It indicated that the self-healing ability of mortar samples was insufficient to repair cracks at room temperature. On the contrary, mortar samples treated with healing agents showed an obvious increase in these mechanical parameters, which implied that healing agents were effective to promote mortar crack healing.

It can also be seen that healing time played an important role in the healing of asphalt binder. As expected, extended healing time could promote the development of crack healing. Among the recovery of strength, stiffness and fracture energy, strength, and fracture energy showed a clear increase trend as the healing time increased, while stiffness did not show a particular change tendency. This, therefore, indicated that stiffness could not be employed as a healing index of crack repair of asphalt mortar. Compared with the recovery of fracture energy after treating with healing agents, the strength gain increased rapidly with healing time and, thus, may well distinguish the development of crack healing from various healing agents. Considering that fracture energy represents the crack resistance and propagation, both of strength and fracture energy were used as healing indicators to evaluate the crack healing performance of asphalt mortar treated with various agents.

Table 3. Test results of strength, stiffness, and fracture energy obtained from blank, sunflower oil-, and aromatic oil-treated mortar samples.

Healing Agents	Healing Time (days)	Strength (kN)	Stiffness (N/mm)	Fracture Energy (J/m ²)
Blank (pure asphalt)	Initial	3.15	9.47	4.35
	1	0.18	0.80	0.09
	2	0.23	0.93	0.11
	4	0.38	2.87	0.18
	8	0.44	2.99	0.27
KY oil	Initial	3.27	9.34	3.90
	1	0.62	5.92	0.56
	2	0.74	6.39	0.67
	4	0.88	7.06	0.69
	8	1.03	6.87	0.81

Table 3. Cont.

Healing Agents	Healing Time (days)	Strength (kN)	Stiffness (N/mm)	Fracture Energy (J/m ²)
FY oil	Initial	2.92	11.81	3.97
	1	0.76	4.83	0.56
	2	0.95	6.91	0.63
	4	1.16	7.58	0.70
	8	1.39	5.34	0.87
KR emulsion	Initial	3.41	8.90	4.55
	1	0.46	2.65	0.27
	2	0.50	2.99	0.30
	4	0.55	2.37	0.44
	8	0.65	3.08	0.57
FR emulsion	Initial	2.74	9.26	3.63
	1	0.66	3.11	0.60
	2	0.84	5.52	0.59
	4	1.02	7.43	0.70
	8	1.19	5.21	0.76

Table 4. Test results of strength, stiffness and fracture energy obtained from base asphalt emulsion and commercial maltene-based emulsion treated mortar samples.

Healing Agents	Healing Time (days)	Strength (kN)	Stiffness (N/mm)	Fracture Energy (J/m ²)
BBE emulsion	Initial	3.20	9.19	4.21
	1	0.86	7.82	0.36
	2	0.95	7.30	0.45
	4	1.28	9.93	0.51
	8	1.32	5.85	0.87
HA-2 emulsion	Initial	2.99	6.67	3.86
	1	1.10	3.66	0.45
	2	1.28	2.94	0.45
	4	1.33	8.86	1.11
	8	1.60	8.63	1.00
HA-3 emulsion	Initial	3.16	8.85	4.20
	1	1.33	3.90	0.49
	2	1.43	8.87	0.54
	4	1.55	6.04	1.03
	8	1.78	7.45	1.10

3.4. Appearance of Fractured Surface for Asphalt Mortar

Figure 7 shows the appearance of the cracked zones for mortar specimens after 1, 2, 4, and 8 days healing. These pictures were taken after the applied load reached the peak value during testing. As can be seen, the cracked zones treated with sunflower oil (KY) and aromatic oil (FY) showed filaments in the initial days. However, these filaments tended to disappear after longer healing time. This similar phenomenon was also observed on the pictures of sunflower oil emulsions (KR) and aromatic oil emulsion (FR). The water in their two emulsions tended to reduce the crack healing when compared with the un-emulsified oil.

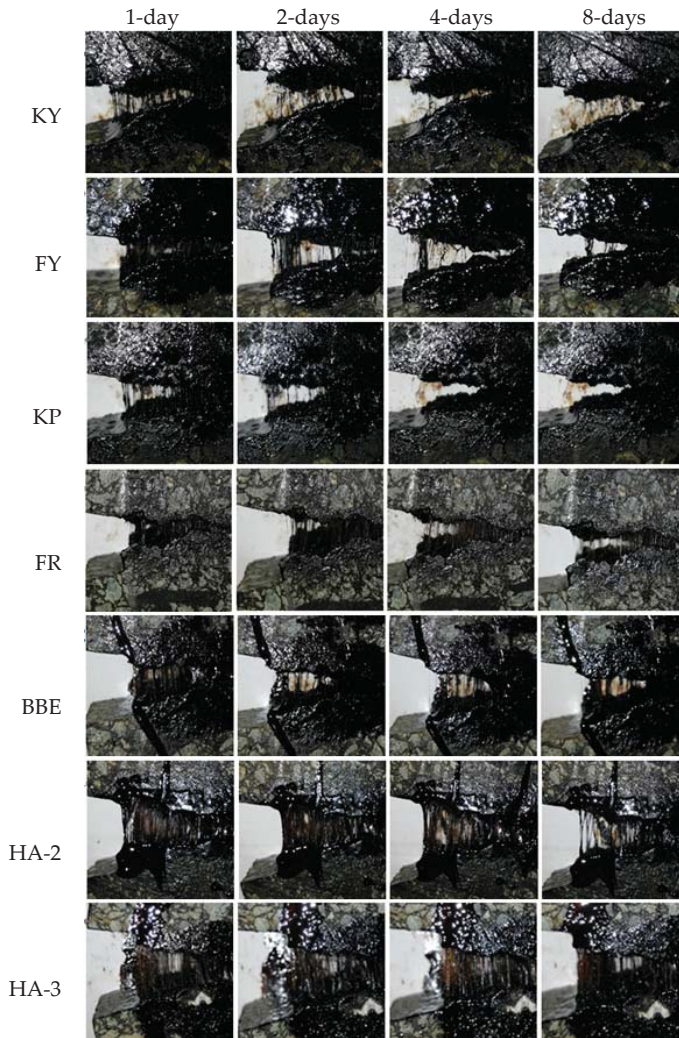


Figure 7. Appearance of the cracked surfaces for healed asphalt mortar after different healing times.

The quantitative data showed in Tables 3 and 4 indicated that BBE, HA-2 and HA-3 had relative better healing performance. This is in agreement with the qualitative data in Figure 7 indicated by large amount of thin filaments which could be seen even after 8 days healing. In addition, the fracture of healed mortar samples was caused by cohesive failure. This indicated that the strength recovery of mortar crack really depends on the interaction between mortar and healing agent. According to Guo’s study, the four components (saturates, aromatics, resins, and asphaltenes) of bitumen had a great influence on diffusion, adhesion, and cohesion work [43]. High diffusion speed of low molecular weight saturates and aromatics helped to activate and soften the asphalt binder on the crack surfaces and thus promote healing. High adhesion work of aromatics and asphaltenes could prevent interfacial adhesive failure. Cohesion strength would benefit from resins and asphaltenes. The results showed in Table 2 indicated that aromatics rich agents could really improve the crack healing. However, the existence of aromatics was likely to act as softening additive for the cracks.

The softened asphalt binder increased self-healing ability, but reduced the cohesive strength. This made the cracks hardly recover to their original strength of the mortar. Combined Figure 7 and Table 2, it is found that healing agents should have high diffusion ability and softening effect to mobilize self-healing, while they should be able to reconstitute the chemical and physical properties of the binder phase between two crack surfaces and recover strength.

3.5. Effect of Healing Agents on Fracture Energy Healing Index

Figure 8 shows the test results of fracture energy healing index (EI) of asphalt mortar treated with various healing agents. The EI value was determined by the ratio of the fracture energy after crack healing compared to the original one. The results indicated the crack healing really depended on the type of healing agent. It also demonstrated that increased healing time led to increase in EI. For instance, mortar samples healed with the oil agents (KY and FY) had an increase in EI from 15.01% to 29.86% and 15.44% to 35.48% when healing time increased from 1 to 60 days. However, the corresponding samples healed using their emulsion KR and FR had a lower EI ranging from 5.84% to 20.36% and 16.59% to 30.61%, respectively. An obvious increase in EI can be seen on mortar samples treated with HA-2 and HA-3. During the initial 8 days of healing, the difference in EI could be considered relatively small. However, the results obtained on 60 days of healing were distinct. The reasons for such a difference could be explained by the short-term healing and long-term healing. For the short-term healing, diffusion and softening effect are primary, which just motivates the self-healing ability of the crack surfaces. As a result, the strength recovery and crack resistance are relatively low. During long-term healing of 60 days, the reconstitution of the binder could lead to improved adhesion and cohesion, thus, recovering strength to a higher level.

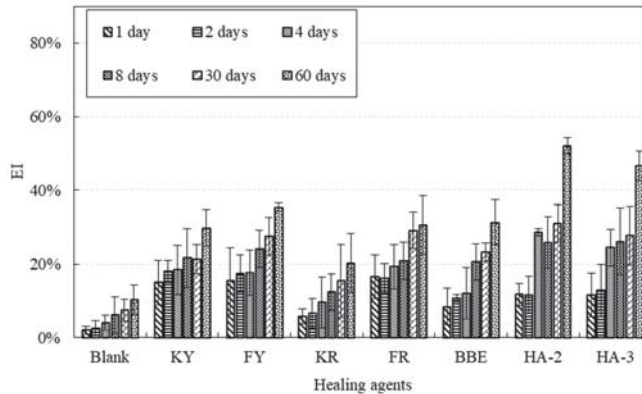


Figure 8. EI of asphalt mortar treated with healing agents after different healing times.

3.6. Effect of Healing Agents on Strength Healing Index

Figure 9 presents the test results of strength healing index (FI) of various healing agents. It should be noted that FI was calculated by ratio of the strength after healing compared to the original strength. As indicated, the strength recovery for mortar samples without applying healing agents was very low. For instance, after 1 day healing, the FI was 5.59%, and it increased to 11.92%, 13.84%, 14.72% and 15.34% for 4, 8, 30, and 60 days, respectively. This showed that the self-healing process reached a maximum value and further healing was limited. Therefore, it is necessary to improve the self-healing ability of asphalt materials to achieve a higher degree of crack healing.

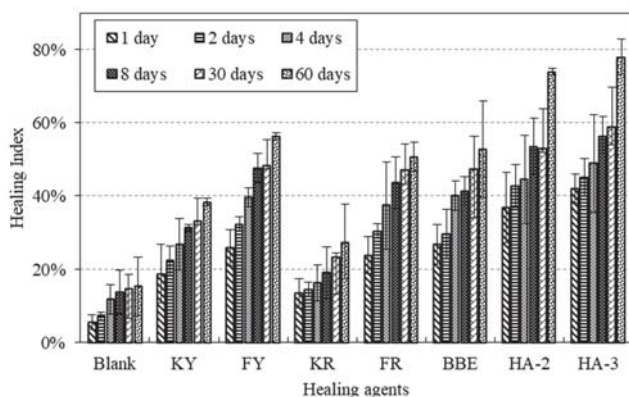


Figure 9. FI of asphalt mortar treated with/without healing agents after different healing times.

Among the seven healing agents, sunflower oil (KY) and its emulsion showed the lowest degree of crack healing, followed by FR, FY, BBE, and HA-2; HA-3 seemed to have the highest healing effect. It indicated that the application of sunflower oil had a limited strength recovery lower than 40%. In general, the application of aromatic oil had a better effect than traditional base bitumen emulsion. Mortar samples healed with the maltene-based emulsion healing agents (HA-2 and HA-3) had an excellent healing effect. For example, the healing index could be up to 50% after eight days of healing.

The effect of healing time on FI was similar to those of EI as indicated in Figure 8. In general, extended healing time resulted in higher FI value. After one day of healing, sunflower oil (KY and KR) had a FI value lower than 20%; BBE and aromatic oil (FY and FR) could increase to 30%, while maltene-based emulsion healing agents (HA-2 and HA-3) could be close to 40%. Extended healing time to 60 days, the FI values of the mentioned four categories could reach around 40%, 55%, 60%, and 75%, respectively. The above data clearly showed that the difference between the initial healing effect and the long-term healing. As mentioned before, the low strength recovery in the initial phase may be due to the diffusion and softening effect, while the obvious strength gain was obtained from the reconstitution of the binder phase including healing agent and original in-mortar bitumen after long-time of healing.

3.7. Modelling of Healing Development

According to above results, the healing time plays a significant role in crack healing of asphalt mortar. To find out the relationship between EI and healing time, Equation (7) was proposed to describe the healing process of the mortar in the entire period of time.

$$HI(t) = A - B \exp\left(\frac{-t}{t_0}\right) \quad (7)$$

where A is the ultimate EI, B is the degree of healing development, $(A - B)$ is the initial EI, and t_0 is the shift point. Below t_0 , the healing rate develops rapidly and above t_0 , the healing rate tends to increase steadily.

The fitting parameters using Equation (7) for various healing agents are shown in Table 5. Good fitting with high R^2 values indicated that Equation (7) was appropriate for modelling the healing development based on fracture energy. Figure 10 presents a comparison of model prediction and test results of EI development over healing time. As indicated, the model predicted well the EI development over healing time. As can be seen in Table 5, the initial EI indicated by the fitting value of $A - B$ varied from 5% to 16%. This implied that the initial recovery of EI was relatively low.

The ultimate EI indicated by the value of A distinguish well the crack healing performance of various healing agents. Sunflower oil (KR and KY) tended to have poor performance while maltene-based emulsion (HA-2 and HA-3) behaved excellently.

For the relation between FI and healing time, a healing model in Equation (8) developed by Wool and O'Connor [44] was used:

$$FI(T, t) = FI_0 + D(T)t^{0.25} \tag{8}$$

where $FI(T, t)$ are the FI of healing agents at the temperature T and time t respectively; T is healing temperature in degree K; t is healing time (s); FI_0 are the initial strength healing index; $D(T)$ indicates the strength gain rate due to the inter-diffusion of molecules between the crack surfaces at temperature T ; $D(T)$ is defined as the strength healing rate which can be explained by the Arrhenius law of diffusion as defined in Equation (9):

$$D(T) = D_0 \exp\left(-\frac{E_a}{RT}\right) \tag{9}$$

where: D_0 is diffusion constant; E_a represents the minimum energy required for healing; R is the universal gas constant ($8.314 \text{ J mol}^{-1} \text{ K}^{-1}$).

In this study, only one healing temperature was involved. Thus, Equation (8) can be further simplified as:

$$FI(t) = FI_0 + Dt^{0.25} \tag{12}$$

where model parameters FI_0 and D can be obtained by fitting the test data.

Table 5. Fitting functions of EI for seven healing agents.

Healing Agents	A	B	A - B	t ₀	Correlation Coefficients
KR	22.7	17.1	5.5	30.4	0.94
KY	30.9	15.3	15.6	14.4	0.99
FR	32.0	15.4	16.6	30.3	0.89
FY	45.5	30.0	15.5	54.9	0.94
BBE	35.8	26.7	9.0	33.2	0.91
HA-2	66.0	55.5	10.5	43.4	0.92
HA-3	51.0	40.0	10.0	24.3	0.90

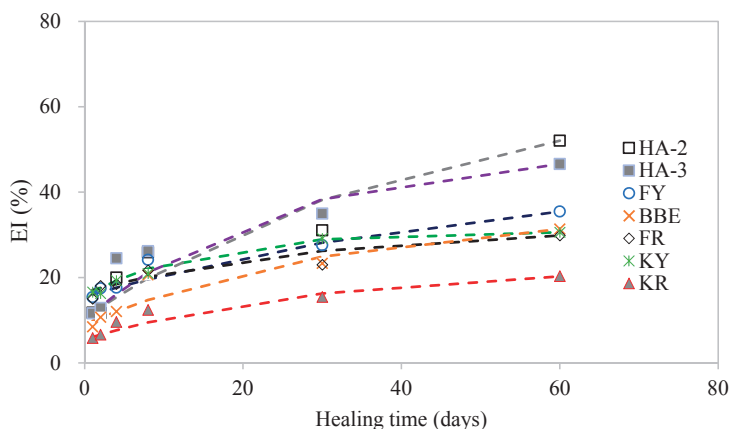


Figure 10. Comparison of model prediction and test results of EI development over healing time.

Table 6 gives the model fitting results on FI development over time for various healing agents. The model parameters FI_0 and D_2 were determined by least squares regression. The correlation

coefficient for each healing agent was larger than 0.87. A comparison analysis between the test and modeled FI results is presented in Figure 11. As indicated, the proposed model could well predict the development of FI over time. The FI increased rapidly at the beginning and then came to a steady state. Sunflower oil had lower value of FI_0 and D_2 , which indicated a lower initial strength gain and healing rate compared with other healing agents. The highest initial strength gain and healing rate was found for HA-3. This further proved a good healing performance of HA-3. With the healing modeling results listed in Table 6, the healing time required for the healing agents to recover 50% of its original strength could be calculated as shown in Figure 12. Sunflower oil (KY and KR) had longest healing times which were 228.6 and 1040.7 days. The time extrapolation based on the model to more than 1000 days were difficult to validate due to the time consuming. This showed the limitation of the model. BBE and aromatic oil (FY and FR) needed 38.2, 27.2, and 41.8 days, respectively. The minimum healing time for maltene-based emulsions (HA-3 and HA-2) to achieve half of healing was 4.6 and 8.2 days respectively, which showed the shortest healing time. The analysis above indicated that sunflower oil lacked strength improvement ability and, thus, was not a good option for crack healing. BBE and aromatic oil exhibited a similar behavior at both initial strength gain and healing rate. Maltene-based emulsions showed the best healing performance. The highest healing rate also indicated a positive reconstitution effect during long-term healing.

Table 6. Fitting functions of FI for seven healing agents.

Healing Agents	Fitting Function	Correlation Coefficients
KY	$FI(t) = 0.5808t^{0.25} + 11.282$	$R^2 = 0.91$
FY	$FI(t) = 0.8789t^{0.25} + 15.597$	$R^2 = 0.87$
FR	$FI(t) = 0.8016t^{0.25} + 15.053$	$R^2 = 0.87$
KR	$FI(t) = 0.4569t^{0.25} + 5.508$	$R^2 = 0.99$
BBE	$FI(t) = 0.7982t^{0.25} + 15.980$	$R^2 = 0.91$
HA-2	$FI(t) = 1.0192t^{0.25} + 20.448$	$R^2 = 0.87$
HA-3	$FI(t) = 1.0511t^{0.25} + 23.653$	$R^2 = 0.92$

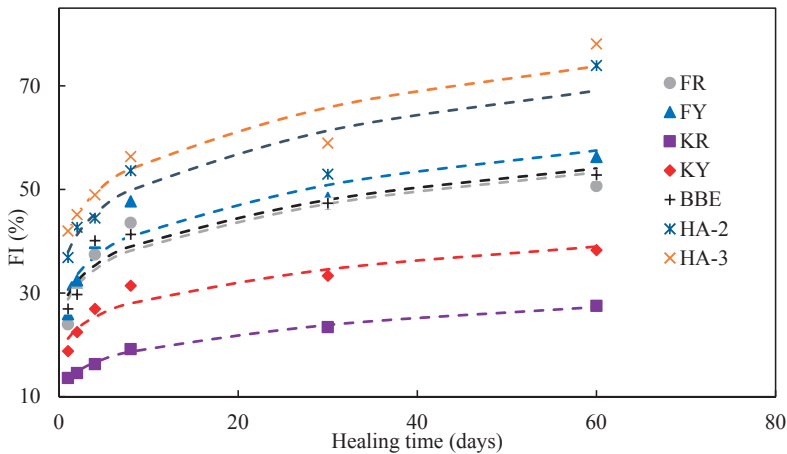


Figure 11. Correlation of healing time and FI.

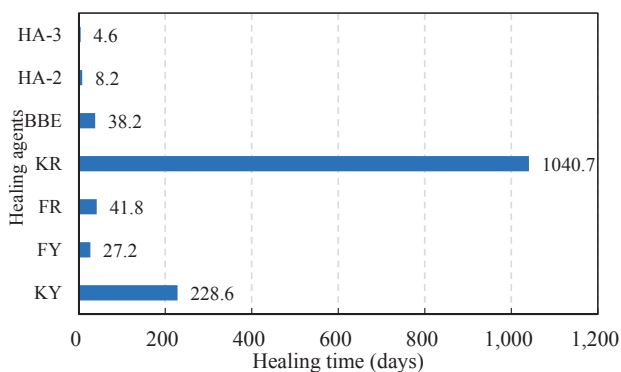


Figure 12. Healing time required for the FI to reach 50%.

4. Conclusions

Seven healing agents, including sunflower oil (KY), sunflower oil emulsion (KR), aromatic oil (FY), aromatic oil emulsion (FR), two commercial maltene-based emulsions (HA-2 and HA-3), and base asphalt emulsion (BBE) were used to heal cracks of fractured long-term aged asphalt and semi-circular samples of long-term aged AC-13 asphalt mortars. The healing ability of these healing agents was evaluated using the strength and fracture energy indicators. In addition, a healing model was introduced to explain the crack healing development over healing time. Based on the data obtained and the analysis presented in this paper, the following conclusions could be drawn:

- Asphalt could have high self-healing ability even after subjecting to long-term aging. The crack healing of asphalt can be well improved by using oil agents but not emulsion agents.
- The healing ability for cracked asphalt mortar without any healing agents was low. The application of healing agent could significantly promote the crack healing. The strength recovery could well distinguish the healing ability of mortar cracks.
- The crack healing of asphalt and its mortar strongly depended on the type of agent used and the dependency was not in agreement with each other, indicating the difference of healing mechanisms of these two materials. Asphalt was much easier to heal compared with its mortar. The diffusion, softening, and reconstitution effects of the healing agent were important for crack healing.
- The healing development of mortar crack can be divided into the initial phase of rapid increase and a steady state. The diffusion and softening effects due to the application of the healing agent contributed to the initial low strength recovery. Long-term healing benefited the bonding reconstitution in the cracks and, thus, improved the final strength.
- Results on the fracture surfaces indicated that the behavior of crack healing was similar to asphalt rejuvenation. Therefore, it could provide a way to optimize the components of healing agent to achieve maximum strength recovery to resist crack, as well as sufficient re-healing ability to deal with crack opening and closing.

Author Contributions: Conceptualization, C.P., T.P. and L.M.; Methodology, C.P., T.P. and M.R.; Software, M.L. and M.G.; Validation, C.P., P.T. and M.R.; Formal Analysis, M.L. and M.G.; Investigation, L.M.; Resources, M.L. and M.G.; Data Curation, C.P. and P.T.; Writing—Original Draft Preparation, C.P. and T.P.; Writing—Review & Editing, L.M. and M.R.; Visualization, L.M. and M.R.; Supervision, L.M.

Funding: This research was funded by National Natural Science Foundation of China (No. U1733121) and the China Scholarship Council.

Acknowledgments: The authors are grateful for the cooperation between the People's Republic of China and the Government of Kenya and express their desire to see a prolonged and stronger cooperation between the two states.

Conflicts of Interest: The authors declare no conflict of interest.

References

1. JTG D20-2017 *Standard of Highway Asphalt Pavement Design*; People's Republic of China Communication Press: Beijing, China, 2017.
2. Sol-Sánchez, M.; Fiume, A.; Moreno-Navarro, F.; Rubio-Gámez, M.C. Analysis of fatigue cracking of warm mix asphalt. influence of the manufacturing technology. *Int. J. Fatigue* **2018**, *110*, 197–203. [[CrossRef](#)]
3. Liu, J.; Zhao, S.; Li, L.; Li, P.; Saboundjian, S. Low temperature cracking analysis of asphalt binders and mixtures. *Cold Reg. Sci. Technol.* **2017**, *141*, 78–85. [[CrossRef](#)]
4. Fang, H.; Luo, H.; Zhu, H. The feasibility of continuous construction of the base and asphalt layers of asphalt pavement to solve the problem of reflective cracks. *Constr. Build. Mater.* **2016**, *119*, 80–88. [[CrossRef](#)]
5. Kakar, M.R.; Hamzah, M.O.; Valentin, J. A review on moisture damages of hot and warm mix asphalt and related investigations. *J. Clean. Prod.* **2015**, *99*, 39–58. [[CrossRef](#)]
6. Qiu, J.; Van de Ven, M.F.C.; Wu, S.; Molenaar, A. Investigating self-healing behavior of pure bitumen using dynamic shear rheometer. *Fuel* **2011**, *90*, 2710–2720. [[CrossRef](#)]
7. Qiu, J.; Van de Ven, M.F.C.; Molenaar, A. Crack-healing investigation in bituminous materials. *J. Mater. Civ. Eng.* **2013**, *25*, 864–870. [[CrossRef](#)]
8. Sun, S.; Sun, G.; Zhu, X.; Pang, Q.; Yu, F.; Lin, T. Identification of wetting and molecular diffusion stages during self-healing process of asphalt binder via fluorescence microscope. *Constr. Build. Mater.* **2017**, *132*, 230–239. [[CrossRef](#)]
9. Lv, Q.; Huang, W.; Xiao, F. Laboratory evaluation of self-healing properties of various modified asphalt. *Constr. Build. Mater.* **2017**, *136*, 192–201. [[CrossRef](#)]
10. González, A.; Norambuena-Contreras, J.; Storey, L.; Schlangene, E. Self-healing properties of recycled asphalt mixtures containing metal waste: An approach through microwave radiation heating. *J. Environ. Manag.* **2018**, *214*, 242–251. [[CrossRef](#)] [[PubMed](#)]
11. García, Á.; Schlangen, E.; Van de Ven, M. Properties of capsules containing rejuvenators for their use in asphalt concrete. *Fuel* **2011**, *90*, 583–591. [[CrossRef](#)]
12. Pamulapati, Y.; Elseifi, M.A.; Cooper, S.B.; Mohammad, L.N.; Elbagalati, O. Evaluation of self-healing of asphalt concrete through induction heating and metallic fibers. *Constr. Build. Mater.* **2017**, *146*, 66–75. [[CrossRef](#)]
13. Al-Mansoori, T.; Norambuena-Contreras, J.; Micaelo, R.; Garcia, A. Self-healing of asphalt mastic by the action of polymeric capsules containing rejuvenators. *Constr. Build. Mater.* **2018**, *161*, 330–339. [[CrossRef](#)]
14. Al-Mansoori, T.; Micaelo, R.; Artamendi, I.; Norambuena-Contreras, J.; Garcia, A. Microcapsules for self-healing of asphalt mixture without compromising mechanical performance. *Constr. Build. Mater.* **2017**, *155*, 1091–1100. [[CrossRef](#)]
15. Ba, H.D.; Park, D.W.; Le, T.H.M. Effect of rejuvenators on the crack healing performance of recycled asphalt pavement by induction heating. *Constr. Build. Mater.* **2018**, *164*, 246–254.
16. Apostolidis, P.; Liu, X.; Scarpas, A.; Kasbergen, C.; van de Ven, M.F.C. Advanced evaluation of asphalt mortar for induction healing purposes. *Constr. Build. Mater.* **2016**, *126*, 9–25. [[CrossRef](#)]
17. Norambuena-Contreras, J.; Yalcin, E.; Garcia, A.; Al-Mansoori, T.; Yilmaz, M.; Hudson-Griffiths, R. Effect of mixing and ageing on the mechanical and self-healing properties of asphalt mixtures containing polymeric capsules. *Constr. Build. Mater.* **2018**, *175*, 254–266. [[CrossRef](#)]
18. Dai, Q.; Wang, Z.; Hasan, M.R.M. Investigation of induction healing effects on electrically conductive asphalt mastic and asphalt concrete beams through fracture-healing tests. *Constr. Build. Mater.* **2013**, *49*, 729–737. [[CrossRef](#)]
19. Gallego, J.; del Val, M.A.; Contreras, V.; Paez, A. Heating asphalt mixtures with microwaves to promote self-healing. *Constr. Build. Mater.* **2013**, *42*, 1–4. [[CrossRef](#)]
20. Vila-Cortavitarte, M.; Jato-Espino, D.; Castro-Fresno, D.; Calzada-Pérez, M.Á. Self-healing capacity of asphalt mixtures including by-products both as aggregates and heating inductors. *Materials* **2018**, *11*, 800. [[CrossRef](#)]
21. Karimi, M.M.; Jahanbakhsh, H.; Jahangiri, B.; Nejad, F.M. Induced heating-healing characterization of activated carbon modified asphalt concrete under microwave radiation. *Constr. Build. Mater.* **2018**, *178*, 254–271. [[CrossRef](#)]
22. Sun, Y.; Wu, S.; Liu, Q.; Zeng, W.; Chen, Z.; Ye, Q.; Pan, P. Self-healing performance of asphalt mixtures through heating fibers or aggregate. *Constr. Build. Mater.* **2017**, *150*, 673–680. [[CrossRef](#)]

23. Gonzalez, A.; Norambuena-Contreras, J.; Storey, L.; Schlangen, E. Effect of RAP and fibers addition on asphalt mixtures with self-healing properties gained by microwave radiation heating. *Constr. Build. Mater.* **2017**, *159*, 164–174. [[CrossRef](#)]
24. Garcia, A.; Jelfs, J.; Austin, C.J. Internal asphalt mixture rejuvenation using capsules. *Constr. Build. Mater.* **2015**, *101*, 309–316. [[CrossRef](#)]
25. Micaelo, R.; Al-Mansoori, T.; Garcia, A. Study of the mechanical properties and self-healing ability of asphalt mixture containing calcium-alginate capsules. *Constr. Build. Mater.* **2016**, *123*, 734–744. [[CrossRef](#)]
26. Xu, S.; Tabaković, A.; Liu, X.; Schlangen, E. Calcium alginate capsules encapsulating rejuvenator as healing system for asphalt mastic. *Constr. Build. Mater.* **2018**, *169*, 379–387. [[CrossRef](#)]
27. Xue, B.; Wang, H.; Pei, J.; Li, R.; Zhang, J.; Fan, Z. Study on self-healing microcapsule containing rejuvenator for asphalt. *Constr. Build. Mater.* **2017**, *135*, 641–649. [[CrossRef](#)]
28. Lin, J.; Hong, J.; Huang, C.; Liu, J.; Wu, S. Effectiveness of rejuvenator seal materials on performance of asphalt pavement. *Constr. Build. Mater.* **2014**, *55*, 63–68. [[CrossRef](#)]
29. Riara, M.; Tang, P.; Mo, L.; Javilla, B.; Wu, S. Investigation into crack healing of asphalt mixtures using healing agents. *Constr. Build. Mater.* **2018**, *161*, 45–52. [[CrossRef](#)]
30. Wang, F.; Wang, Z.; Li, C.; Xiao, Y.; Wu, S.; Pan, P. The rejuvenating effect in hot asphalt recycling by mortar transfer ratio and image analysis. *Materials* **2017**, *10*, 574. [[CrossRef](#)] [[PubMed](#)]
31. *ASTM D6521-18 Standard Practice for Accelerated Aging of Asphalt Binder Using a Pressurized Aging Vessel (PAV)*; ASTM International: West Conshohocken, PA, USA, 2018.
32. Kuang, D.; Jiao, Y.; Ye, Z.; Lu, Z.; Chen, H.; Yu, J.; Liu, N. Diffusibility enhancement of rejuvenator by epoxidized soybean oil and its influence on the performance of recycled hot mix asphalt mixtures. *Materials* **2018**, *11*, 833. [[CrossRef](#)] [[PubMed](#)]
33. Zhang, D.; Chen, M.; Wu, S.; Liu, J.; Amirkhanian, S. Analysis of the relationships between waste cooking oil qualities and rejuvenated asphalt properties. *Materials* **2017**, *10*, 508. [[CrossRef](#)] [[PubMed](#)]
34. Qu, X.; Liu, Q.; Wang, C.; Wang, D.; Oeser, M. Effect of co-Production of renewable biomaterials on the performance of asphalt binder in macro and micro perspectives. *Materials* **2018**, *11*, 244. [[CrossRef](#)] [[PubMed](#)]
35. Zaumanis, M.; Mallick, R.B.; Poulidakos, L.; Frank, R. Influence of six rejuvenators on the performance properties of reclaimed asphalt pavement (RAP) binder and 100% recycled asphalt mixtures. *Constr. Build. Mater.* **2014**, *71*, 538–550. [[CrossRef](#)]
36. Ma, T.; Huang, X.; Zhao, Y.; Zhang, Y. Evaluation of the diffusion and distribution of the rejuvenator for hot asphalt recycling. *Constr. Build. Mater.* **2015**, *98*, 530–536. [[CrossRef](#)]
37. *ASTM D2140-08 Standard Practice for Calculating Carbon-Type Composition of Insulating Oils of Petroleum Origin*; ASTM International: West Conshohocken, PA, USA, 2017.
38. *JTG F40-2004 Technical Specification for Construction of Highway Asphalt Pavements*; People's Republic of China Ministry of Transport: Beijing, China, 2004.
39. Dunn, K.; Chilingarian, G.V.; Lian, H.; Wang, Y.; Yen, T.F. Analysis of asphalt and its components by thin-layer chromatography. In *Asphaltenes and Asphalts*, 2nd ed.; Yen, T.F., Chilingarian, G.V., Eds.; Elsevier Science: Amsterdam, The Netherlands, 2000; Volume 40B, pp. 305–317.
40. Tang, P. Effect of Crack Healing of Bituminous Mortar and Concrete with Healing Agents. Master's Thesis, Wuhan University of Technology, Wuhan, China, May 2018.
41. Riara, M.; Tang, P.; Mo, L.; Hong, W.; Chen, M.; Wu, S. Evaluation of moisture and temperature effect on crack healing of asphalt mortar and mixtures using healing agents. *Constr. Build. Mater.* **2018**, *177*, 388–394. [[CrossRef](#)]
42. *AASHTO TP105 Standard Method of Test for Determining the Fracture Energy of Asphalt Mixtures Using the Semicircular Bend Geometry (SCB)*; AASHTO: Washington, DC, USA, 2015.
43. Guo, M. Study on Mechanism and Multiscale Evaluation Method of Interfacial Interaction between Asphalt Binder and Mineral Aggregate. Ph.D. Thesis, Harbin Institute of Technology, Harbin, China, December 2015.
44. Wool, R.P.; O'Connor, K.M. A theory crack healing in polymers. *J. Appl. Phys.* **1981**, *52*, 5953–5963. [[CrossRef](#)]



Article

Heating Characteristics and Induced Healing Efficiencies of Asphalt Mixture via Induction and Microwave Heating

Quantao Liu ^{1,2}, Cheng Chen ¹, Bin Li ¹, Yihan Sun ³ and Hechuan Li ^{1,*}

- ¹ State Key Laboratory of Silicate Materials for Architectures, Wuhan University of Technology, Luoshi Road 122, Wuhan 430070, China; liuqt@whut.edu.cn (Q.L.); chencc@whut.edu.cn (C.C.); lib@whut.edu.cn (B.L.)
 - ² National & Local Joint Engineering Laboratory for Transportation and Civil Engineering Materials, Chongqing Jiaotong University, Chongqing 400074, China
 - ³ Zhejiang Provincial Institute of Communications Planning, Design & Research, Hangzhou 310015, China; sunyh@whut.edu.cn
- * Correspondence: lihc@whut.edu.cn; Tel.: +86-155-2722-6172

Received: 7 May 2018; Accepted: 28 May 2018; Published: 29 May 2018

Abstract: This paper investigates the heating characteristics and induced healing efficiencies of asphalt mixture containing steel fiber under induction heating and microwave heating. The heating characteristics of an asphalt mixture with different heating methods were studied with an infrared camera. The healing performance of the asphalt mixture specimens in different healing conditions were investigated by observing the crack closure and testing the fracture resistance recovery after healing. The results showed that the heating speed at the surface of asphalt mixture with induction heating was much higher than that with microwave machine heating, under a similar output power and the same method of radiation. While the temperature distribution within the asphalt mixture under induction heating was quite uneven, microwave heating resulted in a more uniform temperature distribution. The effective heating depth of microwave heating is much higher than that of induction heating. Gradient healing occurred within the sample heated with induction heating, while a uniform healing effect can be achieved with microwave heating.

Keywords: asphalt mixture; microwave heating; induction heating; effective heating depth; induced healing

1. Introduction

Asphalt is a typical temperature-sensitive material, and its self-healing ability is highly dependent on temperature. Heating has been used by many researchers to enhance the self-healing properties of asphalt and asphalt mixtures [1–5]. Electromagnetic induction, microwave, and infrared heating methods were widely applied to increase the temperature of an asphalt mixture for healing purpose [6,7]. A suitable temperature can lead to low viscosity and good flow performance of asphalt binders, resulting in significant improvement of the self-healing properties of the asphalt binder and the restoration of micro-structural damages within the asphalt mixture [8,9].

It has been demonstrated that induction heating can be used to improve the healing capability of asphalt mixtures [10–12]. During induction heating, asphalt mortar containing conductive particles is exposed to an alternating electromagnetic field with a frequency in the order of kilohertz [13]. Induction energy heats the metallic fibers by means of high-frequency alternating electromagnetic fields, which are able to induce eddy currents in materials that are electrically and magnetically susceptible. The heat energy diffuses into the asphalt binder to increase the temperature. Asphalt mixture can be

healed quickly, because asphalt binder behaves as a near-Newtonian fluid when its temperature is above the softening point of the binder [14]. Liu et al. prepared electrically porous asphalt mixture by adding steel fibers, and proved that this kind of asphalt concrete can be easily heated via induction heating [15]. It was also demonstrated that long steel wool with a smaller diameter is more effective than short steel fiber with a bigger diameter for increasing the temperature [16]. Wang et al. and Dai et al. also studied the induced healing capability of asphalt mastic and dense-graded asphalt mixture beam samples through induction heating technology [17,18]. It was found that the micro-cracks in the mastic samples could be effectively healed at a heating temperature of 85 °C, whilst 100 °C was identified as the maximum allowable induction heating temperature for asphalt mixtures [15].

Microwave heating is also considered as a promising technique to promote the self-healing of composite materials with metallic fibers [19,20]. Microwave heating causes the polar molecules' orientation to change due to the alternating magnetic field. As a result, the movement of the molecules is disturbed and hindered, and the temperature rises. In addition, if ferrous particles are added to the mixture, they may reflect microwave radiation and accelerate the increase of temperature [21,22]. Ferrous particles can be used to increase heating rates of asphalt mixtures, because they can absorb and conduct more thermal energy than the other components of the mixtures, such as aggregates and asphalt binder. Laboratory experiments have been conducted by adding steel fibers into an asphalt mixture induce healing of that asphalt mixture with microwave heating. Al-Ohaly et al. studied the effects of microwave heating on asphalt adhesion as well as water damage in asphalt mixtures. They emphasized that microwave treatment had the potential to improve the bonding properties of asphalt and aggregate [23]. Sun et al. studied the induced-healing performance of asphalt mixture under microwave irradiation, and proved that microwave heating induced a good heating effect for asphalt mixture containing steel slag [24,25].

It is widely accepted that heating can effectively enhance the induced healing ratios of asphalt mixtures. However, there is debate over which heating method is superior. To compare the heating characteristics and crack healing performance of asphalt mixture via induction heating and microwave heating, and find out which heating technology is more superior, this paper investigates the heating rate, heating uniformity, effective heating depth, and healing ratio of asphalt mixture induced by these two heating methods.

2. Materials and Experiments

2.1. Materials

Penetration-grade 70# asphalt binder obtained from Hubei Guochuang Hi-tech Material Co. Ltd. of Wuhan, China was used in this paper. Steel wool fibers provided by Shanghai Auticar Metal Products Co. Ltd. (Shanghai, China) were used as the heating units for asphalt mixtures with induction and microwave heating. The properties of the asphalt binder and steel wool fibers were shown in Table 1, where Chinese Technical Specification JTG F40-2004 was used. The optimal content of steel wool fibers was 6% by volume of the asphalt binder, according to previous research [26]. Asphalt mixture with 6% steel wool fibers has the highest strength and particle loss resistance, and an acceptable induction heating speed. Basalt aggregates and limestone filler were used as the mineral materials in this research.

Table 1. The properties of asphalt binder and steel wool fibers.

Materials	Properties	Values	Specifications
Steel fiber	Length (mm)	4.2	-
	Equivalent diameter (μm)	70–130	-
	Gravity (g/cm^3)	7.8	-
Bitumen	Penetration (25 °C, 100 g, 5 s, 0.1 mm)	68	60–80
	Ductility (15 °C, cm)	>100	100
	Softening point (°C)	47.5	47

2.2. Sample Preparation

AC-13 asphalt mixture was designed in this paper according to the Marshall Design method, and the asphalt–aggregate ratio was 5.0%. The mixture was mixed and compacted at 160 °C and 150 °C respectively. The air voids (VV) were 4.4%, voids in mineral aggregates (VMA) were 14.3%, and voids filled with asphalt (VFA) were 69.4%. The volume indices of asphalt mixture were tested according to Chinese standards; all the indices met the standard requirements [26]. Asphalt mixture rutting slabs were formed with the wheel-rolling compaction method, according to Technical Specification JTG E20-2011, and divided into several beams with a length of 200 mm, width of 40 mm, and height of 40 mm. A notch with a depth of 5 mm and a width of 4 mm was sawn into the center of the beams to control the position of failure during the fracture test. Asphalt slabs with a length of 30 cm, a width of 30 cm, and a height of 10 cm were also prepared; cores with diameter of 10 cm were drilled in the middle of slabs. The slabs were used for heating under induction and microwave machines, and the cores were used to analyze the vertical temperature distribution after heating with the two heating methods.

2.3. Induction and Microwave Heating

As shown in Figure 1, asphalt samples were heated by an induction heating machine with an output power of 8.3 kW and a frequency of 123 kHz. The distance between the coil and the surface of sample has a significant influence on the heating speed. The distance used in this paper for heating beams was 10 mm to obtain a high heating speed, according to the preliminary study [27], and 30 mm for slabs, the same distance as the microwave machine on slabs.

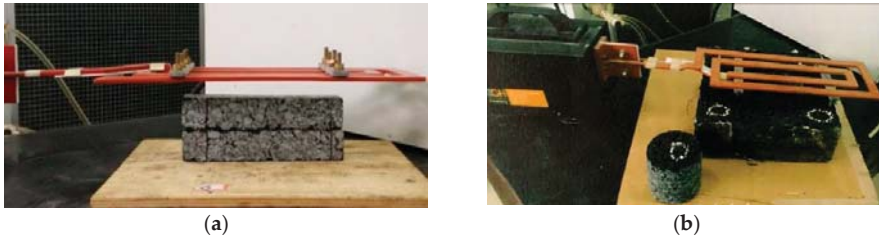


Figure 1. Induction heating of the sample: (a) heating beam, (b) heating slab.

As shown in Figure 2, a self-developed microwave machine with a frequency of 2.45 GHz and an output power of 5 kW was also used in this research. This improved microwave machine contains a microwave magnetron, control panel, and metal cover (to prevent microwave leak). In order to simulate the practical microwave heating process of asphalt pavement, the microwave launcher was installed in the upper section of the metal cover, and the distance between the launcher and asphalt mixture slabs was 30 cm. The microwave launcher radiates waves from the top of the machine, and directly irradiates on the top surface of the samples being heated. This way, the microwave heating can be comparable with induction heating. An infrared image camera with a resolution of 320 × 240 pixels was used to determine the temperature distribution within the samples after induction and microwave heating.

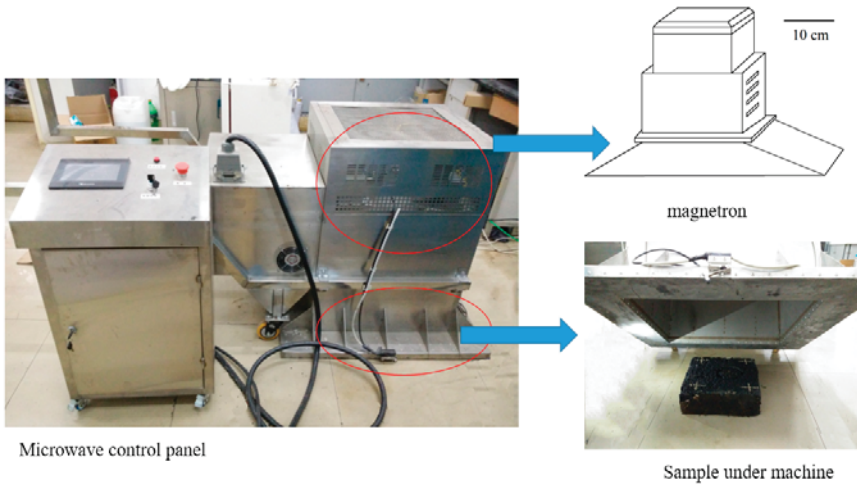


Figure 2. Improved microwave heating machine for slabs.

2.4. Fracture and Healing Test

A universal testing machine (UTM-25, IPC Global, Victoria, Australia) was used to conduct the fracture and healing test. The schematic view of the beam samples and the fracture-healing procedure are shown in Figure 3.

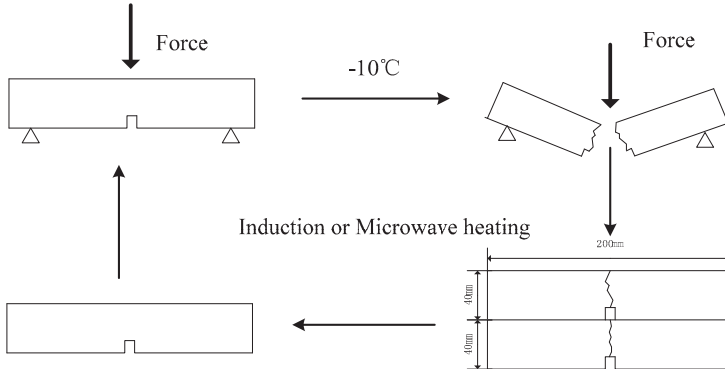


Figure 3. Healing test procedure of beam samples.

All samples were kept in the freezer for 6 h at $-10\text{ }^{\circ}\text{C}$ before the fracture test to decrease the viscoelasticity and unrecovered deformation of the samples during the fracture test. The asphalt beams were broken under a three-point bending setup, to obtain the original fracture force F_1 . The distance between the two supporting points was 160 mm. Loads were applied on the samples with a descending speed of 50 mm/min; the force-displacement curves of the samples were recorded by a computer connected with the loading machine. The fractured beams were placed on a plate until they reached room temperature, and two broken beams were stacked together for heating treatment with induction heating or microwave heating. After the heating process, the samples were cooled to room temperature and fractured again at $-10\text{ }^{\circ}\text{C}$, as in the first fracture test. The second fracture force F_2 was obtained,

and the healing ratio induced by induction; microwave heating was defined as the maximum force after healing divided by original fracture force.

3. Results and Discussion

3.1. Heating Characteristics of Asphalt Mixture with Induction Heating

The sample showed a high heating efficiency with induction heating technology. The infrared images of the sample after 2 and 5 min heating were shown in Figure 4. It can be seen that the sample showed a very obvious rainbow temperature distribution, ranging from 14.3 to 60.9 °C after 2 min heating, which means a gradient heating in the vertical direction. The heating speed decreased gradually with increasing depth. The top part of the core shows an obvious heating performance, thus the crack in this layer can probably be healed soon. The temperature at the bottom of the core was 14.3 °C after 2 min heating, which is not sufficient to induce the healing of the binder. Therefore, an effective healing depth exists for the sample being induction-heated and it is less than the thickness of the sample.

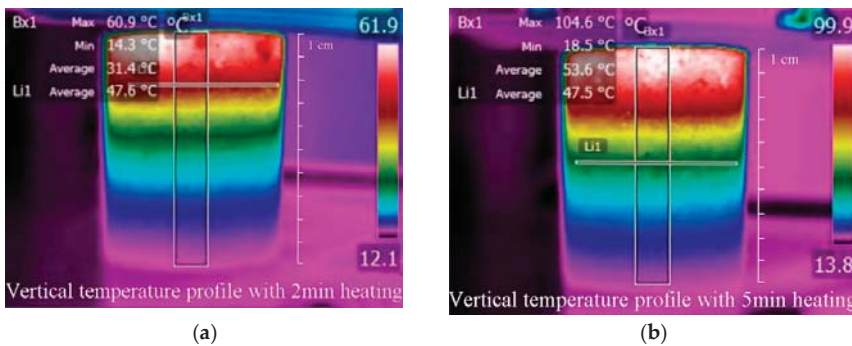


Figure 4. Infrared images of the core after induction heating at a heating distance of 30 mm. (a) Vertical temperature profile of the sample with 2 min heating. (b) Vertical temperature profile of the sample with 5 min heating.

The healing efficiency of an asphalt mixture depends on the capillary flow speed of the binder. The softening point of asphalt binder can be considered as a critical healing temperature for the binder to obtain a good healing property [14]. The softening temperature of the 70# base bitumen used in this paper was 47.5 °C. So the depth at which the temperature reached 47.5 °C was considered as effective healing depth of the sample. At the depth of 2.2 cm, the temperature was 47.6 °C (around the softening point of the binder). Therefore, 2.2 cm was considered as the effective heating depth with 2 min of induction heating. After 5 min of heating, the average temperature at the surface of the slab was 99.8 °C (the heating rate at the surface of the slab was 17.5 °C/min), the allowable surface temperature. As shown in previous research, the surface heating temperature should not be higher than 100 °C, to avoid the swelling of the binder and the excess expansion of the mixture [28]. Therefore, no further heating can be applied, to avoid overheating of the sample surface. In this case, the temperature was 47.6 °C (around the softening point of the binder) at the depth of 4.8 cm. Therefore, 4.8 cm was considered as the maximum heating depth with induction heating. Even within the effective healing depth of 4.8 cm, both the temperature and the induced-healing ratio are not uniform. As temperature is the key parameter controlling the healing rate of the mixture, the upper part of the sample will be healed better than the lower part.

The heating distance between the coil and the top surface of the sample can significantly influence the effective heating depth of an asphalt mixture. A heating distance of 10 mm was recommended

for the practical application of induction heating on asphalt pavement [15]. The vertical temperature distribution and the effective heating depths of the asphalt concrete samples with different heating periods, at a heating distance of 10 mm, are shown in Figure 5. It can be seen that the effective heating depth increased with the increase of the heating time. The effective heating depth was 10.9 mm after heating for 20 s, while the depth increased to 60.1 mm after 100 s of heating. However, the surface temperature of the sample reached 129.9 °C after heating for 100 s, and the beam sample suffered serious swelling deformation. At 60 s of heating, the sample surface approached its allowable heating temperature of 100 °C, and the effective depth of asphalt mixture with induction heating was around 42.8 mm, which can be assumed to be the maximum effective depth of asphalt mixture at this heating distance. Extending the heating time further will result in excess expansion deformation of the mixture. It can be noted that a smaller heating distance between the coil and the sample (higher heating speed) resulted in a lower effective heating depth of the mixture.

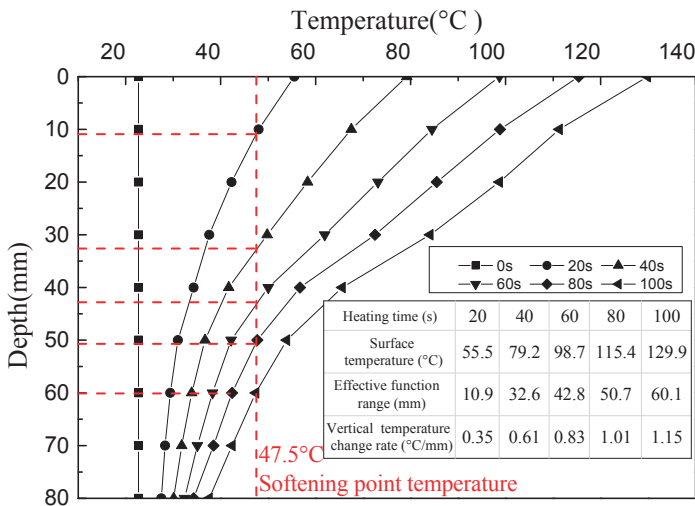


Figure 5. Vertical temperature distribution of the samples at a heating distance of 10 mm.

3.2. Healing Performance of an Asphalt Mixture at Different Induction Heating Temperature Gradients

Figure 6a shows the infrared image of beams after 60 s induction heating at a heating distance of 10 mm. It can be seen from the infrared image that sample showed a good heating effect, especially at the top layers. The temperature distribution presented a rainbow-like gradient, which shows an uneven heating effect in the vertical direction. It can also be seen that the average temperatures of upper and lower beams were 72.1 °C and 39.4 °C, respectively, and the temperature difference between upper and lower beams reached 32.7 °C. The temperature distribution of the beams was analyzed from the infrared image shown in Figure 6b. It is worth noting that the ratio above 46.6 °C (around softening point of asphalt) was 55%, meaning that half of the cracks can be healed at this critical healing temperature, according to Tang’s results [14].

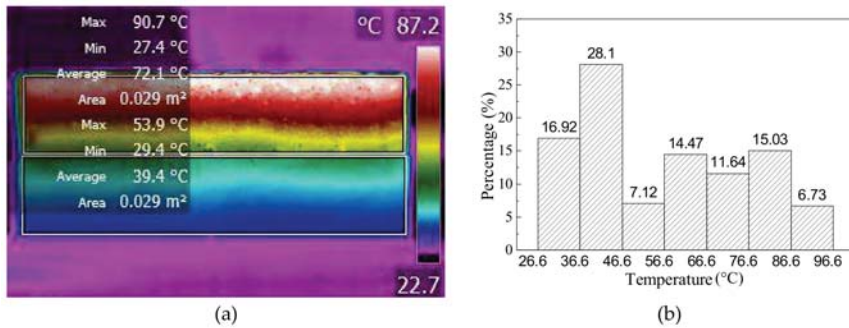


Figure 6. The (a) infrared image and (b) temperature distribution of the beam sample with 60 s induction heating.

In order to obtain the healing efficiency at different depths of the sample, two asphalt beams were stacked together during heating and separated after cooling. The damaged area was photographed in the same position before and after healing, to observe the healing phenomenon of the cracks. The maximum fracture forces before and after healing were measured, and the healing ratio of upper and lower beams was obtained. The healing behaviors of the mixture at three temperature gradients (60 °C, 80 °C, 100 °C, as well as surface temperature) were investigated.

The crack healing phenomenon of the upper beam at different temperatures under induction heating is shown in Figure 7. The gradient healing phenomenon of the beam can be seen by comparing the cracks before and after healing. When the surface temperature of the sample was 60 °C, the crack was not healed, and can be seen clearly after heating due to low heating temperature and the resultant limited healing effect. As shown in Figure 7b, the shallow crack disappeared when the sample surface was heated to 80 °C, while the crack in the lower part can still be seen clearly after healing. This means that the healing effect of the sample tends to deteriorate with as the depth increases. When the surface temperature of the beam reached 100 °C, all cracks disappeared, but partial deformation can be seen at the surface of beams. It should be noted that some broken aggregates cannot be healed, because induced healing only occurs within asphalt mastic due to asphalt flow. The broken of the aggregates will significantly affect the strength recovery ratio of the samples.

Table 2 shows the induction healing ratios of the samples with different surface heating temperatures. It can be seen from the healing efficiency results that the healing ratios of the upper beams increased with the increase of the surface temperature. The healing ratio of the sample at surface temperatures of 60 °C, 80 °C, and 100 °C was 30.8%, 42.8%, and 65.7%, respectively. While there was no healing with the lower beams until the surface temperature reached 100 °C. This is mainly related to the temperature gradient distribution. The asphalt binder in the lower beam had no ability to flow and heal the cracks at the lower surface temperatures of 60 °C and 80 °C. The temperature of the lower beam ranged from 32.4 °C to 47.0 °C when the surface temperature was 80 °C. As the temperature of the lower beams did not reach the softening point temperature of the binder, the cracks in the lower beams were almost not healed, and can be clearly seen after heating. The temperature of a small partial of the lower beam was higher than 47.5 °C when surface temperature reached 100 °C, so a low healing ratio of 12.6% was obtained in the lower beam. Based on the crack healing phenomenon and the corresponding healing ratios, it can be concluded that the gradient healing phenomenon of asphalt mixture exists with induction heating, and is mainly related to temperature gradient distribution within the sample.

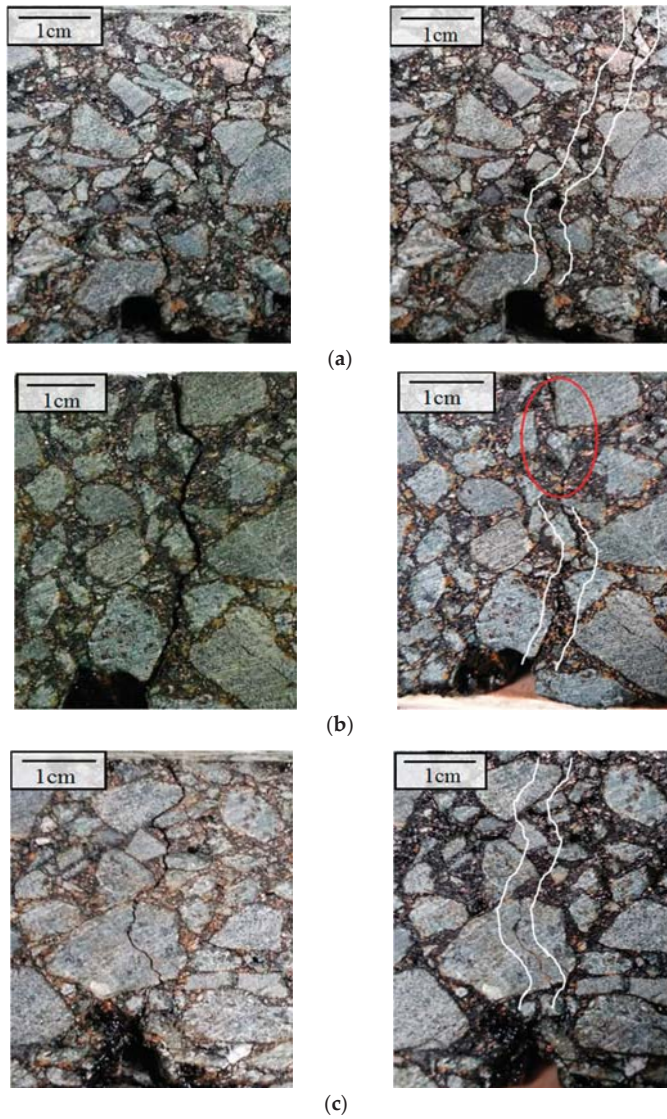


Figure 7. Healing phenomenon at different temperatures under induction heating. (a) Crack healing phenomenon at 60 °C: crack not healed; (b) Crack healing phenomenon at 80 °C: crack partially healed; (c) Crack healing phenomenon at 100 °C: fully healed, except for broken stone.

Table 2. Induction healing ratios of the samples with different surface heating temperatures.

Beams	Surface Temperature		
	60 °C	80 °C	100 °C
Upper beam	30.8%	42.8%	65.7%
Lower beam	0	0	12.6%

3.3. Heating Characteristics of Asphalt Mixture with Microwave Heating

Figure 8 shows the infrared image of the asphalt slab and core after heating for 15 min with the microwave machine. The average temperature of the slab surface reached 58.4 °C, and the temperature of the core ranged from 50.2 °C to 33.2 °C from top to bottom. In the top 7 cm of the core, the temperature ranged from 40.2 °C to 50.2 °C, with an average temperature of 45.4 °C, showing a much more uniform distribution than induction heating. The average temperature at the depth of 4 cm was 46 °C, around the softening point of the binder. It can be considered that the effective depth of the mixture was 4 cm after heating 15 min with the microwave machine.

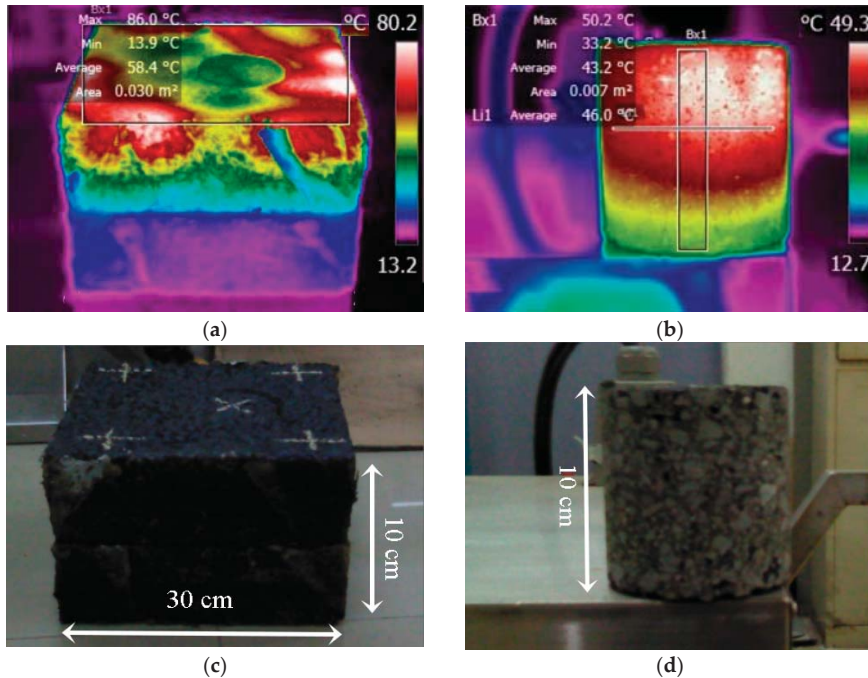


Figure 8. Infrared images of slab and core after heating for 15 min with improved microwave machine. (a) Surface temperature profile of slab after heating; (b) Vertical temperature profile of core after heating; (c) Slab sample; (d) Core sample.

After heating for 25 min, the average surface temperature of the slab was 91.2 °C, and the heating rate at the surface of the slab was 3.12 °C/min. The longitudinal temperature of the core ranged from 55.8 to 82.1 °C, which was higher than the softening point of the binder. This means that the heating depth has increased to the whole depth of the sample with a surface temperature lower than 100 °C. It can be concluded then that extending the heating time can increase the effective heating depth of asphalt mixture heated with the microwave equipment.

To sum up, the heating functional range of the asphalt mixture with the microwave machine was more than 10 cm under 25 min of heating, which was much deeper than the maximum heating depth of induction heating (4.8 cm). However, the heating speed of the mixture under induction heating (17.5 °C/min) was much higher than that with microwave heating (3.12 °C/min). In addition, the uniformity of microwave heating was much higher than that of induction heating, which has a gradient distribution. The two heating methods have their own heating characteristics, which should be considered in practical application.

3.4. Induced Healing Performance of Asphalt Mixture with Microwave Heating

The cracks of the samples before and after microwave heating at different temperatures were shown in Figure 9. It can be seen from Figure 9 that the cracks are healed better with the increase of heating temperature. At a heating temperature of 60 °C, the crack was partially healed. When the heating temperature reached 80 °C, the crack was fully healed, showing a much better healing effect than that of induction heating. This difference can be explained according to the temperature distribution of the samples. The target heating temperature of the sample with induction heating was the surface temperature of the beams, and the beams showed a strong temperature gradient in the longitudinal direction. When the samples were heated uniformly with microwave heating, the temperature of the whole sample reached 80 °C, which is the reason why the crack can be healed all through the depth of the sample. It can be concluded that the healing phenomenon of the sample with microwave heating was much more uniform than that with induction heating. When the heating temperature reached 100 °C, distinct deformation of samples due to excess expansion of the mastic can be observed. For this reason, it is necessary to control the temperature during microwave heating. The deformation of the sample with induction heating only occurred in the surface of sample, due to the lower internal temperatures. While the whole sample heated with microwave heating suffered deformation because of the uniform heating. The deformation at the cracked areas will probably decrease the healing ratio.

The healing ratios of the samples at three different microwave heating temperatures are shown in Table 3. It can be seen from Table 3 that the upper and lower beams showed similar healing ratios and the healing ratio difference was less than 6%, indicating that the microwave-induced healing was quite uniform. The beams obtained their highest healing ratio at a heating temperature of 80 °C. A temperature of 60 °C was too low for asphalt binder to flow to heal all the cracks, while the healing ratio decreased at 100 °C due to excess deformation of the sample. It should be noted that some aggregates were broken during the bending test, which had a strong influence on the recovered fracture resistance of the beams. For this reason, the real crack healing efficiency of asphalt mastic should be much higher than the fracture resistance recovery ratio.

At the same heating temperatures, the samples heated with microwave heating showed quite different healing efficiencies from the samples heated with induction heating, due to the different temperature uniformities. The induction heating speed of the beams is much faster, but the heating depth is shallow, and there exists a strong temperature gradient, resulting in a poor or no healing effect in the lower beams. The microwave machine applies the radiation all around the samples, while the electromagnetic induction was applied only through the upper surface of samples.

At the heating temperatures of 60 and 80 °C, the healing ratios of the lower beams were slightly higher than the upper beams. This can be attributed to the weight of the upper beams, because it has been reported that external loads have a positive effect on the healing of asphalt mixture [29]. The healing ratios of the beams decreased at 100 °C, especially the lower beam. In this case, the excessive thermal expansion of the asphalt mastic increased the internal pressure and damaged the structure. On the other hand, the weight of the upper beam contributed to the deformation of the lower beams, resulting in a decreased healing ratio. It can be concluded that the weight of the sample has a positive effect on healing at lower temperatures, but a negative effect on healing at excessively high temperatures.

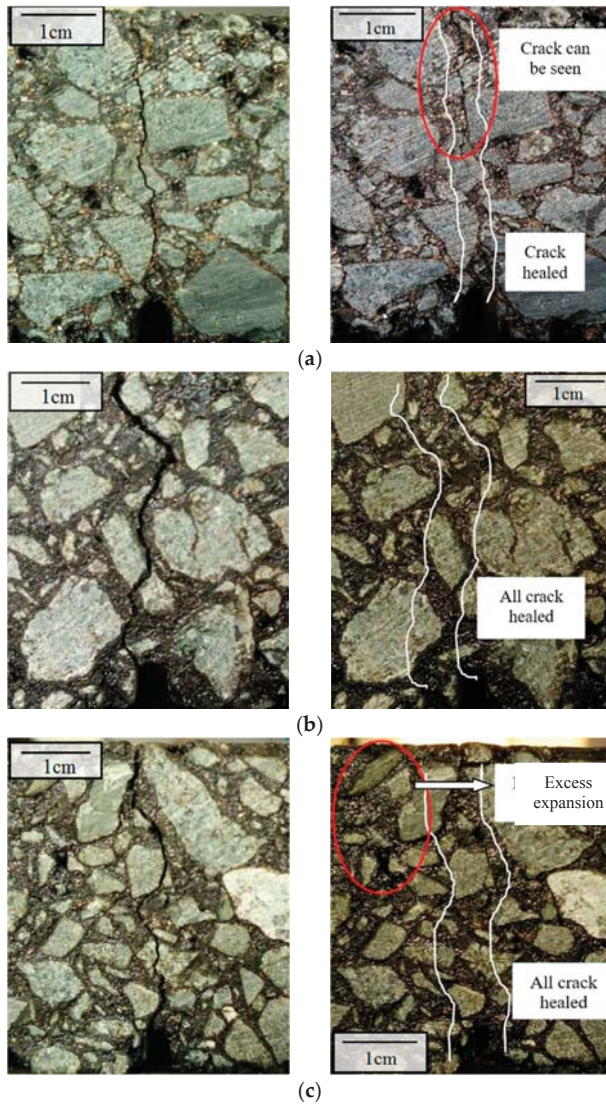


Figure 9. Healing phenomenon of asphalt concrete at different microwave heating temperatures. (a) Crack healing phenomenon at 60 °C: partially healed; (b) Crack haling phenomenon at 80 °C: fully healed; (c) Crack healing phenomenon at 100 °C: fully healed with excess expansion of the binder.

Table 3. Healing ratios of the samples at different microwave heating temperatures.

Beams	Average Temperature		
	60 °C	80 °C	100 °C
Upper beam	30.3%	65.8%	62.9%
Lower beam	36.2%	70.9%	56.9%

4. Conclusions

The heating characteristics and induced healing efficiencies of asphalt mixture containing steel fibers under both induction and microwave heating were studied in this paper. Based on the results, the following conclusions can be drawn:

1. There is a strong temperature gradient through the thickness of asphalt sample heated with induction heating. The temperature difference between the surface and bottom of the sample increased with the heating time. An effective heating depth exists for each induction heating time, and the maximum effective heating depth of asphalt mixture with induction heating is around 48 mm, based on the allowable maximum surface temperature. It is inadvisable to increase the effective heating depth of the sample by extending the induction heating time, which will result in excess expansion deformation of the mixture.
2. Gradient healing phenomenon exists with the sample heated via induction heating, and is mainly related to temperature gradient distribution. The upper part of the sample healed much better than the lower part.
3. Microwave heating is relatively uniform in a longitudinal distribution, and the heating uniformity is independent of heating time.
4. Microwave heating causes more uniform crack healing in an asphalt mixture. The weight of the sample has a positive effect on healing at lower temperatures, but a negative effect on healing at excessively high temperatures.
5. Under the similar power and same radiation way, induction heating is fast and inhomogeneous in the longitudinal direction, while microwave heating is slow and uniform. The effective heating depth of microwave heating is much higher than that of induction heating.

Author Contributions: Conceptualization, Q.L. and Y.S.; Methodology, C.C. and B.L.; Formal Analysis, Q.L.; Investigation, B.L. and H.L.; Writing-Original Draft Preparation, B.L. and C.C.; Writing-Review & Editing, Q.L. and H.L.; Supervision, Y.S.; Project Administration, Q.L.; Funding Acquisition, Q.L.

Funding: This research was funded by National Natural Science Foundation of China (No. 51508433 and No. 51778515); the National & Local Joint Engineering Laboratory for Transportation and Civil Engineering Materials, Chongqing Jiaotong University (No. LHSYS-2016-04); and the National Key Research and Development Program of China (No. 2017YFE0111600). The authors gratefully acknowledge their financial support.

Conflicts of Interest: The authors declare no conflict of interest.

References

1. Norambuena-Contreras, J.; García, Á. Self-healing of asphalt mixture by microwave and induction heating. *Mater. Des.* **2016**, *106*, 404–414. [[CrossRef](#)]
2. Liu, Q.; García, Á.; Schlangen, E.; van de Ven, M. Induction healing of asphalt mastic and porous asphalt concrete. *Constr. Build. Mater.* **2010**, *25*, 3746–3752. [[CrossRef](#)]
3. Li, R.; Wang, C.; Wang, P.; Pei, J. Preparation of a novel flow improver and its viscosity-reducing effect on bitumen. *Fuel* **2016**, *181*, 935–941. [[CrossRef](#)]
4. Qiu, J.; van de Ven, M.F.C.; Wu, S.P.; Yu, J.Y.; Molenaar, A.A.A. Investigating the self healing capability of bituminous binders. *Road Mater. Pavement Des.* **2009**, *10*, 81–94. [[CrossRef](#)]
5. García, Á.; Schlangen, E.; van de Ven, M.; Liu, Q. Induction heating of mastic containing conductive fibers and fillers. *Constr. Build. Mater.* **2009**, *23*, 3175–3181. [[CrossRef](#)]
6. Gallego, J.; del Val, M.A.; Contreras, V.; Paez, A. Heating asphalt mixtures with microwaves to promote self-healing. *Constr. Build. Mater.* **2013**, *42*, 1–4. [[CrossRef](#)]
7. Gómez-Meijide, B.; Ajam, H.; Lastra-González, P.; García, Á. Effect of air voids content on asphalt self-healing via induction and infrared heating. *Constr. Build. Mater.* **2016**, *126*, 957–966. [[CrossRef](#)]
8. Wang, Z.; Dai, Q.; Porter, D.; You, Z. Investigation of microwave healing performance of electrically conductive carbon fiber modified asphalt mixture beams. *Constr. Build. Mater.* **2016**, *126*, 1012–1019. [[CrossRef](#)]

9. Tan, Y.; Shan, L.; Kim, Y.R.; Underwood, B.S. Healing characteristics of asphalt binder. *Constr. Build. Mater.* **2012**, *27*, 570–577. [[CrossRef](#)]
10. Liu, Q.; Wu, S.; Schlangen, E. Induction heating of asphalt mastic for crack control. *Constr. Build. Mater.* **2013**, *41*, 345–351. [[CrossRef](#)]
11. García, Á.; Bueno, M.; Norambuena-Contreras, J.; Partl, M. Induction healing of dense asphalt concrete. *Constr. Build. Mater.* **2013**, *49*, 1–7. [[CrossRef](#)]
12. Ayar, P.; Moreno-Navarro, F.; Rubio-Gámez, M.C. The healing capability of asphalt pavements: A state of the art review. *J. Clean. Prod.* **2016**, *113*, 28–40. [[CrossRef](#)]
13. García, Á.E.; Schlangen, E.; van de Ven, M.; Liu, Q. A simple model to define induction heating in asphalt mastic. *Constr. Build. Mater.* **2012**, *31*, 38–46. [[CrossRef](#)]
14. Tang, J.; Liu, Q.; Wu, S.; Ye, Q.; Sun, Y.; Schlangen, E. Investigation of the optimal self-healing temperatures and healing time of asphalt binders. *Constr. Build. Mater.* **2016**, *113*, 1029–1033. [[CrossRef](#)]
15. Liu, Q.; Schlangen, E.; van de Ven, M.; van Bochove, G.; van Montfort, J. Evaluation of the induction healing effect of porous asphalt concrete through four point bending fatigue test. *Constr. Build. Mater.* **2012**, *29*, 403–409. [[CrossRef](#)]
16. Liu, Q.; Schlangen, E.; van de Ven, M.; García, Á. Healing of porous asphalt concrete via induction heating. *Road Mater. Pavement Des.* **2010**, *11*, 527–542.
17. Wang, Z.; Dai, Q.; Yang, X. Integrated computational-experimental approach for evaluating recovered fracture strength after induction healing of asphalt concrete beam samples. *Constr. Build. Mater.* **2016**, *106*, 700–710. [[CrossRef](#)]
18. Dai, Q.; Wang, Z.; Hasan, M.R.M. Investigation of induction healing effects on electrically conductive asphalt mastic and asphalt concrete beams through fracture-healing tests. *Constr. Build. Mater.* **2013**, *49*, 729–737. [[CrossRef](#)]
19. Norambuena-Contreras, J.; Serpell, R.; Valdes, V.; Gonzalez, A.; Schlangen, E. Effect of fibres addition on the physical and mechanical properties of asphalt mixtures with crack-healing purposes by microwave radiation. *Constr. Build. Mater.* **2016**, *127*, 369–382. [[CrossRef](#)]
20. Pamulapati, Y.; Elseifi, M.; Cooper, S.; Mohammad, L.; Elbagalati, O. Evaluation of self-healing of asphalt concrete through induction heating and metallic fibers. *Constr. Build. Mater.* **2017**, *146*, 66–75. [[CrossRef](#)]
21. Collin, R.E. *Foundations for Microwave Engineering*; Wiley: Hoboken, NJ, USA, 2000.
22. Wang, Z.; Wang, H.; An, D.; Ai, T.; Zhao, P. Laboratory investigation on deicing characteristics of asphalt mixtures using magnetite aggregate as microwave-absorbing materials. *Constr. Build. Mater.* **2016**, *124*, 589–597. [[CrossRef](#)]
23. Alohaly, A.; Terrel, R.L. *Effect of Microwave Heating on Adhesion and Moisture Damage of Asphalt Mixtures*; National Research Council, Transportation Research Board: Washington, DC, USA, 1998.
24. Sun, Y.; Wu, S.; Liu, Q.; Li, B.; Fang, H.; Ye, Q. The healing properties of asphalt mixtures suffered moisture damage. *Constr. Build. Mater.* **2016**, *127*, 418–424. [[CrossRef](#)]
25. Sun, Y.; Liu, Q.; Wu, S.; Shang, F. Microwave heating of steel slag asphalt mixture. *Key Eng. Mater.* **2014**, *599*, 193–197. [[CrossRef](#)]
26. Yu, W. Study of the Induction Healing Behaviors of Hot Warm Mix Asphalt. Master’s Thesis, Wuhan University of Technology, Wuhan, China, 2017.
27. Liu, Q.; Yu, W.; Wu, S.P.; Schlangen, E.; Pan, P. A comparative study of the induction healing behaviors of hot and warm mix asphalt. *Constr. Build. Mater.* **2017**, *144*, 663–670. [[CrossRef](#)]
28. Liu, Q.; Schlangen, E.; van de Ven, M. Induction Healing of porous asphalt concrete beams on an elastic foundation. *J. Mater. Civil Eng.* **2013**, *25*, 880–885. [[CrossRef](#)]
29. Moreno-Navarro, F.; Ayar, P.; Sol-Sanchez, M.; Rubiogamez, M.C. Exploring the recovery of fatigue damage in bituminous mixtures at macro-crack level: the influence of temperature, time, and external loads. *Road Mater. Pavement Des.* **2017**, *18*, 293–303. [[CrossRef](#)]



Article

Initial Self-Healing Temperatures of Asphalt Mastics Based on Flow Behavior Index

Chao Li, Shaopeng Wu *, Guanyu Tao and Yue Xiao 

State Key Laboratory of Silicate Materials for Architectures, Wuhan University of Technology, Wuhan 430070, China; lic@whut.edu.cn (C.L.); 254546@whut.edu.cn (G.T.); xiaoy@whut.edu.cn (Y.X.)

* Correspondence: wusp@whut.edu.cn; Tel.: +86-027-8788-3743

Received: 3 April 2018; Accepted: 24 May 2018; Published: 29 May 2018

Abstract: Increasing temperature is a simple and convenient method to accelerate the self-healing process of bitumen. However, bitumen may not achieve the healing capability at lower temperature, and may be aged if temperature is too high. In addition, the bitumen is mixed with mineral filler and formed as asphalt mastic in asphalt concrete, so it is more accurate to study the initial self-healing from the perspective of asphalt mastic. The primary purpose of this research was to examine the initial self-healing temperature of asphalt mastic, which was determined by the flow behavior index obtained from the flow characteristics. Firstly, the texture and geometry characteristics of two fillers were analyzed, and then the initial self-healing temperature of nine types of asphalt mastic, pure bitumen (PB) and styrene-butadiene-styrene (SBS) modified bitumen were determined by the flow behavior index. Results demonstrate that the average standard deviation of gray-scale texture value of limestone filler (LF) is 21.24% lower than that of steel slag filler (SSF), showing that the steel slag filler has a better particle distribution and geometry characteristics. Also the initial self-healing temperatures of asphalt mastics with 0.2, 0.4 and 0.6 LF-PB volume ratio are 46.5 °C, 47.2 °C and 49.4 °C, which are 1.4 °C, 0.8 °C and 0.4 °C higher than that of asphalt mastics with SSF-PB, but not suitable for the evaluation of asphalt mastic contained SBS modified bitumen because of unique structure and performance of SBS.

Keywords: initial self-healing temperature; asphalt mastic; flow behavior index; steel slag; limestone

1. Introduction

Due to the impacts of the natural environment and traffic load, asphalt pavement is prone to generate rutting, cracking, looseness and other deformations during the service life [1,2]. At present, to recover these deformations, many maintenance techniques have been developed, such as slurry seal, micro surfacing, gravel seal and other pavement rehabilitation techniques [3–5]. However, these methods are passive maintenance after apparent or more serious damages of the road, not only consuming high maintenance cost and affect the safety of pavement and traffic, but also causing a great waste of resources and environmental pollution. Therefore, it is urgent to develop other advanced preventive maintenance technology to prolong the service life of asphalt concrete.

Asphalt concrete can be recognized as a type of self-healing materials according to several researches [6,7]. During the intermittent period of loading, some of the micro cracks in the asphalt concrete can close/repair themselves automatically, resulting in the recovery of the asphalt pavement performance [8,9]. The existing study suggests that the self-healing capacity of bitumen is associated with the temperature variation closely, while in higher temperature, the elastic recovery, viscous flow and molecular diffusion of bitumen can be accelerated to heal the cracks [6,10,11]. Nowadays, researchers have developed so many technics to realize the increase of temperature, such as induction heating, microwave heating, infrared heating and so on. So it still needs efforts to find suitable

temperature to conduct heating process. Bituminous materials may not achieve the healing capability if temperature is below suitable self-healing temperature, also may be aged or deteriorate the pavement performance if temperature is too high. According to the viscosity and flow characteristics of bitumen, researchers can select suitable temperature to be the initial self-healing temperature, and guide the maintenance work.

However, in the asphalt concrete, the bitumen is mixed with mineral filler and formed as asphalt mastic, which finally endows the asphalt concrete with self-healing properties, so it can be considered as a more promising and appropriate perspective to study the viscosity and flow characteristics of asphalt mastic to determine the initial self-healing temperature. According to the former researches, asphalt materials could be recognized as a viscoelastic material and act like a Newtonian liquid at high temperature [12]. The Newtonian flow characteristic can be fitted through the following power law relationship [13,14]:

$$\eta^* = m|\omega|^{n-1} \quad (1)$$

where:

ω represents frequency;

η^* represents complex viscosity;

m and n represents the fitting parameters.

The dimensionless parameter n is also called the flow behavior index. The measured material corresponds to a Newtonian fluid while n equals 1.0, and appears a higher degree of pseudoplastic properties while n is less than 1. If n transfers in the variation from 0.9 to 1.0, asphalt mastic can be recognized as near-Newtonian liquid which processes flow characteristic [15]. The temperature when n equals 0.9 was confirmed as the initial self-healing temperature in this research. In this paper, limestone filler and steel slag filler were blended with pure bitumen and SBS (styrene-butadiene-styrene) modified bitumen by different filler-bitumen volume ratio to form nine types of asphalt mastic. Firstly, the texture and geometry characteristics of two fillers were analyzed in this research. Secondly, the initial self-healing temperature of nine types of asphalt mastic, pure bitumen and SBS modified bitumen were determined by the flow behavior index. Research findings can be beneficial to maintenance work by selecting suitable temperature based on the type of filler, bitumen and filler-bitumen ration, so that contributing to save energy and reduce energy consumption. In addition, selecting suitable temperature can delay the aging and prolong the service life of bituminous materials.

2. Materials and Methods

2.1. Raw Materials

The 60/80 penetration graded pure bitumen (PB) and styrene-butadiene-styrene (SBS) modified bitumen mixed by 60/80 penetration graded pure bitumen and 4.5% dosage of SBS particles which supplied by Guochuang Co., Ltd., Wuhan, Hubei, China, were applied in this research. Limestone filler (LF) was obtained from Agoura Stone Processing Factory, Inner Mongolia, China. While according to former research [16], steel slag filler (SSF) was prepared by milling raw Basic Oxygen Furnace (BOF) steel slags supplied by Wuhan Iron and Steel, Wuhan, China, whose original particle size was 9.5–13.2 mm. The basic properties of raw materials were concluded in Table 1.

Table 1. Basic properties of raw materials.

Properties	Pure Bitumen	SBS Modified Bitumen	Properties	Limestone Filler	Steel Slag Filler
Softening point (°C)	49.4	61.7	Hydrophilic coefficient	0.70	0.66
Ductility (15 °C, mm)	>1000	>1000	Density (g/cm ³)	2.73	3.65
Penetration (25 °C, 0.1 mm)	68.3	61.7	Water absorption (%)	0.55	0.69
Density (15 °C, g/cm ³)	1.025	1.039	Specific surface area (m ² /g)	1.44	1.95

2.2. Experimental Methods

2.2.1. Preparation of Asphalt Mastic

According to the previous studies and results shown in Table 1 [16], the density of steel slag is about 25% higher than that of limestone, if added different filler by the same weight ratio and it may cause the volume distinction of asphalt mastics, so volume control method was used to consistently maintain the same volume composition of different asphalt mastics. In this research, nine types of asphalt mastic were prepared and could be divided into three groups: asphalt mastic contained limestone filler and pure bitumen was named as LF-PB, asphalt mastic contained steel slag filler and pure bitumen was named as SSF-PB, asphalt mastic contained limestone filler and SBS modified bitumen was named as LF-SMB. Each group included three types of asphalt mastic whose filler-volume ratio was 0.2, 0.4 and 0.6. The control group which only contained pure bitumen and SBS modified bitumen were also included. To obtain different types of asphalt mastics, bitumen was firstly heated in sample vessel, which was placed in oil bath pan. Meanwhile the oil bath pan was heated by an electric furnace and a temperature sensor in the sample vessel could guarantee that the modification was constantly kept at 160 °C together with the control of thermostat. Maintaining the shearing rate of 1500 rpm (revolutions per minute) for 3 min through the whole blending, a high-speed shearing machine was applied to ensure homogeneous dispersion of fillers in the bitumen.

2.2.2. Texture Distinction

In previous studies, the scan electronic microscope (SEM) image of steel slag showed a little difference compared to limestone [17], but the comparison was depended on personal subjective judgment through visual observation and lacked of theoretical foundation. Subdivided into different distinct areas which have homogeneity among them, SEM images can represent the texture diversity of analyzed materials. With Matlab software (version 2016a, MathWorks, MA, USA), the SEM image can be transformed into black and white image that is consisted with a gray scale range of different pixels vary from 0 (darker) to 255 (brighter). The pixel diversity of different gray scale can reflect the texture distinction of material. Smooth texture of materials has little difference in the number of different gray scale's pixels, and tough texture has obvious difference in the number of different gray scale's pixels [18]. Finally, we named the gray-scale level as gray-scale texture value, and through Matlab software to run statistical analysis, like average, variance and standard deviation values of pixels of each gray-scale texture value to quantify the fluctuation level of texture distinction accurately.

The texture distinctions of limestone and steel slag fillers were studied by a JSM-5610LV Scan Electronic Microscope manufactured by JEOL, Tokyo, Japan. The resolution of SEM in the high-vacuum and low-vacuum mode was 3.0 nm and 4.0 nm separately. Magnification of 18–300,000× and 100,000× was adopted in this research.

2.2.3. Geometry Characteristics

Barrett [19] pointed that particle geometry of aggregates could be described in three independent properties: surface texture, form and angularity. The surface texture has been evaluated in Section 3.1,

therefore the differences of form and angularity named as geometry characteristics were analyzed by aggregate imaging system (AIMS).

As shown in Figure 1, form represents variations in the proportions of a particle. For the tested filler, the values of form 2D which were analyzed from the relative form of two-dimensional images were used to quantify form distinctions. According to Masad [20], the form 2D was obtained by using incremental change in the particle radius and expressed in the following equation:

$$Form\ 2D = \sum_{\theta=0}^{\theta=360-\Delta\theta} \frac{|R_{\theta+\Delta\theta} - R_{\theta}|}{R_{\theta}} \tag{2}$$

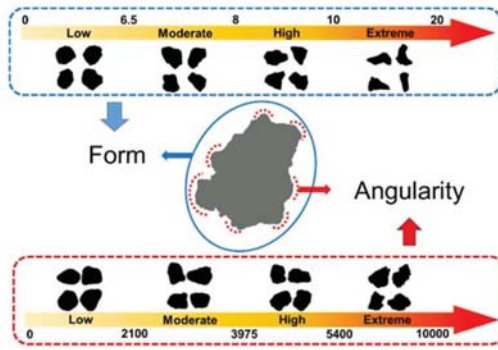


Figure 1. The schematic diagram of aggregate geometry characteristics.

In the equation, where R_{θ} is the radius of the particle at an angle of θ , and $\Delta\theta$ is the incremental difference in the angle, which is taken to be 4° . The values of form 2D range from 0 to 20, and can be divided into four levels: low (0–6.5, circular), moderate (6.5–8, semi-circular), high (8–10, semi-elongated), extreme (10–20, elongated). The closer the form 2D is to 0, the closer the particle resembles a perfect circle.

In the case of angularity index, Masad [20] developed the radius method which measures the difference between the particle radius in a certain direction and that of an equivalent ellipse, the calculation was on the basis of following equation:

$$Angularity\ Index = \sum_{\theta=0}^{355} \frac{|R_{\theta} - R_{EE\theta}|}{R_{EE\theta}} \tag{3}$$

In the equation, R_{θ} is the radius of the particle at an angle of θ , and $R_{EE\theta}$ is the radius of the equivalent ellipse at an angle of θ . The equivalent ellipse has the same aspect ratio of the particle but has no angularity (smooth with no sharp corners). Normalization of the aspect ratio can minimize the effect of form on the angularity index [20]. The values of angularity index range from 0 to 10,000, and can also be divided into four levels: low (0–2100, rounded), moderate (2100–3975, sub-rounded), high (3975–5400, sub-angular), extreme (5400–10,000, angular). The closer the angularity index is to 0, the closer the particle resembles to be rounded.

The geometry characteristics of two fillers were characterized by the AFA2 aggregate imaging system (AIMS), manufactured by PINE, Washington, DC, USA. AIMS captures images of aggregates at different resolutions through a simple setup that consists of one camera and two different types of lighting schemes [21]. The image acquisition setup is configured to capture a typical image of 640 by 480 pixels at these resolutions in order to analyze various sizes of aggregates [22]. Different types of fillers were firstly sieved to select particles which were larger or equal to 0.075 mm, and about

150 particles were analyzed for form 2D and angularity values using black and white images, captured by backlighting under the dedicated sample tray (200#).

2.2.4. Initial Self-Healing Temperature

As the self-healing procedure of asphalt materials depends on temperature, therefore infiltration, dispersion and other thermodynamic motions of bitumen molecules are suffocated at lower temperature, resulting in the resistance to self-healing procedure. However, if temperature achieves the initial self-healing temperature, the molecules can heal the generated cracks more easily and quickly. In the wake of the temperature variation, asphalt mastic could be recognized as a viscoelastic material and act like a Newtonian liquid at high temperature [12]. According to Equation (1), shown in the introduction section, the initial self-healing temperature could be calculated by the relationship between frequency and complex viscosity. In this research, the relationship was obtained through the frequency sweep analysis measured by dynamic shear rheometer (DSR, Anton Paar, Vienna, Austria), which was performed at a dynamic frequency from 0.01 Hz to 10 Hz under different fixed temperature conditions (30 °C, 40 °C, 50 °C and 60 °C). All asphalt mastics were placed on a parallel plate geometry whose diameter was 25 mm, and the thickness of samples was 1 mm.

3. Results and Discussions

3.1. Texture Distinction

In this paper, three main areas of different fillers in SEM images (as shown in Figure 2) were firstly transformed into gray scale images through gray-scale histogram equalization by Matlab software, which could extend the dynamic range of pixel values to improve the contrast and definition of images. Then the software plotted the gray scale histogram which showed the difference in the number of different gray scale's pixels. Finally, the standard deviation value of pixel numbers was applied to quantify the texture distinction of two fillers accurately.

Figure 2 shows the SEM images and gray-scale histogram equalization results of selected areas. It is clear to see that particles of steel slag filler assemble together with holes and are tougher than limestone filler. Figure 3 illustrates the gray-scale histogram of different areas in two fillers. The gradient colored from black to white over horizontal axis represents the gray-scale texture value from 0 to 255, while darker color means lower gray level and brighter color means higher gray level. It can be seen that the distributions of limestone filler's gray-scale texture value are mainly ranging from 0 to 150, and lack pixels in the higher gray-scale texture value. In contrast, the distributions of steel slag filler's gray-scale texture value are more balanced, and mainly centralized from 50 to 200. It can be estimated initially that steel slag filler has a wider pixel diversity of different gray-scale texture value than limestone filler, which can reflect coarser texture distinction. Table 2 shows the statistical analysis of gray scale histogram. Although the average gray-scale texture values of two fillers have little difference and all ranges from 110 pixels to 150 pixels, the variance and standard deviation values shows significant differences. The variance value of LF is around 1500 while the value of SSF is around 2500, causing that the average standard deviation value of three areas in LF is 21.24% lower than that of SSF. Such differences indicate that SSF with irregular surface texture is coarser than LF which authenticated in the basis of numerical value and statistical analysis.

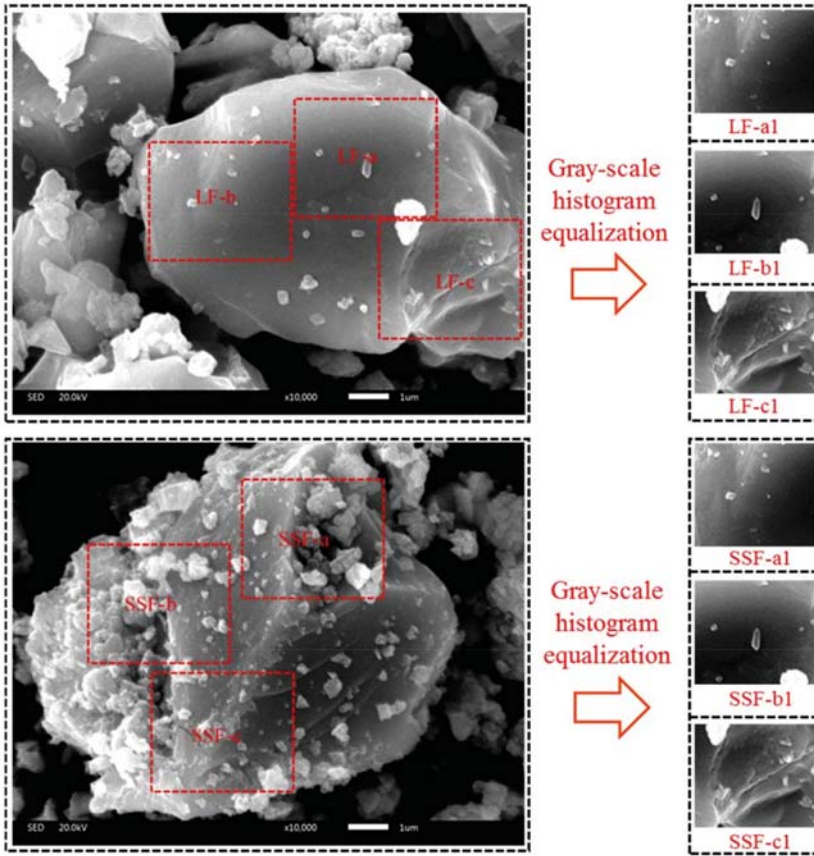


Figure 2. SEM images and gray-scale histogram equalization results of selected areas.

Table 2. The statistical analysis of gray scale histogram.

Filler Classification	Limestone Filler			Steel Slag Filler		
	a1	b1	c1	a1	b1	c1
Average	120.78	111.26	132.22	117.18	141.54	117.52
Variance	1517.42	1774.89	1383.88	2502.78	2459.11	2553.74
Standard deviation	38.95	42.13	37.20	50.03	49.59	50.53

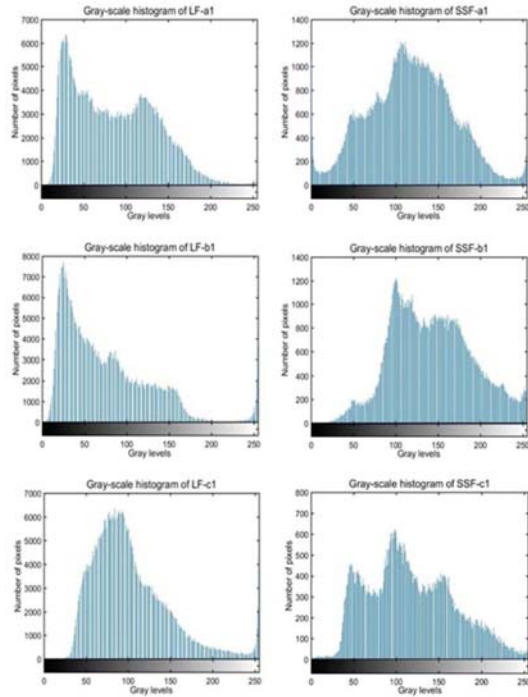


Figure 3. Gray-scale histogram of different areas in two fillers.

3.2. Geometry Characteristics

Figures 4 and 5 illustrate the curves of form 2D and angularity index. It is clearly to see that limestone filler has a wider range than that of steel slag filler both in the form 2D and angularity index curves, representing that limestone is easier to be inhomogeneous and has huge distinctions in form and angularity. Because of more rigid and reliable structure, steel slag can be crushed uniformly and has fewer incidents in the happening of circular, elongated, rounded or angular particles.

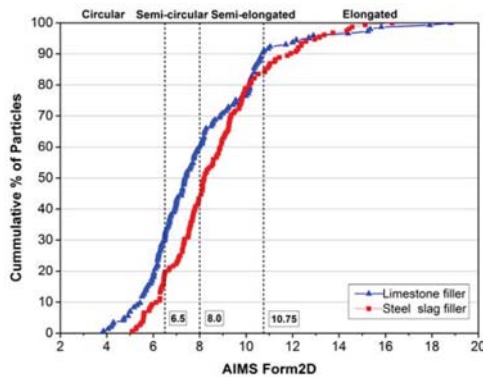


Figure 4. The AIMS form 2D of limestone filler and steel slag filler.

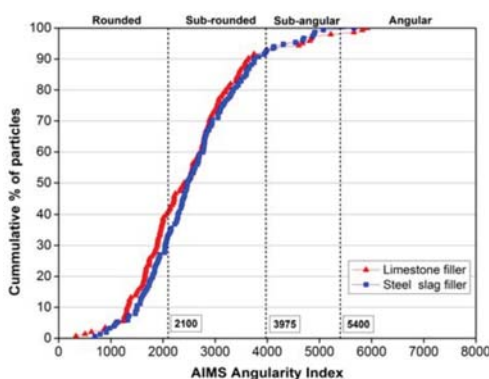


Figure 5. The AIMS angularity Index of limestone filler and steel slag filler.

Table 3 shows the specific distribution and statistical results of tested form 2D and angularity index. For the values of form 2D, the limestone filler accounts for more percentages than steel slag filler at the low and moderate level, presenting more circular and semi-circular particles. However, steel slag filler processes a higher proportion at high and extreme level, presenting more semi-elongated and elongated particles. The standard deviation of limestone filler is 14.56% higher than that of steel slag filler, demonstrating the former opinion that limestone filler has a wider distribution after being crushed, and the average values present that two fillers are both at the high level but steel slag filler shows better form 2D value than limestone filler. With regard to angularity index, two fillers are distributed rarely at high and extreme level. Although the average values of two fillers are almost the same, but the whole distribution and standard deviation still figure out that limestone filler has a wider distribution, presenting more percentages in the rounded and angular categories, and steel slag filler has a better particle distribution and shape property. Former researches have proved that better geometry characteristics can be beneficial to the cohesion between filler and bitumen [23–25]. So under the same deformation factors like sunshine, loading or rainfall, the mastic contained steel slag filler can process better pavement performance, and avoid earlier preventive maintenance than the mastic contained limestone filler.

Table 3. The specific distribution and statistical results of tested form 2D and angularity index.

Form 2D						
Sample	Average	Standard Deviation	Low (≤6.5)	Moderate (6.5–8)	High (8–10.75)	Extreme (10.75–20)
Limestone filler	8.04	2.61	30.6%	29.2%	30.6%	9.7%
Steel slag filler	8.67	2.23	19.1%	24.3%	40.1%	16.4%
Angularity Index						
Sample	Average	Standard Deviation	Low (≤2100)	Moderate (2100–3975)	High (3975–5400)	Extreme (5400–10,000)
Limestone filler	2508.8	1040.3	40.3%	52.1%	5.6%	2.1%
Steel slag filler	2606.2	945.3	32.9%	59.2%	7.2%	0.7%

3.3. Initial Self-Healing Temperature of Different Asphalt Mastics

3.3.1. Asphalt Mastic Contained Pure Bitumen and Limestone Filler

Figure 6 presents the frequency-complex viscosity relationship of LF-PB asphalt mastics. In general, the complex viscosity decreases obviously along with the augment of frequency at 40 °C, but the tendency towards to be flat and smooth as the temperature rises. The curve of

frequency-complex viscosity even becomes a horizontal line at 60 °C, which represents that the complex viscosity remains the same with the change of frequency.

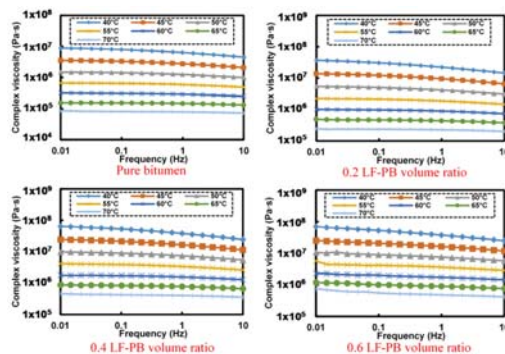


Figure 6. Frequency-complex viscosity relationship of different LF-PB asphalt mastics.

Based on the results of Figure 6, Table 4 concludes the fitting results of LF-PB asphalt mastic’s flow behavior index at different temperature. In summary, it can be seen that the flow behavior indexes of all analyzed asphalt mastics show a growing tendency gradually along with the increasing temperature, representing that the asphalt mastics become Newtonian fluid gradually in higher temperature. The flow behavior index of the pure bitumen increases from 0.901 at 40 °C to 0.985 at 70 °C. Existing a little lower value while adding filler, the variation ranges of flow behavior index for asphalt mastics with 0.2, 0.4 and 0.6 LF-PB volume ratio are from 0.863 at 40 °C to 0.979 at 70 °C, 0.860 at 40 °C to 0.969 at 70 °C, and 0.852 at 40 °C to 0.940 at 70 °C, respectively.

Table 4. Fitting results of LF-PB asphalt mastic’s flow behavior index at different temperature.

LF-PB Volume Ratio	Temperature (°C)	Fitting Formula	$n - 1$	Flow Behavior Index
0	40	$y = (6 \times 10^6)x^{-0.099}$	-0.099	0.901
	45	$y = (3 \times 10^6)x^{-0.077}$	-0.077	0.923
	50	$y = 10^6x^{-0.058}$	-0.058	0.942
	55	$y = 573982x^{-0.043}$	-0.043	0.957
	60	$y = 283129x^{-0.032}$	-0.032	0.968
	65	$y = 145530x^{-0.021}$	-0.021	0.979
	70	$y = 78509x^{-0.015}$	-0.015	0.985
0.2	40	$y = (2 \times 10^7)x^{-0.137}$	-0.137	0.863
	45	$y = (8 \times 10^6)x^{-0.108}$	-0.108	0.892
	50	$y = (4 \times 10^6)x^{-0.082}$	-0.082	0.918
	55	$y = (2 \times 10^6)x^{-0.059}$	-0.059	0.941
	60	$y = 821877x^{-0.043}$	-0.043	0.957
	65	$y = 412182x^{-0.032}$	-0.032	0.968
	70	$y = 215878x^{-0.021}$	-0.021	0.979
0.4	40	$y = (4 \times 10^7)x^{-0.140}$	-0.140	0.860
	45	$y = (2 \times 10^7)x^{-0.111}$	-0.111	0.889
	50	$y = (7 \times 10^6)x^{-0.085}$	-0.085	0.915
	55	$y = (3 \times 10^6)x^{-0.063}$	-0.063	0.937
	60	$y = (2 \times 10^6)x^{-0.045}$	-0.045	0.955
	65	$y = 853056x^{-0.037}$	-0.037	0.963
	70	$y = 446663x^{-0.032}$	-0.032	0.968
0.6	40	$y = (4 \times 10^7)x^{-0.148}$	-0.148	0.852
	45	$y = (2 \times 10^7)x^{-0.12}$	-0.12	0.880
	50	$y = (7 \times 10^6)x^{-0.097}$	-0.097	0.903
	55	$y = (3 \times 10^6)x^{-0.075}$	-0.075	0.925
	60	$y = (2 \times 10^6)x^{-0.063}$	-0.063	0.937
	65	$y = 899443x^{-0.062}$	-0.062	0.938
	70	$y = 489514x^{-0.06}$	-0.060	0.940

3.3.2. Asphalt Mastic Contained Pure Bitumen and Steel Slag Filler

Figure 7 shows the frequency-complex viscosity relationship of SSF-PB asphalt mastics with different filler-bitumen volume ratio. The general variation tendency of curves is consistent with that of LF-PB asphalt mastics, but still demonstrates a little difference that all SSF-PB asphalt mastics behave higher complex modulus than those of corresponding LF-PB asphalt mastics, which means that SSF-PB asphalt mastics are more superior to resist high-temperature deformation.

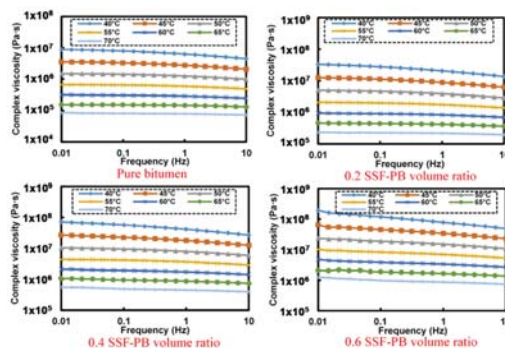


Figure 7. Frequency-complex viscosity relationship of different SSF-PB asphalt mastics.

Based on the results of Figure 7, Table 5 concludes the fitting results of SSF-PB asphalt mastic’s flow behavior index at different temperatures. With regard to SSF asphalt mastics, the flow behavior indexes become higher than that of LF-PB asphalt mastic. The variation ranges of asphalt mastics with 0.2, 0.4 and 0.6 SSF-PB volume ratio are from 0.869 at 40 °C to 0.978 at 70 °C, 0.857 at 40 °C to 0.953 at 70 °C and 0.828 at 40 °C to 0.945 at 70 °C, respectively.

Table 5. Fitting results of SSF-PB asphalt mastic’s flow behavior index at different temperature.

SSF-PB Volume Ratio	Temperature (°C)	Fitting Formula	<i>n</i> - 1	Flow Behavior Index
0	40	$y = (6 \times 10^6)x^{-0.099}$	-0.099	0.901
	45	$y = (3 \times 10^6)x^{-0.077}$	-0.077	0.923
	50	$y = 10^6x^{-0.058}$	-0.058	0.942
	55	$y = 573982x^{-0.043}$	-0.043	0.957
	60	$y = 283129x^{-0.032}$	-0.032	0.968
	65	$y = 145530x^{-0.021}$	-0.021	0.979
	70	$y = 78509x^{-0.015}$	-0.015	0.985
0.2	40	$y = (2 \times 10^7)x^{-0.131}$	-0.131	0.869
	45	$y = (8 \times 10^6)x^{-0.101}$	-0.101	0.899
	50	$y = (4 \times 10^6)x^{-0.077}$	-0.077	0.923
	55	$y = (2 \times 10^6)x^{-0.056}$	-0.056	0.944
	60	$y = 821877x^{-0.042}$	-0.042	0.958
	65	$y = 412182x^{-0.031}$	-0.031	0.969
	70	$y = 215878x^{-0.022}$	-0.022	0.978
0.4	40	$y = (4 \times 10^7)x^{-0.143}$	-0.143	0.857
	45	$y = (2 \times 10^7)x^{-0.108}$	-0.108	0.892
	50	$y = (7 \times 10^6)x^{-0.081}$	-0.081	0.919
	55	$y = (3 \times 10^6)x^{-0.160}$	-0.160	0.940
	60	$y = (2 \times 10^6)x^{-0.052}$	-0.052	0.948
	65	$y = 853056x^{-0.049}$	-0.049	0.951
	70	$y = 446663x^{-0.047}$	-0.047	0.953
0.6	40	$y = (8 \times 10^7)x^{-0.172}$	-0.172	0.828
	45	$y = (3 \times 10^7)x^{-0.125}$	-0.125	0.875
	50	$y = 10^7x^{-0.096}$	-0.096	0.904
	55	$y = (7 \times 10^6)x^{-0.082}$	-0.082	0.918
	60	$y = (3 \times 10^6)x^{-0.074}$	-0.074	0.926
	65	$y = (2 \times 10^6)x^{-0.062}$	-0.062	0.938
	70	$y = 866069x^{-0.055}$	-0.055	0.945

3.3.3. Asphalt Mastic Contained SBS Modified Bitumen and Limestone Filler

Figure 8 presents the frequency-complex viscosity relationship of LF-SMB asphalt mastics with different filler-bitumen volume ratio. In contrast to former curves of pure bitumen’s flow behavior indexes, the general tendency is the same that the complex viscosity decreases along with the augment of frequency. However, the curves at 60 °C are not as smooth as former and they still behave a shape dropping trend, meaning that all LF-SMB asphalt mastics possess a distinct flow behavior at different temperature conditions.

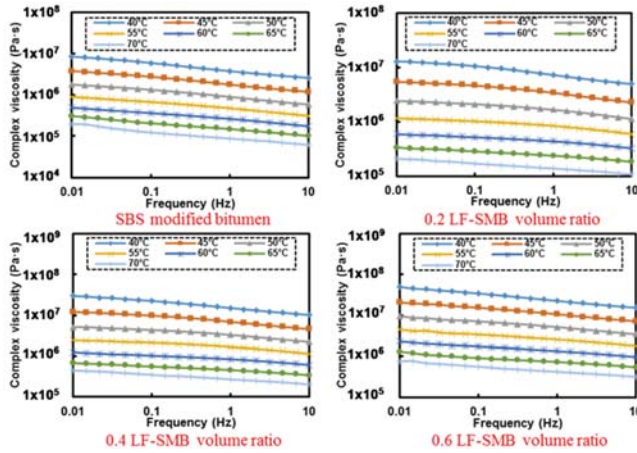


Figure 8. Frequency-complex viscosity relationship of different LF-SMB asphalt mastics.

Based on the results of Figure 8, Table 6 illustrates the fitting results of LF-SMB asphalt mastic’s flow behavior index at different temperature. Figure 9 shows the curves of flow behavior index. In contrast to the former analyzed results of LF-PB and SSF-PB asphalt mastics, the flow behavior index curves of all LF-SMB asphalt mastics present different phenomena. Firstly, all the initial flow behavior indexes are lower than these of LF-PB and SSF-PB asphalt mastics. With the temperature rising, all curves increase to the maximum index and then decrease to the value that is higher than the initial flow behavior index. Secondly, with the augment of LF-SMB volume ratio, the flow behavior index at each temperature presents a decreasing trend gradually, causing that the asphalt mastics with 0.4 and 0.6 LF-SMB volume ratio cannot reach the flow state whose flow behavior index must be greater than 0.9. These phenomena can be explained as follows:

SBS polymer is a thermoplastic elastomer which consists of styrene-butadiene-styrene monomer. Polystyrene segments (S) are at both ends of monomer and gather together to form a physical cross-linked area, which gives the material sufficient strength. Polybutadiene segment (B) is in the center and forms a soft segment, which exhibits high elasticity and gives the material superior elastic properties. When the SBS particles are blended with the pure bitumen, the specific structure of the SBS molecule determines that it must absorb the light components of pure bitumen partly, and occurs physical cross-linking between them which is also regarded as swelling and recombination. SBS particles absorb these light components which can undergo the transition of aggregation states at ambient temperature, making the modified bitumen more difficult to adjust inner components to accommodate temperature variation. So that the SBS modified bitumen has lower temperature sensibility than pure bitumen and cannot reach the same flow state as pure bitumen at the identical temperature. In the initial range of temperature rising, the modified bitumen losses a portion of elastic components and the proportion of viscous components increase gradually. So the modified bitumen can have a better flow state than the beginning and the flow behavior index increases gradually at first.

However, when the temperature rises to a certain value, the contribution of SBS particles, which has a superior elastic property to a shearing action, becomes more obvious. These particles can counteract the loss of elastic components and make the bitumen more viscous, finally resulting that the flow behavior index decreases after reaching the maximum. In addition, the augment of fillers even worsens the flow state and finally makes asphalt mastics with high LF-SMB volume ratio unable to reach the state as near-Newtonian liquid. In summary, because of the existence of SBS modifiers, so the flow behavior index is inadequate to evaluate the initial self-healing temperature of asphalt mastics contained SBS modified bitumen.

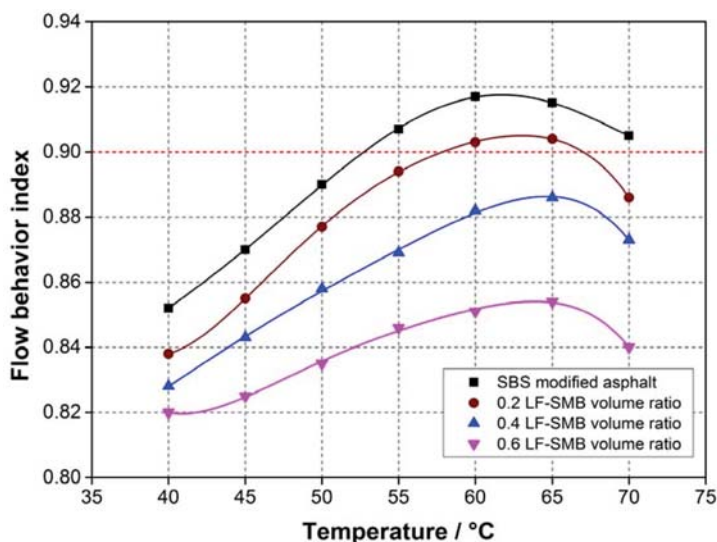


Figure 9. Flow behavior index of different LF-SMB asphalt mastics at different temperatures.

According to Tables 4 and 5, the initial self-healing temperatures of different asphalt mastics at which flow behavior indexes are 0.9 are further described in Figure 10. As shown in Figure 10, no matter LF-PB asphalt mastics or SSF-PB asphalt mastics, the initial self-healing temperature values present a linear growth along with the augment of filler-bitumen ratio, meaning that additions of fillers decrease the fluidity of pure bitumen and requiring a higher temperature to reach the same flow state. The initial self-healing temperature values of asphalt mastics with 0.2, 0.4 and 0.6 LF-PB volume ratio are 46.5 °C, 47.2 °C and 49.4 °C, which are 1.4 °C, 0.8 °C and 0.4 °C higher than that of asphalt mastics with 0.2, 0.4 and 0.6 SSF-PB volume ratio. The results firstly demonstrate that in the same filler-bitumen ratio, SSF-PB asphalt mastics come up to the flow characteristic more quickly than LF asphalt mastics and are prompt to heal the generated cracks easier. Secondly, although the gaps of initial self-healing temperatures between LF-PB and SSF-PB asphalt mastics exist in every same filler-bitumen ratio, the gaps show a dropping tendency that ranging from 1.4 °C to 0.4 °C. This phenomenon can be explained that in lower filler-bitumen ratio, the bitumen occupies mostly in the asphalt mastic and the better interaction between steel slag filler and bitumen can be clearly revealed in the initial self-healing temperature. However, in higher filler-bitumen ratio, the filler occupies mostly and the flow behavior of asphalt mastic is much worse, so the effect of interaction cannot be as distinct as the state of lower filler-bitumen ratio, resulting in the decrease of initial self-healing temperature gaps. Analyzed results give an overview about initial self-healing temperature of different asphalt mastic with 0–0.6 filler-bitumen ratio, in real maintenance of bituminous layer field, maintenance work can select suitable temperature based on the type of filler, bitumen and filler-bitumen ration,

so that contributing to save energy and reduce energy consumption. In addition, selecting suitable temperature can delay the aging and prolong the service life of bituminous materials.

Table 6. Fitting results of LF-SMB asphalt mastic’s flow behavior index at different temperature.

LF-SMB Volume Ratio	Temperature (°C)	Fitting Formula	$n - 1$	Flow Behavior Index
0	40	$y = (4 \times 10^6)x^{-0.180}$	-0.180	0.820
	45	$y = (2 \times 10^6)x^{-0.175}$	-0.175	0.825
	50	$y = 888198x^{-0.165}$	-0.165	0.835
	55	$y = 465088x^{-0.154}$	-0.154	0.846
	60	$y = 255160x^{-0.149}$	-0.149	0.851
	65	$y = 146345x^{-0.156}$	-0.146	0.854
	70	$y = 87869x^{-0.0165}$	-0.160	0.840
0.2	40	$y = (7 \times 10^6)x^{-0.148}$	-0.148	0.852
	45	$y = (3 \times 10^6)x^{-0.130}$	-0.130	0.870
	50	$y = (2 \times 10^6)x^{-0.110}$	-0.110	0.890
	55	$y = 808622x^{-0.093}$	-0.093	0.907
	60	$y = 423220x^{-0.083}$	-0.083	0.917
	65	$y = 233814x^{-0.085}$	-0.085	0.915
	70	$y = 137396x^{-0.095}$	-0.095	0.905
0.4	40	$y = 10^7x^{-0.162}$	-0.162	0.838
	45	$y = (7 \times 10^6)x^{-0.145}$	-0.145	0.855
	50	$y = (3 \times 10^6)x^{-0.123}$	-0.123	0.877
	55	$y = (2 \times 10^6)x^{-0.106}$	-0.106	0.894
	60	$y = 812469x^{-0.097}$	-0.097	0.903
	65	$y = 445488x^{-0.096}$	-0.096	0.904
	70	$y = 269841x^{-0.114}$	-0.114	0.886
0.6	40	$y = (2 \times 10^7)x^{-0.172}$	-0.172	0.828
	45	$y = 10^7x^{-0.157}$	-0.157	0.843
	50	$y = (5 \times 10^6)x^{-0.142}$	-0.142	0.858
	55	$y = (3 \times 10^6)x^{-0.131}$	-0.131	0.869
	60	$y = 10^6x^{-0.118}$	-0.118	0.882
	65	$y = 716159x^{-0.114}$	-0.114	0.886
	70	$y = 420473x^{-0.127}$	-0.127	0.873

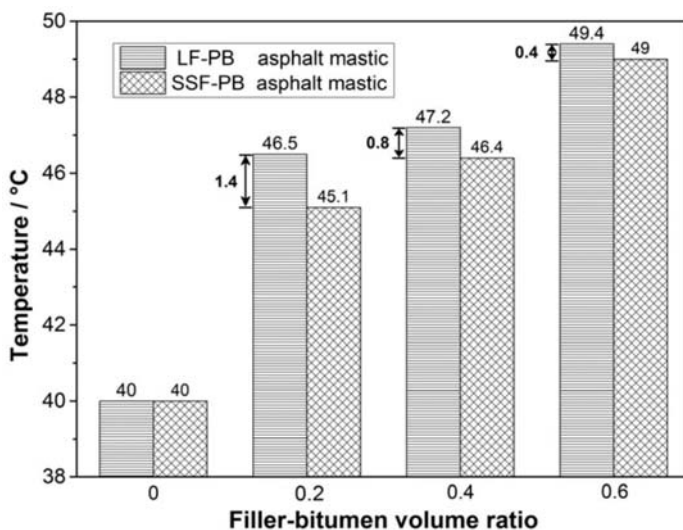


Figure 10. The initial self-healing temperature of different asphalt mastics.

4. Conclusions

This research aimed to study the viscosity and flow characteristics of different asphalt mastic to determine the initial self-healing temperature. The texture and geometry characteristics of limestone

filler and steel slag filler were firstly analyzed. Then the initial self-healing temperature of nine types of asphalt mastic, pure bitumen and SBS modified bitumen were evaluated by flow behavior index. According to the analyzed results, the following conclusions can be obtained:

- (1) Based on the gray-scale histogram SEM images, the average gray-scale texture values of two fillers have little difference and all ranges from 110 pixels to 150 pixels. Nevertheless, the variance value of LF is around 1500 while the value of SSF is around 2500, causing that the average standard deviation value of three evaluated areas in LF is 21.24% lower than that of SSF, indicating that SSF with irregular surface texture is coarser than LF.
- (2) Steel slag filler shows better form 2D value than limestone filler. The standard deviation of limestone filler is 14.56% higher than that of steel slag filler. Limestone filler has a wider distribution of angularity after being crushed, presenting more percentages in the rounded and angular categories. In summary, the steel slag filler has a better particle distribution and geometry characteristics.
- (3) SBS particles can absorb light components in bitumen which can undergo the transition of aggregation states at ambient temperature, making SBS modified bitumen has lower temperature sensibility than pure bitumen and cannot reach the same flow state as pure bitumen at the identical temperature. In addition, the flow behavior indexes all increase to the maximum initially and then decrease to the value that is higher than the initial flow behavior index with the temperature rising. Because of the existence of SBS modifiers, flow behavior index is inadequate to evaluate the initial self-healing temperature of asphalt mastics contained SBS modified bitumen.
- (4) The initial self-healing temperatures of asphalt mastics with 0.2, 0.4 and 0.6 LF-PB volume ratio are 46.5 °C, 47.2 °C and 49.4 °C, which are 1.4 °C, 0.8 °C and 0.4 °C higher than that of asphalt mastics with SSF-PB. It demonstrates that in the same filler-bitumen ratio, SSF asphalt mastics come up to the flow characteristic more quickly than LF asphalt mastics and are prompt to heal the generated cracks easier. Additionally, filler-bitumen ratio can also affect the initial self-healing temperature of asphalt mastic, while higher filler-bitumen ratio needs higher initial self-healing temperature to conduct self-healing process. Results show that the initial self-healing temperature can evaluate the self-healing temperature procedure. In real maintenance of bituminous layer field, maintenance work can select suitable temperature based on the type of filler, bitumen and filler-bitumen ration, so that contributing to save energy and reduce energy consumption. In addition, selecting suitable temperature can delay the aging and prolong the service life of bituminous materials.

Author Contributions: S.W. and C.L. conceived and designed the experiments. C.L. performed the experiments. S.W., Y.X. and C.L. analyzed the data. C.L. contributed reagents/materials/analysis tools. C.L. wrote the paper. G.T. and C.L. designed the software used in analysis. S.W. and Y.X. reviewed the paper.

Funding: This research was funded by the National Natural Science Foundation of China (No. 51778515) and National key research and development plan of China (No. 2017YFE0111600).

Acknowledgments: The authors gratefully acknowledge Wuhan University of Technology for their materials and experimental instruments supports.

Conflicts of Interest: The authors declare no conflict of interest.

References

1. Chen, Z.W.; Wu, S.P.; Xiao, Y.; Zeng, W.B.; Yi, M.W.; Wan, J.M. Effect of hydration and silicone resin on Basic Oxygen Furnace slag and its asphalt mixture. *J. Clean. Prod.* **2016**, *112*, 392–400. [[CrossRef](#)]
2. Cui, P.Q.; Wu, S.P.; Xiao, Y.; Wan, M.; Cui, P.D. Inhibiting effect of layered double hydroxides on the emissions of volatile organic compounds from bituminous materials. *J. Clean. Prod.* **2015**, *108*, 987–991. [[CrossRef](#)]
3. Gong, H.R.; Dong, Q.; Huang, B.S.; Jia, X.Y. Effectiveness analyses of flexible pavement preventive maintenance treatments with LTPP SPS-3 experiment data. *J. Transp. Eng.* **2016**, *142*, 04015045. [[CrossRef](#)]

4. Robati, M.; Carter, A.; Lommerts, B.J.; Cotiuga, I.; Perraton, D. New Colored Micro-surfacing Formulation with Improved Durability and Performance. In Proceedings of the International Conference on Asphalt, Pevement Engineering and Infrastructure, Liverpool, UK, 26–27 February 2014.
5. Barcena, R.; Martin, A.E.; Hazlett, D. Performance-graded binder specification for surface treatments. *Transp. Res. Rec. J. Transp. Res. Board* **2002**, *1810*, 63–71. [[CrossRef](#)]
6. Garcia, A.; Norambuena-Contreras, J.; Partl, M.N. Experimental evaluation of dense asphalt concrete properties for induction heating purposes. *Constr. Build. Mater.* **2013**, *46*, 48–54. [[CrossRef](#)]
7. Demenois, J.; Carriconde, F.; Bonaventure, P.; Maeght, J.L.; Stoke, A.; Rey, F. Impact of plant root functional traits and associated mycorrhizas on the aggregate stability of a tropical Ferralsol. *Geoderma* **2018**, *312*, 6–16. [[CrossRef](#)]
8. Garcia, A. Self-healing of open cracks in asphalt mastic. *Fuel* **2012**, *93*, 264–272. [[CrossRef](#)]
9. Sun, Y.H.; Wu, S.P.; Liu, Q.T.; Li, B.; Fang, H.; Ye, Q.S. The healing properties of asphalt mixtures suffered moisture damage. *Constr. Build. Mater.* **2016**, *127*, 418–424. [[CrossRef](#)]
10. Qiu, J.; van de Ven, M.F.C.; Wu, S.; Yu, J.; Molenaar, A.A.A. Investigating the self healing capability of bituminous binders. *Road Mater. Pavement* **2009**, *10*, 81–94. [[CrossRef](#)]
11. Sun, D.; Zhang, L.; Liang, G. Review on self-healing behavior of asphalt concrete(1) mechanism and characterization methods of self-healing behavior. *Pet. Asph.* **2011**, *5*, 4.
12. Garcia-Morales, M.; Partal, P.; Navarro, F.J.; Martinez-Boza, F.; Gallegos, C.; Gonzalez, N.; Gonzalez, O.; Munoz, M.E. Viscous properties and microstructure of recycled eva modified bitumen. *Fuel* **2004**, *83*, 31–38. [[CrossRef](#)]
13. Sung, Y.T.; Kum, C.K.; Lee, H.S.; Kim, J.S.; Yoon, H.G.; Kim, W.N. Effects of crystallinity and crosslinking on the thermal and rheological properties of ethylene vinyl acetate copolymer. *Polymer* **2005**, *46*, 11844–11848. [[CrossRef](#)]
14. Carreau, P.J. *Rheology of Polymeric Systems: Principles and Application*; Hanser Publishers: München, Germany, 1997.
15. Heyes, D.M.; Mitchell, P.J.; Visscher, P.B. Viscoelasticity and near-newtonian behaviour of concentrated dispersions by Brownian dynamics simulations. In *Trends in Colloid and Interface Science VIII*; Springer: Berlin, Germany, 1994; pp. 179–182.
16. Li, C.; Chen, Z.W.; Wu, S.P.; Li, B.; Xie, J.; Xiao, Y. Effects of steel slag fillers on the rheological properties of asphalt mastic. *Constr. Build. Mater.* **2017**, *145*, 383–391. [[CrossRef](#)]
17. Li, C.; Xiao, Y.; Chen, Z.W.; Wu, S.P. Crack resistance of asphalt mixture with steel slag powder. *Emerg. Mater. Res.* **2017**, *6*, 214–218. [[CrossRef](#)]
18. Baqersad, M.; Hamed, A.; Mohammadafzali, M.; Ali, H. Asphalt mmixture segregation detection: Digital image processing approach. *Adv. Mater. Sci. Eng.* **2017**, *2017*, 9493408. [[CrossRef](#)]
19. Barrett, P.J. The shape of rock particles, a critical review. *Sedimentology* **1980**, *27*, 291–303. [[CrossRef](#)]
20. Masad, E.; Olcott, D.; White, T.; Tashman, L. Correlation of fine aggregate imaging shape indices with asphalt mixture performance. *Geomaterials* **2001**, *1757*, 148–156. [[CrossRef](#)]
21. Masad, E.A. *Aggregate Imaging System (AIMS): Basics and Applications*; Texas Transportation Institute: College Station, TX, USA, 2005.
22. Gudimettla, J.; Myers, L.A. AIMS: The Future in Rapid, Automated Aggregate Shape and Texture Measurement. In Proceedings of the Conference of the Canadian Technical Asphalt Association, Charlottetown, PE, Canada, 5–8 November 2006.
23. Wang, H.; Al-Qadi, I.L.; Faheem, A.F.; Bahia, H.U.; Yang, S.H.; Reinke, G.H. Effect of mineral filler characteristics on asphalt mastic and mixture rutting potential. *Transp. Res. Rec.* **2011**, *2208*, 33–39. [[CrossRef](#)]
24. Chen, Z.W.; Xie, J.; Xiao, Y.; Chen, J.Y.; Wu, S.P. Characteristics of bonding behavior between basic oxygen furnace slag and asphalt binder. *Constr. Build. Mater.* **2014**, *64*, 60–66. [[CrossRef](#)]
25. Cardone, F.; Frigio, F.; Ferrotti, G.; Canestrari, F. Influence of mineral fillers on the rheological response of polymer-modified bitumens and mastics. *J. Traffic Transp. Eng.* **2015**, *2*, 373–381. [[CrossRef](#)]



MDPI
St. Alban-Anlage 66
4052 Basel
Switzerland
Tel. +41 61 683 77 34
Fax +41 61 302 89 18
www.mdpi.com

Materials Editorial Office
E-mail: materials@mdpi.com
www.mdpi.com/journal/materials



MDPI
St. Alban-Anlage 66
4052 Basel
Switzerland

Tel: +41 61 683 77 34
Fax: +41 61 302 89 18

www.mdpi.com



ISBN 978-3-03921-015-2